

Assessment and preservation of climate signals in multi-proxy tree-ring chronologies from Europe

Dissertation

zur Erlangung des Grades

„Doktor der Naturwissenschaften“

im Promotionsfach Geographie

am Fachbereich Chemie, Pharmazie, Geographie und Geowissenschaften

der Johannes Gutenberg-Universität Mainz

Philipp Caspar Marie Römer

geb. in Düsseldorf

Mainz, den 20. August 2024

Gutachter: Not available online.

Tag der mündlichen Prüfung: 5. November 2024

D77 (Dissertation Universität Mainz)

Summary

Tree rings provide precise annual dating of past climatic and ecological events, offering unique insights into the timing, frequency, and magnitude of natural environmental changes and their impact on human history. However, statistical age-trend removal, heteroscedasticity, and non-stationary climate-growth responses frequently challenge tree-ring width (TRW) and maximum latewood density (MXD) measurements in capturing climate information beyond multicentennial to millennial timescales. Novel proxies, including stable carbon ($\delta^{13}\text{C}$), oxygen ($\delta^{18}\text{O}$), and hydrogen ($\delta^2\text{H}$) isotopes, as well as xylem anatomical traits, show great promise in addressing these challenges. Yet, long and well-replicated isotopic and wood anatomical records remain rare and are currently limited to a few sites.

This dissertation addresses the aforementioned topic by (I) analyzing non-stationary TRW and MXD responses to temperature and hydroclimate conditions; (II) introducing a methodological advancement that enables faster and more resource-efficient development of wood anatomical data; (III) evaluating the skill of annually resolved and non-pooled $\delta^{13}\text{C}$ in improving relict wood dating and preserving climate signals in early chronology periods; (IV) examining the presence of age trends in cellulose and lignin methoxy $\delta^{13}\text{C}$, $\delta^{18}\text{O}$, and $\delta^2\text{H}$; and (V) assessing the paleoclimatic skill of TRW, MXD, $\delta^{13}\text{C}$, $\delta^{18}\text{O}$, $\delta^2\text{H}$, radial lumen diameter (D_{rad}), and cell wall thickness (CWT) through a comprehensive evaluation of covariances and climate signals. For this, a new southwest German TRW network, an 850-year-long *Pinus nigra* MXD chronology from Corsica (France), and new isotopic and wood anatomical data of Bosnian pines (*Pinus heldreichii*) from Mt. Smolikas (Greece) are established within the framework of this thesis.

Key findings include the detection of drought-related, non-stationary TRW and MXD responses to temperature in central and southern European forests, the strength of non-pooled cellulose $\delta^{13}\text{C}$ measurements in enhancing the crossdating precision of relict pine stems and preserving climatic signals in early chronology periods, and the advantage of isotopic and anatomical data over TRW for reconstructing past Eastern Mediterranean precipitation variability at interannual to multicentennial timescales. The results of this thesis pave the way for a better understanding of late-Holocene hydroclimate dynamics in the Mediterranean and underscore the importance of integrating isotopic, particularly cellulose $\delta^{13}\text{C}$, and wood anatomical data into existing tree-ring networks to improve paleoclimate reconstructions and future climate projections.

Zusammenfassung

Baumringe ermöglichen die jahrgenaue Datierung vergangener klimatischer und ökologischer Ereignisse und gewähren damit Einblicke in das Timing, die Häufigkeit und das Ausmaß natürlicher Umweltveränderungen sowie deren Auswirkungen auf die Menschheitsgeschichte. Die Entfernung von Alterstrends, Heteroskedastizität und nichtstationäre Klima-Wachstumsreaktionen stellen jedoch erhebliche Herausforderungen für Jahrringbreite (TRW) und maximale Spätholzdichte (MXD) Messungen dar, wenn es darum geht, Klimainformationen auf hundert- bis tausendjährigen Zeitskalen zu erfassen. Neue Proxys wie stabile Kohlenstoff- ($\delta^{13}\text{C}$), Sauerstoff- ($\delta^{18}\text{O}$) und Wasserstoffisotope ($\delta^2\text{H}$) sowie holzanatomische Merkmale zeigen großes Potenzial, diese Herausforderungen zu überwinden. Allerdings sind lange und gut replizierte Zeitreihen dieser Proxys noch selten und auf wenige Standorte begrenzt.

Die vorliegende Dissertation adressiert diese Thematik durch: (I) die Analyse nicht-stationärer TRW- und MXD-Reaktionen auf Temperatur- und Hydroklimabedingungen; (II) die Etablierung einer verbesserten Methode zur effizienteren Erstellung von holzanatomischen Daten; (III) die Bewertung des Potentials von jährlich aufgelösten und individuellen $\delta^{13}\text{C}$ Messungen zur besseren Reliktholzdatierung und zur Erhaltung von Klimasignalen in frühen Zeitperioden; (IV) die Untersuchung von Alterstrends in Zellulose und Lignin-methoxy $\delta^{13}\text{C}$, $\delta^{18}\text{O}$ und $\delta^2\text{H}$; sowie (V) die Bewertung des paläoklimatischen Potentials von TRW, MXD, $\delta^{13}\text{C}$, $\delta^{18}\text{O}$, $\delta^2\text{H}$, des radialen Lumen-Durchmesser (D_{rad}) und der Zellwanddicke (CWT) durch eine umfassende Analyse von Kovarianzen und Klimasignalen. Hierzu wird ein südwestdeutsches Jahrringbreiten-Netzwerk, eine 850-Jahre-lange MXD-Chronologie von korsischen Schwarzkiefern (*Pinus nigra*) sowie neue isotopische und holzanatomische Messungen an Bosnischen Kiefern (*Pinus heldreichii*) vom Smolikas-Berg in Griechenland präsentiert.

Die Schlüsselbefunde dieser Arbeit umfassen die Identifikation von dürrebedingten, nicht-stationären TRW- und MXD-Reaktionen auf Temperaturen in Zentral- und Südeuropa, die Stärke individueller Zellulose- $\delta^{13}\text{C}$ -Messungen zur verbesserten Reliktholzdatierung und Klimasignalerhaltung in frühen Zeitperioden sowie den Vorteil von isotopischen und holzanatomischen Daten gegenüber TRW bei der Rekonstruktion vergangener Niederschlagsvariabilität im östlichen Mittelmeerraum. Die Ergebnisse dieser Dissertation ebnen den Weg zu einem umfangreicheren Verständnis der spätholozänen Hydroklimadynamik im Mittelmeerraum und betonen die Notwendigkeit, isotopische, insbesondere Zellulose- $\delta^{13}\text{C}$, sowie holzanatomische Daten in bestehende Jahrringnetzwerke zu integrieren, um Paläoklimarekonstruktionen und zukünftige Klimaprognosen zu verbessern.

Acknowledgements

Not available online.

Table of contents

Summary	I
Zusammenfassung	II
Acknowledgements	III
Table of contents	IV
1 Introduction	1
1.1 Tree-ring proxies	2
1.2 Objectives and structure of this dissertation.....	4
2 Growth characteristics and drought vulnerability of southwest German spruce and pine	9
2.1 Introduction	10
2.2 Material and methods.....	11
2.2.1 <i>Study area and climate</i>	11
2.2.2 <i>Tree-ring width and basal area increment data</i>	13
2.2.3 <i>Detrending and chronology development</i>	14
2.2.4 <i>Climate data and calibration</i>	15
2.3 Results	15
2.3.1 <i>Southwest German growth characteristics</i>	15
2.3.2 <i>Network covariance</i>	18
2.3.3 <i>Network climate sensitivity</i>	19
2.4 Discussion.....	21
2.4.1 <i>Conifer growth characteristics</i>	21
2.4.2 <i>Network covariance</i>	22
2.4.3 <i>Growth responses to summer drought</i>	23
2.4.4 <i>Growth responses to late-winter temperatures</i>	25
2.5 Conclusion	26
2.6 Acknowledgements	26
2.7 References.....	27
2.8 Supplementary materials	35

3 Reduced temperature sensitivity of maximum latewood density formation in high-elevation Corsican pines under recent warming	41
3.1 Introduction	42
3.2 Material and methods.....	45
3.2.1 <i>Wood density data and chronology development</i>	45
3.2.2 <i>Climate data and signal estimation</i>	47
3.3 Results	48
3.3.1 <i>MXD chronology characteristics</i>	48
3.3.2 <i>Climate sensitivity of Corsican MXD</i>	51
3.4 Discussion.....	54
3.4.1 <i>Chronology variants and characteristics</i>	54
3.4.2 <i>Bimodal temperature signals</i>	55
3.4.3 <i>Fading temperature signals</i>	57
3.5 Conclusion	59
3.6 Acknowledgements	60
3.7 References.....	60
3.8 Supplementary materials	68
4 Review of embedding and non-embedding techniques for quantitative wood anatomy	71
4.1 Introduction	72
4.2 Materials and methods.....	73
4.3 Results and discussion	74
4.4 Conclusion	80
4.5 Acknowledgements	80
4.6 References.....	80
4.7 Supplementary materials	84
5 Multi-proxy crossdating extends the longest high-elevation tree-ring chronology from the Mediterranean	85
5.1 Introduction	86
5.2 Material and methods.....	87
5.2.1 <i>TRW and MXD measurements</i>	87
5.2.2 <i>$\delta^{13}\text{C}$ measurements</i>	89

5.2.3 Chronology development.....	90
5.2.4 Radiocarbon dating.....	90
5.3 Results and discussion	91
5.3.1 TRW, MXD, and $\delta^{13}\text{C}$ chronology statistics	91
5.3.2 Dendrochronological dating of Pine16a	92
5.3.3 Radiocarbon verification	93
5.3.4 Chronology improvements.....	94
5.4 Applications, limitations, and conclusions	96
5.5 Acknowledgments.....	97
5.6 References.....	98
5.7 Supplementary materials	104
6 Tree-ring stable isotopes in cellulose and lignin methoxy groups reveal different age-related behaviour.....	107
6.1 Introduction	108
6.2 Material and methods.....	109
6.2.1 Study site and tree-ring data.....	109
6.2.2 Stable isotope measurements	111
6.2.3 Data treatment.....	112
6.2.4 Age-trend analysis	113
6.3 Results	114
6.3.1 Data characteristics	114
6.3.2 Age-trend observations.....	117
6.4 Discussion.....	119
6.4.1 Inter- and intra-proxy differences	119
6.4.2 Age trends in TRSI series.....	121
6.5 Conclusion	123
6.6 Acknowledgements.....	124
6.7 References.....	124
6.8 Supplementary materials	131
7 Covariance and climate signals among state-of-the-art tree-ring proxies..	135
7.1 Introduction	136
7.2 Material and methods.....	138

7.2.1 <i>TRW and MXD measurements</i>	138
7.2.2 <i>Stable isotope measurements</i>	138
7.2.3 <i>Quantitative wood anatomy</i>	139
7.2.4 <i>Data treatment and chronology development</i>	140
7.2.5 <i>Meteorological data and climate signal detection</i>	141
7.3 Results	142
7.3.1 <i>Proxy characteristics and covariance</i>	142
7.3.2 <i>Climate signals</i>	144
7.3.3 <i>QWA sector chronologies</i>	146
7.4 Discussion.....	149
7.4.1 <i>Proxy characteristics and covariance</i>	149
7.4.2 <i>Climate signals in TRW and MXD</i>	150
7.4.3 <i>Climate signals in stable isotopes</i>	152
7.4.4 <i>Climate signals in wood anatomical traits</i>	153
7.4.5 <i>Paleoclimatic skill of the tree-ring proxies</i>	154
7.5 Conclusion	155
7.6 Acknowledgments.....	156
7.7 References.....	156
7.8 Supplementary materials	165
8 Conclusion and outlook	174
9 References	178
List of figures	191
List of tables	202
List of abbreviations.....	203
Curriculum vitae.....	204
Scientific publications	205
Conference contributions.....	206

1 Introduction

Tree rings are one of the most valuable archives for placing recent environmental changes into the long-term context of Common Era natural climate variability (Büntgen et al. 2021; Esper et al. 2024). Unlike other natural archives, such as ice cores or lake and marine sediments, tree-ring measurements offer precise annual dating of past climatic and ecological events, including post-volcanic cooling (Briffa et al. 1998a; Schneider et al. 2017) and regional insect outbreaks (Büntgen et al. 2009; Esper et al. 2007). This temporal precision makes tree rings essential for understanding the timing, frequency, and magnitude of past environmental changes and their profound implications for human history (Büntgen et al. 2011; McCormick et al. 2012). Furthermore, the extensive distribution of trees across the Earth's temperate and boreal zones, particularly in the Northern Hemisphere, enhances their utility as paleoclimatic archives by providing comprehensive spatial coverage that facilitates the reconstruction of past climate variability at regional to hemispheric scales (Anchukaitis et al. 2017; Briffa et al. 2001, 2004; Büntgen et al. 2020a; D'Arrigo et al. 2006; Esper et al. 2024).

The longevity of trees and the unique possibility of crossdating relict wood, such as subfossil, archeological, or historical construction timber (Fritts 1976), enable the characterization of multicentennial-to-millennial-scale climate variability, surpassing the temporal scope of instrumental observations. However, non-stationary climate-growth responses and a large-scale decoupling of northern-latitude tree-ring records from regional temperature trends since the mid-20th century question the suitability of tree-ring width (TRW) and maximum latewood density (MXD) measurements to accurately reconstruct past climate conditions, particularly temperature fluctuations (Briffa et al. 1998b; D'Arrigo 2008; Jacoby & D'Arrigo 1995). Existing reconstructions based on TRW and MXD might underestimate temperatures during the putative Roman (~250 BCE - 300 CE) and Medieval (~950-1250 CE) Warm Periods, potentially skewing the accurate assessment of recent warming trends (IPCC 2021).

Additionally, the removal of age-related (non-climatic) trends in TRW and MXD through standardization, which is essential for climate calibration of these proxies (Bräker 1981), can result in a loss of valuable low-frequency climate information (Cook et al. 1995). Consequently, TRW- and MXD-derived reconstructions may not capture the full spectrum of climate variability. This potential loss of climate information, along with the fading temperature sensitivity of TRW and MXD chronologies in recent decades, underscores the urgent need for alternative proxy measurements to enhance our understanding of natural climate variability throughout the late Holocene (Büntgen 2022; Esper & Büntgen 2021). Such a long-term perspective is key for disentangling the relative contributions of natural and anthropogenic forcing to recent warming, improving climate model simulations, and developing effective strategies for climate change mitigation and adaptation.

1.1 Tree-ring proxies

Tree-ring formation is based on the annual cycle of tree growth (spring-autumn) and dormancy (winter), resulting from seasonal climate fluctuations in extratropical regions (Fritts 1976). During the growing season, the vascular cambium of gymnosperms, located beneath the bark and composed of meristematic cells, produces undifferentiated xylem cells (tracheids) through periclinal cell division. These tracheids then undergo successive differentiation processes, including cell expansion, secondary cell wall deposition and lignification, and programmed cell death (Plomion et al. 2001; Rathgeber et al. 2016). In spring and early summer, tracheid lumina are notably enlarged for efficient water uptake, resulting in the formation of light-colored earlywood. As the growing season progresses towards late summer and autumn, narrower tracheids with thickened and strongly lignified cell walls develop to ensure mechanical strength before cambial activity ceases. This denser part of the ring represents the latewood. The sharp transitions between the dense latewood cells and enlarged earlywood cells of the following year mark the ring boundaries and enable the annual dating precision of tree rings (Fig. 1.1).

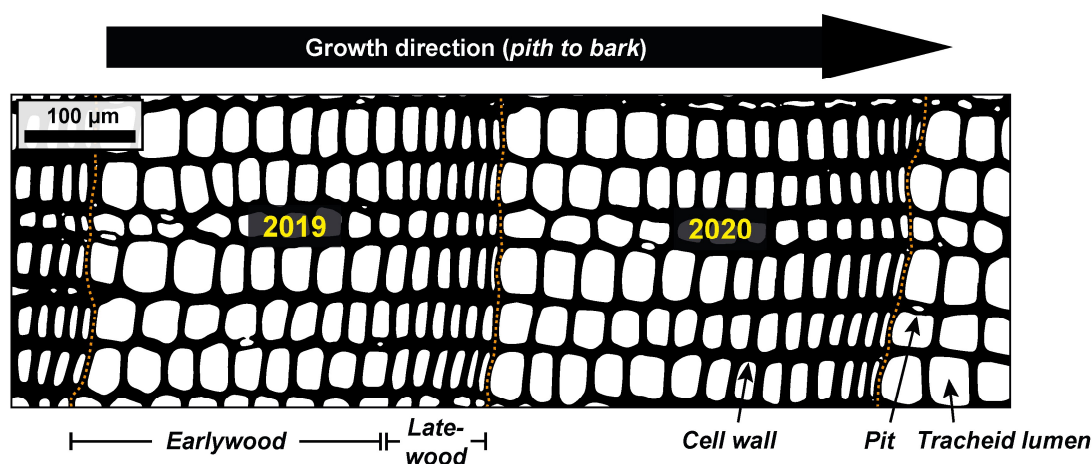


Fig. 1.1 Magnified cross-section of a gymnosperm xylem (*Pinus heldreichii* from Mt. Smolikas, Greece). The image shows two consecutive tree rings with large earlywood and smaller latewood cells. Tree-ring boundaries are marked by orange dashed lines.

The width of each ring generally reflects the growing conditions encountered by the tree, where wider rings often signify favorable conditions such as abundant rainfall or warm temperatures, while narrower rings indicate periods of environmental stress like drought or cold (Fritts 1976). This dependence of **TRW** on climate conditions typically leads to synchronous growth patterns across trees, sites, and regions, facilitating the study of species-specific climate-growth responses at local to continental scales (St. George 2014). Climate signals in TRW are particularly strong in regions where temperature (high latitudes or altitudes) or water availability (arid environments) primarily limit tree growth, thereby enabling the reconstruction of past temperature (Esper et al. 2016), precipitation (Ljungqvist et al. 2020), and drought variability (Cook et al. 2004, 2015). In temperate regions, however, the assessment of climate-growth responses

is more challenging due to the complex interactions of biotic and abiotic factors influencing tree growth (Babst et al. 2013; Neuwirth et al. 2007).

Over past decades, radiodensitometric measurements of wood density have significantly advanced dendroclimatological research (Björklund et al. 2019). Specifically **MXD**, representing the peak latewood density of each ring, has emerged as a valuable warm-season temperature proxy. MXD measurements exhibit strong common signals among trees and sites (Briffa et al. 2002, 2004), demonstrate superior calibration against instrumental temperatures compared to TRW (Esper et al. 2016; Frank & Esper 2005; Hartl et al. 2022), contain less non-climatic noise (Esper et al. 2015; Franke et al. 2013), and are less affected by large-scale disturbances (Rydval et al. 2018). The recent integration of MXD data into hemispheric tree-ring networks has significantly improved the statistical skill of large-scale temperature reconstructions (Christiansen & Ljungqvist 2017; Esper et al. 2018). Moreover, MXD facilitates the reconstruction of past temperature variability in regions where TRW has proven inadequate as a temperature proxy, such as the Mediterranean (Büntgen et al. 2017, 2024; Esper et al. 2020a, 2020b; Leonelli et al. 2017). However, similar to TRW, age-related trends in MXD necessitate standardization for accurate paleoclimatic reconstruction (Bräker 1981).

In addition to TRW and MXD, tree-ring stable isotopes (**TRSI**), including stable carbon ($\delta^{13}\text{C}$), oxygen ($\delta^{18}\text{O}$), and hydrogen ($\delta^2\text{H}$) isotope ratios, have recently emerged as robust proxies to reconstruct past climate fluctuations at interannual to multimillennial timescales (e.g., Büntgen et al. 2021; Nakatsuka et al. 2020; Yang et al. 2021). To minimize non-climatic noise resulting from mobile compounds and their transport along parenchyma cells (Gessler et al. 2014), TRSI measurements are typically performed on α -cellulose. Cellulose TRSIs, in particular $\delta^{13}\text{C}$ and $\delta^{18}\text{O}$, usually exhibit strong covariances across tree species and space (Hartl-Meier et al. 2015; Saurer et al. 2008; Treydte et al. 2007), indicate strong and robust correlations with temperature, hydroclimatic, and radiative variables (Gagen et al. 2022), frequently lack long-term ontogenetic trends (Arosio et al. 2020; Büntgen et al. 2020b; Gagen et al. 2007; Torbenson et al. 2022; Young et al. 2011), and require fewer trees than TRW or MXD for establishing reliable site chronologies (Belmecheri et al. 2022; Leavitt 2010). In addition, $\delta^{13}\text{C}$ and $\delta^{18}\text{O}$ often exhibit strong climatic signals in temperate regions where conventional proxies typically fail as paleoclimate predictors (Büntgen et al. 2021; Hartl-Meier et al. 2015; Labuhn et al. 2016).

Climate signals in cellulose $\delta^2\text{H}$ are generally weaker and more species- and site-specific than those of $\delta^{13}\text{C}$ and $\delta^{18}\text{O}$ (Vitali et al. 2022). $\delta^2\text{H}$ measurements on lignin methoxy groups, however, have shown great potential in reconstructing European-scale temperature changes (Anhäuser et al. 2020; Wieland et al. 2022). Since lignin is formed in the xylem, the $\delta^2\text{H}$ values of methoxy groups are unaffected by the evaporative ^2H enrichment of leaf water and therefore closely reflect the temperature-controlled $\delta^2\text{H}$ signature of precipitation (Anhäuser et al. 2017;

Dansgaard 1964). TRSI measurements on methoxy groups provide a fast and cheap alternative to cellulose isotopes but require more material (Greule et al. 2008, 2009; Keppler et al. 2007). Besides $\delta^2\text{H}$, lignin methoxy $\delta^{13}\text{C}$ has also demonstrated significant temperature signals across various Eurasian sites (Gori et al. 2013; Lu et al. 2020; Riechelmann et al. 2016; Wang et al. 2020; Wieland et al. 2022). However, necessary corrections to address the recent depletion of atmospheric ^{13}C due to anthropogenic CO_2 emissions (Suess effect; Keeling 1979) and the increasing leaf-internal ^{13}C discrimination under elevated CO_2 concentrations (McCarroll et al. 2009; Waterhouse et al. 2004) pose challenges to the calibration efforts of both cellulose and lignin methoxy $\delta^{13}\text{C}$ chronologies.

Recent technological and methodological advancements in quantitative wood anatomy (**QWA**) have further opened new avenues for high-resolution paleoclimatology, significantly enhancing our ability to assess climate signals in tree-ring structures with greater spatiotemporal precision (Fonti et al. 2009; Prendin et al. 2017; von Arx & Carrer 2014). However, the creation of wood anatomical chronologies still requires significantly more labor compared to TRW or MXD (von Arx et al. 2016), resulting in QWA data often being less extensively replicated. Further innovations in microscopic slide preparation and digital image analysis are therefore urgently needed to improve measurement efficiency and enable the development of large-scale QWA networks. Key paleoclimatic QWA metrics include various lumen dimensions such as radial lumen diameter (D_{rad}), hydraulic diameter (D_{h}), and mean lumen area (MLA), as well as measurements of radial and tangential cell wall thickness ($\text{CWT}_{\text{rad}}/\text{CWT}_{\text{tan}}$) and wood anatomical densities (Balanzategui et al. 2021; Björklund et al. 2020, Carrer et al. 2018; Lopez-Saez et al. 2023; Seftigen et al. 2022; Ziaco et al. 2016). Given the potential of these proxies to significantly improve past climate estimates (Björklund et al. 2023), the development of new long-term QWA records is crucial to further advance high-resolution paleoclimatology.

1.2 Objectives and structure of this dissertation

This dissertation examines the aforementioned tree-ring proxies across a variety of European tree species, including *Fagus sylvatica*, *Larix decidua*, *Picea abies*, *Pinus cembra*, *Pinus heldreichii*, *Pinus nigra*, and *Pinus sylvestris* (**Fig. 1.2**), with the aim of providing a comprehensive assessment of their strengths and limitations for paleoclimatic, archaeological, and ecological research. Chapters 2-7 present new findings from dendrochronological case studies, focusing specifically on the covariance among individual series, the climate sensitivity of these proxies, and the presence of ontogenetic trends, in order to identify the most suitable proxies for climate reconstruction trials. Chapter 4 introduces methodological advances aimed at faster and more efficient QWA measurements. Results are compared with previous research to gain a deeper understanding of complementary and redundant climatic information that can be obtained from

the proxies under diverse environmental conditions, thereby providing refined tools and techniques for reconstructing past climate variability from tree-ring data.



Fig. 1.2 Location of the study sites and images of the investigated tree species: *Fagus sylvatica* (FASY), *Larix decidua* (LADE), *Picea abies* (PIAB), *Pinus cembra* (PICE), *Pinus heldreichii* (PIHE), *Pinus nigra* (PINI), and *Pinus sylvestris* (PISY).

Chapter 2, “*Growth characteristics and drought vulnerability of southwest German spruce and pine*”, introduces a tree-ring network of 1943 spruce and pine trees to assess the growth performance and climate-growth responses of *Picea abies* [L.] Karst and *Pinus sylvestris* L. along altitudinal gradients in southwest Germany. Various detrending techniques are applied to identify the optimal frequencies for climate calibration trials, and regional spruce and pine chronologies are created to evaluate species-specific climate-growth responses. The temperature and hydroclimatic signals in spruce and pine growth are discussed in the context of recent climate change and the broader scope of Central European forest growth. By assessing non-stationary climate-growth responses, this chapter highlights the complexity and limitations of TRW measurements for paleoclimate research. The author made significant contributions to the concept and methodological development, conducted data analysis and interpretation, created the figures, and drafted the manuscript with support from the co-authors. The manuscript is currently under review in the *European Journal of Forest Research*.

Chapter 3, “*Reduced temperature sensitivity of maximum latewood density formation in high-elevation Corsican pines under recent warming*”, presents an 850-year-long MXD chronology for the central Mediterranean region. The MXD record calibrates well with instrumental April-

July and September-October temperatures from 1901 to 1980 CE ($r \geq 0.52$), and aligns with the world's best replicated MXD chronology from the Spanish Pyrenees (Büntgen et al. 2017). However, despite addressing sample age issues through age-band decomposition, it fails to capture the most recent temperature increase in the 21st century. Potential plant physiological causes and paleoclimatic consequences of the non-stationary and bimodal MXD response to temperature are discussed in the context of recent warming. The author made significant contributions to the concept and methodological development, conducted data analysis and interpretation, created the figures, and wrote the manuscript with support from the co-authors. The manuscript was published in *Atmosphere* (12) in June 2021 (Römer et al. 2021).

Chapter 4, “*Review of embedding and non-embedding techniques for quantitative wood anatomy*”, examines the necessity of paraffin embedding in QWA. By comparing digital images and wood anatomical chronologies from both embedded and non-embedded microsections across a variety of coniferous and deciduous tree species, this chapter demonstrates that embedding is not essential for producing high-quality wood anatomical slides. Omitting paraffin embedding in the QWA preparation saves time and resources, avoids the utilization of harmful chemicals, and facilitates the development of QWA records with larger sample sizes, marking a significant step toward the faster establishment of QWA networks. The author made significant contributions to the concept and methodological development, participated in data analysis and interpretation, and drafted the manuscript together with Davide Frigo and the support of the other co-authors. The manuscript was published in *Dendrochronologia* (88) in July 2024 (Frigo et al. 2024).

Chapter 5, “*Multi-proxy crossdating extends the longest high-elevation tree-ring chronology from the Mediterranean*”, explores the crossdating potential of TRW, MXD, and $\delta^{13}\text{C}$ measurements and their ability to preserve environmental signals in early chronology periods. For this, new annually resolved and non-pooled $\delta^{13}\text{C}$ measurements were conducted on the α -cellulose of first millennium relict pine (*Pinus heldreichii*) samples from Mt. Smolikas, Greece. The $\delta^{13}\text{C}$ data are used to reassess and correct the crossdating of older TRW and MXD samples through a comprehensive analysis of inter-series correlations. The associated corrections are verified by wiggle-matching annual radiocarbon (^{14}C) data along the 774/775 CE cosmic event (Miyake et al. 2012). Applications and limitations of the high-resolution $\delta^{13}\text{C}$ measurements are derived, evaluated, and discussed in the broader context of archaeological and paleoclimatic research. The author made significant contributions to the concept and methodological development, conducted data analysis and interpretation, created the figures, and wrote the manuscript with support from the co-authors. The manuscript was published in *Dendrochronologia* (79) in June 2023 (Römer et al. 2023).

Chapter 6, “*Tree-ring stable isotopes in cellulose and lignin methoxy groups reveal different age-related behaviour*”, examines the presence of age-related trends in TRW, MXD, cellulose stable carbon ($\delta^{13}\text{C}_c$) and oxygen ($\delta^{18}\text{O}_c$) isotopes, and methoxy carbon ($\delta^{13}\text{C}_m$) and hydrogen ($\delta^2\text{H}_m$) isotopes. Proxy measurements are conducted on living and relict pines from Mt. Smolikas, Greece, spanning various germination and end dates over the past 1500 years. This broad temporal coverage provides an ideal framework for quantifying and evaluating biological, non-climatic age trends. However, significant level offsets between living and relict $\delta^{18}\text{O}_c$ and $\delta^2\text{H}_m$ values prevent the combined use of living and relict wood for reliable age-trend assessment, necessitating sole reliance on relict wood. The relict TRW, MXD, $\delta^{13}\text{C}_c$, and $\delta^{18}\text{O}_c$ series are converted from annual to decadal resolution to match the decadal $\delta^{13}\text{C}_m$ and $\delta^2\text{H}_m$ data and are aligned by cambial age to determine long-term age trends. The chapter draws comparisons with previous age-trend studies and provides suggestions for future paleoclimate research in the Mediterranean. The author made significant contributions to the concept and methodological development, participated in data analysis and interpretation, and drafted the manuscript together with Anna Wieland and the support of the other co-authors. The manuscript was published in *Quaternary International* (693) in May 2024 (Wieland et al. 2024).

Chapter 7, “*Covariance and climate signals among state-of-the-art tree-ring proxies*”, evaluates the potential of TRW, MXD, $\delta^{13}\text{C}_c$, $\delta^{13}\text{C}_m$, $\delta^{18}\text{O}_c$, $\delta^2\text{H}_m$, D_{rad} , and CWT for high-resolution paleoclimatic reconstructions in the Mediterranean. Proxy measurements were conducted on the same living Bosnian pines ($n = 10$ trees) from Mt. Smolikas, Greece, to assess covariance both between and within the proxies and determine their climate sensitivities. Different detrending techniques are applied in search of the optimal choice for climate calibration, and different CO_2 corrections are implemented on the $\delta^{13}\text{C}$ records to evaluate the impact on signal strength. Sub-seasonal time series of anatomical traits are generated to quantify the intra-annual variability of D_{rad} and CWT, and a principal component analysis is used to assess similarities and differences between the QWA sector chronologies and the annual proxy records. The obtained climate signals are compared with those from other Mediterranean sites to assess the proxies’ paleoclimatic skills and provide recommendations for future research. The author made significant contributions to the concept and methodological development, conducted data analysis and interpretation, created the figures, and drafted the manuscript together with Anna Wieland and the support of the other co-authors. The manuscript is currently under review in *Quaternary Science Reviews*.

2 Growth characteristics and drought vulnerability of southwest German spruce and pine

Authors: Philipp Römer*, Edurne Martínez del Castillo, Frederick Reinig, Max Torbenson, Oliver Konter, Lara Klippel, Ulf Büntgen, and Jan Esper

Status: Under review in the *European Journal of Forest Research*

Abstract

Although it is evident that forest management needs to adapt to fast changing climate conditions, there are still many uncertainties about how European tree species will perform under predicted temperature increases and associated hydroclimatic extremes. Here, we present a dendrochronological network of 1934 trees from 46 sites across southwest Germany to assess the growth performance of Norway spruce and Scots pine between 100-820 m asl under recent climatic changes. Growth comparisons including basal area increment (BAI) show that spruce ($BAI_{avg} = 15.4 \text{ cm}^2 \text{ a}^{-1}$) grew twice than pine ($BAI_{avg} = 7.3 \text{ cm}^2 \text{ a}^{-1}$) between 1952-2009 CE. Drought is the dominant driver of conifer growth but shows a transition in seasonality along elevational gradients. Below 550 m asl, both species are strongly limited by water availability during summer, while spruce stands above 550 m asl become increasingly sensitive to previous-year moisture conditions. Positive correlations with February-March temperatures indicate an increasing importance of late-winter conditions for pine growth, likely related to rapidly rising air temperatures since the late 1980s and seasonal changes in photosynthetic activity. While the positive associations with late-winter temperatures appear beneficial for pine, significant moisture limitations and BAI losses up to 68% during the driest summers call for more drought-resistant species in southwest Germany.

Keywords: climate signals, dendroecology, *Picea abies*, *Pinus sylvestris*, temperate forest, tree-ring width.

2.1 Introduction

Central European temperate forests are important terrestrial carbon sinks that mitigate global warming (Harris et al. 2021). However, the health and productivity of these forests under future climate change is highly uncertain (Bonan 2008). While rising temperatures extend the growing season and increase photosynthetic activity in spring and autumn, they also amplify the magnitude and duration of heatwaves and droughts (Masson-Delmotte et al. 2021).

Tree-ring studies offer the opportunity to quantify forest growth at annual resolution and assess its environmental forcing over past decades. Although assessing climate-growth responses in managed forests can be challenging (Esper et al. 2012), tree-ring width (TRW) is a reliable indicator of forest productivity (Xu et al. 2017) and vitality (Dobbertin 2005) that provides valuable insights into multidecadal growth trends at regional to continental scales. In Europe, forest growth has recently shown divergent trends across tree species and space (Kašpar et al. 2024; Martínez del Castillo et al. 2022; Pretzsch et al. 2023). Most species benefit from the rising air temperatures at higher latitudes and altitudes but suffer substantial growth losses at low altitudes and in southern European regions. However, growth trends are less clear in the European lowlands, where precipitation patterns remain ambiguous (Aalbers et al. 2018) and silviculture recently faces unprecedented challenges (Senf et al. 2020).

Norway spruce (*Picea abies* [L.] Karst) and Scots pine (*Pinus sylvestris* L.) are the most economically important coniferous species in Europe, accounting for ~53% of the European-wide growing stock (Korhonen & Stahl 2020). The two conifers were widely cultivated since the 18th century, as they grow fast on various types of soil and ensure high timber yields (Johann et al. 2004; Spiecker 2003). Norway spruce is a shade-tolerant tree species with a shallow root system that prefers nutrient-rich soils and naturally grows in the cold and moist environments of the boreal zone and the European mountains (Caudullo et al. 2016). In Europe, large portions of spruce were planted outside their natural distribution range, specifically in warmer and drier regions (Kölling et al. 2009). In these environments, Norway spruce is particularly susceptible to drought (e.g., Altman et al. 2017; Zang et al. 2014) and growth is frequently limited by summer precipitation (Debel et al. 2021; Esper et al. 2012; Lebourgeois 2007; Rybníček et al. 2010; van der Maaten-Theunissen et al. 2013; Zang et al. 2011), though effects on forest productivity vary with regional climate and site conditions (Krejza et al. 2021; Treml et al. 2021).

Although Scots pine is more drought resilient than Norway spruce due to a distinct plasticity in xylem anatomical structures and effective stomatal control mechanisms (Eilmann et al. 2009; Irvine et al. 1998), Central European pine growth is also frequently limited by summer moisture availability (Bose et al. 2020; Lévesque et al. 2014). In recent decades, late-winter temperatures became important for pine growth (Diers et al. 2023, 2024; Harvey et al. 2020; Janecka et al. 2020; Stolz et al. 2021), possibly reflecting a trade-off between enhanced winter and

reduced summer photosynthesis. While the underlying physiological processes are not yet well understood, there is extensive evidence for analogous late-winter temperature signals in pine growth at several low-elevation temperate forest sites (Friedrichs et al. 2009; Koprowski et al. 2012; Lebourgeois et al. 2010; Nagavciuc et al. 2019; Seidling et al. 2012).

In the lowlands and low mountain ranges of southwest Germany, the region with the highest national forest density (BMEL 2023), there is a lack of TRW data integrating measurements from multiple sites to assess the regional growth of spruce and pine during the recent periods of rapid climate change. Here, we present a TRW network for southwest Germany comprising 46 sites to (I) assess the growth performance of the two conifers during the second half of the 20th and early 21st centuries considering the influence of elevation, tree age, and microclimate, (II) identify climatic drivers of regional spruce and pine growth, and (III) evaluate how climate sensitivities of the two species may have changed under recent climate change.

2.2 Material and methods

2.2.1 Study area and climate

Between 2010 and 2021, a total of 1831 spruce (*Picea abies* [L.] Karst) and 1942 pine (*Pinus sylvestris* L.) samples were collected to establish a network of 46 sites in southwest Germany (49-51°N/6-9°E; **Fig. 2.1a**). The 22 spruce and 24 pine sites are located along altitudinal gradients ranging from 100 m asl in the Upper Rhine Valley to 820 m asl in the Rhenish Massif (**Table 2.1**). Scots pine is the dominant conifer in the lowlands (≤ 400 m asl), while Norway spruce prevails at higher elevations. The pine stands are slightly older (**Fig. 2.1b**) and predominant in the Palatinate Forest and Upper Rhine Plain on less fertile loamy sands and sandy clays, such as lean cambisols and fluvisols. In contrast, spruce grows mainly in the Rhenish massif on silty loams and clays, such as podzolic cambisols, luvisols, regosols, and stagnosols (Richter et al. 2007; Zech et al. 2014).

Table 2.1 Characteristics of the southwest German tree-ring network.

Species	Sites	n series trees	Elevation [m asl]	MSL $\pm 1\sigma$ [years]	AGR $\pm 1\sigma$ [mm]	Rbar
Norway spruce	22	1831 948	340-820	81 \pm 16	2.35 \pm 0.60	0.46
Scots pine	24	1942 986	100-570	115 \pm 26	1.57 \pm 0.47	0.50

MSL: mean segment length ± 1 standard deviation (σ). **AGR**: average growth rate [mm] calculated over the first 60 years of cambial age ($\pm 1\sigma$). **Rbar**: mean inter-series correlation of the 10SP chronologies (1952-2009 CE).

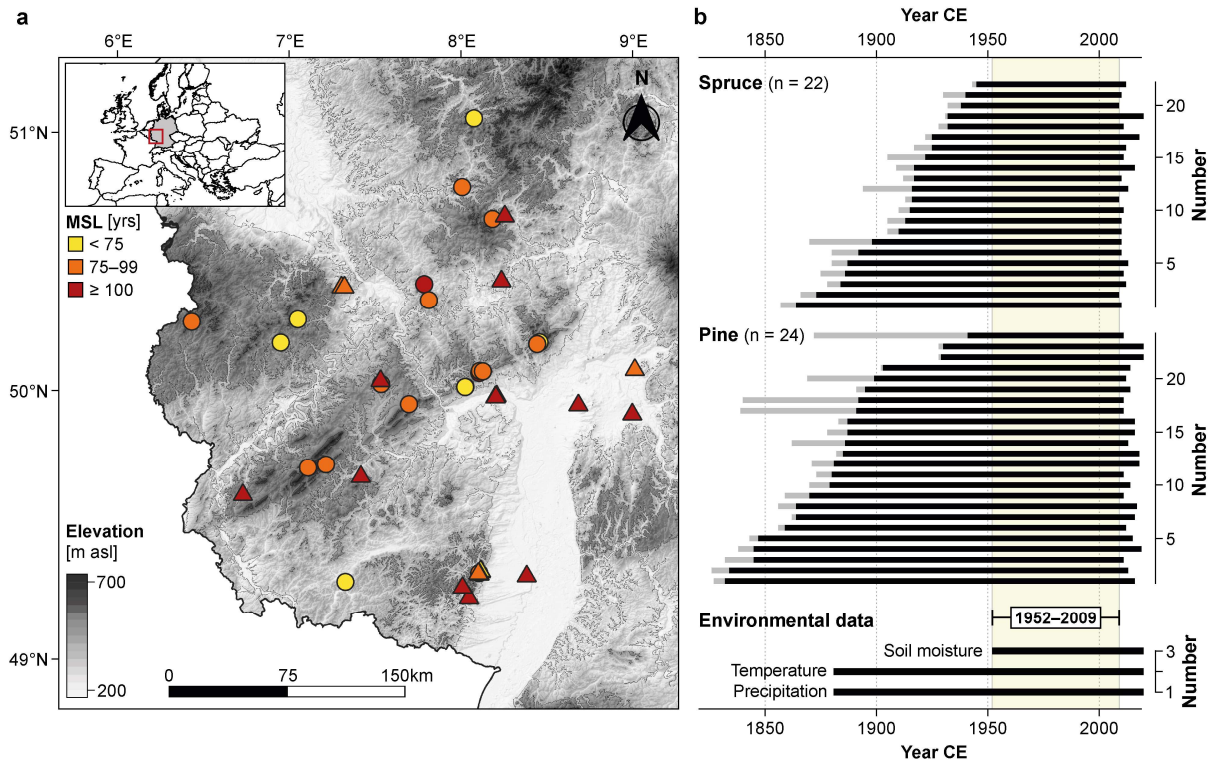


Fig. 2.1 Tree-ring and environmental data. **(a)** Topographic map showing spruce (circles) and pine (triangles) sites colored according to their mean segment lengths (MSL). **(b)** Periods covered by tree-ring chronologies and environmental records. Grey bars show the full tree-ring records, black bars indicate lengths after truncation at $n \geq 10$ series. The common period of all series (1952–2009 CE) is highlighted in light yellow.

Within the southwest German TRW network, mean annual air temperatures vary from 10.5°C at the lowest pine site (109 m asl) to 6.3°C at the highest spruce site (819 m asl), while annual rainfall totals range from 643 mm to 944 mm. Consequently, the lowlands, especially the Upper Rhine Plain, are more affected by summer drought than the low mountain ranges (**Fig. 2.2a-c**). In recent decades (1952–2009 CE), annual maximum air temperatures (T_{max}) and precipitation increased by $0.03^{\circ}\text{C a}^{-1}$ and 1 mm a^{-1} , respectively (**Fig. 2.2d-f**). Temperature and precipitation changes, however, differ notably by month. T_{max} increased distinctly more in July and August, while June–August precipitation decreased contrary to the opposing trends in the other seasons (**Fig. 2.2g-h**). As a result, soil moisture availability increased from fall to spring but decreased in late-summer (**Fig. 2.2i**).

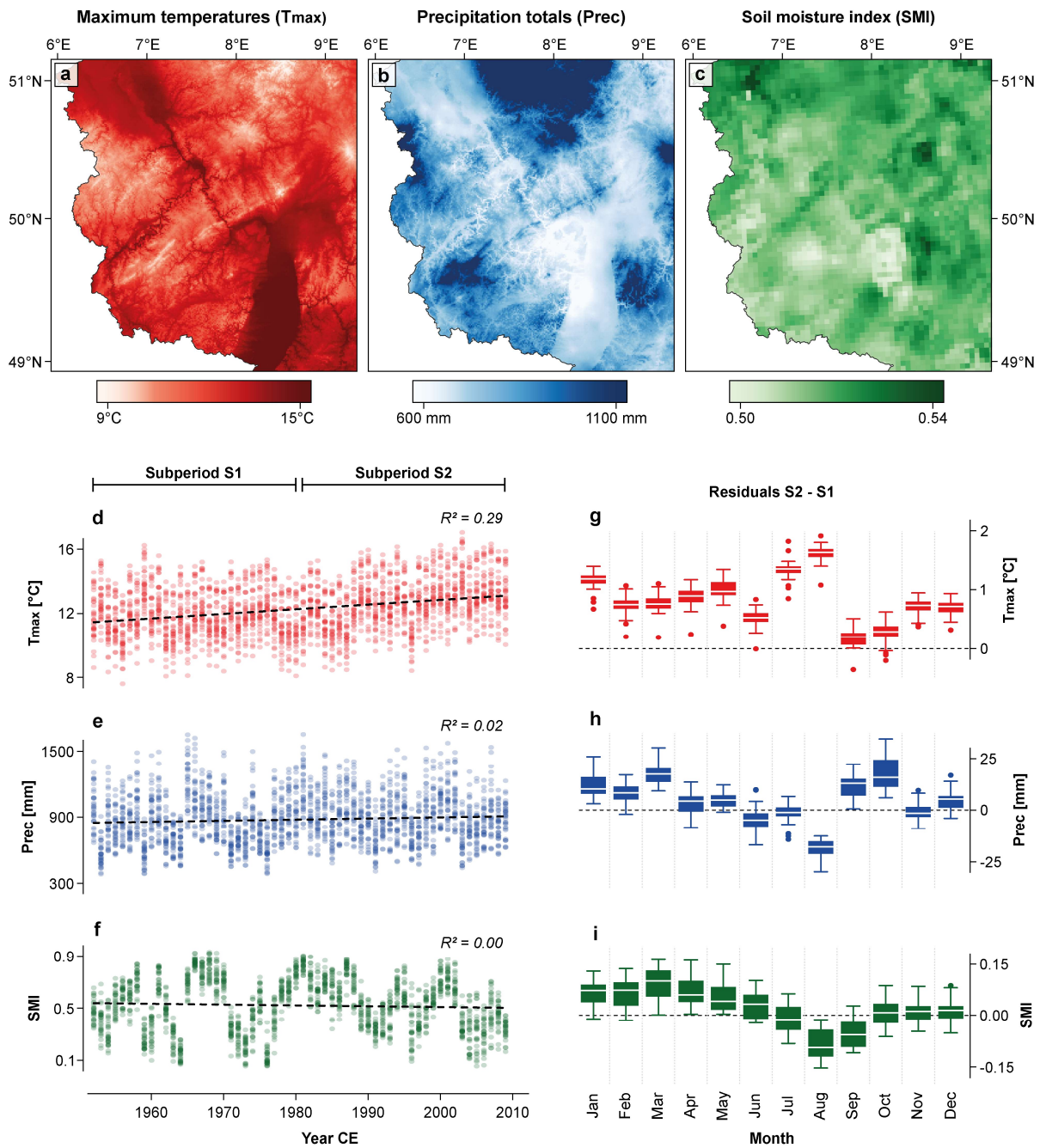


Fig. 2.2 Climate and soil moisture conditions in southwest Germany. Maps of annual (a) maximum air temperatures (T_{max}), (b) precipitation (Prec), and (c) soil moisture indices (SMI). Time series of annual (d) T_{max} , (e) Prec, and (f) SMI derived from nearby gridded data. Each dot represents one grid. Dashed lines show linear trends from 1952-2009 CE, R^2 values are the coefficients of determination. Monthly (g) T_{max} , (h) Prec, and (i) SMI changes between the subperiods S2 (1981-2009 CE) and S1 (1952-1980 CE). Boxplots show the distribution among grid cells. White bars are the medians, boxes the 25%- and 75%-quartiles, whiskers the min and max values within 1.5x the interquartile range, and dots are outliers. Positive residuals indicate higher values in the recent subperiod S2 compared to subperiod S1.

2.2.2 Tree-ring width and basal area increment data

At all sampling sites, one or two increment cores were collected at breast height (~1.3 m) from dominant and suppressed conifers using a 5-mm increment borer. The network includes 948 spruce and 986 pine trees from managed, mostly even-aged monoculture stands. Sample size

per site ranges from 39 to 148 series, with an average of 82 ± 23 (1σ) series per site (**Table S2.1**). If more than one sample was collected, the cores were extracted from opposite stem directions perpendicular to the slope to avoid compression wood. TRW was measured at an accuracy of 0.01 mm using the high-precision LINTAB 6 device (Rinntech, Heidelberg, Germany) and TSAP-Win software (Rinn 2012). Visual and statistical crossdating was performed using skeleton plots (Stokes & Smiley 1996) and the COFECHA software (Holmes 1983).

TRW measurements were averaged (per tree) and converted to basal area increments (BAI; $\text{cm}^2 \text{a}^{-1}$) using the *bai.out* function of the R package *dplR* (Bunn 2008) considering:

$$BAI = \pi (r_n^2 - r_{n-1}^2), \quad (2.1)$$

where r_n is the distance from the pith to the outer tree-ring boundary of the actual year, and r_{n-1} is the distance from the pith to the outer ring boundary of the previous year (**Fig. S2.1a**). Unlike TRW, BAI accounts for geometrical constraints of adding a cross-sectional area to an expanding stem radius. However, as age-related BAI trends may distort comparisons among different tree and stand ages (Weiner & Thomas 2001), we additionally calculated average growth rates (AGR) over the first 60 years of tree age by aligning each TRW series according to its cambial age (**Fig. S2.1b**). The arithmetic means of the age-aligned series are referred to as regional curves (Esper et al. 2003). Potential dependencies of BAI and AGR on tree age, elevation, and microclimatic conditions (air temperature, precipitation, and soil moisture) were evaluated using linear regression models.

2.2.3 Detrending and chronology development

Non-climatic trends were removed from the TRW series by calculating residuals from cubic smoothing splines with a 50% frequency-response cutoff at 10 years (10SP) and from negative exponential curves (EXP; **Fig. S2.1c**). Alternative spline detrendings were applied to evaluate standardization effects on high-to-low frequency chronology variance and network covariance (**Fig. S2.2**). Prior to each detrending, a data-adaptive power transformation was used to minimize the heteroscedastic structure of the TRW data (Cook & Peters 1997). Site chronologies were produced using the ARSTAN software (ARS41d; Cook et al. 2017) by calculating bi-weight robust means of the detrended series. The site chronologies were variance-stabilized (Frank et al. 2007) and truncated at $n < 10$ series. Inter-series correlations (R_{bar}) were computed over 30-year segments with a 29-year overlap to estimate changes in covariance inherent in the site chronologies (Cook & Kairiukstis 1990). Network covariance was assessed by calculating Pearson correlations between the detrended site chronologies over the 1952-2009 CE common period.

2.2.4 Climate data and calibration

High-resolution temperature and precipitation data (1 x 1 km) from the German Weather Service (<http://www.dwd.de/cdc>; Kaspar et al. 2013) and soil moisture data (4 x 4 km) from the German Drought Monitor (<https://www.ufz.de/index.php?en=37937>; Zink et al. 2016) were used to characterize the conditions at each sampling site. We extracted monthly time series of T_{\max} , precipitation, and the soil moisture index (SMI) from grids closest to each site and calculated seasonal means. The SMI indicates water availability in the top 180 cm of the soil (Zink et al. 2016). April-October was defined as the growing season based on monthly temperature and daily dendrometer data (Klippel et al. 2017).

Climate-growth relationships were assessed by computing Pearson correlations between the 10SP site chronologies and the environmental variables using the R package *treeclim* (Zang & Biondi 2015). As with TRW, the environmental data were high-pass filtered prior to correlation analyses by calculating residuals from cubic smoothing splines with a 50% frequency cut-off at 10 years. Bootstrap correlations ($n = 1000$) were computed over the 1952-2009 CE period using an 18-month time window ranging from previous-year May to current-year October. Field correlations were calculated using the regional spruce and pine chronologies with $0.25^\circ \times 0.25^\circ$ gridded EOBS data (v25.0e; Cornes et al. 2018) in the KNMI Climate Explorer (Trouet & van Oldenborgh 2013), and 21-year running correlations were applied to assess the stationarity of climate signals.

2.3 Results

2.3.1 Southwest German growth characteristics

The regional curves of the age-aligned TRW series show distinct negative exponential trends that are fairly homogeneous across the 22 spruce and 24 pine sites (**Fig. 2.3a-d**). TRW decreases as a function of age, though AGRs of spruce are significantly higher than those of pine ($1.2\text{-}3.5 \text{ mm a}^{-1}$ versus $1.0\text{-}2.7 \text{ mm a}^{-1}$, $p < 0.01$). The lower AGRs of pine are due to a steeper TRW decline in the first ~25 years of cambial age and persistently lower values thereafter. The total number of rings per series varies from five to 154 years among the 1831 individual spruce series ($\bar{x} = 82$ years) and from 16 to 190 years among the 1942 individual pine series ($\bar{x} = 118$ years), indicating a higher average tree age for the pine samples.

The BAI chronologies reveal significant ($p < 0.001$) growth differences between spruce ($15.4 \pm 4.6 \text{ cm}^2 \text{ a}^{-1}$) and pine ($7.3 \pm 3.3 \text{ cm}^2 \text{ a}^{-1}$) from 1952-2009 CE (**Fig. 2.3e-f**). While spruce BAI increased strongly by $\sim 0.17 \text{ cm}^2 \text{ a}^{-1}$ throughout the 20th century, the pine BAI rose moderately by $\sim 0.08 \text{ cm}^2 \text{ a}^{-1}$ during the first half of the 20th century, and remained fairly stable thereafter. Alignment of the BAI series by cambial age outlines notable age trends consisting of growth increases up to ~110 years, followed by a stationary growth plateau and declining phase (only

for pine) as the trees become older (**Fig. S2.3**). The initial growth acceleration is much stronger in spruce than in pine, explaining the substantial BAI differences between the overall younger spruce and older pine stands.

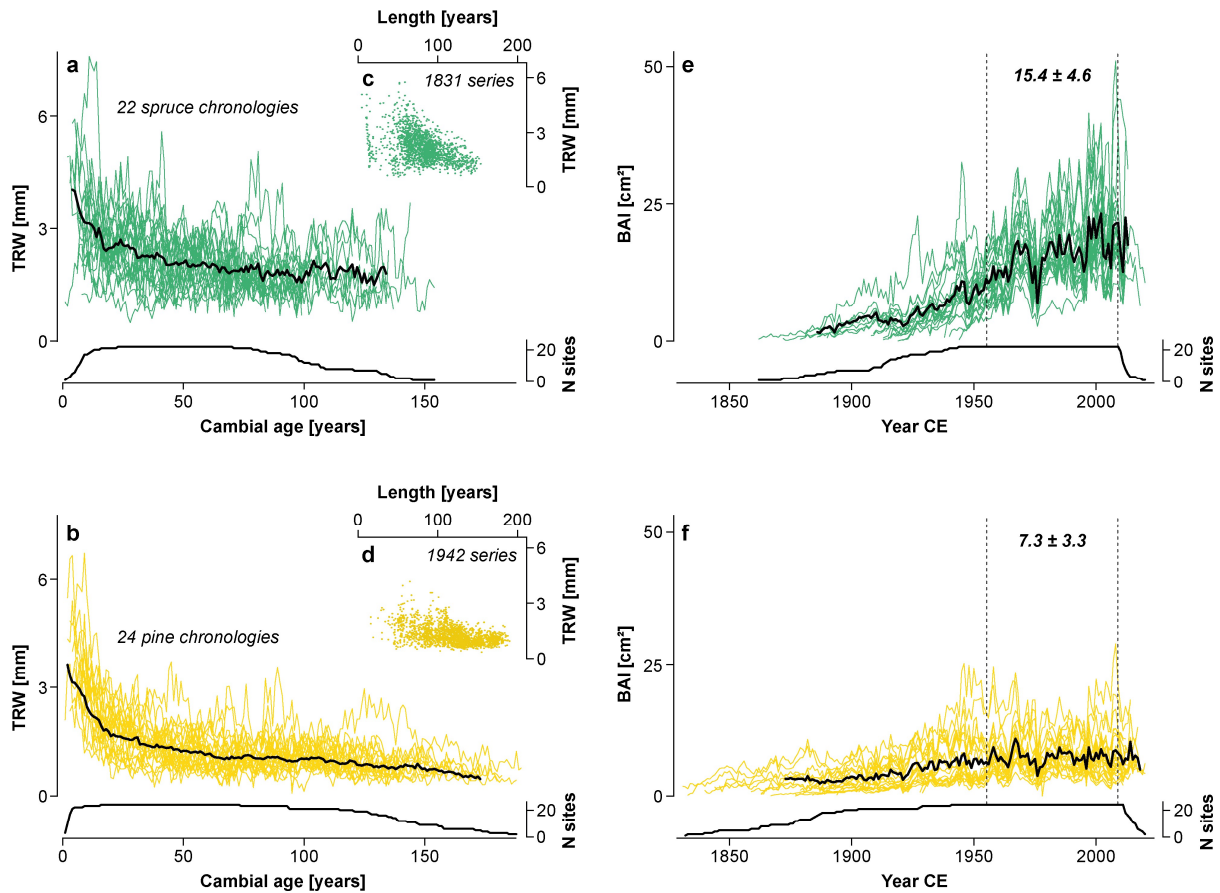


Fig. 2.3 Spruce and pine growth characteristics. Regional curves of the (a) spruce (green) and (b) pine (yellow) sites truncated at < 10 series. Black lines are the arithmetic means at $n \geq 5$ sites. Bottom panels show the number of integrated site chronologies. Relationship between segment length and mean tree-ring width (TRW) of all (c) spruce and (d) pine series. Each dot represents one individual series. Basal area increment (BAI) chronologies of (e) spruce and (f) pine truncated at < 10 series. Black lines are the arithmetic means at $n \geq 5$ sites. Numbers between the vertical dashed lines indicate the mean BAI $\pm 1\sigma$ calculated for 1952-2009 CE. Bottom panels show the number of integrated site chronologies.

Despite the observed growth differences, the mean BAI chronologies of spruce and pine correlate at $r = 0.59$ from 1952-2009 CE, pointing to a common climatic forcing across the network. Covariance is particularly high among the spruce sites ($r_{1952-2009} = 0.66$) compared to pine ($r_{1952-2009} = 0.46$), and the BAI chronologies synchronize particularly well in years of severe growth decline that coincide with low growing-season SMI values (**Fig. 2.4a**). In the six driest growing seasons ($SMI_{A-O} < 0.30$), BAI values drop between -19% and -68% for spruce and -14% and -61% for pine compared to previous years. The greatest growth losses were recorded in 1976 CE for both species. BAI and SMI series correlate at $r = 0.85-0.86$ ($p < 0.001$) after 10-20-year band-pass filtering, indicating the importance of decadal soil moisture variability for southwest German conifer growth (**Fig. 2.4b**).

Inter-site BAI differences are weakly explained by stand age, elevation, growing-season T_{max} , precipitation, or soil moisture availability (**Fig. 2.4c-l**). While none of these factors is significant for pine, spruce BAI indicates a weak but significant positive dependence ($R^2 = 0.19$, $p < 0.05$) on growing-season precipitation and the SMI. Highest BAIs ($> 20 \text{ cm}^2 \text{ a}^{-1}$) are found in young (MSL < 90 years) and moist ($\text{SMI}_{A-O} > 0.52$) spruce stands. AGRs show no significant association with growing-season precipitation or the SMI but a significant ($p < 0.01$) dependence on MSL, explaining 40% of the variance among the spruce sites (**Fig. S2.4**). No significant relationship was found between the stand-specific AGR and MSL of pine.

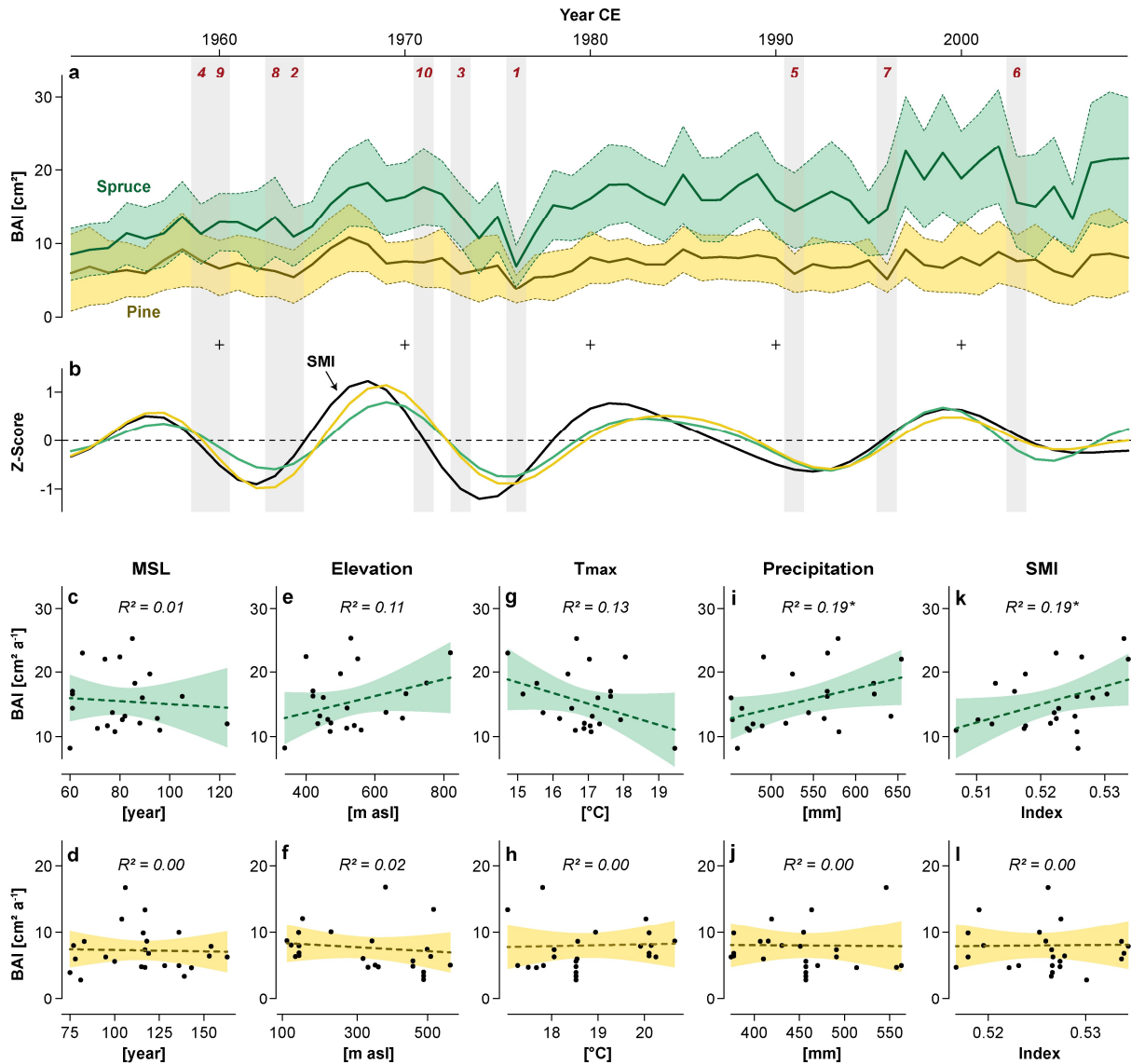


Fig. 2.4 Growth response to soil moisture variability. **(a)** Basal area increment (BAI) of spruce (green) and pine (yellow) from 1952-2009 CE. Thick curves are the average BAI of all spruce and pine sites, respectively. Colored shadings indicate $\pm 1\sigma$. Red numbers and grey shadings label the ten driest growing seasons (1 = lowest SMI). **(b)** Band-pass filtered (10-20 years) z-scores of the growing-season SMI (black) shown together with spruce (green) and pine (yellow) BAI. **(c-d)** Average BAI (1952-2009 CE) of spruce (top panels) and pine (bottom panels) as a function of mean segment length (MSL), **(e-f)** elevation, **(g-h)** maximum air temperature (T_{max}), **(i-j)** precipitation totals, and **(k-l)** soil moisture indices (SMI). The latter three variables are calculated for the growing season (April-October). Each dot represents one site. Dashed lines show linear trends. Colored areas are the 95% confidence intervals of the regression slopes. Asterisks behind R^2 indicate significance at $p < 0.05$.

2.3.2 Network covariance

The detrended TRW chronologies share high fractions of common variance and synchronize well in negative pointer years such as 1976 CE (**Fig. 2.5a**). Covariance among the spruce sites is slightly higher (mean $r_{1952-2009} = 0.66$) than between the pine sites (mean $r_{1952-2009} = 0.62$) considering the 10SP data, and declines faster with inter-site distance (**Fig. 2.5b-c**). The regional spruce and pine chronologies correlate at $r_{10SP} = 0.63$ and $r_{EXP} = 0.71$ from 1952-2009 CE, suggesting that the TRW variability across the network is synchronized by environmental (climatic) forcing and that this forcing is also relevant at decadal scale, as reflected in the EXP data. Inconsistencies among the site chronologies are rare and confined to single years, such as 1978 CE, when two pine 10SP chronologies deviate negatively. Rbar values of the 10SP chronologies fluctuate around a mean of 0.46 (pine) and 0.42 (spruce) and are relatively stable from 1952-2009 CE. Rbar values of the EXP chronologies are lower overall and show a downward trend toward the present.

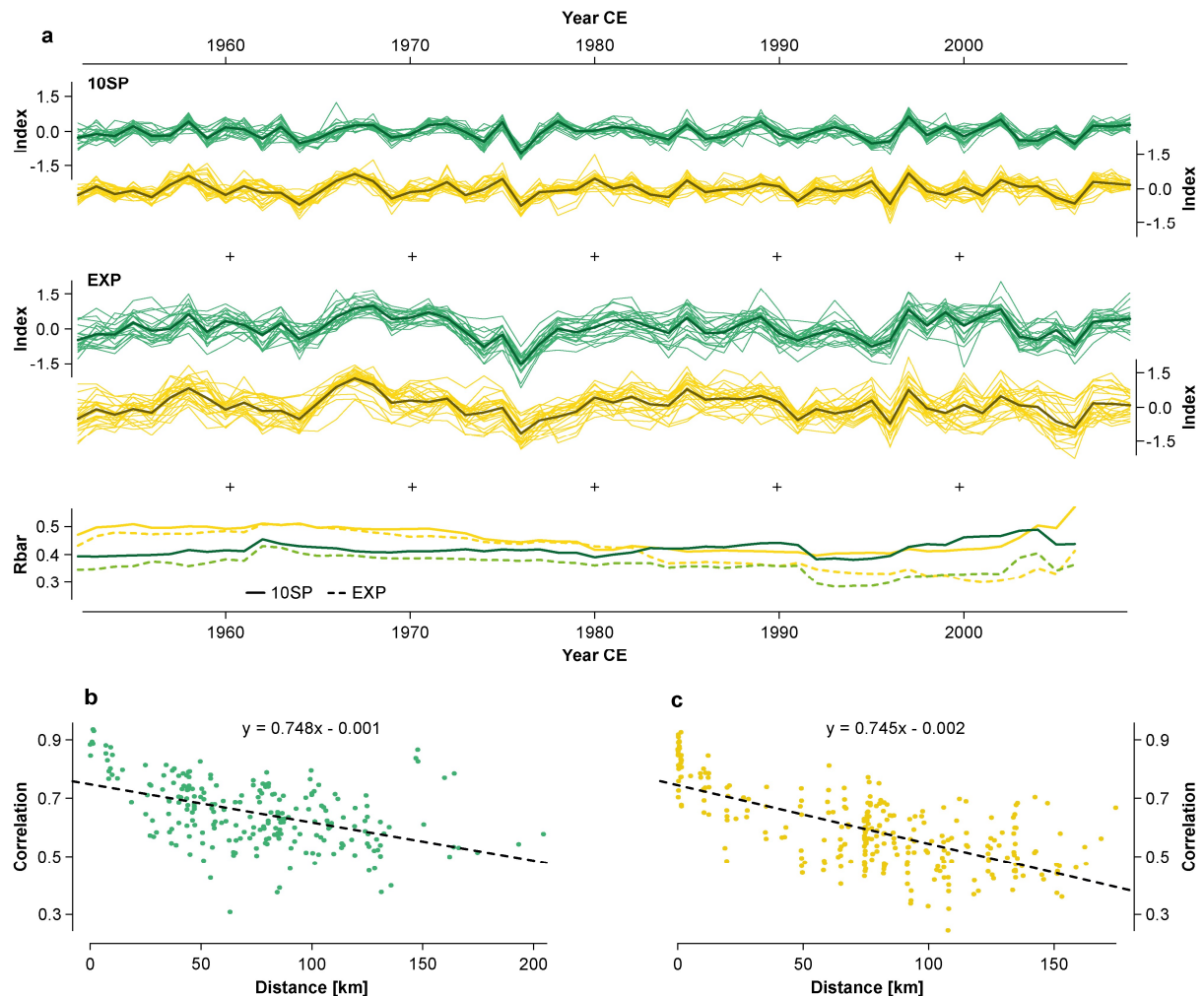


Fig. 2.5 Detrended tree-ring width (TRW) chronologies. **(a)** Spruce (green) and pine (yellow) site chronologies after detrending using 10-year cubic smoothing splines (10SP, top panel) and negative exponential curves (EXP, middle panel), shown together with their 30-year running inter-series correlations (Rbar, bottom panel). Thick curves (top and middle panel) are the regional mean chronologies. **(b-c)** Correlations between the 10SP spruce and pine chronologies as a function of distance. Dashed lines indicate linear trends of all possible spruce ($n = 231$) and pine ($n = 276$) pairings.

2.3.3 Network climate sensitivity

Climate conditions in early spring and mid-summer are most important for southwest German conifer growth (Fig. 2.6a). For spruce, the highest correlations are found with July-September T_{max} of the previous year (pJAS), ranging from $r = -0.15$ to $r = -0.55$ between the sites (1952-2009 CE). Twenty of the 22 spruce stands display significant ($p < 0.05$) correlations with pJAS T_{max} . The regional spruce chronology correlates at $r_{1952-2009} = -0.47$ ($p < 0.001$). In contrast, only seven of the 24 pine stands are significantly correlated with pJAS T_{max} ($p < 0.05$), of which five stands are located at the southern border of the tree-ring network in the Palatinate Forest (49-49.5°N/8-8.25°E). The species-specific differences in pJAS- T_{max} correlations are significant at $p < 0.001$ and are related to a fading temperature sensitivity of pine growth toward the end of the 20th century (Fig. 2.6b).

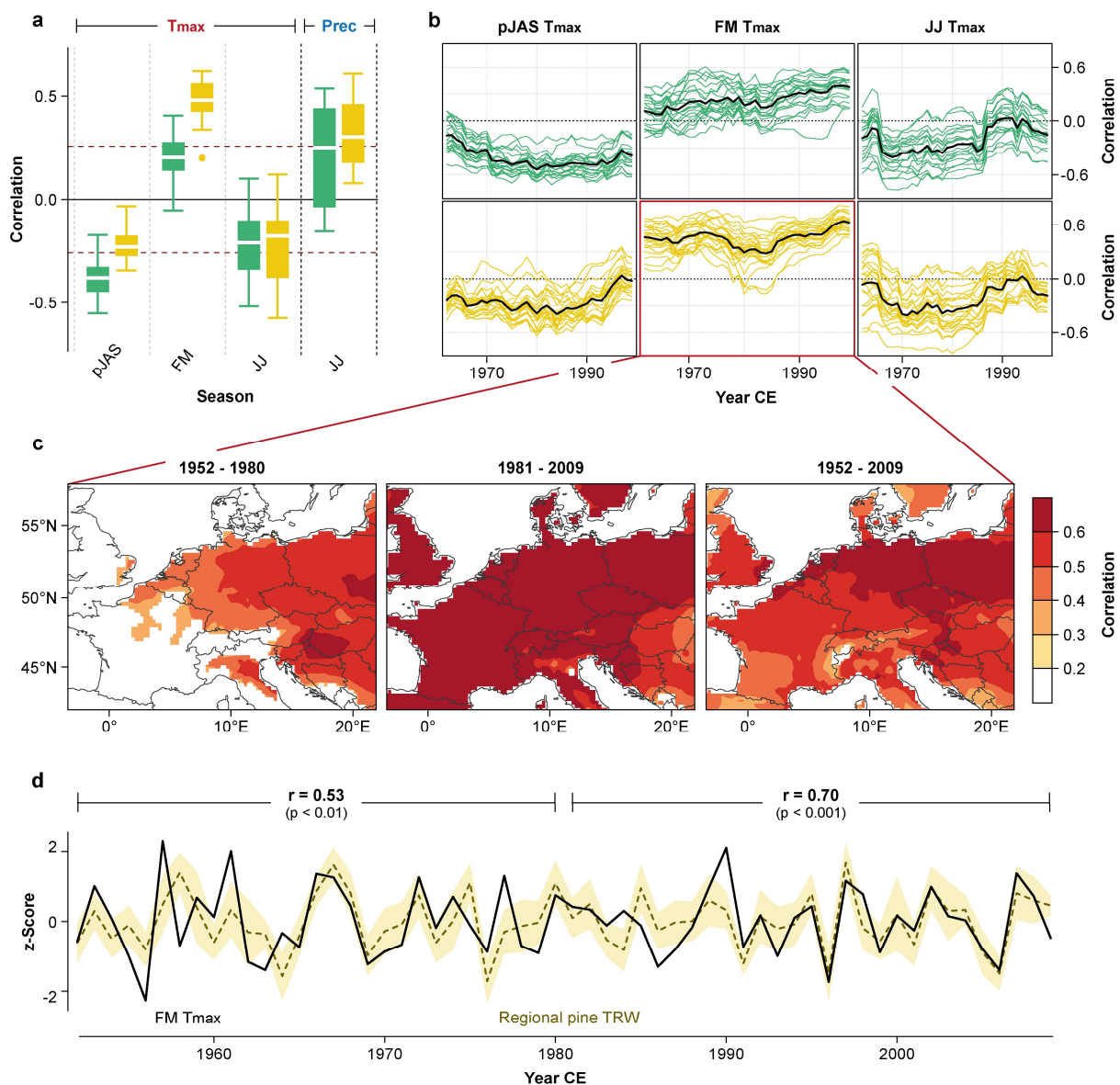


Fig. 2.6 Climate-growth relationships. (a) Distribution of bootstrap correlations of the 10SP chronologies (spruce = green, pine = yellow) with seasonal maximum air temperatures (T_{max}) and precipitation (Prec) from 1951-2009 CE. Boxplots show the median (white bar), 25%- and 75%-quartiles (box), min and max values within 1.5x the interquartile range (whiskers), and outliers (points). Horizontal dashed lines mark

$p < 0.05$. **(b)** Corresponding 21-year running correlations between the TRW site chronologies and seasonal T_{max} . Black curves are the mean. **(c)** Field correlations ($p < 0.05$) between the 10SP regional pine chronology and February-March T_{max} (EOBS). **(d)** Z-Scores of the 10SP regional pine chronology (brown dashed line) and high-pass filtered February-March T_{max} (black solid line). Yellow shadings represent $\pm 1\sigma$ of all pine chronologies. R values refer to 1952-1980 and 1981-2009 CE.

For pine, the highest correlations are found with February-March (FM) T_{max} , ranging from $r = 0.20$ to $r = 0.63$ for 1952-2009 CE (**Fig. 2.6c-d**). Twenty-three of the 24 pine chronologies show significant ($p < 0.05$) positive correlations with FM T_{max} . Southeastern pine sites in the Upper Rhine Plain and the Palatinate Forest show the highest correlations with $r \geq 0.50$. Correlations between spruce TRW and FM T_{max} ($r_{avg} = 0.20$) are substantially lower compared to pine ($r_{avg} = 0.47$) and are only significant ($p < 0.05$) at sites below 550 m asl (eight out of the nine sites). However, correlations between TRW and FM T_{max} have increased noticeably for both species in recent decades.

Correlations of the 46 TRW chronologies with monthly soil moisture indices show that spruce and pine growth are strongly affected by summer drought (**Fig. 2.7a**). Correlations with monthly SMI values are generally higher than with monthly T_{max} and precipitation (**Fig. S2.5**), indicating greater importance of soil water availability compared to individual climate factors. The highest correlations between TRW and SMI values are obtained for July-August (JA). Thirteen spruce (59%) and 18 pine stands (75%) are significantly ($p < 0.05$) positively correlated with the JA SMI, and the regional TRW chronologies correlate at $r_{spruce} = 0.38$ ($p < 0.01$) and $r_{pine} = 0.49$ ($p < 0.001$) from 1952-2009 CE. Running correlations between TRW and the JA SMI remain fairly stable until 1985 CE, but weaken considerably thereafter (**Fig. 2.7b**).

Correlations between TRW and previous-year SMI values are generally weak. However, nine spruce (41%) and five pine (21%) stands show significant ($p < 0.05$) positive correlations with the previous August-December (pA-D) SMI. While running correlations between pine TRW and the pA-D SMI decrease slightly from 1952-2009 CE, increasing correlations between spruce TRW and the pA-D SMI indicate an enhanced growth response to previous-year soil moisture conditions, especially above 550 m asl (**Fig. S2.6**). Linear regression models reveal a significant ($p < 0.01$) dependence of SMI correlations on elevation (**Fig. 2.7c**). With increasing altitude, spruce TRW shows a decreasing response to the JA SMI and an increasing response to the pA-D SMI. No significant relationship was found for pine (**Fig. 2.7d**).

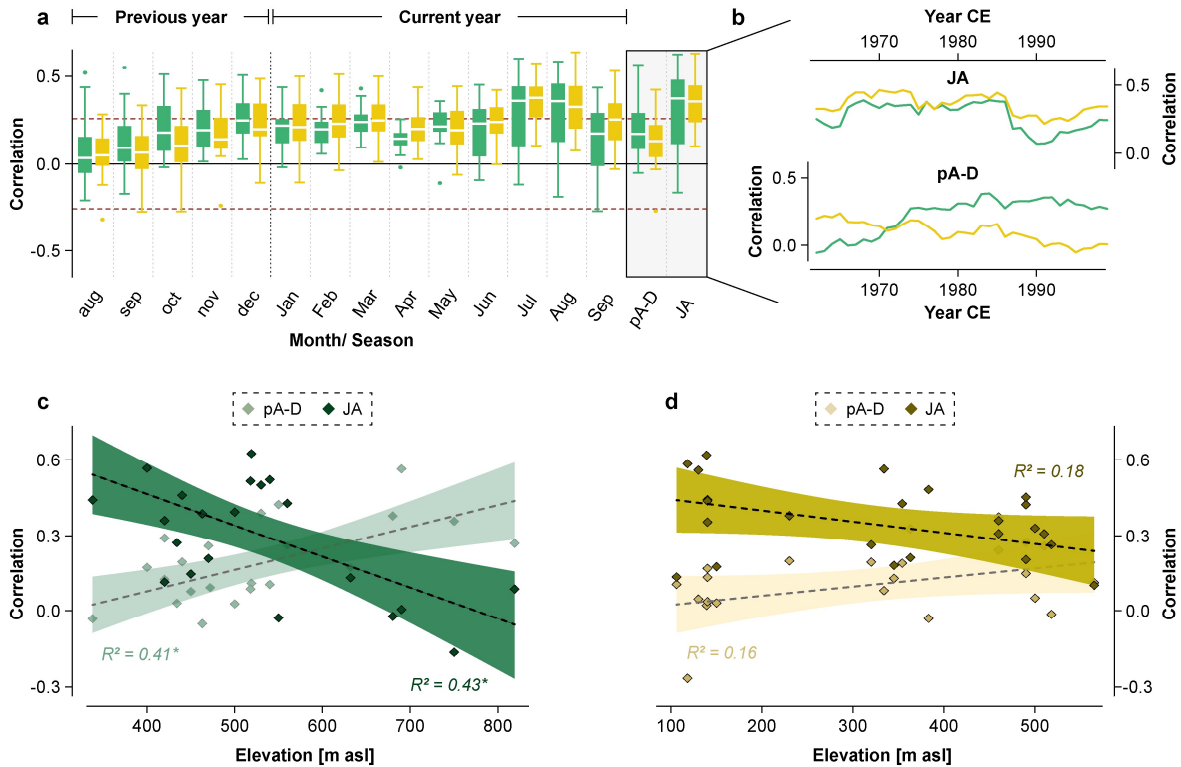


Fig. 2.7 Soil moisture sensitivity. **(a)** Distribution of bootstrap correlations of 10SP chronologies (spruce = green, pine = yellow) with monthly and seasonal soil moisture indices from 1951-2009 CE. Boxplots show the median (white bar), 25%- and 75%-quartiles (box), min and max values within 1.5x the interquartile range (whiskers), and outliers (points). Horizontal dashed lines mark $p < 0.05$. **(b)** Mean 21-year running correlations of the species with current-year July-August (JA) and previous-year August-December (pA-D) SMI. Soil moisture sensitivity of **(c)** spruce and **(d)** pine as a function of elevation. Each dot represents one site. Light colors indicate correlations (1952-2009 CE) with the pA-D SMI, dark colors correlations with the JA SMI. Dashed lines show linear trends. Colored areas are the 95% confidence intervals of the regression slopes. Asterisks behind R^2 indicate significance at $p < 0.01$.

2.4 Discussion

2.4.1 Conifer growth characteristics

By including more than 1900 spruce and pine trees, our network is the largest TRW dataset in southwestern Germany. The well-replicated data fill a spatial gap between networks in northeastern France (Lebourgeois et al. 2010), southern Germany (Boden et al. 2014; Debel et al. 2021; Zang et al. 2014), and the low mountain ranges in central Germany (Esper et al. 2012; Friedrichs et al. 2009), and provide new insights into the regional growth performance of spruce and pine over several decades.

The AGRs of Norway spruce ($2.3 \pm 0.6 \text{ mm a}^{-1}$) and Scots pine ($1.6 \pm 0.5 \text{ mm a}^{-1}$) are similar to nearby sites in western Germany and northeastern France (Friedrichs et al. 2009; Lebourgeois et al. 2010). The average BAI of both conifers is similar during the first 20 years of cambial age ($\sim 2.9 \text{ cm}^2 \text{ a}^{-1}$) but increasingly diverge thereafter due to the strong growth acceleration in spruce. The observed growth trends and spruce-pine differences are in agreement with data across Central European temperate forests (e.g., Bouriaud & Popa 2009; Pretzsch et al. 2023;

Seidling et al. 2012; Treml et al. 2021). The growth differences reported here are likely amplified by elevational site differences and associated soil properties. While spruce predominates above 400 m asl on soils with high water storage capacities, pines are primarily planted below 550 m asl on sandy soils (Richter et al. 2007) and are more exposed to drought (**Fig. S2.7**).

The assessment of BAI data from 1952-2009 CE shows that soil water supply during summer is of decisive importance for spruce growth. Spruce BAI increases with rising growing-season moisture supply, with the highest growth rates ($BAI_{avg} > 20 \text{ cm}^2 \text{ a}^{-1}$) recorded in young (MLS < 90 years) and moist ($SMI_{A-O} > 0.52$) stands. The lower BAI of spruce at drier sites and lack of comparable dependencies in pine likely reflect the higher drought vulnerability of spruce in the Central European lowlands and low mountain ranges (Treml et al. 2021; Zang et al. 2014).

Despite the observed age trends in BAI, differences in stand age do not explain intra-species growth differences. However, the significant negative relationship ($r = -0.63$, $p < 0.01$) between spruce AGR and MSL shows that older stands are characterized by lower initial growth rates than the younger stands. Although only living trees were included in this study and thus maximum tree ages cannot be determined, our results suggest that slow juvenile growth prolongs the life expectancy of spruce (Bigler & Veblen 2009; Castagneri et al. 2013; Rötheli et al. 2012). There are many explanations for such a trade-off between longevity and growth rate including the greater resilience of slow-growing trees to external disturbances (Schulman 1954), slower regulation of growth-related processes in taller trees (McDowell et al. 2008), as well as differences in root architecture (Hamberg et al. 2018) and hydraulic resilience (Ryan & Yoder 1997). No significant relationship was found between stand-level AGR and MSL in pine. However, a weak but significant correlation ($r = -0.24$, $p < 0.001$) was found when accounting for the individual growth rates of all 986 pines (**Fig. S2.8**), supporting similar findings from other European sites (Bigler 2016; Büntgen et al. 2019).

2.4.2 Network covariance

Cross-correlation, principal component gradient and hierarchical cluster analyses (**Fig. S2.2**) reveal that network covariance is most distinct in the high-frequency domain and likely driven by several environmental (climatic) factors (Debel et al. 2021; Friedrichs et al. 2009; Lebourgeois 2007; Mäkinen et al. 2002; Vitali et al. 2017). Compared to treeline sites, where interannual TRW variability is synchronized and increased by a single growth-limiting climatic factor, the more favourable conditions in temperate forests promote the formation of more invariable (complacent) tree rings. High-pass filters, such as the 10-year splines, emphasize interannual variance by eliminating low-frequency information (Esper & Gärtner 2001) and thereby synchronize TRW variance within and between the sites. Higher inter-site correlations in the 10SP

data compared to the EXP data support this conclusion and indicate a stronger climatic forcing in the high-frequency domain.

The lower covariance in the EXP data may also be related to the impact of silvicultural treatments such as wood harvesting and thinning, which can induce long-term growth releases by reducing the competition for light and nutrients (Kramer 2019). The EXP detrending does not mitigate such rapid non-climatic trends and thereby distorts the synchronizing influence of climate variability across the network. Although this contradicts findings of Esper et al. (2012), who report only minor effects of logging on spruce precipitation sensitivity in western Germany, several studies support that silvicultural practices and local disturbances can alter long-term growth (Lehtonen et al. 2023; Mehtätalo et al. 2014; Mörling 2002). Insect outbreaks can affect high-frequency covariance strongly, as shown by the strong TRW deviations of two pine stands in the late 1980s caused by pine sawfly (*Diprion pini* L.) outbreaks in 1977 CE near Speyer and Aschaffenburg (Bogenschütz 1981). The singularity of such striking events, however, does not substantially affect the covariance of the 10SP data across southwest Germany.

2.4.3 Growth responses to summer drought

The assessment of species-specific climate-growth relationships shows that summer drought is the dominant climatic driver of southwest German spruce and pine growth. Although correlations between TRW and climate variables are generally weak, the uniform network growth response to current-year summer T_{\max} and precipitation underlines the importance of adequate water supply during the time of xylem formation. The positive association of TRW with summer precipitation and the negative association with T_{\max} appear physiologically meaningful, as low summer rainfall and high temperatures intensify evapotranspiration and soil moisture deficits, and thereby reduce turgor pressure in the xylem and associated cell enlargement processes (Peters et al. 2021). Stronger correlations with rainfall than with T_{\max} point to a higher relevance of summer rain for both conifers, but the significant inverse relationship between summer temperature and precipitation ($r_{\text{JJA}} = -0.65$) makes a clear distinction between the two factors difficult. The precipitation sensitivity is in line with findings by Esper et al. (2012) and Friedrichs et al. (2009), who report similar growth responses to May-July precipitation at several spruce and pine stands in the Rhenish Massif. Comparable relationships between TRW and May-July precipitation were found in lowland Poland (Koprowski & Zielski 2006) and the lower French Alps (Desplanque et al. 1998). SMI correlations peak slightly later in summer (July-August), likely due to delayed responses of the hydro-pedological system (Entekhabi et al. 1996).

Besides the drought response during xylem formation, spruce reveals a definite sensitivity to previous-year late-summer (July-September) conditions. This lag-response is consistent with other tree-ring studies (Rybníček et al. 2010; Seidling et al. 2012; van der Maaten-Theunissen

et al. 2013; Zang et al. 2011) and supports the significance of carry-over effects on earlywood formation (Lebourgeois et al. 2010). The negative relationship between spruce TRW and prior-summer T_{\max} can likely be attributed to drought-induced reductions in carbohydrate accumulation, impairment of fine root formation, and increased crown dieback, limiting radial growth in the following year (St. George 2014). The latter explanation is supported by results of Seidling et al. (2012) and Solberg (2004), who found positive correlations between summer temperature and the crown transparency of spruce. Summer droughts can favor needle defoliation and discoloration, thereby reducing photosynthesis and growth in the subsequent growing seasons (Solberg 2004). High summer temperatures can also promote flowering and seed production in consecutive years and thereby inhibit growth by limiting the amount of available resources (Selås et al. 2002).

Even though TRW variations among the spruce stands are highly synchronous ($r_{\text{avg}} = 0.66$ for 10SP data), the SMI signals are significantly altered by elevation. Current-summer SMI correlations decrease by ~ 0.1 per 100 m, while previous-year SMI correlations increase towards higher elevations. Twelve of the thirteen spruce stands that are significantly correlated with the JA SMI are located below 550 m asl, and six of the eight stands that are significantly correlated with the pA-D SMI are above 550 m asl. Linear regression models show that elevation explains 43% of the drought signal differences. Van der Maaten-Theunissen et al. (2013) found a similar gradient ($R^2 = 0.33$) along elevational transects in the Black Forest. These variations in drought sensitivity are consistent with the fact that spruce growing at drier sites are most susceptible to current growing-season conditions, while wetter stands at intermediate elevations often lack such signals (Hartl-Meier et al. 2014; Jevšenak et al. 2021; Leal et al. 2007; Sidor et al. 2015; Wilson & Hopfmueller 2001). Park & Spiecker (2005) show that spruce growing at drier sites tend to form more latewood cells with thicker walls, while spruce at wetter sites generally form larger earlywood cells, which might explain the stronger response to previous-year conditions at mid-elevations, as earlywood formation is closely related to the mobilization of stored photoassimilates (Kagawa et al. 2006).

Running correlations between TRW and SMI values indicate that previous August-December moisture conditions became increasingly important for spruce. Although these correlations are calculated over a short time window, coherent patterns across the network point to an increasing growth response to previous-year climatic conditions, particularly above 550 m asl. These results support findings of previous studies from eastern Europe (Čermák et al. 2019; Rybníček et al. 2010). The increasing growth responses to water availability in previous late-summer and autumn may be related to the strong warming and decreasing rainfall totals in July and August, limiting accessible soil moisture. Summer droughts can reduce fine root formation and recovery (Nikolova et al. 2009), which may adversely affect growth in the following growing season,

especially as late-summer is a distinct growth period for spruce roots in southwestern Germany (Xu et al. 1997).

2.4.4 Growth responses to late-winter temperatures

FM temperature signals in pine growth have previously been reported from several temperate forest sites (Debel et al. 2021; Diers et al. 2023, 2024; Friedrichs et al. 2009; Koprowski et al. 2012; Lebourgeois et al. 2010; Seidling et al. 2012; Stolz et al. 2021), suggesting a large-scale growth-promoting influence of warm temperatures during the dormancy period across Central Europe. However, despite extensive empirical evidence, physiological mechanisms explaining the growth-stimulating influence of winter temperatures are poorly understood. While an onset of growth in February-March is unlikely, elevated air temperatures during late winter may favor physiological processes that support cambial reactivation during quiescent dormancy (Begum et al. 2013). At the lowest elevations (~100 m asl), 38% of the February-March days exceed a mean temperature of 6°C, and 25% exceed 8°C (**Fig. S2.9**), indicating that thermal thresholds for xylogenetic activity are only sporadically reached, but FM temperatures could be sufficient to promote photosynthesis (Rossi et al. 2008; Tanja et al. 2003). Such effects appear plausible as evergreen conifers can remain photosynthetically active in winter and modulate their capacities within a few days (Mäkelä et al. 2004; Nippert et al. 2004). A temperature-driven stimulation of photosynthesis could also explain the lack of significant correlations between spruce TRW and FM T_{\max} above 550 m asl.

In the temperate regions of France, early- and latewood width of fir, pine, and spruce are positively associated with February temperatures, suggesting that warm late winters not only promote growth in spring but also favor growth processes throughout the growing season, probably related to an enhanced photoassimilate accumulation prior to the onset of cambial activity (Lebourgeois et al. 2010). This inference is supported by findings of Giberti et al. (2022), who reported positive relationships between January-March temperatures and carbon sequestration in Polish pines. Since warmer winters are accompanied by higher rainfall, as shown by the positive correlation between FM T_{\max} and precipitation ($r = 0.43$), the FM response might also reflect an increased water availability in late winter and spring. The lack of significant precipitation correlations, however, indicates that FM temperature is the key climatic driver. Besides the effects on photosynthetic biochemistry, high late-winter temperatures might also promote soil warming and mycorrhizal growth (Domisch et al. 2002), and reduce the risk of winter desiccation (Ensminger et al. 2008; Sevanto et al. 2006).

Increasing running correlations between TRW and FM T_{\max} indicate that late-winter temperatures have become distinctly more important for southwest German spruce and pine growth in recent decades. Our results support previous studies from the south Baltic region (Diers et al.

2023, 2024; Harvey et al. 2020; Janecka et al. 2020) and add evidence that late-winter temperatures are gaining importance for Central European forest growth. Decreasing correlations with JJ T_{\max} and increasing correlations with FM T_{\max} since the 1980s point to putative trade-offs between enhanced winter and reduced summer photosynthesis (Stolz et al. 2021), which may result from a strong inter-seasonal warming (**Fig. S2.10a**). Even if the FM T_{\max} correlations may be strengthened by the higher variance of cold-season temperatures (**Fig. S2.10b**), the increasing relevance of late-winter temperatures is consistent with phenological observations indicating earlier plant development and fruiting (Büntgen et al. 2022; Chmielewski et al. 2004).

2.5 Conclusion

We introduce a TRW network to assess the growth performance of Norway spruce and Scots pine along elevational gradients from 100-820 m asl in southwest Germany and identify climate drivers of regional forest growth. The data reveals that spruce has grown twice that of pine in recent decades. Decadal BAI fluctuations of both conifers are closely related to long-term soil moisture variability, but only spruce shows a significant dependence on growing-season water supply, which likely reflects the higher drought vulnerability of this species at locations beyond its natural distribution range. Correlations using high-pass filtered TRW and climate data support that summer drought is the dominant climatic driver of southwest German conifer growth, but the seasonality of the signal changes with elevation. Sites below 550 m asl show a stronger growth response to current-summer soil moisture conditions, whereas spruce sites above 550 m asl are particularly sensitive to previous-year moisture conditions. Possible reasons for the changing seasonality along the elevational gradient are discussed, but remain conjectural due to the sole focus on radial stem growth, underlining the need to address the complex interactions between above- and below-ground biomass productivity in future research. In addition, increasing growth responses to late-winter temperatures hint at potential changes in the photosynthetic seasonality of pine, likely related to an abrupt cold-season temperature increase in the late 1980s and possibly reflecting a trade-off between enhanced winter and reduced summer photosynthesis. Our study provides new insights into the growth performance of southwest German spruce and pine under recent environmental changes, which call for a change in planting strategies towards more drought-resistant tree species.

2.6 Acknowledgements

Not available online.

2.7 References

- Aalbers EE, Lenderink G, van Meijgaard E, van den Hurk BJJ (2018) Local-scale changes in mean and heavy precipitation in Western Europe, climate change or internal variability? *Clim Dyn* 50: 4745-4766.
- Altman J, Fibich P, Santruckova H, Dolezal J, Stepanek P, Kopacek J, Hunova I, Oulehle F, Tumajer J, Cienciala E (2017) Environmental factors exert strong control over the climate-growth relationships of *Picea abies* in Central Europe. *Sci Total Environ* 609: 506-516.
- Begum S, Nakaba S, Yamagishi Y, Oribe Y, Funada R (2013) Regulation of cambial activity in relation to environmental conditions: understanding the role of temperature in wood formation of trees. *Physiol Plant* 147: 46-54.
- Bigler C (2016) Trade-offs between growth rate, tree size and lifespan of mountain pine (*Pinus montana*) in the Swiss National Park. *PLoS One* 11: e0150402.
- Bigler C, Veblen TT (2009) Increased early growth rates decrease longevities of conifers in subalpine forests. *Oikos* 118: 1130-1138.
- Boden S, Kahle H-P, von Wilpert K, Spiecker H (2014) Resilience of Norway spruce (*Picea abies* (L.) Karst) growth to changing climatic conditions in Southwest Germany. *For Ecol Manag* 315: 12-21.
- Bogenschütz H (1981) Deutsche Forstschutz-Literatur 1977/78: Insekten. *Zeitschrift für Pflanzenkrankheiten und Pflanzenschutz* 88: 293-316.
- Bonan GB (2008) Forests and climate change: forcings, feedbacks, and the climate benefits of forests. *Science* 320: 1444-1449.
- Bose AK, Gessler A, Bolte A, Bottero A, Buras A, Cailleret M, Camarero JJ, Haeni M, Hereş AM, Hevia A, et al. (2020) Growth and resilience responses of Scots pine to extreme droughts across Europe depend on predrought growth conditions. *Glob Change Biol* 26: 4521-4537.
- Bouriaud O, Popa I (2009) Comparative dendroclimatic study of Scots pine, Norway spruce, and silver fir in the Vrancea Range, Eastern Carpathian Mountains. *Trees* 23: 95-106.
- Bundesministerium für Ernährung und Landwirtschaft (BMEL) (2023) *Ergebnisse der Waldzustandserhebung 2022*. Bonn, Germany.
- Bunn AG (2008) A dendrochronology program library in R (dpIR). *Dendrochronologia* 26: 115-124.
- Büntgen U, Krusic PJ, Piermattei A, Coomes DA, Esper J, Myglan V, Kirilyanov AV, Camarero JJ, Crivellaro A, Körner C (2019) Limited capacity of tree growth to mitigate the global greenhouse effect under predicted warming. *Nat Commun* 10: 2171.
- Büntgen U, Piermattei A, Krusic PJ, Esper J, Sparks T, Crivellaro A (2022) Plants in the UK flower a month earlier under recent warming. *Proc R Soc B* 289: 20212456.

- Castagneri D, Storaunet KO, Rolstad J (2013) Age and growth patterns of old Norway spruce trees in Trillemarka forest, Norway. *Scand J For Res* 28: 232-240.
- Caudullo G, Tinner W, de Rigo D (2016) *Picea abies* in Europe: distribution, habitat, usage and threats. In: San-Miguel-Ayanz J, de Rigo D, Caudullo G, Houston Durrant T, Mauri A (eds) *European Atlas of Forest Tree Species*. Publ Off EU, Luxembourg: pp 114-116.
- Čermák P, Kolář T, Žid T, Trnka M, Rybníček M (2019) Norway spruce response to drought forcing in area affected by forest decline. *For Syst* 28: e016.
- Chmielewski F-M, Müller A, Bruns E (2004) Climate changes and trends in phenology of fruit trees and field crops in Germany, 1961-2000. *Agric For Meteorol* 121: 69-78.
- Cook ER, Kairiukstis LA (1990) *Methods of dendrochronology: applications in the environmental sciences*. Kluwer Academic Publishers, Dordrecht, Boston, and London, The Netherlands, USA and UK.
- Cook ER, Peters K (1997) Calculating unbiased tree-ring indices for the study of climatic and environmental change. *Holocene* 7: 361-370.
- Cook ER, Krusic PJ, Peters K, Holmes RL (2017) *Program ARSTAN (ARS41d), autoregressive tree-ring standardization program*. Tree-ring laboratory of the Lamont-Doherty Earth Observatory, Palisades, NY, USA.
- Cornes R, van der Schrier G, van den Besselaar EJM, Jones PD (2018) An ensemble version of the E-OBS temperature and precipitation data sets. *J Geophys Res Atmos* 123: 9391-9409.
- Debel AC, Meier WJH, Bräuning A (2021) Climate signals for growth variations of *F. sylvatica*, *P. abies*, and *P. sylvestris* in southeast Germany over the past 50 years. *Forests* 12: 1433.
- Desplanque C, Rolland C, Michalet R (1998) Dendroécologie comparée du sapin blanc (*Abies alba*) et de l'épicéa commun (*Picea abies*) dans une vallée alpine de France. *Can J For Res* 28: 737-748.
- Diers M, Leuschner C, Dulamsuren C, Schulz TC, Weigel R (2024) Increasing winter temperatures stimulate Scots pine growth in the North German Lowlands despite stationary sensitivity to summer drought. *Ecosystems* 27: 428-442.
- Diers M, Weigel R, Leuschner C (2023) Both climate sensitivity and growth trend of European beech decrease in the North German Lowlands, while Scots pine still thrives, despite growing sensitivity. *Trees* 37: 523-543.
- Dobbertin M (2005) Tree growth as indicator of tree vitality and of tree reaction to environmental stress: a review. *Eur J For Res* 124: 319-333.
- Domisch T, Finér L, Lehto T, Smolander A (2002) Effect of soil temperature on nutrient allocation and mycorrhizas in Scots pine seedlings. *Plant Soil* 239: 173-185.

- Eilmann B, Zweifel R, Buchmann N, Fonti P, Rigling A (2009) Drought-induced adaptation of the xylem in Scots pine and pubescent oak. *Tree Physiol* 29: 1011-1020.
- Ensminger I, Schmidt L, Lloyd J (2008) Soil temperature and intermittent frost modulate the rate of recovery of photosynthesis in Scots pine under simulated spring conditions. *New Phytol* 177: 428-442.
- Entekhabi D, Rodriguez-Iturbe I, Castelli F (1996) Mutual interaction of soil moisture state and atmospheric processes. *J Hydrol* 184: 3-17.
- Esper J, Gärtner H (2001) Interpretation of tree-ring chronologies. *Erdkunde* 55: 277-288.
- Esper J, Benz M, Pederson N (2012) Influence of wood harvest on tree-ring time-series of *Picea abies* in a temperate forest. *For Ecol Manag* 284: 86-92.
- Esper J, Cook ER, Krusic PJ, Peters K, Schweingruber FH (2003) Tests of the RCS method for preserving low-frequency variability in long tree-ring chronologies. *Tree-Ring Res* 59: 81-98.
- Frank DC, Esper J, Cook ER (2007) Adjustment for proxy number and coherence in a large-scale temperature reconstruction. *Geophys Res Lett* 34: L16709.
- Friedrichs D, Trouet V, Büntgen U, Frank DC, Esper J, Neuwirth B, Löffler J (2009) Species-specific climate sensitivity of tree growth in Central-West Germany. *Trees* 23: 729-739.
- Giberti GS, Wellstein C, Giovannelli A, Bielak K, Uhl E, Aguirre-Ráquira W, Giammarchi F, Tonon G (2022) Annual carbon sequestration patterns in trees: a case study from Scots pine monospecific stands and mixed stands with sessile oak in Central Poland. *Forests* 13: 582.
- Hamberg L, Velmala SM, Sievänen R, Kalliokoski T, Pennanen T (2018) Early root growth and architecture of fast- and slow-growing Norway spruce (*Picea abies*) families differ – potential for functional adaptation. *Tree Physiol* 38: 853-864.
- Harris NL, Gibbs DA, Baccini A, Birdsey RA, de Bruin S, Farina M, Fatoyinbo L, Hansen MC, Herold M, Houghton RA, et al. (2021) Global maps of twenty-first century forest carbon fluxes. *Nat Clim Change* 11: 234-240.
- Hartl-Meier C, Zang C, Dittmar C, Esper J, Göttlein A, Rothe A (2014) Vulnerability of Norway spruce to climate change in mountain forests of the European Alps. *Clim Res* 60: 119-132.
- Harvey JE, Smiljanić M, Scharnweber T, Buras A, Cedro A, Cruz-García R, Drobyshev I, Janecka K, Jansons Ā, Kaczka R, et al. (2020) Tree growth influenced by warming winter climate and summer moisture availability in northern temperate forests. *Glob Change Biol* 26: 2505-2518.
- Holmes RL (1983) Computer-assisted quality control in tree-ring dating and measurement. *Tree-Ring Bull* 43: 69-78.

- Irvine J, Perks M, Magnani F, Grace J (1998) The response of *Pinus sylvestris* to drought: stomatal control of transpiration and hydraulic conductance. *Tree Physiol* 18: 393-402.
- Janecka K, Harvey JE, Trouillier M, Kaczka RJ, Metslaid S, Metslaid M, Buras A, Wilmking M (2020) Higher winter-spring temperature and winter-spring/summer moisture availability increase Scots Pine growth on coastal dune microsites around the south Baltic Sea. *Front For Glob Change* 3: 578912.
- Jevšenak J, Tychkov I, Gričar J, Levanič T, Tumajer J, Prislán P, Arnič D, Popkova M, Shishov VV (2021) Growth-limiting factors and climate response variability in Norway spruce (*Picea abies* L.) along an elevation and precipitation gradients in Slovenia. *Int J Biometeorol* 65: 311-324.
- Johann E, Agnoletti M, Axelsson AL, Bürgi M, Östlund L, Rochel X, Schmidt UE, Schuler A, Skovsgaard JP, Winiwarter V (2004) History of secondary Norway spruce forests in Europe. In: Spiecker H, Hansen J, Klimo E, Skovsgaard JP, Sterba H, von Teuffel K (eds) *Norway spruce conversion – options and consequences*. Brill, Leiden, The Netherlands: pp 25-62.
- Kagawa A, Sugimoto A, Maximov TC (2006) ¹³CO₂ pulse-labelling of photoassimilates reveals carbon allocation within and between tree rings. *Plant Cell Environ* 29: 1571-1584.
- Kaspar F, Müller-Westermeier G, Penda E, Mächel H, Zimmermann K, Kaiser-Weiss A, Deuschländer T (2013) Monitoring of climate change in Germany – data, products and services of Germany's National Climate Data Centre. *Adv Sci Res* 10: 99-106.
- Kašpar J, Tumajer J, Altman J, Altmanová N, Čada V, Čihák T, Doležal J, Fibich P, Janda P, Kaczka R, et al. (2024) Major tree species of Central European forests differ in their proportion of positive, negative, and nonstationary growth trends. *Glob Change Biol* 30: e17146.
- Klippel L, Hartl-Meier C, Lindén J, Kochbeck M, Emde K, Esper J (2017) Hourly resolved climate response of *Picea abies* beyond its natural distribution range. *Balt For* 23: 556-563.
- Kölling C, Knoke T, Schall P, Ammer C (2009) Überlegungen zum Risiko des Fichtenanbaus in Deutschland vor dem Hintergrund des Klimawandels. *Forstarchiv* 80: 42-54.
- Koprowski M, Przybylak R, Zielski A, Pospieszńska A (2012) Tree rings of Scots pine (*Pinus sylvestris* L.) as a source of information about past climate in northern Poland. *Int J Biometeorol* 56: 1-10.
- Koprowski M, Zielski A (2006) Dendrochronology of Norway spruce (*Picea abies* (L.) Karst.) from two range centres in lowland Poland. *Trees* 20: 383-390.
- Korhonen K, Stahl G (2020) Criterion 1: maintenance and appropriate enhancement of forest resources and their contribution to global carbon cycles. In: Forest Europe (ed) *State of Europe's forests 2020*. Ministerial conference on the protection of forests in Europe, Bratislava, Slovenia: pp 30-51.

- Kramer H (2019) *Waldwachstumslehre. Ökologische und anthropogene Einflüsse auf das Wachstum des Waldes, seine Massen- und Wertleistung und die Bestandessicherheit*. Kessel, Remagen-Oberwinter, Germany.
- Krejza J, Cienciala E, Světlík J, Bellan M, Noyer E, Horáček P, Štěpánek P, Marek MV (2021) Evidence of climate-induced stress of Norway spruce along elevation gradient preceding the current dieback in Central Europe. *Trees* 35: 103-119.
- Leal S, Melvin TM, Grabner M, Wimmer R, Briffa KR (2007) Tree ring-growth variability in the Austrian Alps: the influence of site, altitude, tree species and climate. *Boreas* 36: 426-440.
- Lebourgeois F (2007) Climatic signal in annual growth variation of silver fir (*Abies alba* Mill.) and spruce (*Picea abies* Karst.) from the French Permanent Plot Network (REN-ECO-FOR). *Ann For Sci* 64: 333-343.
- Lebourgeois F, Rathgeber CBK, Ulrich E (2010) Sensitivity of French temperate coniferous forests to climate variability and extreme events (*Abies alba*, *Picea abies* and *Pinus sylvestris*). *J Veg Sci* 21: 364-376.
- Lehtonen A, Leppä K, Rinne-Garmston KT, Sahlstedt E, Schiestl-Aalto P, Heikkinen J, Young GHF, Korkiakoski M, Peltoniemi M, Sarkkola S, et al. (2023) Fast recovery of suppressed Norway spruce trees after selection harvesting on a drained peatland forest site. *For Ecol Manag* 530: 120759.
- Lévesque M, Rigling A, Bugmann H, Weber P, Brang P (2014) Growth response of five co-occurring conifers to drought across a wide climatic gradient in Central Europe. *Agric For Meteorol* 197: 1-12.
- Mäkelä A, Hari P, Berninger F, Hänninen H, Nikinmaa E (2004) Acclimation of photosynthetic capacity in Scots pine to the annual cycle of temperature. *Tree Physiol* 24: 369-376.
- Mäkinen H, Nöjd P, Kahle H-P, Neumann U, Tveite B, Mielikäinen K, Röhle H, Spiecker H (2002) Radial growth variation of Norway spruce (*Picea abies* (L.) Karst.) across latitudinal and altitudinal gradients in central and northern Europe. *For Ecol Manag* 171: 243-259.
- Martínez del Castillo E, Zang C, Buras A, Hacket-Pain A, Esper J, Serrano-Notivoli R, Hartl C, Weigel R, Klesse S, Resco de Dios V, et al. (2022) Climate-change-driven growth decline of European beech forests. *Commun Biol* 5: 163.
- Masson-Delmotte V, Zhai P, Pirani A, Connors SL, Péan C, Berger S, Caud N, Chen Y, Goldfarb L, Gomis MI, et al. (2021) *Climate change 2021. The physical science basis. Working group I contribution to the sixth assessment report of the Intergovernmental Panel on Climate Change*. Cambridge University Press, Cambridge and New York, UK and USA.

- McDowell N, Pockman WT, Allen CD, Breshears DD, Cobb N, Kolb T, Plaut J, Sperry J, West A, Williams DG, et al. (2008) Mechanisms of plant survival and mortality during drought: why do some plants survive while others succumb to drought? *New Phytol* 178: 719-739.
- Mehtätalo L, Peltola H, Kilpeläinen A, Ikonen V-P (2014) The response of basal area growth of Scots pine to thinning: a longitudinal analysis of tree-specific series using a nonlinear mixed-effects model. *For Sci* 60: 636-644.
- Mörling T (2002) Evaluation of annual ring width and ring density development following fertilisation and thinning of Scots pine. *Ann For Sci* 59: 29-40.
- Nagavciuc V, Roibu C-C, Ionita M, Mursa A, Cotos M-G, Popa I (2019) Different climate response of three tree ring proxies of *Pinus sylvestris* from the Eastern Carpathians, Romania. *Dendrochronologia* 54: 56-63.
- Nikolova PS, Raspe S, Andersen CP, Mainiero R, Blaschke H, Matyssek R, Häberle K-H (2009) Effects of the extreme drought in 2003 on soil respiration in a mixed forest. *Eur J Forest Res* 128: 87-98.
- Nippert JB, Duursma RA, Marshall JD (2004) Seasonal variation in photosynthetic capacity of montane conifers. *Funct Ecol* 18: 876-886.
- Park Y-I, Spiecker H (2005) Variations in the tree-ring structure of Norway spruce (*Picea abies*) under contrasting climates. *Dendrochronologia* 23: 93-104.
- Peters RL, Steppe K, Cuny HE, De Pauw DJW, Frank DC, Schaub M, Rathgeber CBK, Carbon A, Fonti P (2021) Turgor – a limiting factor for radial growth in mature conifers along an elevational gradient. *New Phytol* 229: 213-229.
- Pretzsch H, del Río M, Arcangeli C, Bielak K, Dudzinska M, Forrester DI, Klädtke J, Kohnle U, Ledermann T, Matthews R, et al. (2023) Forest growth in Europe shows diverging large regional trends. *Sci Rep* 13: 15373.
- Richter A, Adler GH, Fahrak M, Eckelmann W (2007) *Erläuterungen zur nutzungsdifferenzierten Bodenübersichtskarte der Bundesrepublik Deutschland BÜK 1000 N*. Bundesanstalt für Geowissenschaften und Rohstoffe, Hannover, Germany.
- Rinn F (2012) *TSAP-Win: time series analysis and presentation for dendrochronology and related applications – version 4.6x for Microsoft Windows*. Rinntech GmbH, Heidelberg, Germany.
- Rossi S, Deslauriers A, Gričar J, Seo J-W, Rathgeber CBK, Anfodillo T, Morin H, Levanič T, Oven P, Jalkanen R (2008) Critical temperatures for xylogenesis in conifers of cold climates. *Glob Ecol Biogeogr* 17: 696-707.
- Rötheli E, Heiri C, Bigler C (2012) Effects of growth rates, tree morphology and site conditions on longevity of Norway spruce in the northern Swiss Alps. *Eur J For Res* 131: 1117-1125.

- Ryan MG, Yoder BJ (1997) Hydraulic limits to tree height and tree growth. *Bioscience* 47: 235-242.
- Rybníček M, Čermák P, Žid T, Kolář T (2010) Radial growth and health condition of Norway Spruce (*Picea abies* (L.) Karst.) stands in relation to climate (Silesian Beskids, Czech Republic). *Geochronometria* 36: 9-16.
- Schulman E (1954) Longevity under adversity in conifers. *Science* 119: 396-399.
- Seidling W, Ziche D, Beck W (2012) Climate responses and interrelations of stem increment and crown transparency in Norway spruce, Scots pine, and common beech. *For Ecol Manag* 284: 196-204.
- Selås V, Piovesan G, Adams JM, Bernabei M (2002) Climatic factors controlling reproduction and growth of Norway spruce in southern Norway. *Can J For Res* 32: 217-225.
- Senf C, Buras A, Zang C, Rammig A, Seidl R (2020) Excess forest mortality is consistently linked to drought across Europe. *Nat Commun* 11: 6200.
- Sevanto S, Tanja S, Pumpanen J, Grönholm T, Kolari P, Nikinmaa E, Hari P, Vesala T (2006) Wintertime photosynthesis and water uptake in a boreal forest. *Tree Physiol* 26: 749-757.
- Sidor CG, Popa I, Vlad R, Cherubini P (2015) Different tree-ring responses of Norway spruce to air temperature across an altitudinal gradient in the Eastern Carpathians (Romania). *Trees* 29: 985-997.
- Solberg S (2004) Summer drought: a driver for crown condition and mortality of Norway spruce in Norway. *For Pathol* 34: 93-104.
- Spiecker H (2003) Silvicultural management in maintaining biodiversity and resistance of forests in Europe – temperate zone. *J Environ Manag* 67: 55-65.
- St George S (2014) An overview of tree-ring width records across the Northern Hemisphere. *Quat Sci Rev* 95: 132-150.
- Stokes MA, Smiley TL (1996) *An introduction to tree-ring dating*. The University of Arizona Press, Tucson, AZ, USA.
- Stolz J, van der Maaten E, Kalanke H, Martin J, Wilmking M, van der Maaten-Theunissen M (2021) Increasing climate sensitivity of beech and pine is not mediated by adaptation and soil characteristics along a precipitation gradient in northeastern Germany. *Dendrochronologia* 67: 125834.
- Tanja S, Berninger F, Vesala T, Markkanen T, Hari P, Mäkelä A, Ilvesniemi H, Hänninen H, Nikinmaa E, Huttula T, et al. (2003) Air temperature triggers the recovery of evergreen boreal forest photosynthesis in spring. *Glob Change Biol* 9: 1410-1426.
- Tremli V, Mašek J, Tumajer J, Rydval M, Čada V, Ledvinka O, Svoboda M (2021) Trends in climatically driven extreme growth reductions of *Picea abies* and *Pinus sylvestris* in Central Europe. *Glob Change Biol* 28: 557-570.

- Trouet V, van Oldenborgh GJ (2013) KNMI climate explorer: a web-based research tool for high-resolution paleoclimatology. *Tree-Ring Res* 69: 3-13.
- van der Maaten-Theunissen M, Kahle H-P, van der Maaten E (2013) Drought sensitivity of Norway spruce is higher than that of silver fir along an altitudinal gradient in southwestern Germany. *Ann For Sci* 70: 185-193.
- Vitali V, Büntgen U, Bauhus J (2017) Silver fir and Douglas fir are more tolerant to extreme droughts than Norway spruce in south-western Germany. *Glob Change Biol* 23: 5108-5119.
- Weiner J, Thomas SC (2001) The nature of tree growth and the "age-related decline in forest productivity". *Oikos* 94: 374-376.
- Wilson R, Hopfmueller M (2001) Dendrochronological investigations of Norway spruce along an elevational transect in the Bavarian Forest, Germany. *Dendrochronologia* 19: 67-79.
- Xu Y-J, Röhrig E, Fölster H (1997) Reaction of root systems of grand fir (*Abies grandis* Lindl.) and Norway spruce (*Picea abies* Karst.) to seasonal waterlogging. *For Ecol Manag* 93: 9-19.
- Xu K, Wang X, Liang P, An H, Sun H, Han W, Li Q (2017) Tree-ring widths are good proxies of annual variation in forest productivity in temperate forests. *Sci Rep* 7: 1945.
- Zang C, Biondi F (2015) Treeclim: an R package for the numerical calibration of proxy-climate relationships. *Ecography* 38: 431-436.
- Zang C, Hartl-Meier C, Dittmar C, Rothe A, Menzel A (2014) Patterns of drought tolerance in major European temperate forest trees: climatic drivers and levels of variability. *Glob Change Biol* 20: 3767-3779.
- Zang C, Rothe A, Weis W, Pretzsch H (2011) Zur Baumarteneignung bei Klimawandel: Ableitung der Trockenstress-Anfälligkeit wichtiger Waldbaumarten aus Jahrringbreiten. *Allg Forst Jagdztg* 182: 98-112.
- Zech W, Schad P, Hintermaier-Erhard G (2014) *Böden der Welt: Ein Bildatlas*. Springer Spektrum, Berlin and Heidelberg, Germany.
- Zink M, Samaniego L, Kumar R, Thober S, Mai J, Schäfer D, Marx A (2016) The German Drought Monitor. *Environ Res Lett* 11: 074002.

2.8 Supplementary materials

Table S2.1 Characteristics of the 46 TRW chronologies.

ID	Spec	Elevation [m asl]	Lat [°N]	Lon [°E]	n	Period	MSL	Rbar	AGR $\pm 1\sigma$
1	PISY	106	49.33	8.38	97	1886-2013	118	0.61	1.2 \pm 0.4
2	PISY	118	50.12	9.01	94	1887-2016	77	0.52	1.9 \pm 0.5
3	PISY	130	50.02	8.20	91	1834-2013	163	0.52	1.9 \pm 0.5
4	PISY	139	50.01	8.19	96	1832-2016	116	0.39	2.1 \pm 0.6
5	PISY	140	49.98	8.68	94	1847-2015	154	0.53	1.5 \pm 0.3
6	PISY	140	50.01	8.19	74	1885-2018	119	0.51	1.9 \pm 0.4
7	PISY	140	50.01	8.19	101	1845-2019	153	0.38	1.3 \pm 0.3
8	PISY	150	49.95	9.00	70	1895-2014	104	0.54	2.0 \pm 0.5
9	PISY	230	50.46	8.22	54	1864-2017	136	0.35	1.9 \pm 0.6
10	PISY	320	50.42	7.26	41	1930-2020	78	0.56	2.1 \pm 0.5
11	PISY	334	50.70	8.23	113	1859-2012	143	0.52	1.0 \pm 0.3
12	PCAB	338	49.30	7.32	52	1940-2010	60	0.27	2.2 \pm 1.0
13	PISY	345	50.42	7.28	60	1929-2020	83	0.54	2.0 \pm 0.5
14	PISY	354	49.70	7.40	90	1881-2018	128	0.56	1.3 \pm 0.4
15	PISY	363	49.24	8.05	95	1879-2014	117	0.56	1.0 \pm 0.3
16	PISY	383	49.62	6.71	98	1903-2014	106	0.53	2.7 \pm 0.7
17	PCAB	400	49.34	8.11	59	1916-2013	80	0.38	2.7 \pm 0.8
18	PCAB	420	50.43	7.76	77	1913-2010	61	0.32	3.5 \pm 1.3
19	PCAB	420	50.43	7.76	80	1892-2010	105	0.51	2.1 \pm 0.5
20	PCAB	434	50.10	8.09	96	1864-2010	123	0.42	1.4 \pm 0.3
21	PCAB	440	50.81	7.97	90	1917-2010	82	0.48	2.3 \pm 0.7
22	PCAB	450	50.06	7.51	77	1910-2010	89	0.44	2.7 \pm 0.6
23	PISY	460	49.34	8.11	50	1892-2011	100	0.58	1.4 \pm 0.3
24	PISY	460	49.34	8.11	48	1880-2011	115	0.51	1.0 \pm 0.3
25	PCAB	463	50.11	8.09	81	1898-2010	81	0.45	2.1 \pm 0.8
26	PCAB	470	50.38	7.78	106	1915-2011	78	0.52	2.1 \pm 0.6
27	PCAB	472	50.10	8.11	98	1887-2013	88	0.47	1.5 \pm 0.4
28	PISY	490	49.34	8.11	80	1891-2011	81	0.36	1.2 \pm 0.5
29	PISY	490	49.34	8.12	46	1845-2011	139	0.49	1.2 \pm 0.3
30	PISY	490	49.35	8.11	39	1941-2011	75	0.48	1.4 \pm 0.4
31	PCAB	500	50.05	8.01	45	1873-2009	92	0.33	1.2 \pm 0.3
32	PISY	500	49.33	8.11	148	1870-2011	117	0.54	1.0 \pm 0.4
33	PISY	510	49.34	8.10	100	1899-2012	95	0.48	1.4 \pm 0.4
34	PCAB	518	50.20	6.91	97	1917-2016	71	0.51	2.3 \pm 0.8
35	PISY	518	50.07	7.51	63	1887-2016	117	0.50	2.1 \pm 0.5
36	PCAB	519	50.29	7.01	101	1945-2012	61	0.49	2.8 \pm 0.7
37	PCAB	530	50.69	8.16	92	1884-2012	85	0.51	2.5 \pm 0.8
38	PCAB	540	50.05	8.01	96	1925-2012	75	0.51	2.0 \pm 0.5
39	PCAB	550	51.08	8.04	91	1932-2011	74	0.53	3.1 \pm 0.6
40	PCAB	560	49.98	7.68	96	1925-2018	96	0.56	2.1 \pm 0.6
41	PISY	565	49.28	8.01	100	1864-2016	136	0.51	1.2 \pm 0.3
42	PCAB	632	50.22	8.43	99	1932-2020	77	0.52	2.4 \pm 0.6
43	PCAB	680	49.74	7.20	87	1886-2011	95	0.46	1.9 \pm 0.5
44	PCAB	690	50.27	6.38	94	1922-2011	61	0.49	2.4 \pm 0.7
45	PCAB	750	49.73	7.09	57	1916-2009	86	0.43	2.8 \pm 0.5
46	PCAB	819	50.22	8.45	60	1938-2009	65	0.51	3.5 \pm 0.7

Spec: Species: *Picea abies* (PCAB) and *Pinus sylvestris* (PISY). **Lat:** latitude. **Lon:** longitude. **n:** total number of series. **Period:** chronology period at ≥ 10 series. **MSL:** mean segment length. **Rbar:** mean inter-series correlation of the 10SP site chronologies. **AGR:** average growth rate [mm/year] ± 1 standard deviation (1σ) calculated over the first 60 years of cambial age.

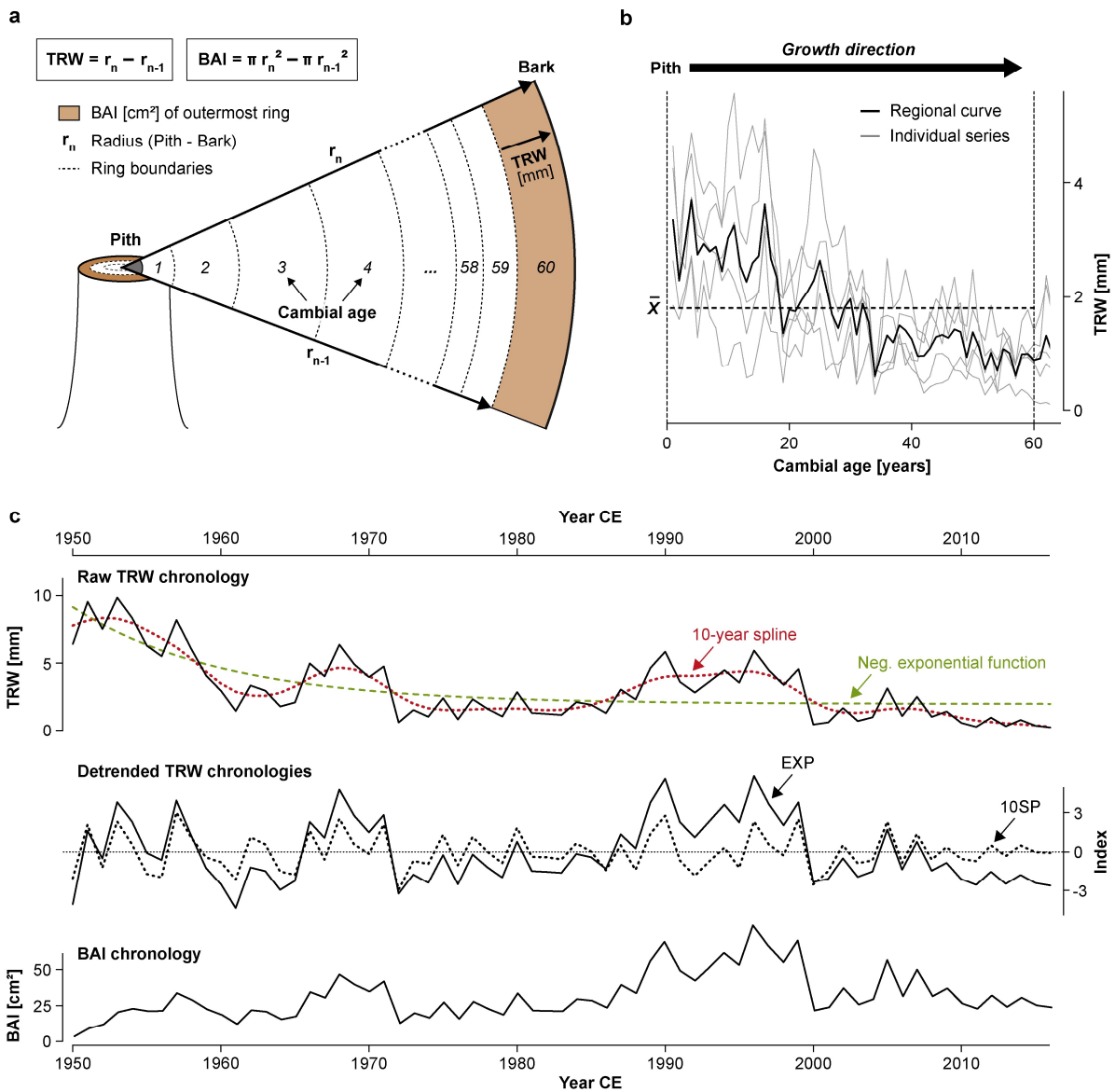


Fig. S2.1 Tree-ring width (TRW) and basal area increment (BAI) data. **(a)** Stem cross-section of a 60-year-old tree showing the two growth parameters. **(b)** The AGR of each site is calculated over the first 60 years of cambial age (highlighted by vertical dashed lines) as mean (\bar{X} ; horizontal dashed line) of the regional curve. **(c)** Effects of standardization and BAI calculation. Top panel shows a raw TRW chronology together with a fitted 10-year cubic smoothing spline (red) and negative exponential curve (green). Middle panel shows the index chronologies after spline (10SP, dotted curve) and negative exponential detrending (EXP, solid curve). Bottom panel shows the BAI record derived from the TRW measurements using the equation shown in panel a.

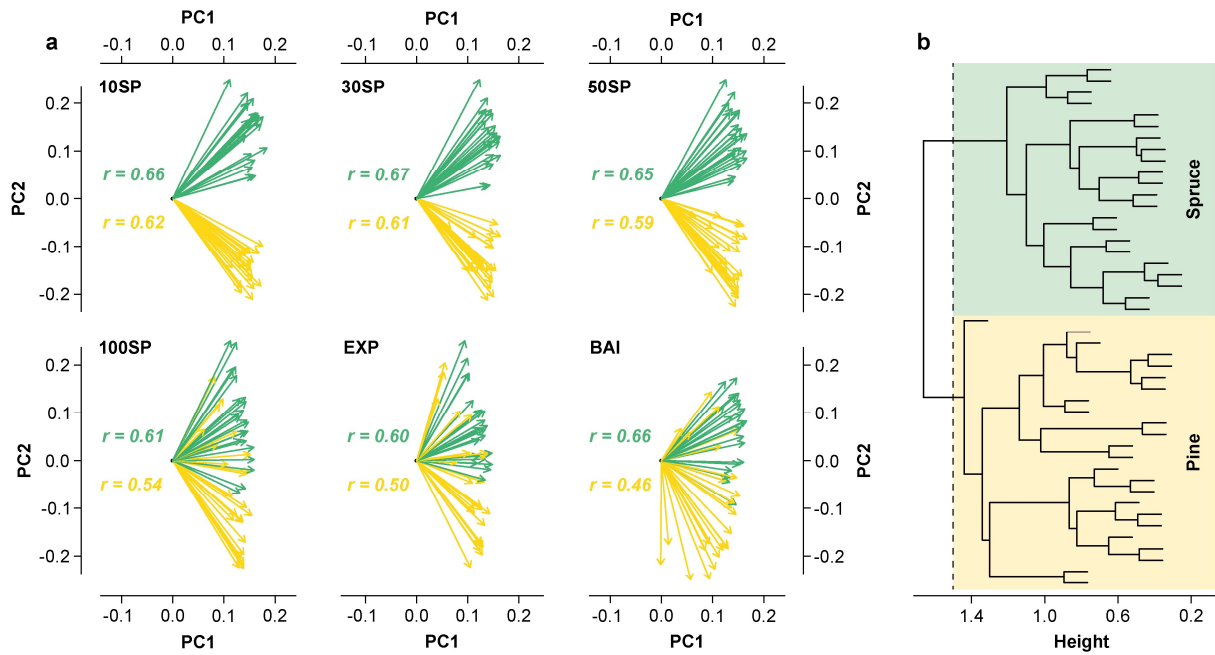


Fig. S2.2 (a) Principal component gradient analyses (Buras et al. 2016) using 10-year (10SP), 30-year (30SP), 50-year (50SP), 100-year (100SP) spline, negative exponential (EXP), and basal area increment (BAI) chronologies (1952-2009 CE). Each arrow represents a spruce (green) or pine (yellow) site. R values indicate average intra-species correlations. **(b)** Hierarchical cluster analysis of the 10SP site chronologies. Note the distinct separation between spruce and pine in the 10SP data.

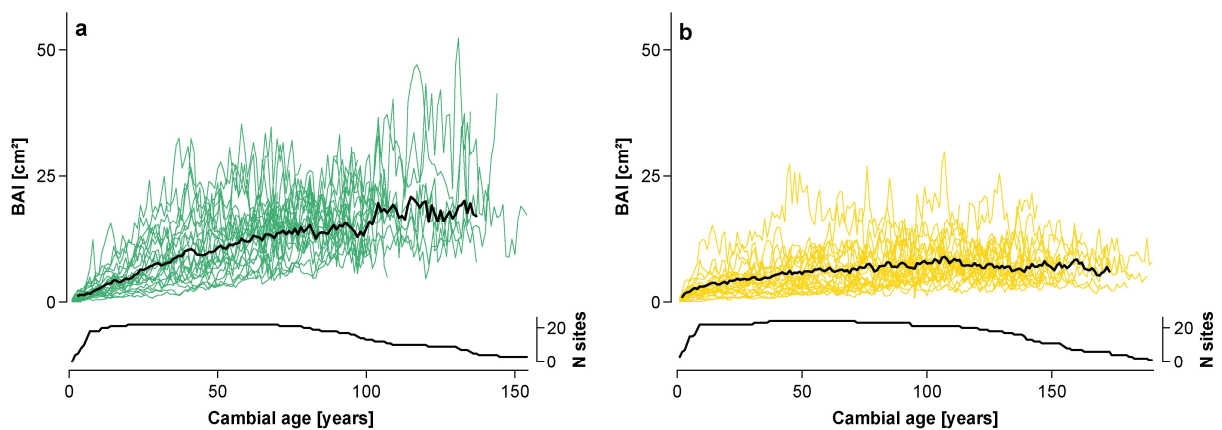


Fig. S2.3 Age-aligned basal area increment (BAI) chronologies of the **(a)** 22 spruce and **(b)** 24 pine sites truncated at < 10 series. Black lines represent species-specific means calculated for $n \geq 5$ sites. Bottom panels show site chronology replications.

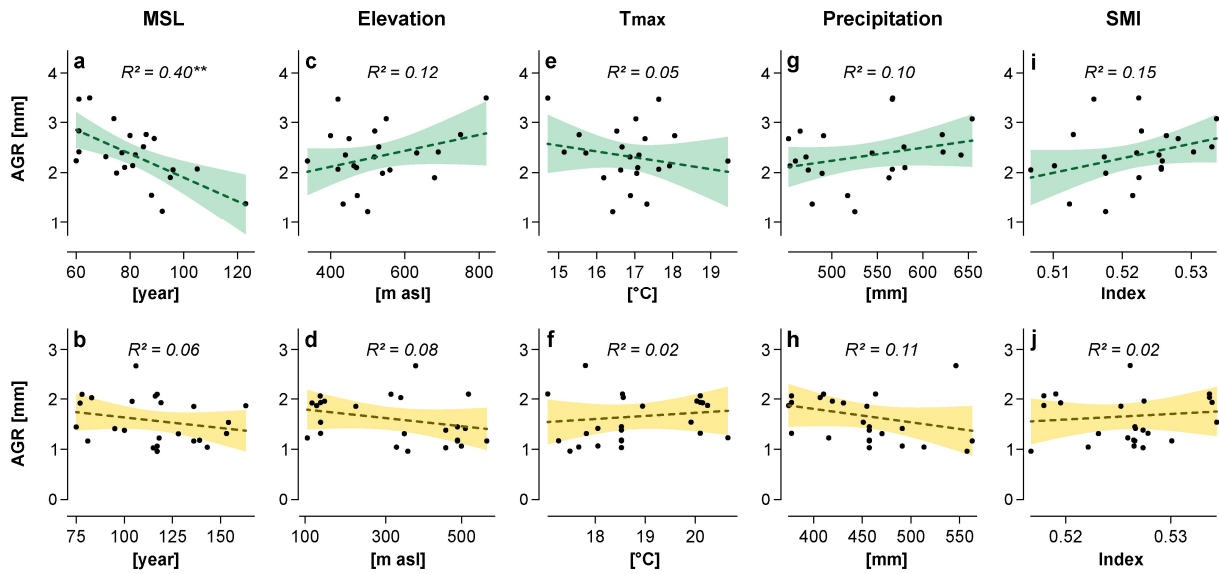


Fig. S2.4 Average growth rate (AGR) of spruce (top panels) and pine (bottom panels) as a function of (a-b) mean segment length (MSL), (c-d) elevation, (e-f) maximum air temperature (T_{max}), (g-h) precipitation totals, and (i-j) soil moisture indices (SMI). The latter three variables are calculated for the growing season (April-October). Each dot represents one site. Dashed lines show linear trends. Colored areas are 95% confidence intervals of the regression slopes for spruce (green) and pine (yellow). Asterisks behind R^2 indicate $p < 0.05$.

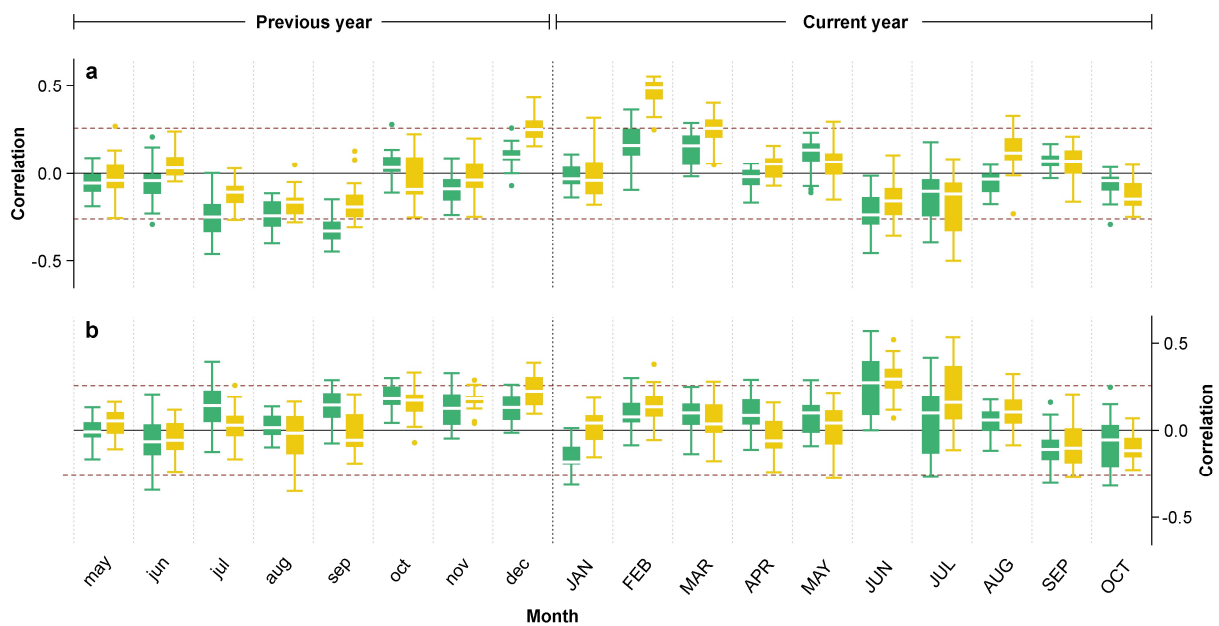


Fig. S2.5 Monthly climate-growth correlations for 1952-2009 CE. Distribution of bootstrap correlations of the 10SP TRW chronologies (spruce = green, pine = yellow) with (a) maximum air temperatures and (b) precipitation from previous-year (lower case letters) May to current-year (upper case letters) October. Boxplots show the median (white bar), 25%- and 75%-quartiles (box), min and max values within 1.5x the interquartile range (whiskers), and outliers (points). Dashed lines mark $p < 0.05$.

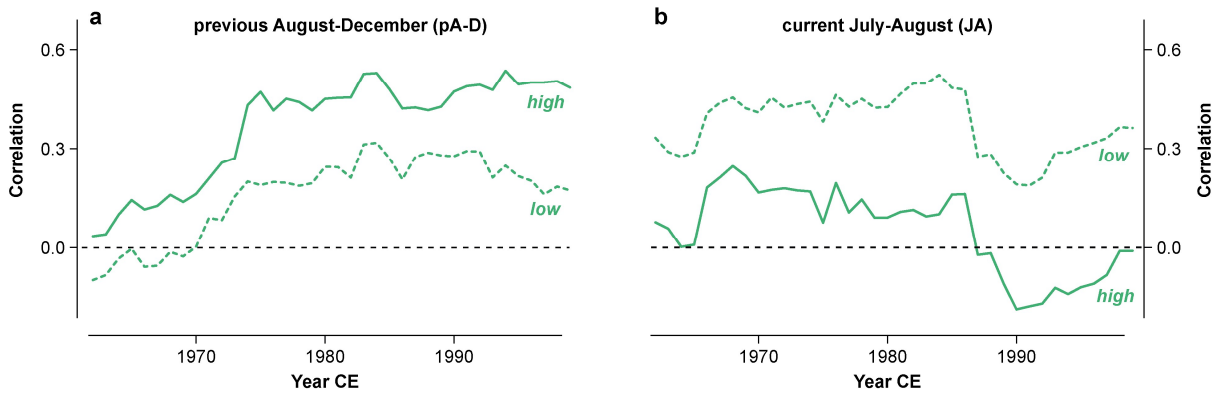


Fig. S2.6 Mean 21-year running correlations of spruce sites below 550 m asl (dashed curves) and above 550 m asl (solid curves) with (a) previous-year August-December (pA-D) and (b) current-year July-August (JA) soil moisture indices (10SP data).

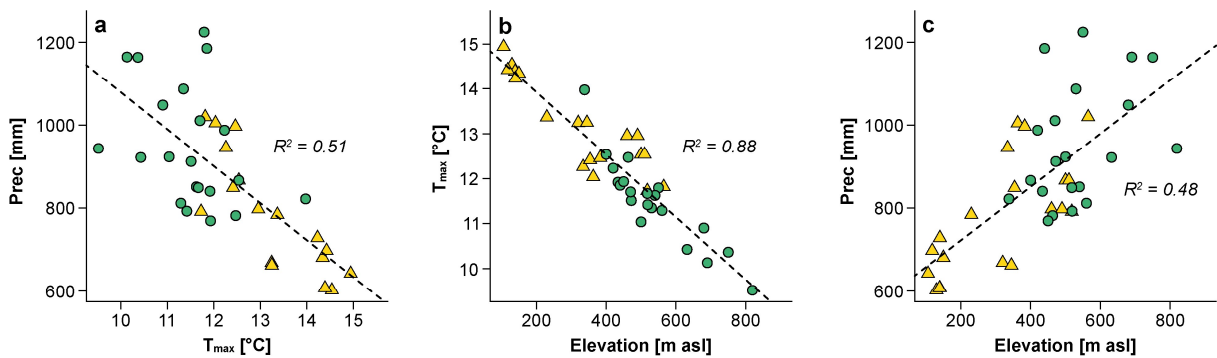


Fig. S2.7 Linear regressions between (a) annual maximum air temperatures (T_{max}) and annual precipitation (Prec), (b) elevation and T_{max} , and (c) elevation and Prec. Green circles represent the spruce sites, yellow triangles the pine sites.

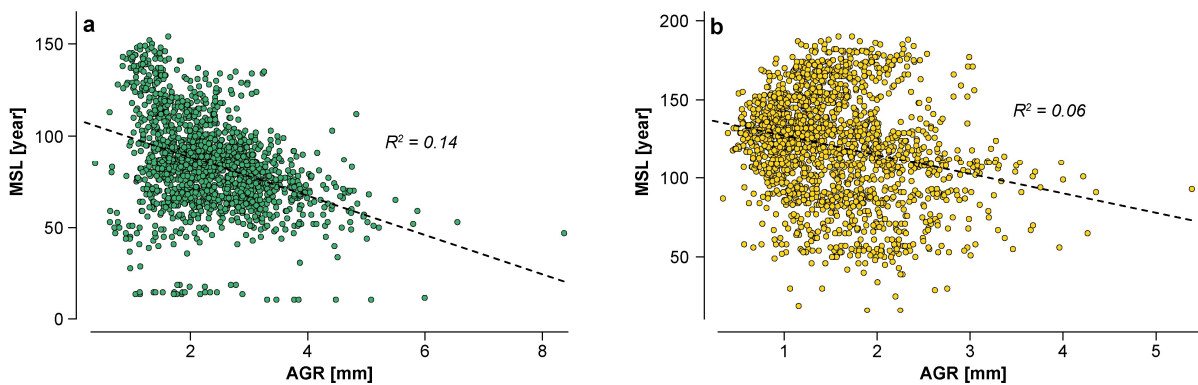


Fig. S2.8 Linear regressions between average growth rates (AGR) calculated over the first 60 years of cambial age and mean segment lengths (MSL) of the (a) 1831 spruce and (b) 1942 pine series. Each circle represents one series.

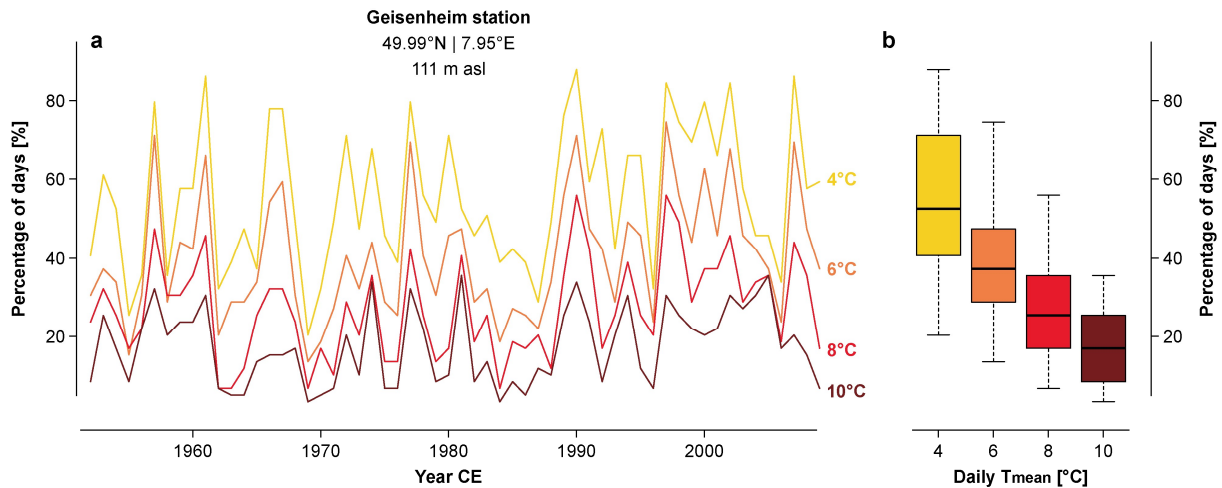


Fig. S2.9 (a) Percentage of February-March days exceeding daily mean temperatures (daily T_{mean}) of 4°C (yellow), 6°C (orange), 8°C (red), and 10°C (dark red) at the meteorological station in Geisenheim from 1952-2009 CE. **(b)** Value distributions of the various temperature thresholds from panel a. Boxplots show the median (black bar), 25%- and 75%-quartiles (box), and min and max values within 1.5x the interquartile range (whiskers). The climate station data was downloaded from the German Weather Service (<https://cdc.dwd.de/portal>).

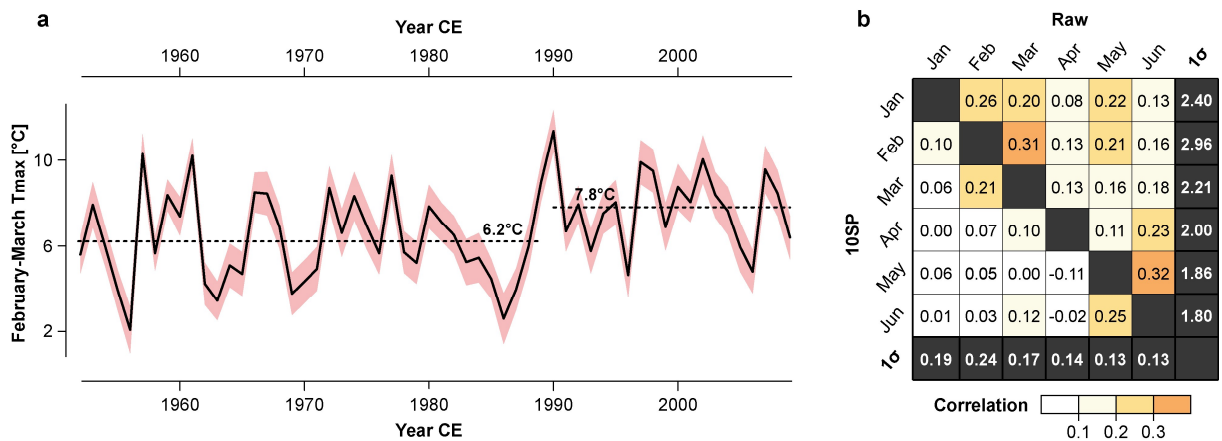


Fig. S2.10 (a) February-March maximum air temperatures (T_{max}) from 1952-2009 CE. Red shading represents ± 1 standard deviation of the 24 grid cells covering the pine sites. Horizontal dashed lines show mean T_{max} from 1951-1989 and 1990-2009 CE. **(b)** Correlation matrix of the raw and high-pass filtered monthly T_{max} series (Jan-Jun). 1 σ indicates one standard deviation of the T_{max} series.

Supplemental references

Buras A, van der Maaten-Theunissen M, van der Maaten E, Ahlgrimm S, Hermann P, Simard S, Heinrich I, Helle G, Unterseher M, Schnittler M, et al. (2016) Tuning the voices of a choir: detecting ecological gradients in time-series populations. *PLoS ONE* 11: e0158346.

3 Reduced temperature sensitivity of maximum latewood density formation in high-elevation Corsican pines under recent warming

Authors: Philipp Römer*, Claudia Hartl, Lea Schneider, Achim Bräuning, Sonja Szymczak, Frédérick Huneau, Sébastien Lebre, Frederick Reinig, Ulf Büntgen, and Jan Esper

Status: Published in *Atmosphere* 12 (2021): 804. <https://doi.org/10.3390/atmos12070804>

Abstract

Maximum latewood density (MXD) measurements from long-lived Black pines (*Pinus nigra* spp. *laricio*) growing at the upper treeline in Corsica are one of the few archives to reconstruct southern European summer temperatures at annual resolution back into medieval times. Here, we present a compilation of five MXD chronologies from Corsican pines that contain high-to-low frequency variability between 1168 and 2016 CE and correlate significantly ($p < 0.01$) with the instrumental April-July and September-October mean temperatures from 1901 to 1980 CE ($r = 0.52-0.64$). The growth-climate correlations, however, drop to -0.13 to 0.02 afterward, and scaling of the MXD data results in a divergence of $> 1.5^{\circ}\text{C}$ between colder reconstructed and warmer measured temperatures in the early 21st century. Our findings suggest a warming-induced shift from initially temperature-controlled to drought-prone MXD formation, and therefore question the suitability of using Corsican pine MXD data for climate reconstruction.

Keywords: climate change, climate signals, dendroclimatology, France, Mediterranean, *Pinus nigra*, tree-ring density.

3.1 Introduction

Southern Europe is predicted to experience increasing aridity in the 21st century mainly due to rising temperatures (Diffenbaugh & Giorgi 2012; Gao & Giorgi 2008; Hertig & Jacobeit 2008), and the intensity, frequency, and duration of heatwaves and droughts are expected to increase (Beniston et al. 2007; Sánchez et al. 2004). The precise assessment of climate changes requires proxy-based reconstructions of pre-instrumental conditions to place recent changes into a long-term context. The employment of trees as high-resolution natural climate archives can provide such valuable insights into past climate fluctuations (Fritts 1976). Although ancient trees growing under extreme conditions and still preserved in their natural state are difficult to find, dendroclimatic studies in Corsica offer the opportunity to reconstruct southern European climate variability over several centuries (Hetzer 2013; Szymczak et al. 2012, 2014).

Located in the central-western Mediterranean region (**Fig. 3.1a**), Corsica is characterized by strong elevational gradients between the coastal plains and the central mountain massif (**Fig. 3.1b**). Due to the island's steep relief, altitude-dependent local climate regimes can be observed (Knerr et al. 2020; Rome & Giorgetti 2007). Coastal regions are characterized by typical Mediterranean climate with hot dry summers (June-August) and temperate rainy winters (October-April). Meteorological observations along the coast record an annual mean temperature of 15.1°C and precipitation sums of 694 mm from 1961-1990 CE (**Fig. 3.1c**), with driest conditions in July (22.7°C and 12 mm). Over recent decades (1951-2016 CE), a warming trend has been observed, which is higher in the June-August summer season (+0.035°C/year) than in the December-February winter season (+0.014°C/year), and has been stronger since 1980 CE (KNMI 2020). With increasing elevation, temperature generally decreases by 0.31-0.49°C/100 m and precipitation increases by approx. 160 mm/100 m (Rome & Giorgetti 2007). However, spatial precipitation patterns are strongly influenced by topographical features and are, therefore, geographically much more diverse than temperature. Although precipitation generally increases with altitude, high elevation areas can be subject to severe droughts during summer, especially between July-August. Consequently, the Corsican mountains can be characterized as xeric in summer and alpine in winter (Rome & Giorgetti 2006).

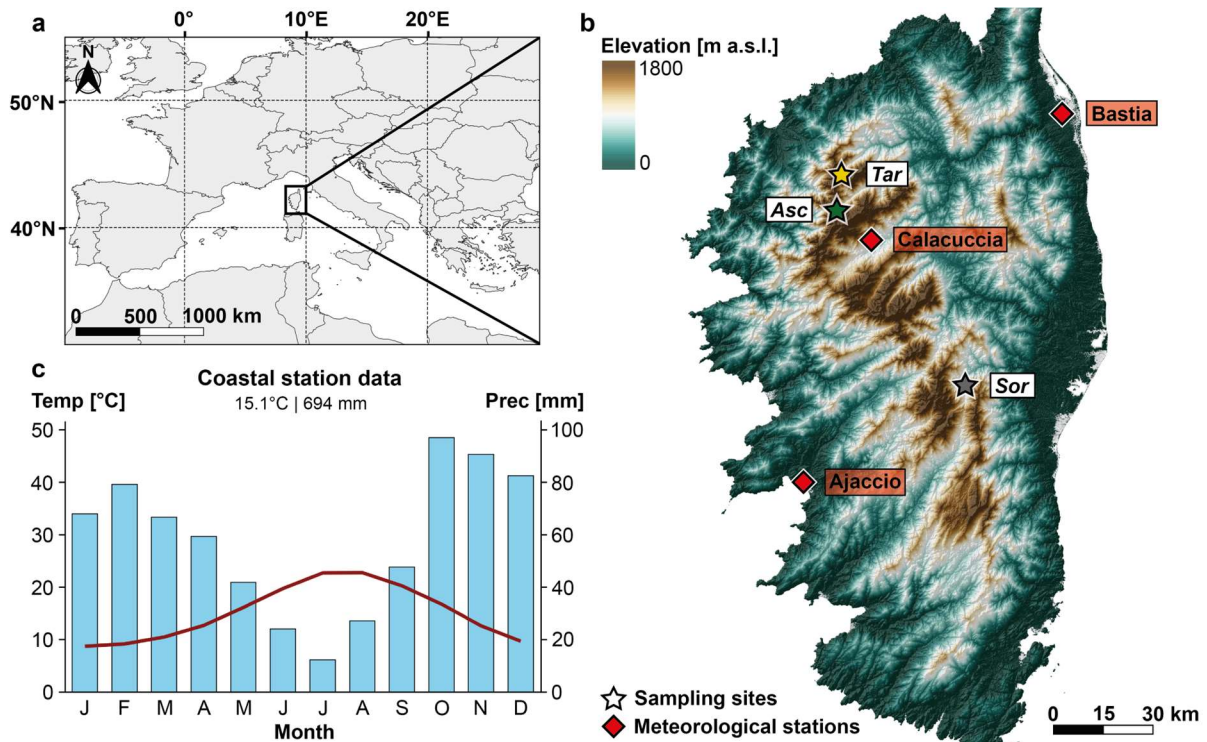


Fig. 3.1 Study site and climate. (a) Geographical location of Corsica in the Mediterranean. (b) Topographic map of Corsica indicating the sampling sites and meteorological stations. (c) Climate diagram showing monthly temperatures (red curve) and precipitation (blue bars) of the combined station data from Ajaccio and Bastia (1961-1990 CE).

Due to the great variety of microclimates, the Corsican mountains feature a high ecological biodiversity (Médail & Verlaque 1997), including two native pine species: Maritime pine (*Pinus pinaster* AITON) and Corsican Black pine (*Pinus nigra* ssp. *laricio* MAIRE). The former mainly covers lower elevations < 1300 m asl that are strongly influenced by anthropogenic activities. Black pine forests are in the high elevation belt between 1400-1800 m with remnants of natural stands near the upper treeline (**Fig. 3.2a**). The drought- and frost-tolerant *Pinus nigra* (Eilmann & Rigling 2012; Fernández-Pérez et al. 2018) may reach ages up to 850 years (Hetzer 2013), ranking these trees among the oldest in the Mediterranean Basin (Luterbacher et al. 2012). Particularly resistant to parasites and decomposition due to their high resin content (Tintner & Smidt 2018), relict pine stems can remain for centuries on the rocky slopes (**Fig. 3.2b**). The presence of these well-preserved trunks in the vicinity of old living stands offers the opportunity to develop multicentennial tree-ring chronologies.

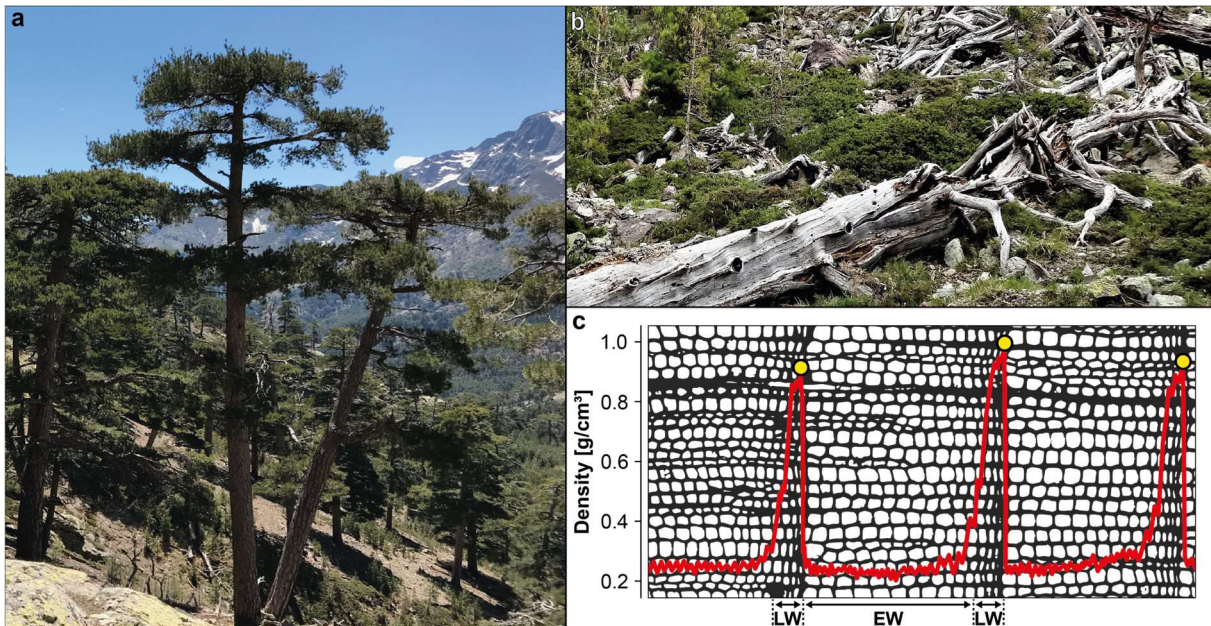


Fig. 3.2 Corsican pines and wood density. **(a)** Living trees and **(b)** relict trunks of *P. nigra* at the upper treeline. **(c)** Thin section of three consecutive tree rings and their density profile (red curve) across the earlywood (EW) and latewood (LW). Yellow dots indicate the maximum latewood density (MXD).

In drought-dominated regions, tree growth is typically determined by water availability resulting from the mutual interaction of temperature, precipitation, and evapotranspiration (Seim et al. 2015; Touchan et al. 2017). Due to low water supply in summer, Mediterranean forest productivity is dependent on the frequency and amount of rainfall events before and during the growing season. Consequently, tree-ring width (TRW) chronologies have been used as proxies to reconstruct precipitation (Esper et al. 2021; Griggs et al. 2007; Ruiz-Labourdette et al. 2014; Touchan et al. 2008) and hydroclimatic variability across southern Europe (Cook et al. 2015; Esper et al. 2007; Klippel et al. 2018; Nicault et al. 2008; Tejedor et al. 2016). High-resolution summer temperature reconstructions are restricted to other tree-ring parameters, such as maximum latewood density (MXD), as TRW is less temperature sensitive in Mediterranean environments (Büntgen et al. 2010).

MXD chronologies are less influenced by biological memory effects and correlate more closely with instrumental temperature data (Esper et al. 2015). However, compared to the extensive networks in Fennoscandia (Esper et al. 2012, 2014) and the Alps (Büntgen et al. 2006), the availability of temperature-sensitive density records spanning 500+ years in the Mediterranean is restricted to the Spanish Central Pyrenees (Büntgen et al. 2017; Dorado-Liñán et al. 2012), the Cazorla Natural Park in southern Spain (Esper et al. 2020a), and the Pindos National Park in northern Greece (Esper et al. 2020b; Klippel et al. 2019). With respect to the central Mediterranean region, comparably long-term MXD chronologies are still missing. Nonetheless, two annually resolved temperature reconstructions provide initial insight into the region's past climate variability: Leonelli et al. (2017) developed a 300-year temperature reconstruction based

on a multi-site MXD network in Italy, while the only temperature reconstruction for Corsica was derived from stable carbon isotopes ($\delta^{13}\text{C}$) extending 560 years into the past (Szymczak et al. 2012). Hence, a long-term MXD-based temperature reconstruction from Corsica is still lacking and remains key to unfold the region's climate history into the early second millennium.

Here, we present the longest MXD record for the Central-Western Mediterranean based on 35 *P. nigra* trees growing at three high-elevation sites on the island of Corsica (France). Covering the period 1168-2016 CE, the dataset extends existing MXD measurements (1518-1980 CE; Schweingruber 2020a) back to medieval times as well as into the 21st century. To evaluate the application of Regional Curve Standardization (RCS), age-band chronologies are produced and different chronology variants are correlated against regional climate data. In this study, we (I) assess climate signals in five chronology variants of the new Corsican MXD compilation, (II) compare the new density data with existing records and summer temperature reconstructions across the southern European region, and (III) evaluate the potential of Corsican pine MXD for climate reconstruction.

3.2 Material and methods

3.2.1 Wood density data and chronology development

In 2017, 39 increment cores from 20 living and relict Black pines (*Pinus nigra* ssp. *laricio*) were sampled at two high-elevation sites in the Asco (Asc, 1600 m asl) and Tartagine valleys (Tar, 1450 m asl), located near the upper treeline in the northwestern mountains of Corsica. Long-lived trees from these valleys were previously used to develop multicentennial tree-ring records (Hetzer 2013; Szymczak et al. 2012, 2014); however, no wood density measurements have been performed. To obtain the longest possible time series, mainly old and dominant trees as well as relict stems were selected for this study. Following standard radiodensitometric techniques (Björklund et al. 2019; Eschbach et al. 1995; Schweingruber et al. 1978), all cores were heated in 96% ethanol in a Soxhlet extraction system to remove hydrophobic components. The purified samples were split into 3-cm segments to saw out 1.2-mm thick laths orthogonally to the longitudinal stem axis. The laths were acclimatized at 20°C and 50% relative humidity for 4 hours to ensure a homogeneous cell wall moisture content of ~10%. Subsequently, the samples were radiographed for 14 min at 10 kV and 20 mA, and wood densities were determined at 0.01 g/cm³ resolution using a Walesch high-precision DENDRO2003 X-ray densitometer. The density peaks in each ring were used to produce interannual MXD data (**Fig. 3.2c**).

After aligning the data by cambial age, a Hugershoff-shaped age trend was observed, including an average MXD increase of 0.1 g/cm³ over the first 70 years of growth and a gradual decrease of 0.13 g/cm³ over the subsequent 330 years (71-400 years). To remove this characteristic biological trend from the raw MXD data (Esper et al. 2012, 2014), a Hugershoff Standardization

(HGS) and a Regional Curve Standardization (RCS) were applied in the detrending program ARSTAN (Cook & Krusic 2005), resulting in two chronology variants: COR_{HGS} and COR_{RCS} . After applying a data adaptive power-transformation to minimize heteroscedasticity within the individual series (Cook & Peters 1997), all data were detrended by calculating residuals from the smoothed HGS-/RCS-mean curves and variance-stabilized using a 300-year spline with a fixed 50% cutoff to avoid deviations caused by changing sample replications and inter-series correlations (Frank et al. 2007). Robust bi-weight mean chronologies were computed (Cook 1985), and the covariance of each chronology was assessed by calculating the inter-series correlation (R_{bar}) and the expressed population signal (EPS) over semi-overlapping 30-year periods (Wigley et al. 1984).

The new density data produced in our laboratory in Mainz (Germany) were compared with older measurements ($n = 30$ series), produced in the early 1980s in Birmensdorf (Switzerland) covering the period 1518-1980 CE (Schweingruber 2020a) (data available at the International Tree-Ring Data Bank, www.ncdc.noaa.gov/data-access/paleoclimatology-data, accessed on 5 October 2020). The latter were derived from Black pines growing at the mountain pass Col de Sorba on Monte Renoso (Sor, 1400 m asl), which is located ~45 km southeast of the new sites. Given the significant correlation ($r_{avg} = 0.46$) among the three site chronologies *Asc*, *Tar*, and *Sor* from 1636 to 1980 CE (**Fig. 3.3**, **Table S3.1**), we produced a merged dataset integrating all Corsican MXD data (*COR*). The composite dataset contained 69 MXD series and exceeded a robust EPS of ≥ 0.85 back to 1425 CE (**Fig. S3.1**). When merging the data, absolute MXD values were adjusted among the sites to mitigate significant ($p < 0.001$) elevational MXD effects between *Tar* and *Sor* (0.96 g/cm^3) and *Asc* (0.89 g/cm^3) calculated for the first 200 years of growth (**Fig. S3.2**).

Both detrending techniques applied in this study – HGS and RCS – are able to preserve multi-centennial variability in dimensionless index chronologies (Esper et al. 2003; Fang et al. 2010), although HGS is an individual detrending method and is restricted by the “segment length curse” (Cook et al. 1995). Accurate RCS detrending, however, requires the mean cambial age of the series combined in a chronology to be constant over time (Briffa et al. 1992; Esper et al. 2016). To avoid the typical increase in mean tree age toward the present, age-band chronologies (*ABC*; Briffa et al. 2001) were produced by removing tree rings younger than 30 years and older than 200 years (*ABC200*), 300 years (*ABC300*), and 400 years (*ABC400*) of cambial age (**Table S3.2**). Accordingly, five methodologically different chronologies were developed considering HGS and RCS with all data, as well as RCS with the three age bands: COR_{HGS} , COR_{RCS} , *ABC200*, *ABC300*, and *ABC400*.

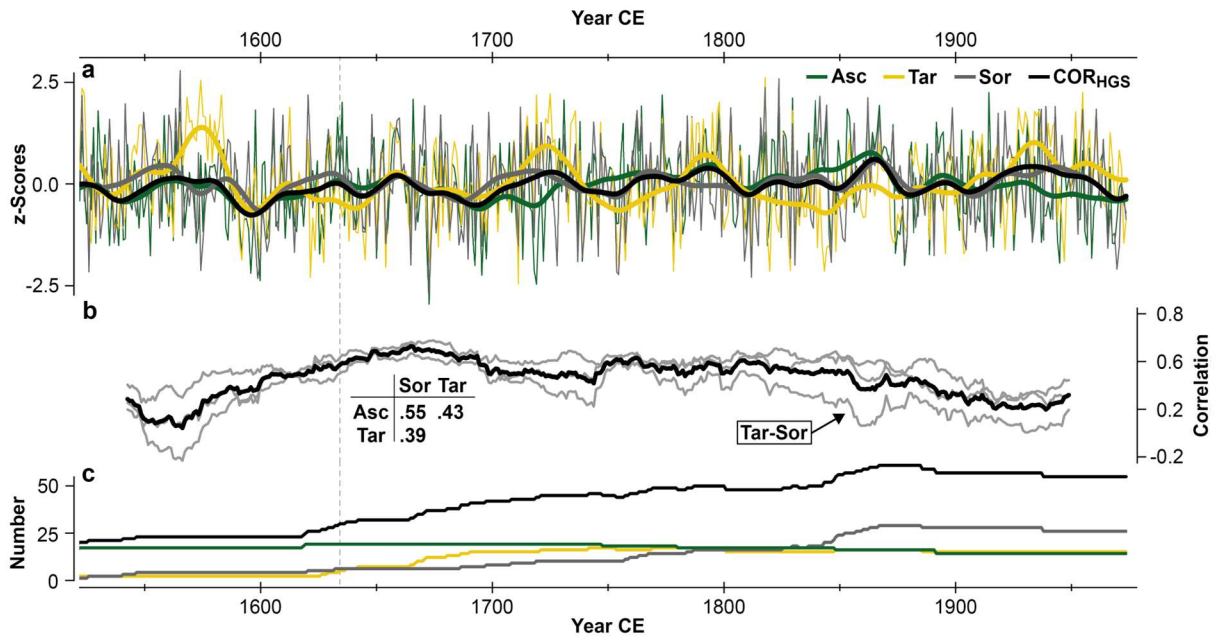


Fig. 3.3 (a) Hegershoff-detrended MXD composite (COR_{HGS}) and site chronologies (*Asc*, *Tar*, and *Sor*) (thin curves), and their 31-year smoothing splines (bold curves). (b) 51-year running correlations between the site chronologies (grey) shown together with their mean (black). The inserted table indicates inter-site correlations calculated over the sufficiently replicated ($n \geq 5$ series) common period 1636-1980 CE (1636 CE is marked by a vertical dashed line). (c) Sample replication of each chronology.

3.2.2 Climate data and signal estimation

To assess the climate sensitivity of Corsican Black pine MXD and evaluate its suitability for reconstruction purposes, climate data from the meteorological stations in Ajaccio (41.92°N/8.80°E, 9 m asl) and Bastia (42.54°N/9.49°E, 10 m asl), CRU TS4.04 temperature data (Harris et al. 2020), and GPCC v2020 precipitation data (Schneider et al. 2021) were compiled using the KNMI Climate Explorer (Trouet & van Oldenborgh 2013). The CRU and GPCC grids extend across 42-42.5°N and 8.5-9.5°E, covering the entire study area. The GPCC data were chosen for the analysis of precipitation signals due to the high station density in Europe and long temporal coverage back to 1891 CE (Schneider et al. 2021). The temperature means and precipitation totals were converted into monthly and seasonal anomalies with respect to 1961-1990 CE. The observations from Ajaccio and Bastia were merged by calculating arithmetic means from 1951 to 2016 CE. Comparison of the coastal station means with recordings from a local station in Calacuccia (42.34°N/9.01°E, 875 m asl) back to 1975 CE (Météo-France 2021) reveals 3.76°C warmer conditions from April-October in Ajaccio and Bastia. The local temperatures are, however, closely correlated with the coastal records ($r = 0.86$) and CRU temperatures ($r = 0.84$). In contrast, the annual precipitation totals from Calacuccia are less correlated with the coastal records ($r = 0.53$) and GPCC data ($r = 0.67$). We, therefore, used the coastal means and CRU temperatures, as well as the GPCC precipitation data, to assess the climate sensitivity of the high-elevation MXD records.

All MXD chronologies were correlated (Pearson's r) with monthly and seasonal climate data over the 1951-1980 CE period to compare climate signals contained in the old and new density measurements, as well as over the 1951-2016 CE period to account for recent climate variability. To evaluate the temporal robustness of the climate signals, 31-year running correlations were calculated between the density indices and different seasonal averages of meteorological data (April-July and September-October temperatures, as well as June-July and August-September precipitation). Further, all MXD chronologies were correlated with 0.5° gridded monthly and seasonal CRU TS4.04 data using the KNMI Climate Explorer to assess spatial correlation patterns over the Mediterranean Basin from $37-47^\circ\text{N}$ and $-3-21^\circ\text{E}$.

3.3 Results

3.3.1 MXD chronology characteristics

The *COR* MXD compilation consists of 69 radii from 35 pine trees and spans the period 1168-2016 CE, including an increasing number of measurements toward the present. Replication falls below five series at 1359 CE, while the maximum of 61 series is reached from 1872 to 1890 CE. *COR* replication decreases again in the late 20th century from 55 series in 1980 CE to 29 series in 1981 CE, when the *Sor* data terminate. Over the first 400 years of cambial age, average MXD (AMXD) is 0.91 g/cm^3 ($\pm 0.05 \text{ g/cm}^3$) with a minimum of 0.78 g/cm^3 in the fifth year of growth and a maximum of 1.00 g/cm^3 in the 107th year of growth. This juvenile AMXD increase is followed by a small but persistent decrease (**Fig. S3.3**).

The lengths of the individual series range from 67 to 849 years with a mean segment length (MSL) of 325 years, whereas the age classes are unevenly distributed across the sites. Trees sampled at the *Asc* site are significantly ($p < 0.01$) older ($\text{MSL}_{\text{Asc}} = 543$ years) than those at the two lower sites ($\text{MSL}_{\text{Tar}} = 290$ and $\text{MSL}_{\text{Sor}} = 211$ years). Consequently, *COR* is characterized by a heterogeneous age structure and site composition over time. All five *COR* chronologies share annual to multidecadal scale variability. Further, *COR*_{HGS} shows a significant ($p < 0.001$) agreement in correlation with the site chronologies ($r = 0.67-0.82$) over the sufficiently replicated ($n \geq 5$ series) 1636-1980 CE period. Compared to *COR*, the age-band chronologies – *ABC200*, *ABC300*, and *ABC400* – are characterized by flatter mean age and replication curves (**Fig. 3.4**). Due to the removal of rings older than 200, 300, and 400 years (and younger than 30 years), the age-band chronologies cover different periods. Whereas all chronologies extend back to 1365 CE with $n \geq 5$ series, *ABC200* already ends in 1980 CE, *ABC300* in 1988 CE, and only *ABC400* reaches into the 21st century until 2016 CE. Inter-chronology differences in replication and site contributions, thus, increase toward the present.

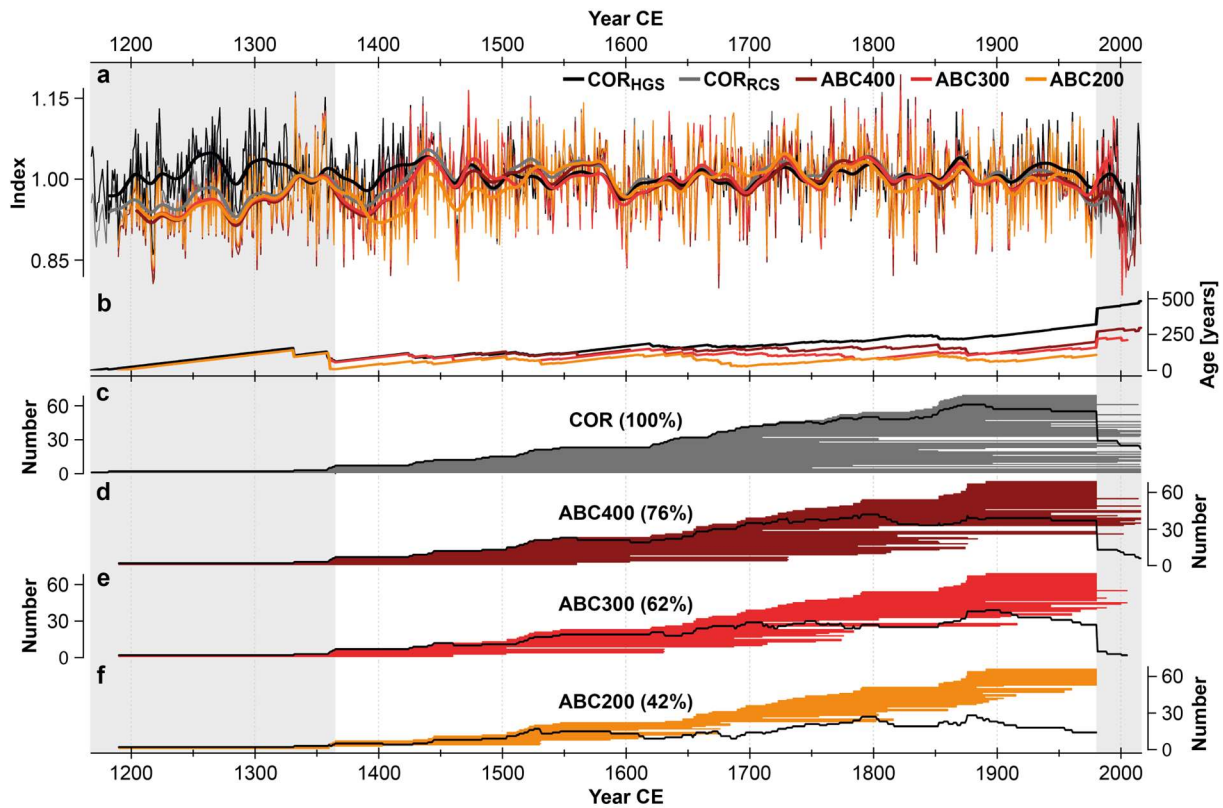


Fig. 3.4 Effects of age-band decomposition. **(a)** Detrended composite chronologies (thin curves) and their 31-year smoothing splines (bold curves) considering all MXD data (COR), data from 30-400 years ($ABC400$), 30-300 years ($ABC300$), and 30-200 years ($ABC200$). COR was detrended using HGS (COR_{HGS}) and RCS (COR_{RCS}), while all age-band chronologies were detrended using RCS. **(b)** Mean tree age of the chronologies. **(c-f)** Samples (bar plots) and replication (black lines) of the chronologies. Each horizontal bar depicts one individual series. Percentages in brackets indicate the remaining data compared to COR (= 100%). Grey-shaded areas mark the periods when replication in at least one record is $n < 5$ series.

The age-band chronologies show substantial agreement in high-to-low frequency covariance ($r_{avg} = 0.91$) and correlate significantly at $r_{avg} = 0.92$ with the untruncated chronology COR_{RCS} over the well-replicated ($n \geq 5$ series) 1365-1980 CE common period. On multidecadal scales, MXD indices of all chronologies increase from around 1400-1440, 1600-1660, 1700-1730 and 1760-1790 CE, and decrease from 1360-1390, 1440-1460, 1580-1600, 1730-1760, 1790-1820, 1860-1910, and 1950-1980 CE. In the 20th century, however, the smoothed chronologies diverge considerably: COR_{RCS} and $ABC400$ both show a minor increase from 1975-1990 CE and a sharp decline thereafter; the smoothed $ABC300$ ends in 1990 CE and shows a striking post-1975 CE increase due to low sample replication; while $ABC200$ only extends until 1980 CE and shows no remarkable deviations from the other chronologies in the 20th century, but does in periods of $n < 10$ series, such as the late 17th century and before ~1510 CE. Furthermore, large differences are observed between the HGS- and RCS-indices prior to ~1425 CE, as evidenced by a downward shift in RCS-values in the earliest density measurements. These differences are slightly higher between COR_{HGS} and the age-bands than between COR_{HGS} and COR_{RCS} .

The comparison of COR_{HGS} with other long-term density records from southern Europe reveals a generally decreasing correlation with increasing geographic distance (**Table 3.1**, **Fig. 3.5a**). COR_{HGS} correlates significantly ($p < 0.001$) with the pine MXD records from the Spanish Pyrenees (*GER*, $r = 0.53$; Büntgen et al. 2017) and southern Italy (*CRI*, $r = 0.42$; Schweingruber 2020b) from 1360-2004 CE, while weaker associations are found with more distant (> 1000 km) records from southern Spain (*CAZ*, $r = 0.33$; Esper et al. 2020a) and northwestern Greece (*SMO*, $r = 0.28$; Esper et al. 2020b). Correlations with western Mediterranean sites are slightly higher than with equidistant sites in the eastern Mediterranean.

Table 3.1 Characteristics of Mediterranean MXD records.

Code	Site	Species	Radii	Period	Season	Correlation	Distance
CAZ	Cazorla	PINI	88	1288-2014	FMAM&SO	0.53 0.45	1150 km
COR	Corsica	PINI	69	1360-2016	AMJJ&SO	0.56 0.16	0 km
CRI	Serra di Crispo	PIHE	21	1604-1980	JAS	0.60 0.60	650 km
GER	Gerber	PIUN	414	1095-2014	MJ&AS	0.59 0.38	650 km
LOE	Loetschental	LADE	180	748-2004	JJAS	0.77 0.78	450 km
SMO	Mt. Smolikas	PIHE	192	672-2017	AS	0.52 0.56	1050 km

Species: LADE: *Larix decidua*, PIHE: *Pinus heldreichii*, PINI: *Pinus nigra*, PIUN: *Pinus uncinata*. **Period:** start and end dates were set considering a replication of $n \geq 5$ radii. **Correlation:** Pearson correlations of HGS-detrended MXD chronologies calibrated against nearby seasonal CRU TS4.04 temperatures over the 1901-1980 CE common period (left value), and from 1901 to the actual end date of each chronology (right value). **Distance:** linear distance from Corsica.

The weakest association is found with the nearest record from the Alps (*LOE*, $r = 0.23$; Büntgen et al. 2006), located only ~450 km north of COR_{HGS} , which is the only chronology based on *Larix decidua* instead of pine. The smoothed density records from the Mediterranean outline both periods of high and low inter-regional correlations (**Fig. 3.5b**). High covariance is primarily found in periods of pronounced variability, such as 1440-1500, 1580-1610, 1650-1670, 1810-1830, and 1850-1890 CE, whereby the z-score levels differ among the sites. Moreover, some chronologies indicate substantially deviating behavior, e.g., *CAZ* from 1760-1810 CE. Comparisons with tree-ring-based temperature reconstructions (**Fig. 3.5c**) from Corsica ($COR_{\delta^{13}C}$; Szymczak et al. 2012) and the Spanish Pyrenees (PYR_{MXD} ; Dorado-Liñán et al. 2012) demonstrate that the interannual MXD variability of *P. nigra* is more strongly associated with reconstructed May-September temperatures from the Iberian Peninsula ($r_{1582-2005} = 0.55$) than with reconstructed August-September temperatures from Corsica ($r_{1582-2005} = 0.16$), although the latter is derived from stable carbon isotopes of Black pines close to the *COR* sites (Szymczak et al. 2012). In contrast, the reconstruction from the Pyrenees is based on a multi-site *Pinus uncinata* MXD network (Dorado-Liñán et al. 2012).

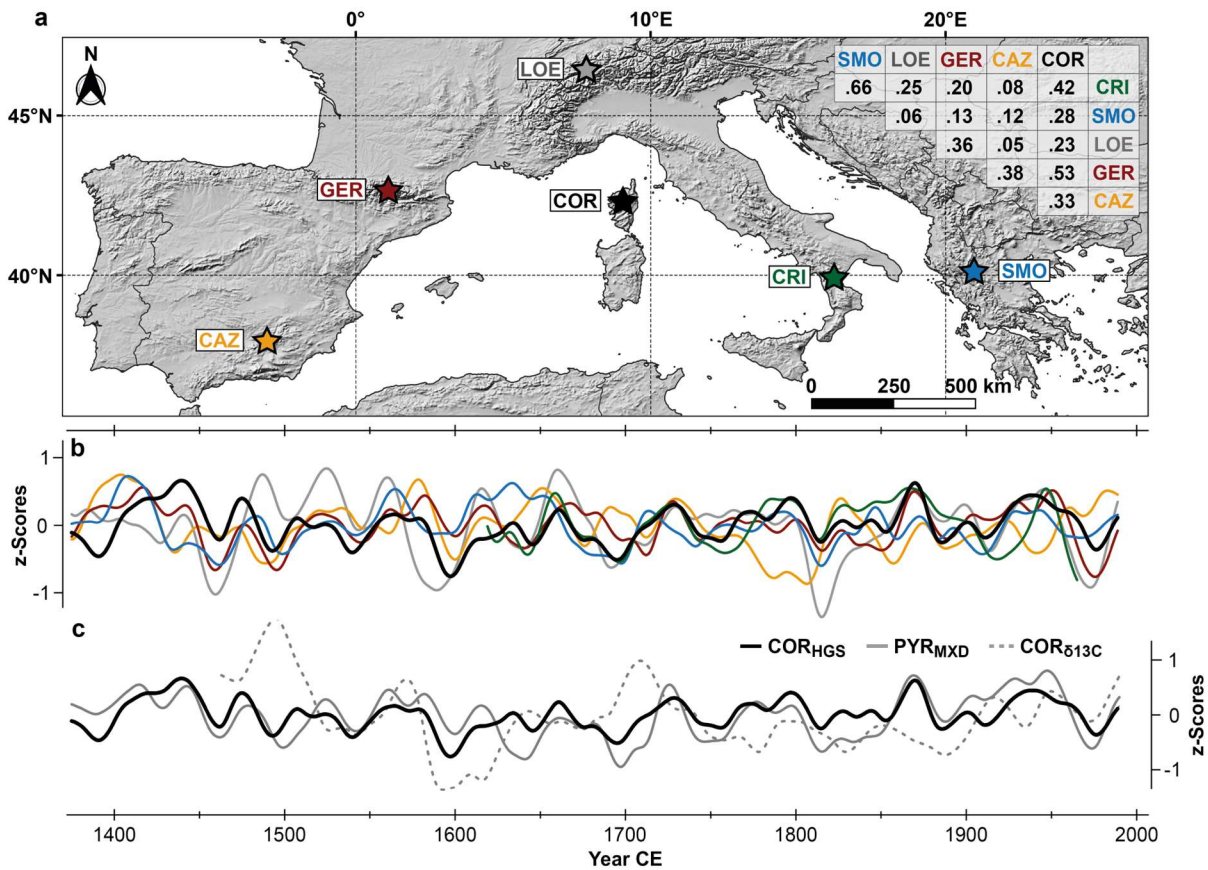


Fig. 3.5 Comparison of long MXD chronologies from southern Europe. **(a)** Location of the MXD sites: Cazorla (CAZ), Gerber (GER), Corsica (COR), Serra di Crispo (CRI), and Mt. Smolikas (SMO). The matrix shows correlations between the HGS-detrended chronologies over their 1360-2004 CE common period – except for CRI, which covers 1604-1980 CE. **(b)** 31-year smoothing splines of the normalized HGS-detrended MXD chronologies from 1375-1989 CE ($n \geq 5$ series). **(c)** COR_{HGS} shown together with the August-September temperature reconstruction from Corsican pine stable carbon isotopes ($COR_{\delta^{13}C}$) and a May-September temperature reconstruction from the Pyrenees based on MXD (PYR_{MXD}). All records were normalized (COR_{HGS} and PYR_{MXD} from 1360-2005 CE and $COR_{\delta^{13}C}$ from 1448-2005 CE) and smoothed using 31-year splines.

3.3.2 Climate sensitivity of Corsican MXD

MXD in Mediterranean conifers is primarily influenced by warm-season temperatures (**Table 3.1**). In Corsica, correlations between the site chronologies and regional observations reveal local differences in temperature sensitivity as well as temporal changes in signal strength. The site chronologies show weak to moderate associations to the regional April-July and September-October mean temperatures (AMJJ&SO) over the 1951-1980 CE period (**Fig. 3.6a**), ranging from $r = 0.17$ at *Tar* to $r = 0.47$ at *Sor*. Although correlations with regional July temperatures are low overall ($r = 0.03$ - 0.15), analysis with CRU temperatures indicate a significant ($p < 0.01$) association of $r = 0.42$ at *Sor* (**Fig. S3.4**).

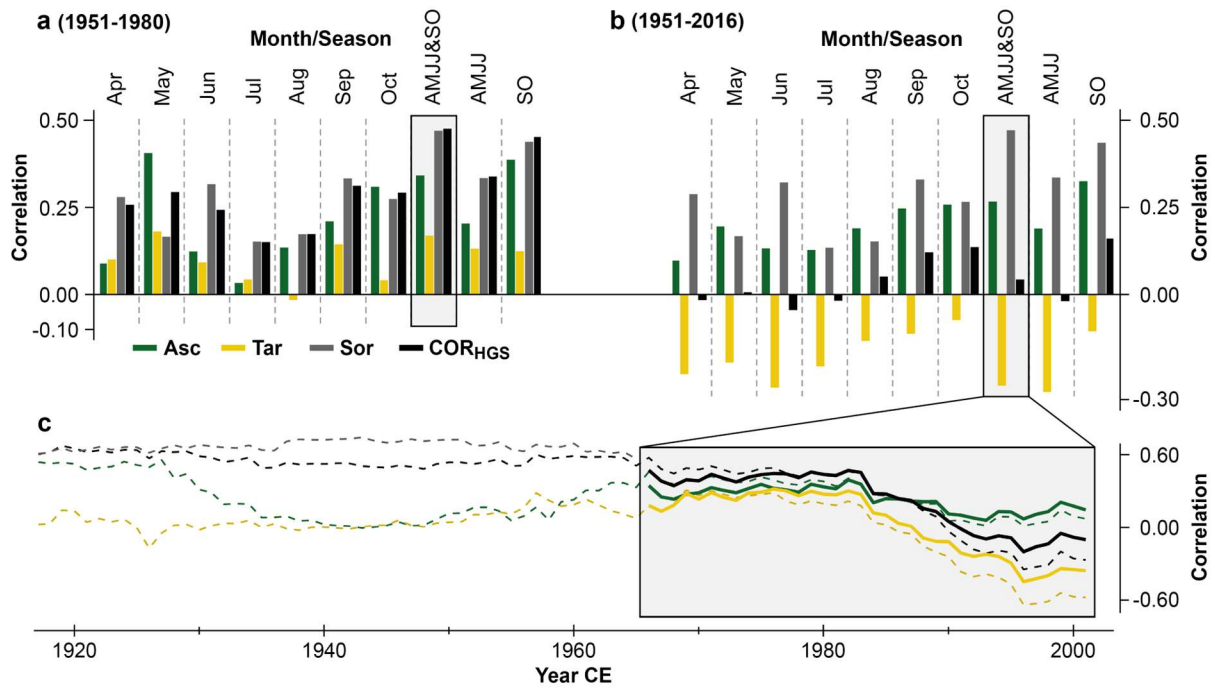


Fig. 3.6 Site-specific temperature signals. Correlations between the Hegershoff-detrended chronologies and monthly and seasonal temperatures of the combined station records from (a) 1951-1980 and (b) 1951-2016 CE. Note that *Sor* only extends to 1980 CE and indicates same correlations in (a) and (b). (c) Thirty-one-year running correlations between the chronologies and seasonal AMJJ and SO temperatures of the station records (thick solid curves) and CRU data (thin dashed curves).

The COR_{HGS} composite record shows a similar temperature sensitivity to *Sor*, with the highest correlation found for the AMJJ and SO season ($r = 0.47$, $p < 0.01$) from 1951-1980 CE. Extending the calibration period into the 21st century results in a systematic decrease in temperature sensitivities (Fig. 3.6b). While the *Asc* correlation with AMJJ and SO temperatures marginally weakens from $r_{1951-1980} = 0.34$ to $r_{1951-2016} = 0.27$, the originally positive correlation of *Tar* turns negative when extended into the 21st century, from $r_{1951-1980} = 0.17$ to $r_{1951-2016} = -0.26$. In line with these *Asc* and *Tar* responses (*Sor* terminates in 1980 CE), a decline toward insignificant temperature correlations is also seen in COR_{HGS} when including the post-1980 CE data ($r_{1951-2016} = 0.04$). Thirty-one-year running correlations between the chronologies and seasonal AMJJ and SO temperatures confirm these findings (Fig. 3.6c). COR_{HGS} indicates a temporally stable temperature signal until 1983 CE against station ($r_{1966-1983} = 0.34-0.47$) and CRU data ($r_{1916-1983} = 0.42-0.67$). The pre-1983 CE running correlations of COR_{HGS} are higher than those of *Asc* and *Tar*, but slightly lower than those of *Sor*. However, the running correlations of all chronologies decrease sharply after 1983 CE, and this decline is stronger in *Tar* and weaker in *Asc*, whereas COR_{HGS} remains in-between.

The five MXD composite chronologies show similar temperature sensitivities from 1901-1980 CE (Fig. 3.7). Correlations with April-July CRU temperatures ($r = 0.43-0.53$) are slightly higher than with September-October means ($r = 0.33-0.44$), but the AMJJ and SO season fits best ($r = 0.52-0.64$). The strongest association with temperature is found for the most truncated age-

band chronology *ABC200* ($r = 0.64$, $p < 0.01$). Spatial analyses using gridded CRU temperatures reveal strong correlations with the April-October means across the western and central Mediterranean regions. The highest correlations ($r \geq 0.40$) are found with June-July temperatures over Corsica, Iberia, and Maghreb (**Fig. 3.7a**).

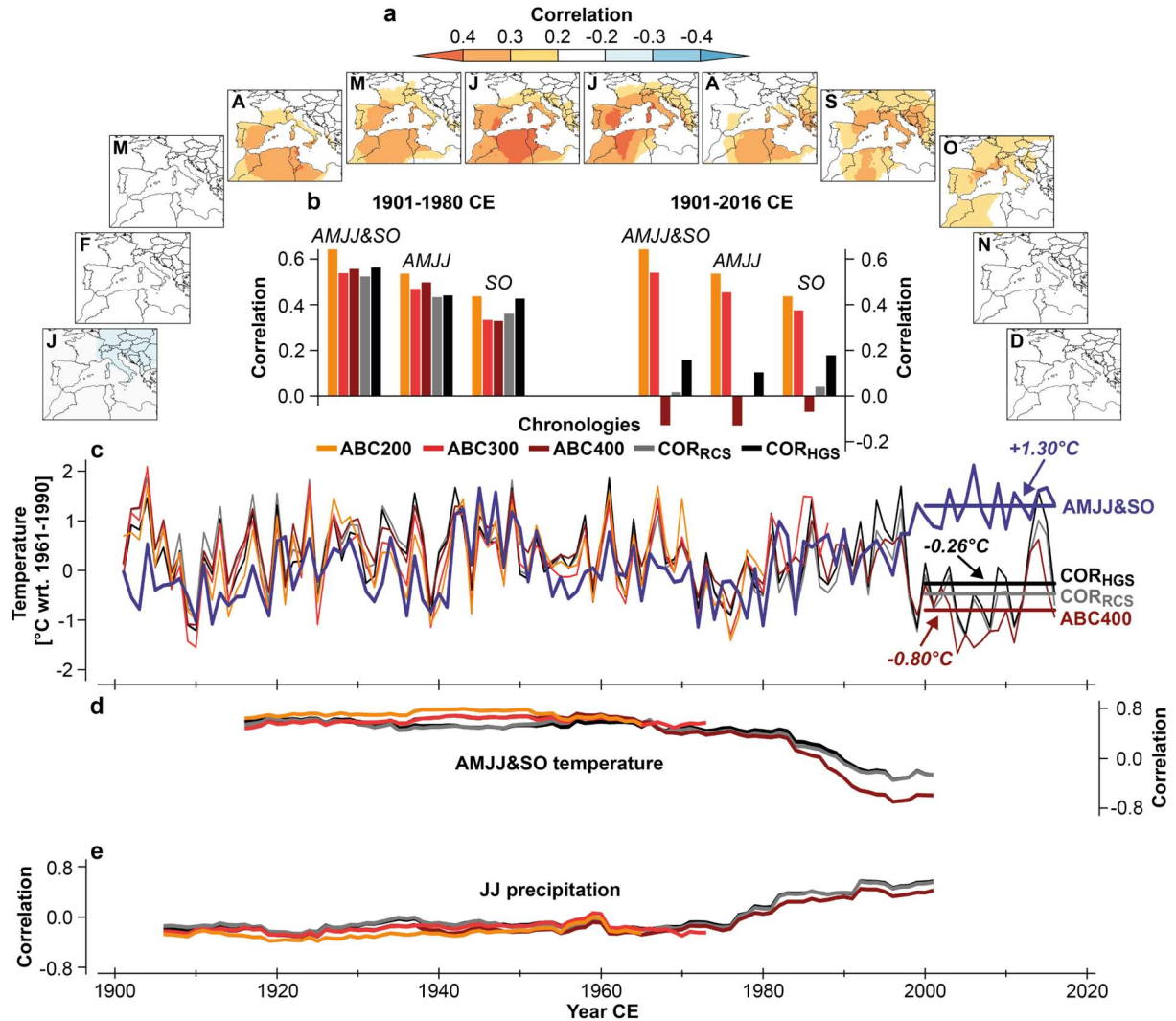


Fig. 3.7 Climate signals of the Corsican MXD composite chronologies. **(a)** Spatial correlations between *ABC200* and 0.5° gridded monthly temperatures (CRU) over the Mediterranean Basin (1901-1980 CE). Significant correlations at $p < 0.1$ are colored. **(b)** Correlations between the composite chronologies and seasonal temperatures from 1901-1980 (left) and 1901-2016 CE (right). Note that *ABC200* and *ABC300* only extend until 1980 and 1988 CE, respectively. **(c)** MXD chronologies scaled from 1901-2016 CE against AMJJ and SO temperature anomalies (CRU). Horizontal lines display mean temperatures from 2000 to 2016 CE. 31-year running correlations between the MXD chronologies and **(d)** CRU AMJJ and SO temperatures, and **(e)** GPCP JJ precipitation.

In August, however, correlations over the study area decline ($r = 0.21$). As for the site chronologies, a systematic decrease in signal strength is observed in the composite records when the calibration period is extended into the 21st century (**Fig. 3.7b**). All MXD chronologies reaching 2016 CE with $n \geq 5$ series (*COR_{HGS}*, *COR_{RCS}*, *ABC₄₀₀*) show non-significant low correlations with AMJJ and SO temperatures over the 1901-2016 CE period. A simple scaling of *COR_{HGS}*

against post-1900 CE temperatures highlights a substantial divergence of 1.56°C between the colder reconstructed ($-0.26 \pm 0.78^{\circ}\text{C}$) and warmer measured temperatures ($+1.30 \pm 0.38^{\circ}\text{C}$) from 2000 to 2016 CE, although the MXD and temperature records display similar interannual-to-decadal scale variability over most of the 20th century (**Fig. 3.7c**). The observed 21st-century divergence is caused by opposing low-frequency trends starting in the late 1990s and is even greater when considering COR_{RCS} and $ABC400$, respectively. The 31-year running correlations support these findings (**Fig. 3.7d**), as all composite chronologies show temporally stable temperature correlations of $r \geq 0.45$ before 1967 CE, followed by $r = 0.30$ - 0.45 from 1968 to 1983 CE, and a sharp decrease thereafter. Simultaneously, running correlations with June-July precipitation increase since the 1980s (**Fig. 3.7e**).

Analyses using the GPCP data show that the Corsican MXD records are only weakly associated with precipitation (**Fig. S3.5**). Between 1891-1980 CE, all chronologies correlate significantly ($p < 0.05$) negatively with June-September precipitation ($r = -0.28$ to -0.36). Correlations are lower and insignificant over the full 1981-2016 CE calibration period for COR_{HGS} , COR_{RCS} , and $ABC400$; however, the running correlations with June-July precipitation show a sharp post-1980 CE increase, while correlations with August-September precipitation remain stable.

3.4 Discussion

3.4.1 Chronology variants and characteristics

The combination of MXD data from three valleys enabled the development of a regional record (COR) characterized by a high sample replication ($n = 69$) and robust common signal ($EPS \geq 0.85$) back to 1425 CE. The five methodologically different composite chronologies share high fractions of high-to-low frequency variance from 1500 to 1980 CE. Noticeable trend differences are recorded before ~ 1500 CE and in the late 20th and early 21st centuries. The age-band data more closely meet the requirements for RCS (Esper et al. 2002, 2003), as these chronologies are characterized by more balanced replication and age curves. Thus, our findings imply that age-band decomposition – as introduced by Briffa et al. (2001) for a large network of Northern Hemisphere MXD data to improve the preservation of long-timescale variability and successfully applied in recent studies by Esper et al. (2014, 2020a) – produces a sample structure that is likely more applicable for RCS. However, the differences between $ABC200$, $ABC300$, and $ABC400$ remain small and restricted to periods of weaker sample replications ($n < 10$ series). This is particularly the case in $ABC200$, as this chronology is most affected by the systematic removal of old tree rings. The substantial data reduction together with the marked discrepancies with all other chronologies during low-replication periods raises questions regarding the overall reliability of $ABC200$. $ABC300$ and $ABC400$, on the other hand, are characterized by less variable replication curves. Even after the removal of rings older than 400 years, $ABC400$

extends until 2016 CE with sufficient data replication. Yet removing data from the comparably small Corsica MXD dataset remains challenging.

Large differences between the HGS and RCS indices before ~1425 CE and smaller deviations after 1900 CE raise doubts regarding the suitability of RCS for our dataset. While HGS, as a tree-by-tree standardization technique, is barely able to preserve multicentennial variability and produces a quasi-stationary chronology fluctuating around a mean index of one, the composite RCS technique retains more low frequency variance and produces lower values at each chronology end. Whether these low frequency trends are valid is difficult to estimate; however, we hypothesize that the regional curves established in the RCS runs (Esper et al. 2003) do not adequately represent the earliest and latest density measurements, particularly during the low-replication period prior to ~1425 CE. This bias might originate from the selective sampling approach that focuses on old living trees and leads to younger trees being underrepresented in all chronologies (Briffa et al. 1996). However, to clarify these methodological limitations, a larger MXD dataset including different age classes is required.

3.4.2 *Bimodal temperature signals*

Various studies have reported that warm-season temperatures are the main climatic driver of MXD formation in high-elevation Mediterranean conifers (Büntgen et al. 2010, 2017; Dorado-Liñán et al. 2012; Esper et al. 2020a, 2020b; Klippel et al. 2019; Leonelli et al. 2017). Regarding the calibration with pre-1980 CE instrumental data, our results are consistent with these findings, revealing significant temperature correlations throughout the growing season from April to October, with a lack of forcing in August. In contrast, the influence of precipitation on MXD appears to be minor. The resulting bimodal seasonality of temperature signals is comparable to findings reported by Büntgen et al. (2017) and Esper et al. (2020a) from Spanish sites.

Whereas bimodality at the Cazorla Natural Park in southern Spain is characterized by a weakened response during mid-summer months from June-August (Esper et al. 2020a), it was less pronounced in the Pyrenees (Büntgen et al. 2017), as well as in Corsica, where only one month (July and August, respectively) is insignificant. Bimodal response patterns have only been observed at western Mediterranean sites so far; eastern Mediterranean sites, such as *SMO* (Esper et al. 2020b; Klippel et al. 2019), as well as MXD chronologies from central (Büntgen et al. 2006; Frank et al. 2005) and northern European regions (Esper et al. 2012, 2014) have not been found to exhibit bimodality. Given the temperature insensitive MXD formation in Morocco (Esper et al. 2006) and the bimodal signals at the Spanish sites (Büntgen et al. 2017; Esper et al. 2020), our findings suggest a tendency toward increased seasonal bimodality with decreasing latitude and/or greater aridity throughout the Western Mediterranean. However, additional

studies need to be conducted across the region to identify mechanisms and climatic thresholds responsible for bimodal temperature signals.

The physiological reasons for this lack of response during peak warmth are not yet fully understood but are potentially related to a temperature-decoupled carbohydrate production (Esper et al. 2020a) and/or the effect of drought limiting xylogenesis (Camarero et al. 2010; De Micco et al. 2016). The latter assumption is in line with previous work by Trouet (2014), who found the MXD of *P. nigra* to be more sensitive to August precipitation than to temperature at several sites in southern Italy and Greece, whereas Esper et al. (2006) reported MXD formation in the xeric regions of Morocco to be primarily controlled by drought variability. Since the high mountain regions of Corsica can also be subject to drought from June-August (Rome & Giorgetti 2006), our results imply that high evapotranspiration rates limit July-August soil water contents, thus, temporally altering the sensitivity of latewood formation toward precipitation. This hypothesis is supported by dendrometer data obtained along an elevational transect of pines in Corsica, revealing fast changes in stem circumference after precipitation events in summer and rainfall-induced cambial reactivation in autumn (Szymczak et al. 2020a). The latter might also explain the negative correlations of MXD with September precipitation.

The wood anatomical traits of *P. nigra* latewood, such as tracheid diameter, lumen width, and cell wall thickness, are strongly determined by the trees' water status, as their expression results from trade-offs between the hydraulic requirements of the xylem and the avoidance of embolism (Hetzer et al. 2014; Martín-Benito et al. 2013; Petrucco et al. 2016). Protecting the trees from cavitation, smaller tracheids with thicker cell walls are formed in summer, whereas larger tracheids with thinner walls are needed to improve hydraulic efficiency (Pittermann et al. 2006; Szymczak et al. 2014). Since the trees vascular system can be severely damaged by embolism, cavitation protection appears to be primarily important. Thus, latewood cells tend to be denser in years with higher monthly temperatures and adequate water supply (Fonti et al. 2010; Hetzer et al. 2014).

Temperatures at the beginning and end of the growing season appear to have a strong influence on latewood formation, as sufficient precipitation falls in spring and autumn. The positive relationship between April-May temperatures and MXD is likely related to a combination of early snowmelt, reinforced photosynthetic activity, and the production of non-structural carbohydrates prior to the onset of cambial activity (Büntgen et al. 2017; Hetzer 2013). In contrast, correlations in September-October demonstrate the direct influence of air temperature on secondary cell wall deposition and lignification (Fonti et al. 2010; Piermattei et al. 2015). Although latewood cell formation generally proceeds from July to September, cell wall thickening and the lignification of terminal tracheids can continue into October (Gričar et al. 2005; Hetzer 2013; Lebourgeois 2000), leaving discernible imprints in MXD.

Moderate inter-site correlations and varying temperature correlations at *Asc*, *Tar*, and *Sor* suggest that the temperature sensitivity of MXD was co-influenced by local site conditions. Since the duration and intensity of summer drought generally decreases with altitude, trees at lower sites generally contain stronger hydroclimatic signals (Hartl-Meier et al. 2014; Häusser et al. 2019; Szymczak et al. 2020a). This tendency might also impact the reduced temperature correlations at *Tar* (1450 m asl), as this site is located ~150 m beneath *Asc* in the adjacent valley. The MXD chronology from *Sor* at only 1400 m asl, however, indicates the highest temperature sensitivity, suggesting that elevational differences are less influential overall. Previous studies point to combined biogeographical effects of local topography, slope exposure, soil formation, and water supply when discussing climate signals in Corsican TRW networks (Hetzer 2013), tree-ring stable isotopes (Szymczak et al. 2012, 2019), and intra-annual density fluctuations (Hetzer et al. 2014). This might also be applicable for MXD; however, further measurements and a network across the island are necessary to disentangle the impact of local site conditions on *P. nigra* MXD formation.

3.4.3 Fading temperature signals

In environments where temperature is the limiting factor for tree growth, MXD has proven ideal for reconstructing past summer temperature variability (Briffa et al. 1992; Büntgen et al. 2006; Esper et al. 2012). However, hemispheric studies reported a decreasing temperature sensitivity since the second half of the 20th century (Briffa et al. 1998, 2004). This phenomenon, known as the “divergence problem”, describes the inability of temperature-sensitive tree-ring chronologies to adequately capture 20th-century warming. The lack of mirroring recent warming questions the reliability of tree-ring-derived temperature reconstructions during putative pre-instrumental warm periods. Despite widespread evidence in a network of MXD data obtained from multiple sites across the Northern Hemisphere (Briffa et al. 1998), divergence appears to be more prevalent at northern latitudes (D’Arrigo et al. 2007). As most records were developed in the 1980s and 1990s, respectively, and only a few extend to the 21st century (Briffa et al. 1998; Schweingruber & Briffa 1996), there is a need to update MXD records toward the present for further in-depth-investigations on the divergence problem.

Our Corsican MXD chronologies reveal a similar decoupling from temperature in the late 20th century, resulting in an underestimate of $\geq 1.56^{\circ}\text{C}$ between the warmer instrumental and colder reconstructed temperatures in the 21st century. In contrast to the results by Briffa et al. (1998, 2004), this decoupling starts in the late 1990s and not in the 1960s. We suggest that the rising temperatures throughout recent decades have resulted in more severe summer drought periods with higher evapotranspiration rates at our study sites. Instrumental observations support this assumption and reveal that warm-season temperatures have continuously increased over

the past 100 years, particularly after 1980 CE. While AMJJ and SO temperatures from 1980-2000 CE are comparable to those of the 1940s or 1950s, warming amplified rapidly thereafter surpassing nearly all 20th-century observations. Since this temperature increase is not accompanied by increasing rainfall, the offset between precipitation and potential evapotranspiration is widening toward the present (Laffoley et al. 2018).

Drought episodes have begun to occur more frequently and persist longer, particularly since the 1990s, when hydroclimate extreme events were most severe in the Western and Central Mediterranean (Cook et al. 2016; Spinoni et al. 2015). In Corsica, the frequency of dry years since intensified rapidly from 20% to 50%, while heavy rainfall events occurred more frequently (Laffoley et al. 2018), further promoting summer drought as water infiltration is impeded by the rocky slopes and large portions of precipitation are lost to surface runoff (Szymczak et al. 2020a). We therefore conclude that the *P. nigra* trees growing at the upper treeline suffer from enhanced drought stress since the 1990s, causing the decrease in MXD sensitivity to warm-season temperatures toward the end of the 20th century. At the same time, running correlations reveal that June-July precipitation became increasingly important for MXD formation, although precipitation signals are weak overall. The 1990s are identified as the turning point in climate sensitivity. It appears that the succession of several severe drought events caused a shortage of carbohydrate reserves due to inhibited photosynthetic activity during summer (Martín-Benito et al. 2013; Medrano et al. 2002).

Although Black pines feature an effective stomatal control mechanism (Lebourgeois et al. 1998) and indicate a plastic response to dryness with a rapid recovery thereafter (Eilmann et al. 2012), trees at *Tar* have suffered particularly from prolonged drought stress since the 1990s. This could explain the anticorrelations with temperature over the most recent calibration period. The effects of high temperatures and low water availability stimulate stomatal closure, limit the absorption of carbon dioxide, and further a shortage of non-structural carbohydrates required for cell wall formation (Hartl-Meier et al. 2015; Medrano et al. 2002; Olano et al. 2014). This conclusion is consistent with previous dendroclimatological studies detailing drought as an important driver of Mediterranean tree growth and suggesting that the increasing frequency and duration of summer aridity has reduced the temperature-growth relationship at southern European sites (Büntgen et al. 2012; Castagneri et al. 2014; Galván et al. 2015; Martín-Benito et al. 2010; Thiel et al. 2012).

The Corsican pine forests are also affected by regular wildfires characteristic for Mediterranean forests (Mouillot et al. 2003; Soulères 2000). Wildfires have been recognized as disturbance events in dendroclimatic studies as they can leave distinct fingerprints in the tree-ring series of pines (Fulé et al. 2008; Szymczak et al. 2020b; Touchan et al. 2012). However, whereas the number of recorded fires increased throughout the 20th century in many Mediterranean

regions (Pausas et al. 2008), there was no indication of a change in Corsican fire regime coinciding with the altered climate sensitivity in high-elevation MXD data as reported here. The striking coherence among TRW chronologies from multiple Corsican pine sites, extending well into the 21st century (Szymczak et al. 2014), supports the conclusion that local fire events are of minor importance for the climate signals recorded in tree-ring growth proxies.

Despite possible uncertainties in climate signal estimation emerging from the application of gridded and instrumental station data from the coastal plain, the Corsican composite chronologies contain crucial temperature information, as COR_{HGS} indicates a high coherence in low-frequency variability with the world's best replicated ($n = 414$) MXD record from the Spanish Pyrenees (*GER*). The *GER* chronology correlates significantly ($r_{1950-2014} = 0.72$, $p < 0.01$) with May-June and August-September temperatures over large parts of the Western Mediterranean (Büntgen et al. 2017). Similar spatial correlations are recorded between the *ABC200* and AMJJ and SO temperatures prior to 1980 CE. Despite the greater geographical distance, COR_{HGS} is more closely related to the May-September temperature reconstruction based on MXD from Pyrenean mountain pines (Dorado-Liñán et al. 2012) than to the August-September temperature reconstruction derived from stable carbon isotopes of Corsican Black pines (Szymczak et al. 2012). This discrepancy could result from both the different seasonalities and/or the climate proxies, as carbon isotopes are more closely influenced by the mutual interactions of temperature, precipitation, and transpiration, and carry a mixed climate signal (Szymczak et al. 2012). Based on these findings, we hypothesize that interannual MXD variability derived from Corsican Black pines can reliably represent large-scale temperature patterns across the Central-Western Mediterranean over more than 500 years. However, due to the decreasing sensitivity since the late 20th century, a formal reconstruction of past temperatures is not warranted. The development of more and better-replicated MXD chronologies are required to determine how the increasing drought sensitivity affects *P. nigra* growth and to improve our understanding of past climate dynamics in Corsica.

3.5 Conclusion

By combining 69 MXD measurements from three high-elevation sites in Corsica, we update previously established density data by 36 years into the 21st century and by 350 years back to the Middle Ages. After applying two detrending techniques that are able to preserve multicentennial variability, as well as age-band decomposition, all chronologies of the now longest MXD record for the Central-Western Mediterranean indicate similar associations with climate data. The strongest correlations are observed with April-July and September-October temperatures over calibration periods prior to 1980 CE. August temperatures are found to play a minor role in MXD formation, accentuating a bimodal seasonality in temperature response that is similar

to observations at Spanish sites in the Pyrenees and Andalusia. The bimodality in temperature sensitivity is likely related to (I) an unimpeded carbohydrate production during mid-summer, when temperatures do not fall below the physiological thresholds; while, at the same time, (II) distinct drought conditions cause stomatal closure inhibiting photosynthetic activity. Comparisons with other temperature-sensitive MXD chronologies from the Mediterranean region show that the Corsican density record contains large-scale climate information over more than 500 years. However, weakening temperature associations since the 1990s caused by differing low-frequency trends between wood density and instrumental temperature data raise doubts regarding the reliability of *P. nigra* MXD for climate reconstruction. We demonstrate that the post-1990 CE divergence was likely due to a shift from thermal to hydroclimate forcing. In context of recent warming, our results underline the significance of updating tree-ring density data into the present to assess whether MXD-based temperature reconstructions derived from 20th century calibration periods remain valid into the 21st century. For a better understanding of underlying physiological mechanisms and the influence of drought on MXD formation, additional studies of wood anatomical traits would be helpful.

3.6 Acknowledgements

Not available online.

3.7 References

- Beniston M, Stephenson D, Christensen OB, Ferro C, Frei C, Goyette S, Halsnaes K, Holt T, Jylhä K, Koffi B, et al. (2007) Future extreme events in European climate: an exploration of regional climate model projections. *Clim Change* 81: 71-95.
- Björklund J, von Arx G, Nievergelt D, Wilson R, van den Bulcke J, Günther B, Loader NJ, Rydval M, Fonti P, Scharnweber T, et al. (2019) Scientific merits and analytical challenges of tree-ring densitometry. *Rev Geophys* 57: 1224-1264.
- Briffa KR, Jones PD, Bartholin TS, Eckstein D, Schweingruber FH, Karlén W, Zetterberg P, Eronen M (1992) Fennoscandian summers from AD 500: temperature changes on short and long timescales. *Clim Dyn* 7: 111-119.
- Briffa KR, Jones PD, Schweingruber FH, Karlen W, Shiyatov SG (1996) Tree-ring variables as proxy-climate indicators: problems with low-frequency signals. In: Jones PD, Bradley RS, Jouzel J (eds) *Climatic variations and forcing mechanisms of the last 2000 years*. Springer, Berlin and Heidelberg, Germany: pp 9-41.

- Briffa KR, Osborn TJ, Schweingruber FH (2004) Large-scale temperature inferences from tree-rings: a review. *Glob Planet Change* 40: 11-26.
- Briffa KR, Osborn TJ, Schweingruber FH, Harris IC, Jones PD, Shiyatov SG, Vaganov EA (2001) Low-frequency temperature variations from a northern tree ring density network. *J Geophys Res Atmos* 106: 2929-2941.
- Briffa KR, Schweingruber FH, Jones PD, Osborn TJ, Shiyatov SG, Vaganov EA (1998) Reduced sensitivity of recent tree-growth to temperature at high northern latitudes. *Nature* 391: 678-682.
- Büntgen U, Frank DC, Neuenschwander T, Esper J (2012) Fading temperature sensitivity of Alpine tree growth at its Mediterranean margin and associated effects on large-scale climate reconstructions. *Clim Change* 114: 651-666.
- Büntgen U, Frank DC, Nievergelt D, Esper J (2006) Summer temperature variations in the European Alps, A.D. 755-2004. *J Clim* 19: 5606-5623.
- Büntgen U, Frank DC, Trouet V, Esper J (2010) Diverse climate sensitivity of Mediterranean tree-ring width and density. *Trees* 24: 261-273.
- Büntgen U, Krusic PJ, Verstege A, Sangüesa-Barreda G, Wagner S, Camarero JJ, Ljungqvist FC, Zorita E, Oppenheimer C, Konter O, et al. (2017) New tree-ring evidence from the Pyrenees reveals western Mediterranean climate variability since medieval times. *J Clim* 30: 5295-5318.
- Camarero JJ, Olano JM, Parra A (2010) Plastic bimodal xylogenesis in conifers from continental Mediterranean climates. *New Phytol* 185: 471-480.
- Castagneri D, Nola P, Motta R, Carrer M (2014) Summer climate variability over the last 250 years differently affected tree species radial growth in a mesic *Fagus-Abies-Picea* old-growth forest. *For Ecol Manag* 320: 21-29.
- Cook ER (1985) *A time series analysis approach to tree-ring standardization*. Dissertation, University of Arizona, Tucson, AZ, USA.
- Cook ER, Krusic PJ (2005) *Program ARSTAN, A tree-ring standardization program based on detrending and autoregressive timeseries modeling with interactive graphics*. Lamont-Doherty Earth Observatory, Columbia University, Palisades, NY, USA.
- Cook ER, Peters K (1997) Calculating unbiased tree-ring indices for the study of climatic and environmental change. *Holocene* 7: 361-370.
- Cook BI, Anchukaitis KJ, Touchan R, Meko DM, Cook ER (2016) Spatiotemporal drought variability in the Mediterranean over the last 900 years. *J Geophys Res Atmos* 121: 2060-2074.
- Cook ER, Briffa KR, Meko DM, Graybill DA, Funkhouser G (1995) The 'segment length curse' in long tree-ring chronology development for palaeoclimatic studies. *Holocene* 5: 229-237.

- Cook ER, Seager R, Kushnir Y, Briffa KR, Büntgen U, Frank DC, Krusic PJ, Tegel W, van der Schrier G, Andreu-Hayles L, et al. (2015) Old World megadroughts and pluvials during the Common Era. *Sci Adv* 1: e1500561.
- D'Arrigo R, Wilson R, Liepert B, Cherubini P (2008) On the 'divergence problem' in northern forests: a review of the tree-ring evidence and possible causes. *Glob Planet Change* 60: 289-305.
- De Micco V, Campelo F, De Luis M, Bräuning A, Grabner M, Battipaglia G, Cherubini P (2016) Intra-annual density fluctuations in tree rings: how, when, where, and why? *IAWA J* 37: 232-259.
- Diffenbaugh NS, Giorgi F (2012) Climate change hotspots in the CMIP5 global climate model ensemble. *Clim Change* 114: 813-822.
- Dorado-Liñán I, Büntgen U, González-Rouco F, Zorita E, Montavez JP, Gómez-Navarro JJ, Brunet M, Heinrich I, Helle G, Gutiérrez E (2012) Estimating 750 years of temperature variations and uncertainties in the Pyrenees by tree-ring reconstructions and climate simulations. *Clim Past* 8: 919-933.
- Eilmann B, Rigling A (2012) Tree-growth analyses to estimate tree species drought tolerance. *Tree Physiol* 32: 178-187.
- Eschbach W, Nogler P, Schär E, Schweingruber FH (1995) Technical advances in the radiodensitometrical determination of wood density. *Dendrochronologia* 13: 155-168.
- Esper J, Büntgen U, Frank DC, Nievergelt D, Treydte K, Verstege A (2006) Multiple tree-ring parameters from Atlas cedar (Morocco) and their climatic signal. In: Heidrich I, Gärtner H, Monbaron M, Schleser G (eds) *Schriften des Forschungszentrums Jülich, Reihe Umwelt: TRACE, Tree rings in Archaeology, Climatology and Ecology*, 4th edition. Forschungszentrum Jülich, Germany: pp 46-55.
- Esper J, Cook ER, Krusic PJ, Peters K, Schweingruber FH (2003) Tests of the RCS method for preserving low-frequency variability in long tree-ring chronologies. *Tree-Ring Res* 59: 81-98.
- Esper J, Cook ER, Schweingruber FH (2002) Low-frequency signals in long tree-ring chronologies and the reconstruction of past temperature variability. *Science* 295: 2250-2253.
- Esper J, DÜthorn E, Krusic P, Timonen M, Büntgen U (2014) Northern European summer temperature variations over the Common Era from integrated tree-ring density records. *J Quat Sci* 29: 487-494.
- Esper J, Frank DC, Büntgen U, Verstege A, Luterbacher J, Xoplaki E (2007) Long-term drought severity variations in Morocco. *Geophys Res Lett* 34: L17702.
- Esper J, Frank DC, Timonen M, Zorita E, Wilson R, Luterbacher J, Holzkämper S, Fischer N, Wagner S, Nievergelt D, et al. (2012) Orbital forcing of tree-ring data. *Nat Clim Change* 2: 862-866.

- Esper J, Hartl C, Tejedor E, de Luis M, Günther B, Büntgen U (2020a) High-resolution temperature variability reconstructed from Black pine tree ring densities in southern Spain. *Atmosphere* 11: 748.
- Esper J, Klippel L, Krusic PJ, Konter O, Raible CC, Xoplaki E, Luterbacher J, Büntgen U (2020b) Eastern Mediterranean summer temperatures since 730 CE from Mt. Smolikas tree-ring densities. *Clim Dyn* 54: 1367-1382.
- Esper J, Konter O, Klippel L, Krusic PJ, Büntgen U (2021) Pre-instrumental summer precipitation variability in northwestern Greece from a high-elevation *Pinus heldreichii* network. *Int J Climatol* 41: 2828-2839.
- Esper J, Krusic PJ, Ljungqvist FC, Luterbacher J, Carrer M, Cook ER, Davi NK, Hartl C, Kiryandov A, Konter O, et al. (2016) Ranking of tree-ring based temperature reconstructions of the past millennium. *Quat Sci Rev* 145: 134-151.
- Esper J, Schneider L, Smerdon JE, Schöne BR, Büntgen U (2015) Signals and memory in tree-ring width and density data. *Dendrochronologia* 35: 62-70.
- Fang K, Gou X, Peters K, Li J, Zhang F (2010) Removing biological trends from tree-ring series: testing modified Hugershoff curves. *Tree-Ring Res* 66: 51-59.
- Fernández-Pérez L, Villar-Salvador P, Martínez-Vilalta J, Toca A, Zavala MA (2018) Distribution of pines in the Iberian peninsula agrees with species differences in foliage frost tolerance, not with vulnerability to freezing-induced xylem embolism. *Tree Physiol* 38: 507-516.
- Fonti P, von Arx G, García-González I, Eilmann B, Sass-Klaassen U, Gärtner H, Eckstein D (2010) Studying global change through investigation of the plastic responses of xylem anatomy in tree rings. *New Phytol* 185: 42-53.
- Frank DC, Esper J (2005) Temperature reconstructions and comparisons with instrumental data from a tree-ring network for the European Alps. *Int J Climatol* 25: 1437-1454.
- Frank DC, Esper J, Cook ER (2007) Adjustment for proxy number and coherence in a large-scale temperature reconstruction. *Geophys Res Lett* 34: L16709.
- Fritts HC (1976) *Tree rings and climate*. Blackburn Press, Caldwell, NJ, USA.
- Fulé PZ, Ribas M, Gutiérrez E, Vallejo R, Kaye MW (2008) Forest structure and fire history in an old *Pinus nigra* forest, eastern Spain. *For Ecol Manag* 255: 1234-1242.
- Galván JD, Camarero JJ, Ginzler C, Büntgen U (2014) Spatial diversity of recent trends in Mediterranean tree growth. *Environ Res Lett* 9: 084001.
- Gao X, Giorgi F (2008) Increased aridity in the Mediterranean region under greenhouse gas forcing estimated from high resolution simulations with a regional climate model. *Glob Planet Change* 62: 195-209.
- Gričar J, Čufar K, Oven P, Schmitt U (2005) Differentiation of terminal latewood tracheids in silver fir trees during autumn. *Ann Bot* 95: 959-965.

- Griggs C, DeGaetano A, Kuniholm P, Newton M (2007) A regional high-frequency reconstruction of May-June precipitation in the north Aegean from oak tree rings, A.D. 1089-1989. *Int J Climatol* 27: 1075-1089.
- Harris I, Osborn TJ, Jones P, Lister D (2020) Version 4 of the CRU TS monthly high-resolution gridded multivariate climate dataset. *Sci Data* 7: 1-18.
- Hartl-Meier C, Dittmar C, Zang C, Rothe A (2014) Mountain forest growth response to climate change in the Northern Limestone Alps. *Trees* 28: 819-829.
- Hartl-Meier C, Zang C, Büntgen U, Esper J, Rothe A, Göttelein A, Dirnböck T, Treydte K (2015) Uniform climate sensitivity in tree-ring stable isotopes across species and sites in a mid-latitude temperate forest. *Tree Physiol* 35: 4-15.
- Häusser M, Szymczak S, Garel E, Santoni S, Huneau F, Bräuning A (2019) Growth variability of two native pine species on Corsica as a function of elevation. *Dendrochronologia* 54: 49-55.
- Hertig E, Jacobeit J (2008) Downscaling future climate change: temperature scenarios for the Mediterranean area. *Glob Planet Change* 63: 127-131.
- Hetzer T (2013) *Xylem variability as a proxy for environmental and climate change in Corsica during the past millennium*. Dissertation, Friedrich-Alexander-University Erlangen-Nürnberg, Erlangen, Germany.
- Hetzer T, Bräuning A, Leuschner HH (2014) High-resolution climatic analysis of wood anatomical features in Corsican pine from Corsica (France) using latewood tracheid profiles. *Trees* 28: 1279-1288.
- Klippel L, Krusic PJ, Brandes R, Hartl C, Belmecheri S, Dienst M, Esper J (2018) A 1286-year hydro-climate reconstruction for the Balkan peninsula. *Boreas* 47: 1218-1229.
- Klippel L, Krusic PJ, Konter O, St George S, Trouet V, Esper J (2019) A 1200+ year reconstruction of temperature extremes for the northeastern Mediterranean region. *Int J Climatol* 39: 2336-2350.
- Knerr I, Trachte K, Garel E, Huneau F, Santoni S, Bendix J (2020) Partitioning of large-scale and local-scale precipitation events by means of spatio-temporal precipitation regimes on Corsica. *Atmosphere* 11: 417.
- Koninklijk Nederlands Meteorologisch Instituut (KNMI) (2020) *Climate Explorer. Climate data from Ajaccio (Station Code 7761) and Bastia (Station Code 7790)*. <http://climexp.knmi.nl> (accessed 5 October 2020).
- Laffoley D, Baxter J, Pergent-Martini C, Pergent G, Otero M, Simard F (2018) *Climate change and the marine environment in Corsica, Report Card 2018*. International Union for Conservation of Nature (IUCN), Gland, Switzerland.
- Lebourgeois F (2000) Climatic signals in earlywood, latewood and total ring width of Corsican pine from western France. *Ann For Sci* 57: 155-164.

- Lebourgeois F, Lévy G, Aussenac G, Clerc B, Willm F (1998) Influence of soil drying on leaf water potential, photosynthesis, stomatal conductance and growth in two black pine varieties. *Ann Sci For* 55: 287-299.
- Leonelli G, Coppola A, Salvatore MC, Baroni C, Battipaglia G, Gentilesca T, Ripullone F, Borghetti M, Conte E, Tognetti R, et al. (2017) Climate signals in a multispecies tree-ring network from central and southern Italy and reconstruction of the late summer temperatures since the early 1700s. *Clim Past* 13: 1451-1471.
- Luterbacher J, García-Herrera R, Akcer-On S, Allan R, Alvarez-Castro MC, Benito G, Booth J, Büntgen U, Cagatay N, Colombaroli D, et al. (2012) A review of 2000 years of paleoclimatic evidence in the Mediterranean. In: Lionello P (ed) *The climate of the Mediterranean region: from the past to the future*. Elsevier, Amsterdam, The Netherlands: pp 87-185.
- Martín-Benito D, Beeckman H, Cañellas I (2013) Influence of drought on tree rings and tracheid features of *Pinus nigra* and *Pinus sylvestris* in a mesic Mediterranean forest. *Eur J For Res* 132: 33-45.
- Martín-Benito D, del Río M, Cañellas I (2010) Black pine (*Pinus nigra* Arn.) growth divergence along a latitudinal gradient in western Mediterranean mountains. *Ann For Sci* 67: 401.
- Médail F, Verlaque R (1997) Ecological characteristics and rarity of endemic plants from south-east France and Corsica: implications for biodiversity conservation. *Biol Conserv* 80: 269-281.
- Medrano H, Escalona JM, Bota J, Gulías J, Flexas J (2002) Regulation of photosynthesis of C3 plants in response to progressive drought: stomatal conductance as a reference parameter. *Ann Bot* 89: 895-905.
- Météo-France (2021) *Climate data from Calacuccia weather station (20224)*. <https://météofrance.com/previsions-meteo-france/calacuccia/20224> (accessed 7 January 2021).
- Mouillot F, Ratte JP, Joffre R, Moreno JM, Rambal S (2003) Some determinants of the spatio-temporal fire cycle in a Mediterranean landscape (Corsica, France). *Landsc Ecol* 18: 665-674.
- Nicault A, Alleaume S, Brewer S, Carrer M, Nola P, Guiot J (2008) Mediterranean drought fluctuation during the last 500 years based on tree-ring data. *Clim Dyn* 31: 227-245.
- Olano JM, Linares JC, García-Cervigón AI, Arzac A, Delgado A, Rozas V (2014) Drought-induced increase in water-use efficiency reduces secondary tree growth and tracheid wall thickness in a Mediterranean conifer. *Oecologia* 176: 273-283.
- Pausas JG, Llovet J, Rodrigo A, Vallejo R (2008) Are wildfires a disaster in the Mediterranean basin? – a review. *Int J Wildland Fire* 17: 713-723.
- Petrucco L, Nardini A, von Arx G, Saurer M, Cherubini P (2017) Isotope signals and anatomical features in tree rings suggest a role for hydraulic strategies in diffuse drought-induced dieback of *Pinus nigra*. *Tree Physiol* 37: 523-535.

- Piermattei A, Crivellaro A, Carrer M, Urbinati C (2015) The “blue ring”: anatomy and formation hypothesis of a new tree-ring anomaly in conifers. *Trees* 29: 613-620.
- Pittermann J, Sperry JS, Wheeler JK, Hacke UG, Sikkema EH (2006) Mechanical reinforcement of tracheids compromises the hydraulic efficiency of conifer xylem. *Plant Cell Environ* 29: 1618-1628.
- Rome S, Giorgetti JP (2006) Du climat de la montagne corse et ses aléas. In: Beltrando G, Madelin MM, Quénel H (eds) *Les risques liés au temps et au climat, XIXe Colloque de l'Association Internationale de Climatologie*. Épernay, France: pp 486-492.
- Rome S, Giorgetti JP (2007) La montagne corse et ses caractéristiques climatiques. *Météorologie* 59: 39-50.
- Ruiz-Labourdette D, Génova M, Schmitz MF, Urrutia R, Pineda FD (2014) Summer rainfall variability in European Mediterranean mountains from the sixteenth to the twentieth century reconstructed from tree rings. *Int J Biometeorol* 58: 1627-1639.
- Sánchez E, Gallardo C, Gaertner MA, Arriba A, Castro M (2004) Future climate extreme events in the Mediterranean simulated by a regional climate model: a first approach. *Glob Planet Change* 44: 163-180.
- Schneider U, Finger P, Rustemeier E, Ziese M, Becker A (2021) *Global precipitation analysis products of the GPCP*. Deutscher Wetterdienst, Abt. Hydrometeorologie, Offenbach am Main, Germany.
- Schweingruber FH (2020a) *NOAA/WDS Paleoclimatology – Schweingruber – Col de Sorba – PINI – ITRDB FRAN027*. NOAA National Centers for Environmental Information. <https://www.ncdc.noaa.gov/paleo-search/study/4389> (accessed 5 October 2020).
- Schweingruber FH (2020b) *NOAA/WDS Paleoclimatology – Schweingruber – Sierra de Crispo – PILE – ITRDB ITAL015*. NOAA National Centers for Environmental Information. <https://www.ncdc.noaa.gov/paleo-search/study/4644> (accessed 5 October 2020).
- Schweingruber FH, Briffa KR (1996) Tree-ring density networks for climate reconstruction. In: Jones PD, Bradley RS, Jouzel J (eds) *Climatic variations and forcing mechanisms of the last 2000 years*, volume 41. Springer, Heidelberg and Berlin, Germany: pp 43-66.
- Schweingruber FH, Fritts HC, Bräker OU, Drew LG, Schär E (1978) The X-ray technique as applied to dendroclimatology. *Tree-Ring Bull* 38: 61-91.
- Seim A, Treydte K, Trouet V, Frank DC, Fonti P, Tegel W, Panayotov M, Fernández-Donado L, Krusic P, Büntgen U (2015) Climate sensitivity of Mediterranean pine growth reveals distinct east-west dipole. *Int J Climatol* 35: 2503-2513.
- Soulères O (2000) Les incendies de Haute-Corse. *Rev For Fr* 52: 401-406.
- Spinoni J, Naumann G, Vogt JV, Barbosa P (2015) The biggest drought events in Europe from 1950 to 2012. *J Hydrol Reg Stud* 3: 509-524.

- Szymczak S, Bräuning A, Häusser M, Garel E, Huneau F, Santoni S (2019) The relationship between climate and the intra-annual oxygen isotope patterns from pine trees: a case study along an elevation gradient on Corsica, France. *Ann For Sci* 76: 1-76.
- Szymczak S, Bräuning A, Häusser M, Garel E, Huneau F, Santoni S (2020b) A dendroecological fire history for central Corsica/France. *Tree-Ring Res* 76: 40-53.
- Szymczak S, Häusser M, Garel E, Santoni S, Huneau F, Knerr I, Trachte K, Bendix J, Bräuning A (2020a) How do Mediterranean pine trees respond to drought and precipitation events along an elevation gradient? *Forests* 11: 758.
- Szymczak S, Hetzer T, Bräuning A, Joachimski MM, Leuschner HH, Kuhlemann J (2014) Combining wood anatomy and stable isotope variations in a 600-year multi-parameter climate reconstruction from Corsican black pine. *Quat Sci Rev* 101: 146-158.
- Szymczak S, Joachimski MM, Bräuning A, Hetzer T, Kuhlemann J (2012) A 560 yr summer temperature reconstruction for the Western Mediterranean basin based on stable carbon isotopes from *Pinus nigra* ssp. *laricio* (Corsica/France). *Clim Past* 8: 1737-1749.
- Tejedor E, de Luis M, Cuadrat JM, Esper J, Saz MA (2016) Tree-ring-based drought reconstruction in the Iberian range (east of Spain) since 1694. *Int J Biometeorol* 60: 361-372.
- Thiel D, Nagy L, Beierkuhnlein C, Huber G, Jentsch A, Konnert M, Kreyling J (2012) Uniform drought and warming responses in *Pinus nigra* provenances despite specific overall performances. *For Ecol Manag* 270: 200-208.
- Tintner J, Smidt E (2018) Resistance of wood from Black pine (*Pinus nigra* var. *austriaca*) against weathering. *J Wood Sci* 64: 816-822.
- Touchan R, Anchukaitis KJ, Meko DM, Kerchouche D, Slimani S, Ilmen R, Hasnaoui F, Guibal F, Camarero JJ, Sánchez-Salguero R, et al. (2017) Climate controls on tree growth in the Western Mediterranean. *Holocene* 27: 1429-1442.
- Touchan R, Baisan C, Mitsopoulos ID, Dimitrakopoulos AP (2012) Fire history in European black pine (*Pinus nigra* Arn.) forests of the Valia Kalda, Pindus mountains, Greece. *Tree-Ring Res* 68: 45-50.
- Touchan R, Meko DM, Aloui A (2008) Precipitation reconstruction for northwestern Tunisia from tree rings. *J Arid Environ* 72: 1887-1896.
- Trouet V (2014) A tree-ring based late summer temperature reconstruction (AD 1675-1980) for the Northeastern Mediterranean. *Radiocarbon* 56: 69-78.
- Trouet V, van Oldenborgh GJ (2013) KNMI climate explorer: a web-based research tool for high-resolution paleoclimatology. *Tree-Ring Res* 69: 3-13.
- Wigley TML, Briffa KR, Jones PD (1984) On the average of correlated time series, with applications in dendroclimatology and hydrometeorology. *J Appl Meteorol Clim* 23: 201-213.

3.8 Supplementary materials

Table S3.1 MXD site chronology characteristics.

Code	Site [elevation]	Radii	Period	MSL	Rbar	EPS	AC1	AMXD
<i>Asc</i>	Asco [1600 m asl]	19	1360-2016	543	0.34	0.90	0.33	0.83
<i>Tar</i>	Tartagine [1450 m asl]	20	1636-2016	282	0.29	0.91	0.44	0.95
<i>Sor</i>	Col de Sorba [1400 m asl]	30	1622-1980	211	0.36	0.94	0.26	0.94

Period: start and end dates when replication ≥ 5 radii. **MSL:** mean segment length [years]. **Rbar:** mean inter-series correlation. **EPS:** expressed population signal. **AC1:** first-order autocorrelation. **AMXD:** average MXD [g/cm^3].

Table S3.2 MXD composite chronology characteristics.

Chronology	Radii	Period	MSL	Rbar	EPS	AC1	AMXD
<i>COR_{RCS}</i>	69	1360-2016	325	0.23	0.91	0.44	0.92
<i>ABC400</i>	69	1361-2016	247	0.27	0.93	0.38	0.93
<i>ABC300</i>	69	1361-1988	200	0.27	0.93	0.37	0.94
<i>ABC200</i>	66	1365-1980	141	0.27	0.90	0.35	0.95

Period: start and end dates when replication ≥ 5 radii. **MSL:** mean segment length [years]. **Rbar:** mean inter-series correlation. **EPS:** expressed population signal. **AC1:** first-order autocorrelation. **AMXD:** average MXD [g/cm^3].

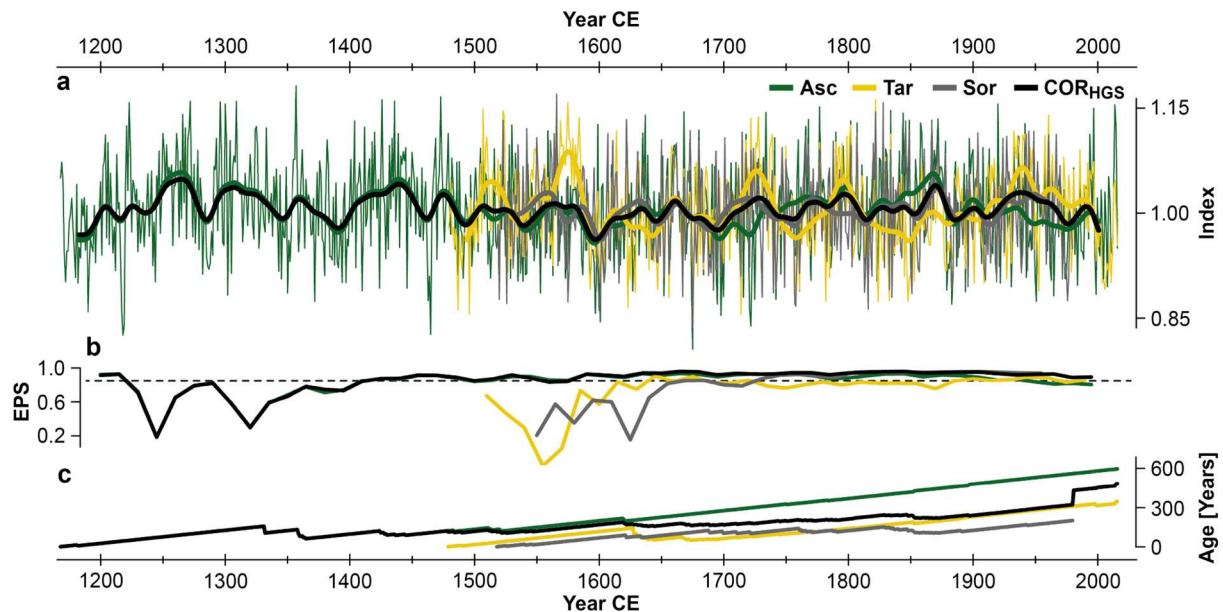


Fig. S3.1 Effects of merging site measurements. **(a)** Hugerhoff-detrended MXD composite (COR_{HGS}) and site chronologies (*Asc*, *Tar*, *Sor*) (thin curves) shown together with their 31-year smoothing splines (bold curves), **(b)** their expressed population signal (EPS) computed for 30-year segments with 15-year overlaps, and **(c)** their mean tree age curves.

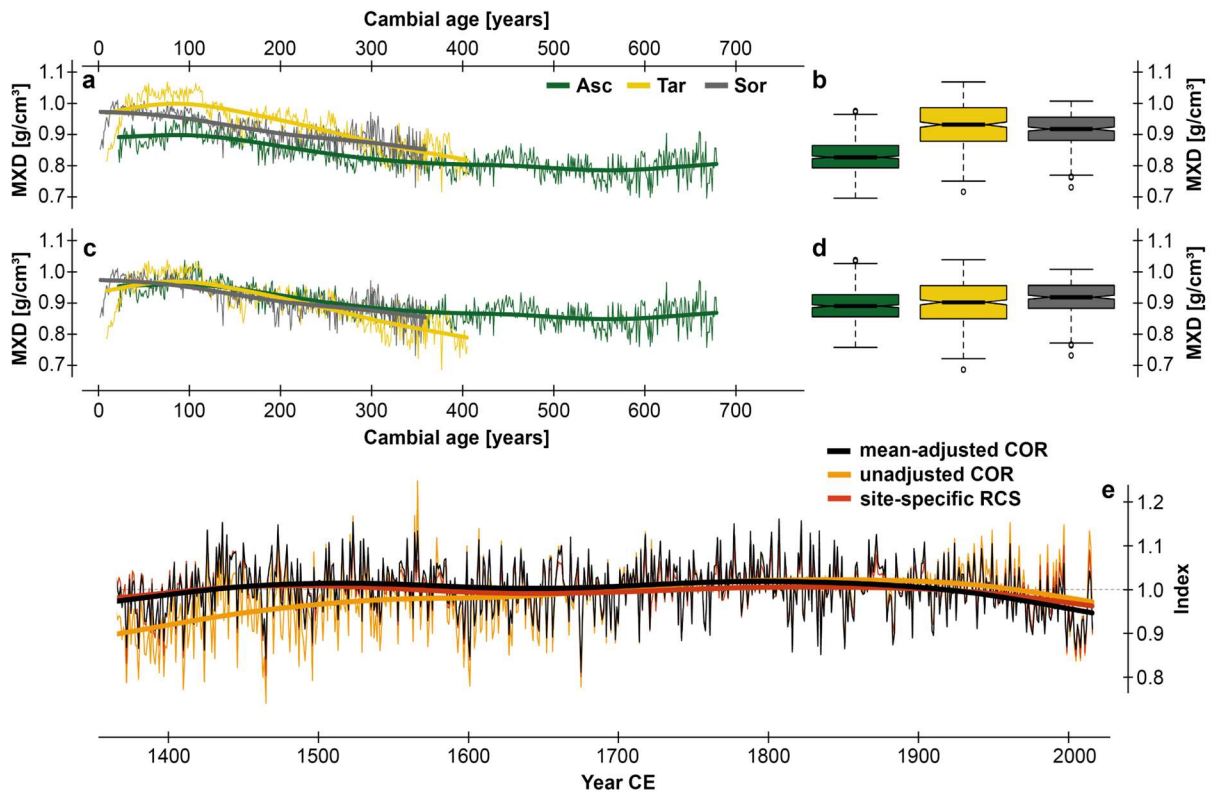


Fig. S3.2 Effects of mean adjustment. Regional curves (thin curves) shown together with their 300-year splines (bold curves) and boxplots displaying growth rates of the site-specific MXD data (a-b) before mean-adjustment and (c-d) after mean-adjustment. (e) COR chronologies (thin curves) and their 300-year splines (bold curves) after applying RCS to the mean-adjusted data (black), to the unadjusted data (orange), and to the site-specific data before merging (red). Start and end dates were set to $n \geq 5$ series. Note the considerably lower indices of the unadjusted chronology version before ~1600 CE (caused by the dominance of higher elevated trees from Asc).

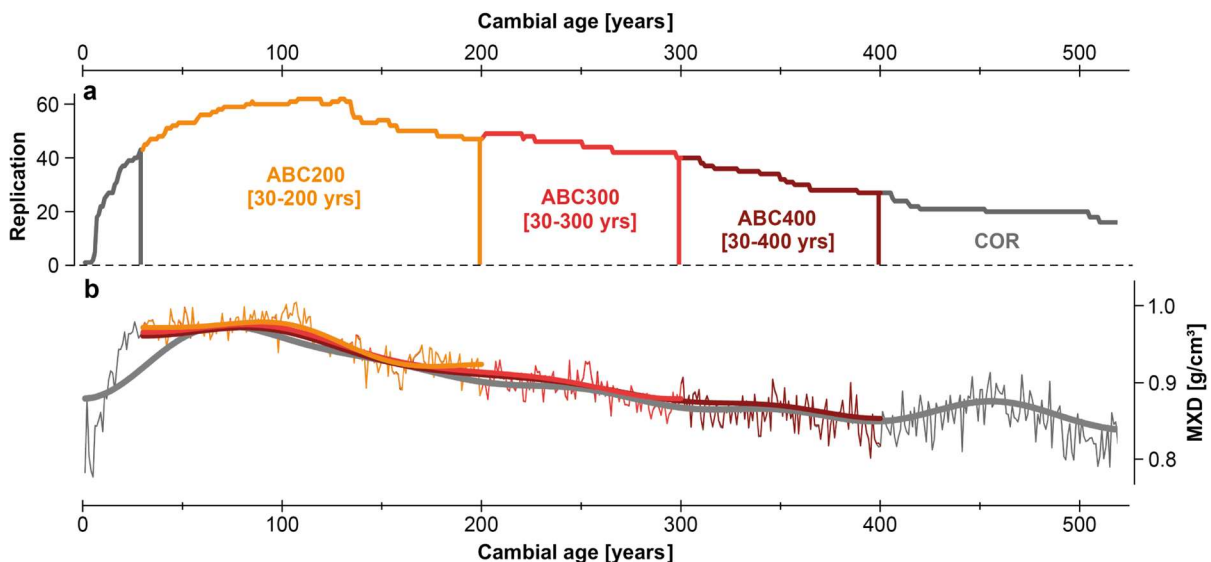


Fig. S3.3 Sample replication and regional curves of the composite MXD data. (a) Replication curves of age-aligned tree rings highlighting the data sections: *ABC200* contains rings from 30-200 years, *ABC300* from 30-300 years, and *ABC400* from 30-400 years. Rings younger than 30 years and older than 400 years are only included in *COR*. (b) Regional curves of the chronologies (light) shown together with their 100-year low pass filters (bold). Pith-offset estimates are considered. Note the Hugerhoff-shaped age trend in *COR*.

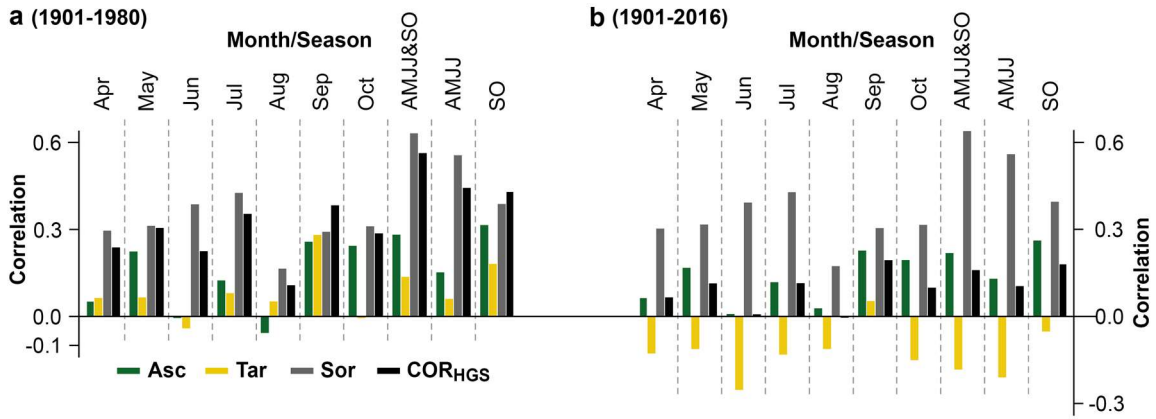


Fig. S3.4 Temperature signal estimation using the CRU TS4.04 data. Correlations between the HGS-detrended chronologies and monthly and seasonal temperatures from (a) 1901-1980 and (b) 1901-2016 CE. Note that *Sor* ends in 1980 CE.

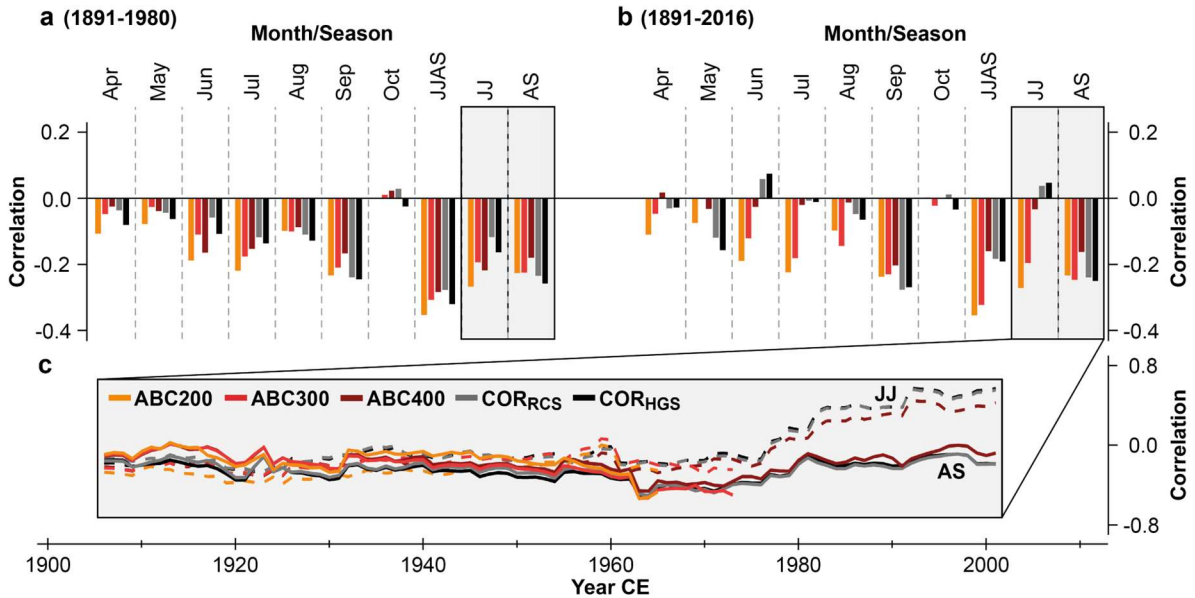


Fig. S3.5 Precipitation signal estimation using the GPCP v2020 data. Correlations between the composite chronologies and monthly and seasonal precipitation totals from (a) 1891-1980 and (b) 1891-2016 CE. Note that *ABC200* and *ABC300* end in 1980 and 1988 CE, respectively. (c) 31-year running correlations between the chronologies and June-July (JJ) and August-September (AS) precipitation totals.

4 Review of embedding and non-embedding techniques for quantitative wood anatomy

Authors: Davide Frigo*, Philipp Römer*, Lucrezia Unterholzner, Heike Zimmer-Zachmann, Jan Esper, Marco Carrer, and Emanuele Ziaco

Status: Published in *Dendrochronologia* 88 (2024): 126241.

<https://doi.org/10.1016/j.dendro.2024.126241>

Abstract

In recent decades, xylem anatomical traits have become increasingly important in dendrochronological research, as they offer the unique opportunity to assess eco-physiological drivers of tree growth at intra-annual resolution. However, standard protocols for generating such data are still missing, leading to methodological uncertainty and complicating data exchange among laboratories. Here, we compare protocols for high-quality permanent slide preparation in dendroanatomy and address effects of paraffin embedding vs. non-embedding approaches. Tests are conducted on both gymnosperm and angiosperm wood types of widely distributed European tree species, considering cell wall thickness (CWT), mean lumen area (MLA), and hydraulic diameter (D_h). Results indicate that non-embedding does not significantly alter the qualitative and quantitative characteristics of permanent slides compared to embedded samples. Whereas the mean chronologies of MLA and D_h and their non-embedded counterparts share substantial high-frequency variance, CWT chronologies reveal slightly larger discrepancies at interannual scale. However, methodological differences do not exceed 11.1% for any parameter. While these results reveal high similarity between the two approaches, we recommend adopting the non-embedding procedure, since it saves resources and therefore allows to produce larger datasets. Regardless of the protocol used to build wood anatomical datasets, assembling large-scale networks of wood anatomical data could transform our understanding of forest responses to global changes.

Keywords: cell wall thickness, dendroanatomy, hydraulic diameter, mean lumen area, paraffin embedding, xylem.

4.1 Introduction

Microscopic analyses of xylem anatomical features provide a unique opportunity to study the response of tree and forest growth to environmental changes at intra-annual resolution (Lopez-Saez et al. 2023; Piermattei et al. 2020). Methodological and technological advances in quantitative wood anatomy (QWA) progressively enabled detailed and resource-efficient analyses of xylem-specific components (Katzenmaier et al. 2023; Prendin et al. 2017; von Arx & Carrer 2014; von Arx et al. 2016), namely the structural and conductive elements forming wood, such as fibers, vessels, and tracheids. As a result, recent tree-ring studies increasingly focused on the analyses of wood anatomical traits, indicating dendroanatomy to be a powerful tool to study tree responses to environmental changes (Arnič et al. 2021; Carrer et al. 2016, 2018; von Arx et al. 2016). Among numerous wood anatomical traits, cell wall thickness (CWT), mean lumen area (MLA), and hydraulic diameter (D_h) are most commonly used to address a variety of physiological, ecological and palaeoclimatological research questions (Castagneri et al. 2017; Fonti et al. 2009; Piermattei et al. 2020; von Arx et al. 2016; Ziaco et al. 2023).

Whereas QWA adds cell-specific information to traditional tree-ring proxies such as ring width (TRW) or maximum latewood density (MXD), data development is quite time consuming compared to conventional dendrochronological techniques. Standard protocols for generating wood anatomical data are still lacking, while methodological assessments (Björklund et al. 2019) routinely enable the construction of large-scale TRW and MXD networks, providing a powerful tool for studying regional to continental forest responses to climate change (Briffa et al. 2001; Esper et al. 2002, 2012). In fact, tree-ring laboratories across the world currently use slightly different methodological approaches to prepare wood samples for the wide spectrum of QWA (Carrer et al. 2018; Seftigen et al. 2022), xylogenesis (Martínez del Castillo et al. 2018; Rossi et al. 2006), and other eco-physiological analyses (Schneider & Gärtner 2013; Yeung et al. 2015). These methodological differences hamper the seamless comparison and exchange of data and material among laboratories and research groups, and hinder the development of large-scale dendroanatomical networks that would likely add new insights to our understanding of large-scale forest changes.

One of the main methodological differences in sample preparation for QWA involves the procedure of sealing xylem tissue into an embedding medium, such as paraffin, versus boiling the sample in water or in baths of glycerin to soften the cellular walls before sectioning (Gärtner & Schweingruber 2013; von Arx et al. 2016). While embedding is routinely used to prevent cell wall collapse during cutting by injecting liquid paraffin into cell lumina under vacuum pressure, especially in soft and living cells of the cambial zone (Rossi et al. 2006), non-embedding allows for a faster sample processing, simultaneously preventing the employment of harmful chemicals (e.g., xylol) intrinsic to the embedding procedure. Here, we compare these two protocols

for high-quality permanent slides preparation in dendroanatomy, demonstrating the covariance of QWA data from embedding and non-embedding approaches. We use three major European tree species, including deciduous hardwoods and coniferous softwoods, and compare microsections obtained with and without paraffin embedding for any quantitative differences in CWT, D_h , and MLA.

4.2 Materials and methods

Two coniferous and one deciduous tree species were selected for the comparison: Stone pine (*Pinus cembra* L., PICE), European larch (*Larix decidua* L., LADE), and European beech (*Fagus sylvatica* L., FASY), growing in montane and subalpine belts between 1000 and 2200 m asl in the Italian Southern Alps (PICE and LADE) and the Northern Apennines (FASY). One sample per tree, selected based on visual appearance to avoid damage, decay, and structural anomalies, was taken at breast height (~1.3 m) using a 10-mm-increment borer. Samples were split orthogonally to the longitudinal stem axis to produce two datasets of transverse microsections, one with and one without embedding. For the latter, core halves were separated into 4-5 cm long pieces and boiled in distilled water to soften these (5-10 min for PICE and LADE; 20-25 min for FASY). Ten μm thick transverse microsections were obtained using a Leica rotary microtome (Leica Biosystems, Wetzlar, Germany) and bleached in 10% sodium hypochlorite for 10 minutes to decolor cell walls. After removing the bleach with water, microsections were stained in a 1:1 safranin-astra blue solution, dehydrated in successive ethanol baths (50% and 100% purity), permanently mounted onto glass microscope slides with Euparal (Carl Roth, Karlsruhe, Germany), and dried in an oven at 60°C for 48 hours. The remaining core halves were separated and embedded in paraffin using an automatic Slee MTP Tissue Processor (Slee, Nieder-Olm, Germany) and a Medite Tissue Embedding Center TES 99 (Medite, Burgdorf, Germany) before cutting 10 μm microsections. Digital images at a resolution of 2.2 pixels/ μm were obtained from all microsections using a NanoZoomer slide scanner (Hamamatsu Photonics, Shizuoka, Japan). For both paraffin-embedded (*PAR*) and non-embedded sections (*NoPAR*), digital images were taken exactly for the same areas, verified considering peculiarities in the xylem structure, including resin ducts and parenchyma rays.

Images were processed using the ROXAS software (v4.0) to automatically identify individual tracheids in softwood and vessels in hardwood by using specific settings for both groups (von Arx & Carrer 2014). Wood anatomical traits, namely conduit size (mean lumen area, MLA), cell wall thickness (CWT_{all} , the average between tangential and radial CWT), and hydraulic diameter (D_h), were measured on 15 rings in each section. While MLA was measured for all species, CWT was measured exclusively for LADE and PICE, whereas D_h was computed only for FASY (after Sperry et al. 1994). For all three parameters, the arithmetic mean and standard

deviation were calculated for each ring, thus building two chronologies per parameter. All tree-ring series were visually crossdated using TRW measurements obtained from ROXAS to accurately compare the embedded and non-embedded slides.

To assess differences between the measurements derived from embedded vs. non-embedded sections, we measured the relative difference (|%) between mean ring values of each anatomical trait as follows:

$$\Delta\bar{A} = \left| \frac{\bar{A}_{NoPAR} - \bar{A}_{PAR}}{\bar{A}_{PAR}} \right|, \quad (4.1)$$

where $\Delta\bar{A}$ is the absolute value of the ratio between the difference of the mean anatomical parameter measured on the non-embedded (\bar{A}_{NoPAR}) and embedded sections (\bar{A}_{PAR}) over the value for the embedded section. To quantify average values of MLA, D_h , and CWT, and assess their variability within each ring, we considered the relationship between absolute differences in the mean ($\Delta\bar{A}$) with annual means and standard deviations measured on the paraffin-embedded sections by using linear regressions. We used the absolute value since the aim was to quantify differences regardless of sign. High-frequency variability for the anatomical parameter was assessed by calculating the “Gleichläufigkeit” (GLK; Eckstein & Bauch 1969) of the mean and standard deviation series for MLA, D_h , and CWT, using embedded and non-embedded samples. Standardized tracheidograms (Campelo et al. 2016; Olano et al. 2012; Vaganov 1990; Ziaco 2020), averaging 15 rings on each sample, were computed to evaluate intra-annual variability of MLA and CWT in LADE and PICE. The tracheidograms were computed by aligning cell radial files for each ring using RAPTOR (Peters et al. 2018) and then normalizing the number of cells to 20 (LADE) and 50 (PICE) using *tgram* (DeSoto et al. 2011). All statistical analyses were performed in the R environment (R Core Team 2022).

4.3 Results and discussion

Visual assessment of the images of paraffin-embedded and non-embedded sections reveals no significant differences between the two approaches. Considering the minimal intrinsic differences due to the progressive cutting of a given sample, *PAR* and *NoPAR* sections are essentially indistinguishable from a qualitative perspective (**Fig. 4.1**). Mean and standard deviation chronologies show overall good interannual agreement in all parameters (**Fig. 4.2, S4.1**).

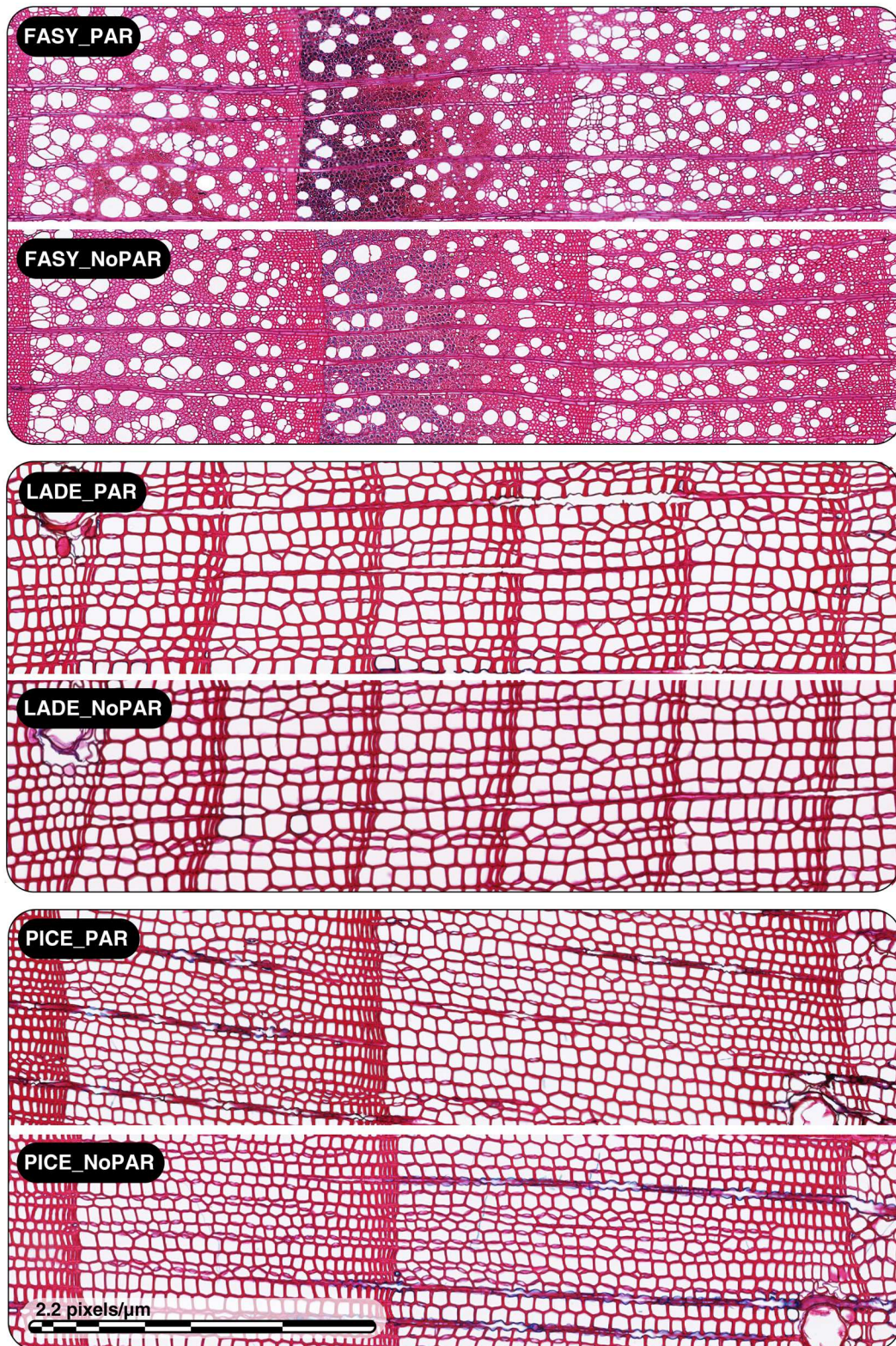


Fig. 4.1 Visual comparison of microscopic sections (100x magnification) produced from the same samples of *Fagus sylvatica* (FASY), *Larix decidua* (LADE), and *Pinus cembra* (PICE) processed with both paraffin embedding (PAR) and without paraffin embedding (NoPAR) (scale bar = 1 mm).

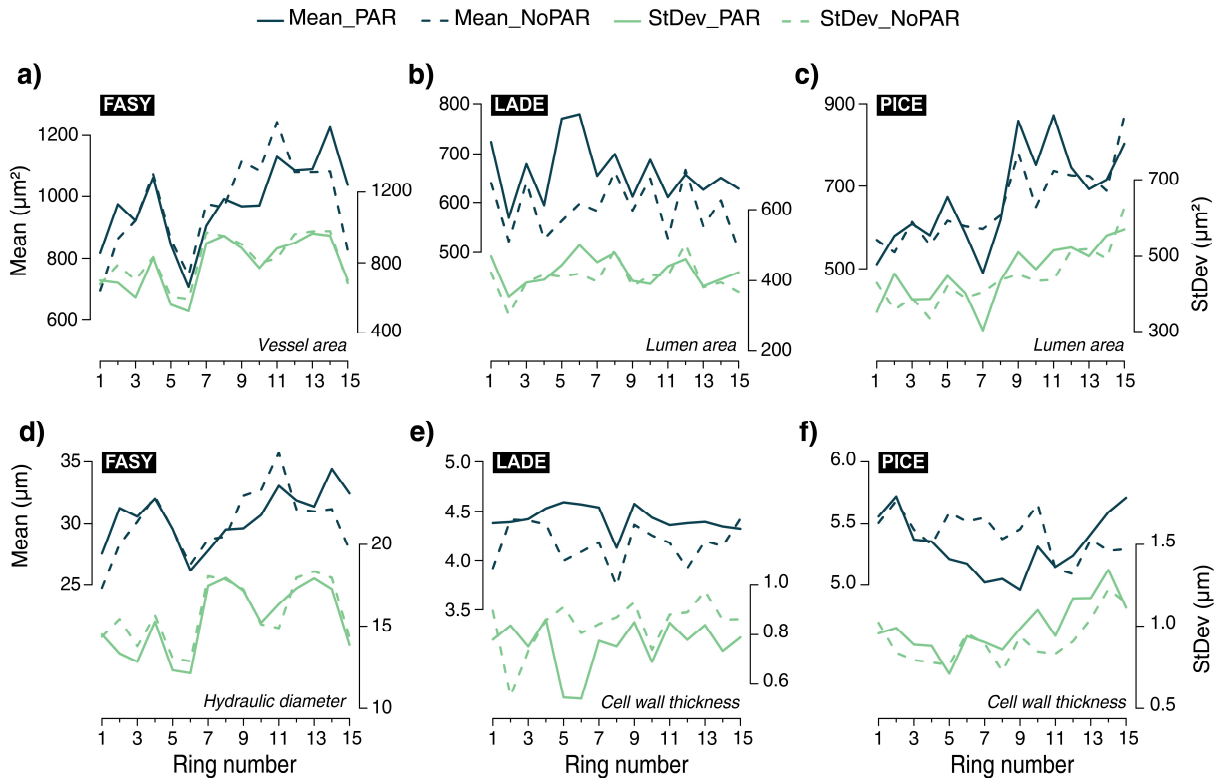


Fig. 4.2 Mean (blue curves) and standard deviation (green curves) chronologies of (a) vessel area, (b-c) tracheid lumen area, (d) hydraulic diameter, and (e-f) cell wall thickness measured on the paraffin-embedded (*PAR*) and non-paraffin-embedded (*NoPAR*) samples of *Fagus sylvatica* (*FASY*), *Larix decidua* (*LADE*), and *Pinus cembra* (*PICE*).

The CWT chronologies, however, display larger high-frequency discrepancies, though their $\Delta\bar{A}$ values are notably lower compared to MLA and D_h (Table 4.1). The largest $\Delta\bar{A}$ value (11.1%) is recorded in MLA of LADE. For all species, $\Delta\bar{A}$ values are higher in MLA than in CWT or D_h , indicating a higher absolute measurement error for the larger anatomical features. High GLK values among the *PAR* and *NoPAR* MLA chronologies ($GLK_{FASY} = 0.64$, $GLK_{LADE} = 1$, $GLK_{PICE} = 0.86$), on the other hand, prove that interannual variability is less affected by this bias compared to CWT. GLK values calculated between *PAR* and *NoPAR* CWT chronologies are comparably lower ($GLK_{LADE} = 0.5$, $GLK_{PICE} = 0.57$). The visible differences between the CWT chronologies may be due to minor cutting imprecisions affecting the smaller CWT parameter more than the other features; the aforementioned progressive cutting issue, which inevitably causes the comparison of two sections with minimal differences between each other; and/or the tolerance of the instrument we used: even though microtomes are precise tools, they can still cause 0.5-1 μm errors in the cutting (cutting thickness range is usually 0.5-100 μm; Leica Biosystems 2023), leading to slight differences in thickness among and within individual QWA samples. However, the overall good agreement of the mean and standard deviation chronologies shows that both approaches are able to capture the intra-annual variability of the cellular parameters and describe their dispersion around the mean.

Table 4.1 Summary of the measured wood anatomical traits on the paraffin-embedded (*PAR*) and non-paraffin-embedded sections (*NoPAR*).

	<i>PAR</i>		<i>NoPAR</i>		Difference $\Delta\bar{A}$	GLK	
	Mean	SD	Mean	SD		<i>PAR</i>	<i>NoPAR</i>
<i>Fagus sylvatica</i>							
MLA (μm^2)	982	789	974	817	7.7%	0.64	0.79
D_h (μm)	30.5	15.4	30.1	15.8	5.3%	0.93	0.79
<i>Larix decidua</i>							
MLA (μm^2)	663	426	588	407	11.1%	1	0.71
CWT (μm)	4.4	0.7	4.2	0.8	6.0%	0.5	0.64
<i>Pinus cembra</i>							
MLA (μm^2)	672	454	660	443	7.7%	0.86	0.57
CWT (μm)	5.3	1	5.4	0.9	4.5%	0.57	0.86

Mean: mean of lumen area (MLA), hydraulic diameter (D_h), and cell wall thickness (CWT). **SD:** one standard deviation. **$\Delta\bar{A}$:** relative differences between *PAR* and *NoPAR* sections (mean interannual ratio between the difference of the mean anatomical parameter measured on non-embedded (\bar{A}_{NoPAR}) and embedded sections (\bar{A}_{PAR}) over the value for the embedded section). **GLK:** gleichläufigkeit.

Differences in MLA between *PAR* and *NoPAR* are unaffected by the average size of the vessels and tracheid lumina. There is neither a significant relationship between ring-specific $\Delta\bar{A}$ values and MLA in the *PAR* sections for any species (**Fig. 4.3a**), nor between $\Delta\bar{A}$ and standard deviation (**Fig. 4.3b**). Similar results are observed for D_h and CWT, considering both parameter-specific mean values and standard deviations (**Fig. 4.3c-f**). Only the CWT of LADE shows a significant ($p < 0.05$) negative relationship between $\Delta\bar{A}$ and standard deviation, which is in line with the low GLK value of 0.64 and suggests that differences between *PAR* and *NoPAR* decrease toward high-frequency (intra-annual) CWT variability. This might indicate that during periods of increased CWT variability fewer cells with particularly larger walls collapse, thereby mitigating damage (Hacke & Sperry 2001) and reducing *PAR* versus *NoPAR* differences.

The tracheidograms of *PAR* and *NoPAR* sections show only minor differences reaching ~10% for MLA and ~5% for CWT in LADE and PICE (**Fig. 4.4**). While the CWT differences ($\Delta\bar{A}$) are relatively stable throughout the ring, a sharp increase of > 15% in $\Delta\bar{A}$ values is recorded in the latewood sections. The increasing MLA difference between *PAR* and *NoPAR* tracheidograms in these last ring sections can be attributed to an improved preservation of very small latewood cells after embedding or to a potential lack of paraffin infiltration in the thinnest latewood cells, compromising the integrity of these cells while cutting. Even though this effect must be considered when choosing one of the two approaches, it only affects a small portion of the ring and has no detectable impact on annually resolved MLA values. CWT measurements in the latewood appear to be completely unaffected by this tendency. Differences in late-season MLA chronologies may be less relevant, as climate signals typically derived from these ring portions are usually weak, while CWT data from the same portions often retain highly significant climatic information (Carrer et al. 2018; Castagneri et al. 2017; Puchi et al. 2020).

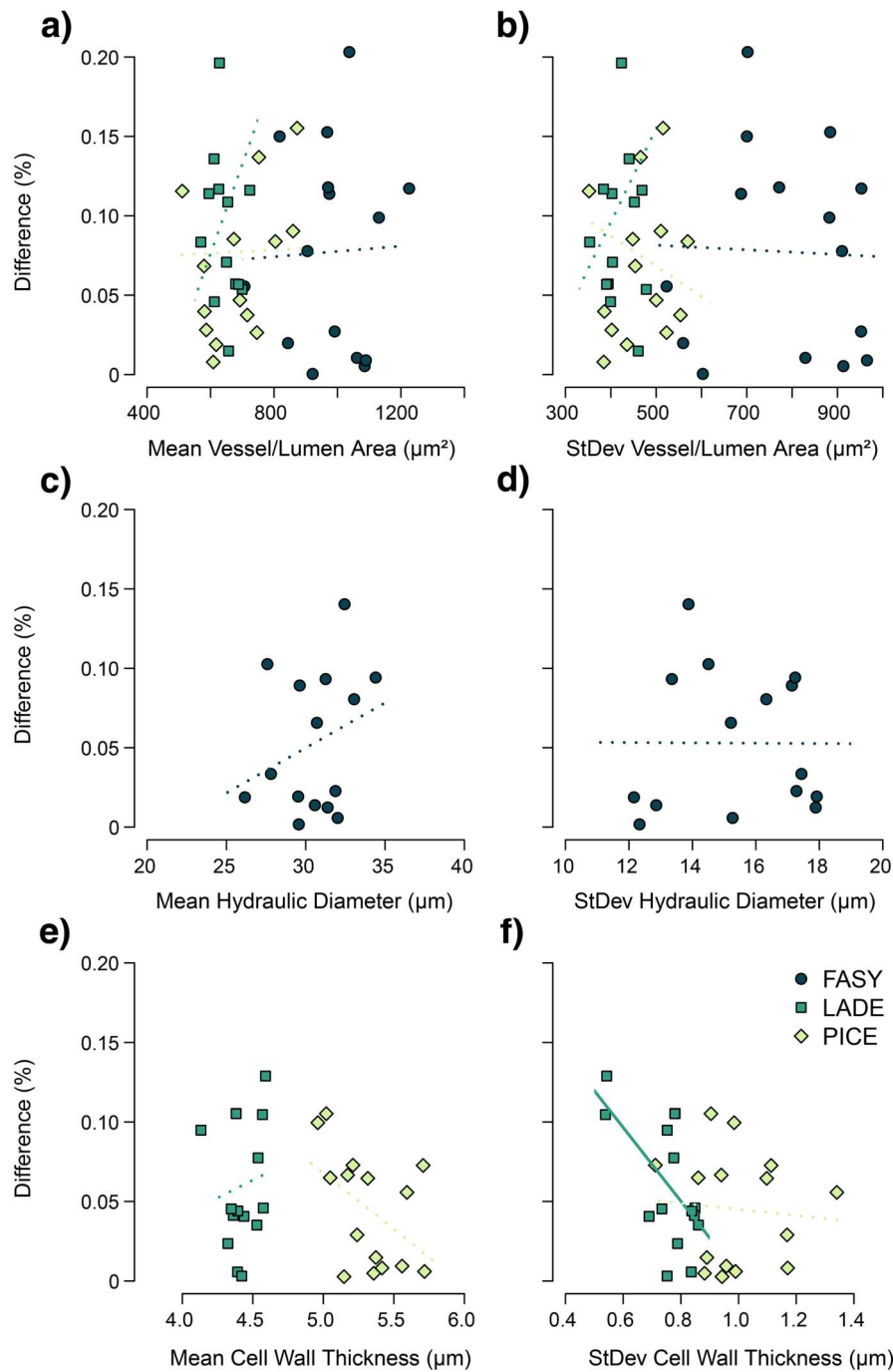


Fig. 4.3 Scatterplots showing the relationships between the average values of **(a)** vessel/tracheid lumen area, **(c)** hydraulic diameter, **(e)** cell wall thickness, and **(b, d, f)** respective standard deviations measured on paraffin-embedded sections (*PAR*) with the absolute difference between the mean values measured on *PAR* and *NoPAR* samples. Colored lines are linear regressions (dashed lines indicate $p > 0.05$; solid lines $p < 0.05$).

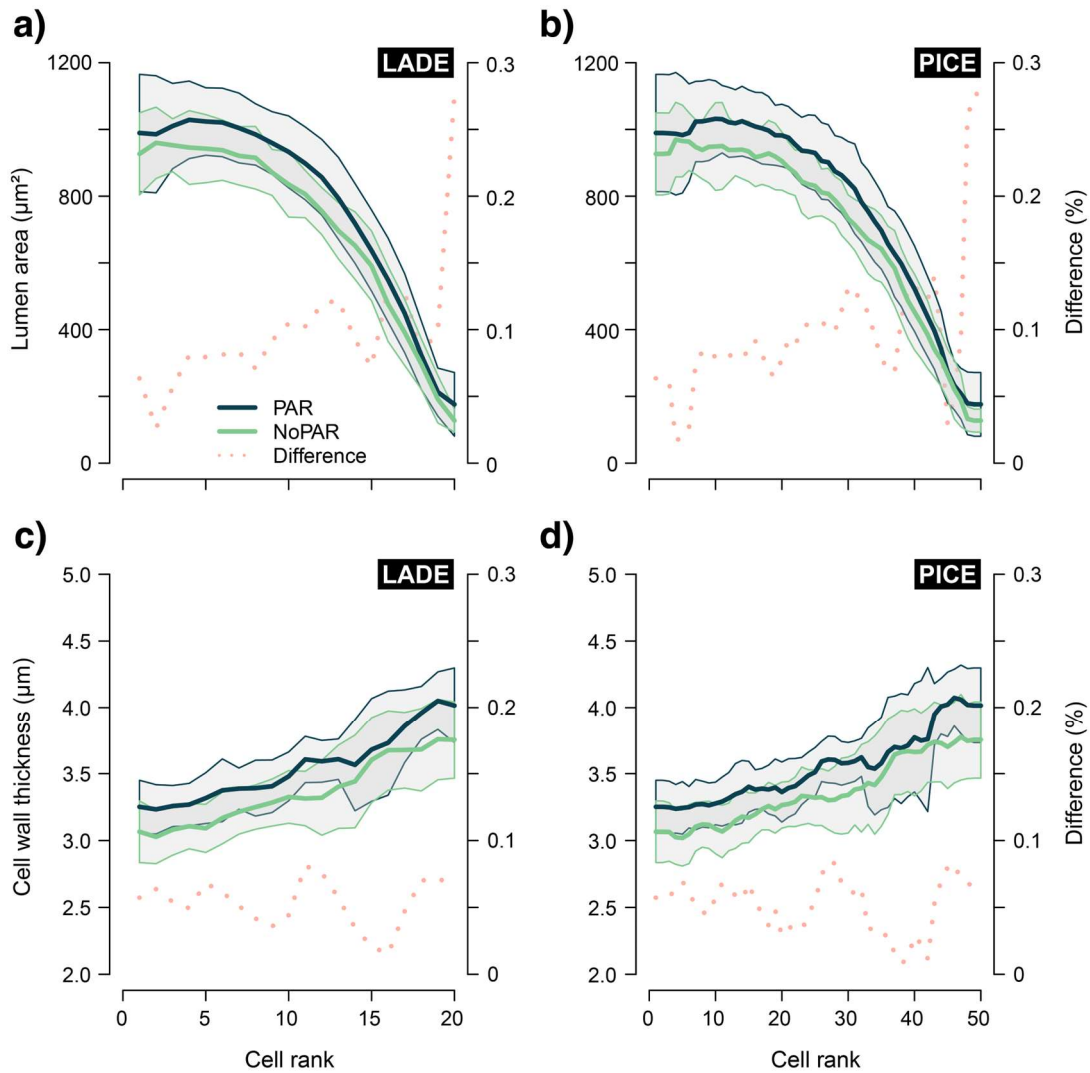


Fig. 4.4 Standardized tracheidograms (solid bold lines) of lumen area and cell wall thickness from paraffin-embedded (*PAR*, dark blue lines) and non-paraffin-embedded (*NoPAR*, green lines) samples of (a-b) LADE and (c-d) PICE. Thin curves represent ± 1 standard deviation. Dotted curves show the mean differences between the tracheidograms.

Several factors might prevent a perfect match of the two approaches, including twisted fiber orientation, localized damage to woody tissue due to insufficient cutting precision, and arbitrary decisions of the sample section chosen for the analysis. Nevertheless, the small differences found in MLA, D_h , and CWT between *PAR* and *NoPAR* are considered minor, since the errors are toward the lower end of the range of 5-30% typically introduced by inaccurate microslide preparation (von Arx et al. 2016). This conclusion is supported by the decision to exclude manual editing of images and filter application from this comparison, which are expected to further mitigate methodological differences. Moreover, it is important to note that the differences between the two approaches are probably accentuated by the exceptionally thin cutting thickness of 10 μm . By producing thicker slides, deviations in wood anatomical traits between *PAR* and *NoPAR* are likely to decrease. Lastly, necessary chemical treatments required to produce high-quality wood anatomical sections, such as bleaching with hypochlorite, might add some minor

uncertainties on absolute QWA metrics through chemical reactions with the wood compounds, but are unproven and negligible due to the major benefit of minimizing other sources of error during the preparation (von Arx et al. 2016).

4.4 Conclusion

We show that the non-embedding procedure does not significantly alter the quality of permanent slides prepared for QWA analysis. The lack of substantial biases between embedding and non-embedding approaches reinforces the reliability of diverse QWA protocols, data exchange, and the development of joint networks. Given the high similarity between the two approaches, we recommend following the non-embedding procedure since it is less time-consuming, less expensive, while it also prevents the utilization of harmful chemicals. Such approach, by saving more resources, allows to produce larger data and is therefore recommended for experienced applicants. However, attention might be required with certain tree species, such as *Larix decidua*, and anatomical features, such as particularly thin cell walls that are susceptible to tissue damage. In these cases, embedding is recommended, particularly for less experienced applicants. Deciduous species are generally less prone to tissue damage and can be processed and combined regardless of the preparation approach. The establishment of large-scale, robust, and unbiased wood anatomical networks is essential for studying inter-regional forest growth responses to rapidly changing environmental conditions. We advise to continue working on the other steps of the QWA protocol to maximize the quality of the material used for anatomical measurements. Accurate sample collection, starting from the correct functioning of the tools (i.e., increment borers), boiling time, cutting precision, as well as specific ROXAS settings, are crucial steps in the QWA protocol that should always be considered and performed in the best possible way to obtain high-quality dendroanatomical data.

4.5 Acknowledgements

Not available online.

4.6 References

- Arnič D, Gričar J, Jevšenak J, Božič G, von Arx G, Prislán P (2021) Different wood anatomical and growth responses in European Beech (*Fagus sylvatica* L.) at three forest sites in Slovenia. *Front Plant Sci* 12: 669229.
- Björklund J, von Arx G, Nievergelt D, Wilson R, van den Bulcke J, Günther B, Loader NJ, Rydval M, Fonti P, Scharnweber T, et al. (2019) Scientific merits and analytical challenges of tree-ring densitometry. *Rev Geophys* 57: 1224-1264.

- Briffa KR, Osborn TJ, Schweingruber FH, Harris IC, Jones PD, Shiyatov SG, Vaganov EA (2001) Low-frequency temperature variations from a northern tree ring density network. *J Geophys Res* 106: 2929-2941.
- Campelo F, Nabais C, Carvalho A, Vieira J (2016) TracheideR – an R package to standardize tracheidograms. *Dendrochronologia* 37: 64-68.
- Carrer M, Brunetti M, Castagneri D (2016) The imprint of extreme climate events in century-long time series of wood anatomical traits in high-elevation conifers. *Front Plant Sci* 7: 1-12.
- Carrer M, Unterholzner L, Castagneri D (2018) Wood anatomical traits highlight complex temperature influence on *Pinus cembra* at high elevation in the Eastern Alps. *Int J Biometeorol* 62: 1745-1753.
- Castagneri D, Fonti P, von Arx G, Carrer M (2017) How does climate influence xylem morphogenesis over the growing season? Insights from long-term intra-ring anatomy in *Picea abies*. *Ann Bot* 119: 1011-1020.
- DeSoto L, De la Cruz M, Fonti P (2011) Intra-annual patterns of tracheid size in the Mediterranean tree *Juniperus thurifera* as an indicator of seasonal water stress. *Can J For Res* 41: 1280-1294.
- Eckstein D, Bauch J (1969) Beitrag zur Rationalisierung eines dendrochronologischen Verfahrens und zur Analyse seiner Aussagesicherheit. *Forstwiss Cent bl* 88: 230-250.
- Esper J, Cook ER, Schweingruber FH (2002) Low-frequency signals in long tree-ring chronologies for reconstructing past temperature variability. *Science* 295: 2250-2253.
- Esper J, Frank DC, Timonen M, Zorita E, Wilson R, Luterbacher J, Holzkämper S, Fischer N, Wagner S, Nievergelt D, et al. (2012) Orbital forcing of tree-ring data. *Nat Clim Change* 2: 862-866.
- Fonti P, Treydte K, Osenstetter S, Frank DC, Esper J (2009) Frequency-dependent signals in multi-centennial oak vessel data. *Palaeogeogr Palaeoclimatol Palaeoecol* 275: 92-99.
- Gärtner H, Schweingruber FH (2013) *Microscopic preparation techniques for plant stem analysis*. Kessel, Remagen-Oberwinter, Germany.
- Hacke UG, Sperry JS (2001) Functional and ecological xylem anatomy. *Perspect Plant Ecol Evol Syst* 4: 97-115.
- Katzenmaier M, Garnot VSF, Björklund J, Schneider L, Wegner JD, von Arx G (2023) Towards ROXAS AI: deep learning for faster and more accurate conifer cell analysis. *Dendrochronologia* 81: 126126.
- Lopez-Saez J, Corona C, von Arx G, Fonti P, Slamova L, Stoffel M (2023) Tree-ring anatomy of *Pinus cembra* trees opens new avenues for climate reconstructions in the European Alps. *Sci Total Environ* 855: 158605.

- Martínez del Castillo E, Prislán P, Gričar J, Gryc V, Merela M, Giagli K, de Luis M, Vavrčík H, Čufar K (2018) Challenges for growth of beech and co-occurring conifers in a changing climate context. *Dendrochronologia* 52: 1-10.
- Olano JM, Eugenio M, García-Cervigón AI, Folch M, Rozas V (2012) Quantitative tracheid anatomy reveals a complex environmental control of wood structure in continental Mediterranean climate. *Int J Plant Sci* 173: 137-149.
- Peters RL, Balanzategui D, Hurley AG, von Arx G, Prendin AL, Cuny HE, Björklund J, Frank DC, Fonti P (2018) RAPTOR: row and position tracheid organizer in R. *Dendrochronologia* 47: 10-16.
- Piermattei A, von Arx G, Avanzi C, Fonti P, Gärtner H, Piotti A, Urbinati C, Vendramin GG, Büntgen U, Crivellaro A (2020) Functional relationships of wood anatomical traits in Norway Spruce. *Front Plant Sci* 11: 1-14.
- Prendin AL, Petit G, Carrer M, Fonti P, Björklund J, von Arx G (2017) New research perspectives from a novel approach to quantify tracheid wall thickness. *Tree Physiol* 37: 976-983.
- Puchi P, Castagneri D, Rossi S, Carrer M (2020) Wood anatomical traits in black spruce reveal latent water constraints on the boreal forest. *Glob Change Biol* 26: 1767-1777.
- R Core Team (2022) *R: a language and environment for statistical computing*. R Foundation for Statistical Computing, Vienna, Austria. <https://www.r-project.org>.
- Rossi S, Anfodillo T, Menardi R (2006) Trephor: a new tool for sampling microcores from tree stems. *IAWA J* 27: 89-97.
- Schneider L, Gärtner H (2013) The advantage of using a starch based non-Newtonian fluid to prepare micro sections. *Dendrochronologia* 31: 175-178.
- Seftigen K, Fonti MV, Luckman B, Rydval M, Stridbeck P, von Arx G, Wilson R, Björklund J (2022) Prospects for dendroanatomy in paleoclimatology – a case study on *Picea engelmannii* from the Canadian Rockies. *Clim Past* 18: 1151-1168.
- Sperry JS, Nichols KL, Sullivan JEM, Sonda EE (1994) Xylem embolism in ring-porous, diffuse-porous, and coniferous trees of northern Utah and interior Alaska. *Ecology* 75: 1736-1752.
- Vaganov EA (1990) The tracheidogram method in tree-ring analysis and its application. In: Cook ER, Kairiukstis, LA (eds) *Methods of dendrochronology*. Kluwer Academic Publishers, Dordrecht, Boston, and London, The Netherlands, USA and UK: pp 63-76.
- von Arx G, Carrer M (2014) ROXAS – a new tool to build centuries-long tracheid-lumen chronologies in conifers. *Dendrochronologia* 32: 290-293.
- von Arx G, Crivellaro A, Prendin AL, Čufar K, Carrer M (2016) Quantitative wood anatomy – practical guidelines. *Front Plant Sci* 7: 1-13.

Yeung ECT, Stasolla C, Sumner MJ, Huang BQ (2015) *Plant microtechniques and protocols*. Springer, Cham, Switzerland.

Ziaco E (2020) A phenology-based approach to the analysis of conifers intra-annual xylem anatomy in water-limited environments. *Dendrochronologia* 59: 125662.

Ziaco E, Liu X, Biondi F (2023) Dendroanatomy of xylem hydraulics in two pine species: efficiency prevails on safety for basal area growth in drought-prone conditions. *Dendrochronologia* 81: 126116.

4.7 Supplementary materials

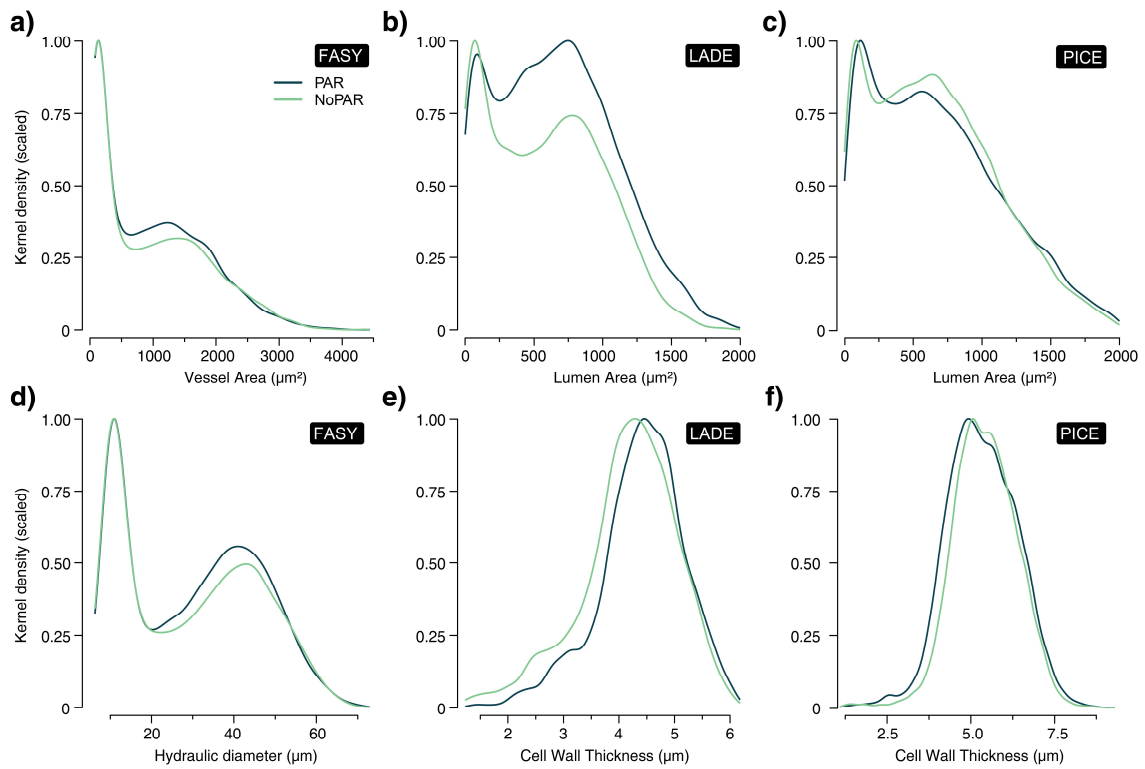


Fig. S4.1 PAR (blue curves) and NoPAR (green curves) distribution of (a) vessel area, (b-c) tracheid lumen area, (d) hydraulic diameter, and (e-f) cell wall thickness measured over 15 rings on *Fagus sylvatica* (FASY), *Larix decidua* (LADE), and *Pinus cembra* (PICE).

5 Multi-proxy crossdating extends the longest high-elevation tree-ring chronology from the Mediterranean

Authors: Philipp Römer*, Frederick Reinig, Oliver Konter, Ronny Friedrich, Otmar Urban, Josef Čáslavský, Natálie Pernicová, Miroslav Trnka, Ulf Büntgen, and Jan Esper

Status: Published in *Dendrochronologia* 79 (2023): 126085.

<https://doi.org/10.1016/j.dendro.2023.126085>

Abstract

Annually precise dating is the cornerstone of dendrochronology. The accurate crossdating of relict wood is, however, frequently challenged during early chronology periods when sample replication is typically low. Here we present a multi-proxy approach in which stable carbon ($\delta^{13}\text{C}$) and radiocarbon (^{14}C) isotope data are used to evaluate and correct dating errors in the early period of the longest high-elevation tree-ring chronology from the Mediterranean Basin. The record was initially developed using 878 tree-ring width (TRW) and 192 maximum late-wood density (MXD) series from living and relict Bosnian pines (*Pinus heldreichii*) from Mt. Smolikas in Greece to reconstruct hydroclimate and temperature variability back to the 8th century. New annually resolved and non-pooled $\delta^{13}\text{C}$ series now suggest a re-dating of first millennium relict pine samples during a period when sample replication was too low for proper TRW and/or MXD crossdating. The associated correction shifts the start of the Mt. Smolikas chronology from 575 back to 468 CE, a change independently confirmed by wiggle-matching annual ^{14}C data along the 774/775 CE cosmic event. Our study demonstrates the importance of independent age validation for robust chronology development and shows how multi-proxy crossdating can improve dating success during periods of low sample replication.

Keywords: Bosnian pine, Mt. Smolikas, paleoclimate, radiocarbon isotopes, relict wood, tree-ring stable isotopes.

5.1 Introduction

The fundamental principle of dendrochronology is crossdating, a method used to accurately assign tree rings to their exact year of formation, routinely accomplished by determining coherent patterns of interannual ring-width (TRW) variability (Stokes & Smiley 1996). This matching technique allows the dating of relict samples, such as subfossil, archeological or historical construction timber, an indispensable step in developing multicentennial to millennial-long tree-ring records (Esper et al. 2016; Ljungqvist et al. 2020). Absolute calendric dating is advantageous compared to other proxy archives and enables the development of high-resolution environmental reconstructions that provide unique information to study, for example, the climate response to volcanic forcing (Büntgen et al. 2020a; Sigl et al. 2015) or the history of natural forest disturbances (Esper et al. 2007) at annual resolution.

Crossdating is most effective when tree growth is constrained by a single limiting environmental factor (Fritts 1976). Dating success based on TRW can be hampered either by favorable conditions resulting in invariant (complacent) rings or structural anomalies such as false, missing, and wedging rings, or intra-annual density fluctuations (Schweingruber et al. 2008). Compared to TRW, maximum latewood density (MXD) measurements typically contain less non-climatic noise, such as biological memory effects (Esper et al. 2015) and spectral biases (Franke et al. 2013), and are less susceptible to large-scale disturbances (Rydval et al. 2018), improving crossdating success. Despite various methodological advances in recent decades (Björklund et al. 2019), dating relict wood of unknown age using well-established TRW/MXD records as a reference, however, remains challenging. This is particularly noticeable in the early period of many tree-ring chronologies, where sample replication and overlap usually decrease substantially. Incorrectly dated series can lead to critical errors in composite chronologies, propagating back through time and eliminating crucial high-frequency signals (Black et al. 2016). Hence, only samples with high dating certainty are routinely included in final records. As a result, a large number of undated relict wood is neglected, often limiting the further extension of absolutely dated tree-ring chronologies into the past.

Besides TRW and MXD, stable carbon ($\delta^{13}\text{C}$) and oxygen ($\delta^{18}\text{O}$) isotopes have proven valuable tools for dating living (Roden 2008) and historic construction timber (Loader et al. 2019, 2021). As $\delta^{13}\text{C}$ reflects the balance between stomatal conductivity and photosynthetic CO_2 assimilation, and $\delta^{18}\text{O}$ is determined by source water and leaf transpiration (McCarroll & Loader 2004), both tree-ring stable isotopes (TRSI) contain crucial information on past climatic conditions and show strong coherences across species and sites (Hartl-Meier et al. 2015; Saurer et al. 2008; Treydte et al. 2007). Climate signals in TRSIs are less dependent on ecological conditions and thus increasingly used for paleoclimate reconstructions, particularly in lowland regions where traditional parameters are less sensitive to climate (Büntgen et al. 2021;

Labuhn et al. 2016). Moreover, despite juvenile effects (Gagen et al. 2008), TRSIs often lack long-term biological age trends (Büntgen et al. 2020b; Gagen et al. 2007; Young et al. 2011) and require comparatively small sample sizes (4-6 trees) to produce reliable site-representative chronologies (Belmecheri et al. 2022; Leavitt 2010).

Independent of regional growth and climate, high-precision radiocarbon (^{14}C) measurements calibrated against the International Northern Hemisphere Radiocarbon Age Calibration Curve (*IntCal20*; Reimer et al. 2020) allow the determination of sample ages. Recent methodological advances have made annually resolved Accelerator Mass Spectrometer (AMS) measurements more readily available and reasonably affordable (Sookdeo et al. 2016; Wacker et al. 2014), opening new opportunities for independent crossdating confirmation. To minimize ^{14}C dating uncertainties resulting from the non-monotonicity of *IntCal20*, so-called ^{14}C “wobble-matching” is performed where multiple rings along a single wood sample are measured and systematically compared to the calibration curve (Bronk Ramsey et al. 2001). Furthermore, abrupt, singular, and globally coherent ^{14}C enrichment events, likely due to short-term enhanced cosmic radiation, represent objective time markers allowing for absolute dating beyond the methodological dating uncertainty of ^{14}C (Büntgen et al. 2018; Miyake et al. 2012).

Here, we apply state-of-the-art multi-proxy crossdating, including TRW, MXD, $\delta^{13}\text{C}$, and ^{14}C , to overcome dating issues of relict pine logs from Mt. Smolikas in Greece. We show that annually resolved and non-pooled $\delta^{13}\text{C}$ measurements of α -cellulose from whole wood samples enable the correction of TRW-based dating errors in the earliest period of the chronology despite weak sample replication. Verified by high-precision ^{14}C wobble-matching, our findings extend the longest Mediterranean tree-ring record more than a century back in time.

5.2 Material and methods

5.2.1 TRW and MXD measurements

A total of 878 TRW and 192 MXD measurements on living (5-mm increment cores) and relict (discs) Bosnian pines (*Pinus heldreichii*) from Mt. Smolikas (≥ 2000 m asl) in northwestern Greece (**Fig. 5.1a**) enabled the development of tree-ring records dating back to early medieval times (Esper et al. 2020a, 2021). The distinct climate seasonality (i.e., warm-dry summers and cold-snowy winters) of the Mediterranean mountain massif permitted the preservation of relict logs for centuries. Core and disc samples were processed according to standard dendrochronological techniques (Stokes & Smiley 1996). TRW was measured along two stem radii per tree (labeled as a-core and b-core; e.g., *Pine16a* and *Pine16b*) using the high-precision LINTAB 6 (Rinntech, Heidelberg, Germany) and Velmex (Velmex, Bloomfield, NY, USA) devices, while MXD data were produced using the DENDRO2003 X-ray densitometer (Walesch Electronic,

Effretikon, Switzerland). Visual and statistical crossdating was performed using the TSAP-Win (Rinn 2012) and COFECHA (Holmes 1983) software, respectively.

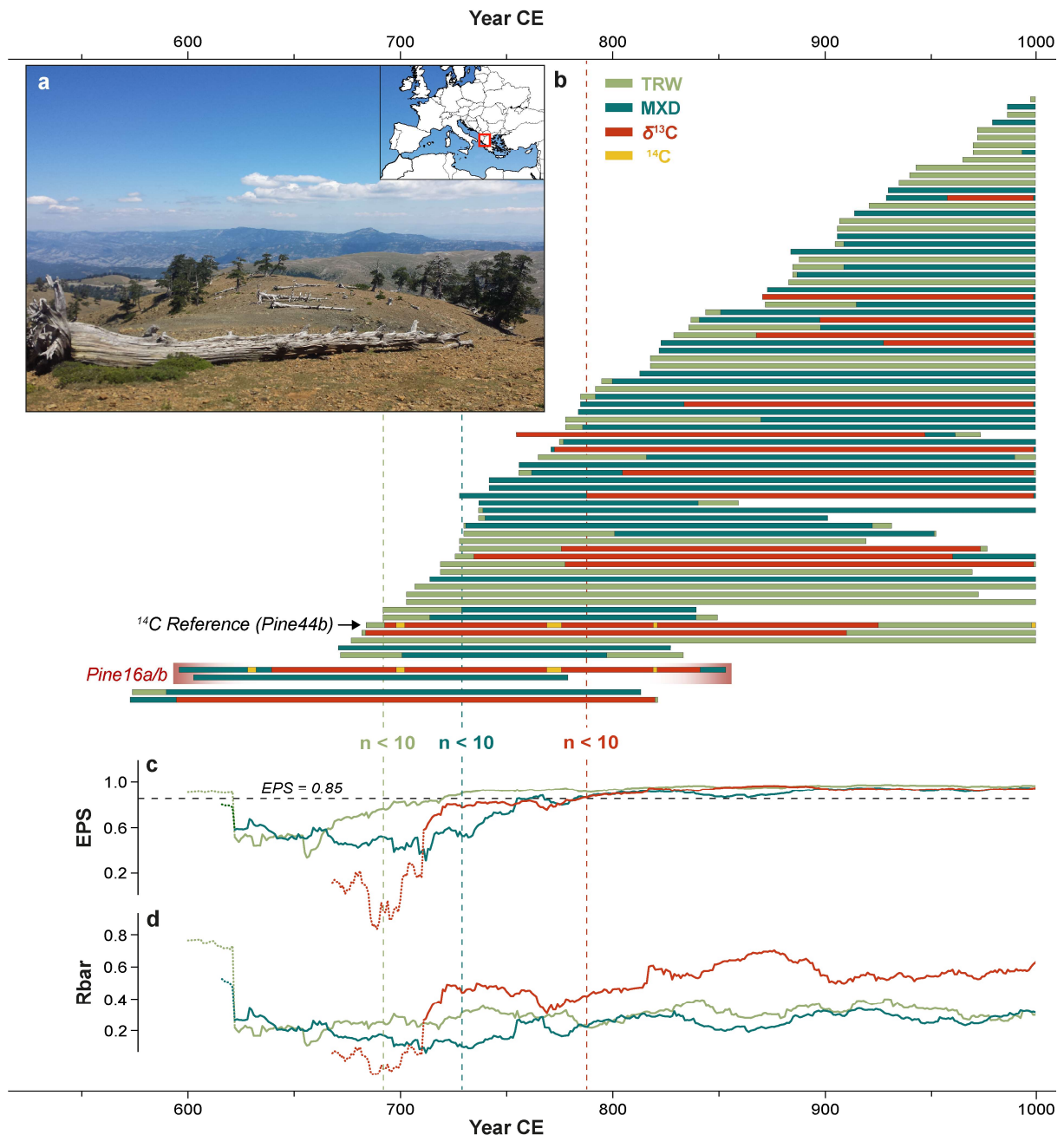


Fig. 5.1 Mt. Smolikas tree-ring data (as published in Esper et al. 2020a, 2021). **(a)** Photograph of relict *Pinus heldreichii* trunks and map showing the geographical location of Mt. Smolikas in Europe. **(b)** Segment length plot indicating the sample replication of the tree-ring width (TRW), maximum latewood density (MXD), stable carbon ($\delta^{13}\text{C}$) and radiocarbon isotope (^{14}C) data in the first millennium CE. Each horizontal bar represents one measurement series. Vertical dashed lines mark the years when sample replication falls below 10 series/year. **(c)** Expressed population signal (EPS) and **(d)** mean inter-series correlation (Rbar) for each proxy calculated over 50-year windows, lagged by 49 years. Dotted curves highlight periods when Rbar/EPS-calculations are based on two series only. Note the sharp decrease in Rbar/EPS of $\delta^{13}\text{C}$ at the early chronology end caused by the misdating of *Pine16a*.

5.2.2 $\delta^{13}\text{C}$ measurements

A total of 78 TRW series (~17% of the entire relict wood material) date to the first millennium. From this collection, 17 well-preserved discs were selected to develop a continuous, annually resolved $\delta^{13}\text{C}$ chronology including 4151 individual measurements. In contrast to TRW and MXD, $\delta^{13}\text{C}$ was measured along a single radius per tree. The disc samples were sawn into ~7-mm-wide radial sections to allow the precise separation of individual rings using a scalpel under a stereomicroscope. To avoid potential juvenile effects (Gagen et al. 2008), the 50 innermost rings of each sample (considering pith offset) were omitted as a conservative precaution. After carefully cutting and dividing each tree ring into similarly sized fiber flakes, the α -cellulose was extracted from the whole wood via the modified Jayme-Wise isolation method (Boettger et al. 2007) at the Global Change Research Institute (CzechGlobe) in the Czech Republic. For this, the shredded wood fibers of each ring were packed in Teflon filter bags and washed successively with 5% NaOH (twice for 2 hours at 60°C) and 7% NaClO₂ solution (30 hours at 60°C) to remove hemicellulose, resin, fatty acids, ethereal oils, and lignin. Acetic acid (99.8%) was added to the latter solution to set a pH of 4-5. The remaining α -cellulose was rinsed three times with 90°C distilled water, dried at 50°C for 24 hours, locked in Eppendorf microtubes, and stored in a dark room at constant room temperature (21°C).

For $\delta^{13}\text{C}$ measurements, 0.2-1.0 mg of α -cellulose was placed in tin capsules and combusted to CO₂ at 960°C using the varioPYRO cube elemental analyzer (Elementar Analysensysteme, Langensfeld, Germany). From the CO₂ gas, the ratio of heavy (¹³C) to light (¹²C) carbon isotopes was determined using the ISOPRIME100 mass spectrometer (Isoprime, Manchester, UK) operating in a continuous flow mode. The ion source of the mass spectrometer was centered, tuned, and tested for stability ($1\sigma \leq 0.04\text{‰}$ on ten pulses over three runs) and linearity ($1\sigma \leq 0.03\text{‰}/\text{nA}$) before each measurement. ¹³C/¹²C ratios were referenced to caffeine (IAEA-600) and graphite (USGS24) and expressed in the conventional δ notation (in ‰), relative to the Vienna Pee Dee Belemnite standard according to the formula:

$$\delta^{13}\text{C} = (R_{\text{sample}}/R_{\text{standard}} - 1) \times 1000, \quad (5.1)$$

where R is the ratio between heavy and light carbon isotopes (¹³C/¹²C). Six consecutive measurements of the same α -cellulose sample were made to determine the precision of $\delta^{13}\text{C}$ ratios. The range between minimum and maximum values and standard deviation (1σ) were 0.12‰ and 0.042‰, respectively.

5.2.3 Chronology development

To normalize the TRW, MXD, and $\delta^{13}\text{C}$ data, the individual tree-ring series were power-transformed and high-pass filtered by calculating residuals from cubic smoothing splines with a 50% frequency cutoff at 30 years (Cook & Peters 1981; Wigley et al. 1987), removing large portions of low-frequency variability, positive autocorrelation, and skewness. Master chronologies were developed using ARSTAN (Cook & Krusic 2016) by calculating the bi-weight robust mean (Cook 1985) and performing variance stabilization to account for altering sample replication and covariance over time (Frank et al. 2007). Coherences among the individual series were assessed using the inter-series correlation (R_{bar}) and the expressed population signal (EPS; Wigley et al. 1984) computed over 50-year segments with a 49-year overlap. Although the new $\delta^{13}\text{C}$ series were dated according to their respective TRW/MXD measurements (Esper et al. 2020a, 2021), their degree of internal crossdating was evaluated using COFECHA (Holmes 1983). Moving correlations between the high-pass filtered $\delta^{13}\text{C}$ series and the COFECHA master chronology thereby cast doubt on the age of the second oldest relict pine (*Pine16*) by proposing a putative redating of the *a*-core (*Pine16a*) from its original TRW-derived placement at 597-852 CE (*Opt1*) to 468-723 CE (*Opt2*).

5.2.4 Radiocarbon dating

For independent age validation, annually resolved ^{14}C measurements were performed on two samples, *Pine16a* with a total ring number of 256 and *Pine44b* with 325 rings. The latter provided a high dendrochronological dating confidence due to significant ($p < 0.001$) strong correlations with the TRW ($r = 0.57$) and $\delta^{13}\text{C}$ ($r = 0.87$) master chronologies over the well-replicated period 695-925 CE ($n \geq 10$ series/year). From each sample, 13 rings from the initial, middle, and end section, ideally from identical calendric dates derived from TRW, were precisely cut and fragmented into equally sized fiber flakes using a scalpel. Material believed to cover the 772-777 CE period was selected to use the 774/775 CE cosmic event as an independent time marker.

At the Curt-Engelhorn-Centre of Archaeometry (Mannheim, Germany), holocellulose was extracted from each ring using the BABA bleaching method (Brock et al. 2010) by washing the wood fibers sequentially at 60°C in 4% NaOH (overnight), 4% HCl (30 min), 4% NaOH (30 min), 4% HCl (30 min), and repeatedly 5% NaClO₂ (60 min) until cellulose turned white. HCl was added to the NaClO₂ solution to set a pH of 3. The material was rinsed 1-3 times between each step with Milli-Q water. After chemical extraction, samples were dried overnight at 60°C. Holocellulose yield ($m_{\text{holocellulose}}/m_{\text{wood}}$) ranged from 48 to 62%. Holocellulose was combusted using the vario MICROcube elemental analyzer (Elementar Analysensysteme, Langenselbold, Germany), and the resulting CO₂ gas was catalytically graphitized using either a custom build

or the commercially available graphitization system AGE3 (IonPlus, Dietikon, Switzerland; Němec et al. 2010; Wacker et al. 2010a). The cellulose-based graphite was pressed into aluminum targets and analyzed for its ^{14}C concentration using the high-precision MICADAS-type (IonPlus, Dietikon, Switzerland) AMS (Kromer et al. 2013; Synal et al. 2007; Wacker et al. 2010b). To determine absolute calendrical dates (CE), the ^{14}C measurements from *Pine16a* and *Pine44b* were wiggle-matched against the *IntCal20* curve (Reimer et al. 2020) using the *D_Sequence* function in OxCal 4.4 (Bronk Ramsey 2009; Bronk Ramsey et al. 2001).

5.3 Results and discussion

5.3.1 TRW, MXD, and $\delta^{13}\text{C}$ chronology statistics

Although the statistical properties of raw $\delta^{13}\text{C}$ are less problematic for correlation analyses than those of TRW and MXD, a first-order autocorrelation of 0.41 and pronounced skewness highlight the need for detrending. High-pass filters effectively remove multidecadal-scale variability while emphasizing high-frequency variability and moving the data closer to normal distribution (**Fig. S5.1**). In the first millennium, the chronology replication decreases continuously toward the past, falling below a threshold of $n < 10$ series/year before 693 CE for TRW, 730 CE for MXD, and 790 CE for $\delta^{13}\text{C}$ (**Fig. 5.1b**). Over the well-replicated 790-1000 CE period, the detrended records (excluding *Pine16*) correlate < 0.5 , indicating a high independence between the tree-ring proxies, with more than 75% of the variance unexplained. Mean segment length of the $\delta^{13}\text{C}$ data (244 years) is 60-70 years shorter than those of TRW and MXD (**Table 5.1**), while mean tree age decreases almost equally for all proxies, from an average of 154 years in 1000 CE to 61 years in 790 CE.

Table 5.1 TRW, MXD, and $\delta^{13}\text{C}$ statistics of the Mt. Smolikas tree-ring chronology.

	n	Period	MSL	Mean $\pm 1\sigma$	Rbar RAW DET	AC1 RAW DET	Reference
TRW	449 878	468-2019	314	0.82 ± 0.38	0.30 0.31	0.77 0.25	<i>Esper et al. (2021)</i>
MXD	103 192	468-2017	303	0.69 ± 0.04	0.21 0.30	0.51 0.08	<i>Esper et al. (2020a)</i>
$\delta^{13}\text{C}$	17 17	514-1235	244	-21.09 ± 0.55	0.47 0.60	0.41 0.08	<i>This study</i>

n: total number of trees | radii. **Period:** first and last year (CE) of the chronologies. **MSL:** mean segment length [years]. **Mean:** average raw TRW [mm], MXD [g/cm^3] and $\delta^{13}\text{C}$ [‰] values $\pm 1\sigma$. **Rbar:** mean inter-series correlation. **AC1:** first-order autocorrelation. The latter two statistics are provided for raw and detrended (DET) data. Chronologies are *Pine16*-corrected.

In periods of sufficient sample replication ($n \geq 10$ series/year), the EPS values of all detrended proxy chronologies persistently exceed 0.85 (**Fig. 5.1c**), indicating an adequate signal strength for robust chronology development (Wigley et al. 1984). Rbar values, however, are substantially higher in $\delta^{13}\text{C}$ than in TRW and MXD throughout the first millennium (**Fig. 5.1d**), despite

the constantly lower $\delta^{13}\text{C}$ replication ($n_{\text{avg}} \sim 25\%$ of TRW). Since the isotope data include only one radial measurement per tree – unlike TRW and MXD – the high Rbar values in $\delta^{13}\text{C}$ reflect strong correlations among the Bosnian pines. These results are in line with previous studies from the Mediterranean reporting high Rbar values for $\delta^{13}\text{C}$ in several pine species, e.g., *Pinus heldreichii* from the Dinarides in Montenegro (Lukač et al. 2021), *Pinus nigra* from Corsica (Szymczak et al. 2012), *Pinus uncinata* from the Spanish Pyrenees (Konter et al. 2014) and the Cazorla Natural Park in southern Spain (Dorado-Liñán et al. 2011). The strong correlations among the individual trees outline $\delta^{13}\text{C}$ as a valuable crossdating proxy, especially in periods where the Mt. Smolikas record is based on less than ten replicates.

5.3.2 Dendrochronological dating of Pine16a

While 16 of the 17 $\delta^{13}\text{C}$ series display highly consistent year-to-year variations, a strikingly low correlation with the isotopic master chronology ($r_{643-840} = 0.15$) is found for *Pine16a* at its TRW-based dating position (*Opt1*, 597-852 CE), causing a sharp decline in Rbar/EPS values. At an alternative $\delta^{13}\text{C}$ -derived position (*Opt2*, 468-723 CE) proposed by COFECHA and supported by visual inspection, *Pine16a* shows higher agreement in all proxies (**Fig. 5.2**). However, only the $\delta^{13}\text{C}$ ($r_{597-711} = 0.62$) and TRW ($r_{575-723} = 0.26$) correlations are significant at $p < 0.001$, while MXD correlations are not. The lack of MXD coherence is striking, especially since its annual-to-decadal scale variability is highly temperature-sensitive (Esper et al. 2020a; Klippel et al. 2019). However, this is likely related to the insufficient replication after 850 CE, which is up to 50% lower than for TRW. Similar replication-related inconsistencies are found in *Larix decidua* MXD from the Tatra Mountains in Slovakia, hindering the further extension of living tree chronologies utilizing historical construction wood (Klippel et al. 2020).

While sole TRW and MXD crossdating yields inconclusive results, the synergistic combination with non-pooled $\delta^{13}\text{C}$ data provides convincing evidence for the actual age of *Pine16*. Although the $\delta^{13}\text{C}$ chronology is only based on a single tree between 597-683 CE, the agreement with *Pine16a* at *Opt2* is remarkably high after detrending ($r_{\text{det}} = 0.57$, $p < 0.001$) and still significant in the raw $\delta^{13}\text{C}$ data ($r_{\text{raw}} = 0.27$, $p < 0.05$). Visual inspection reveals distinct marker years (e.g., 660-661 CE) and periods (654-681 CE) in both time series (**Fig. S5.2**), with only a brief period of high-frequency discrepancies between 613-625 CE. Minor level offsets in raw $\delta^{13}\text{C}$ values are likely related to a mixture of varying microsite conditions (Hartl-Meier et al. 2015) and tree-internal variability (Esper et al. 2020b). However, unlike the observed TRW results (Klippel et al. 2017), the high-frequency variability in $\delta^{13}\text{C}$ appears to be less or not at all affected, reinforcing its high suitability for crossdating.

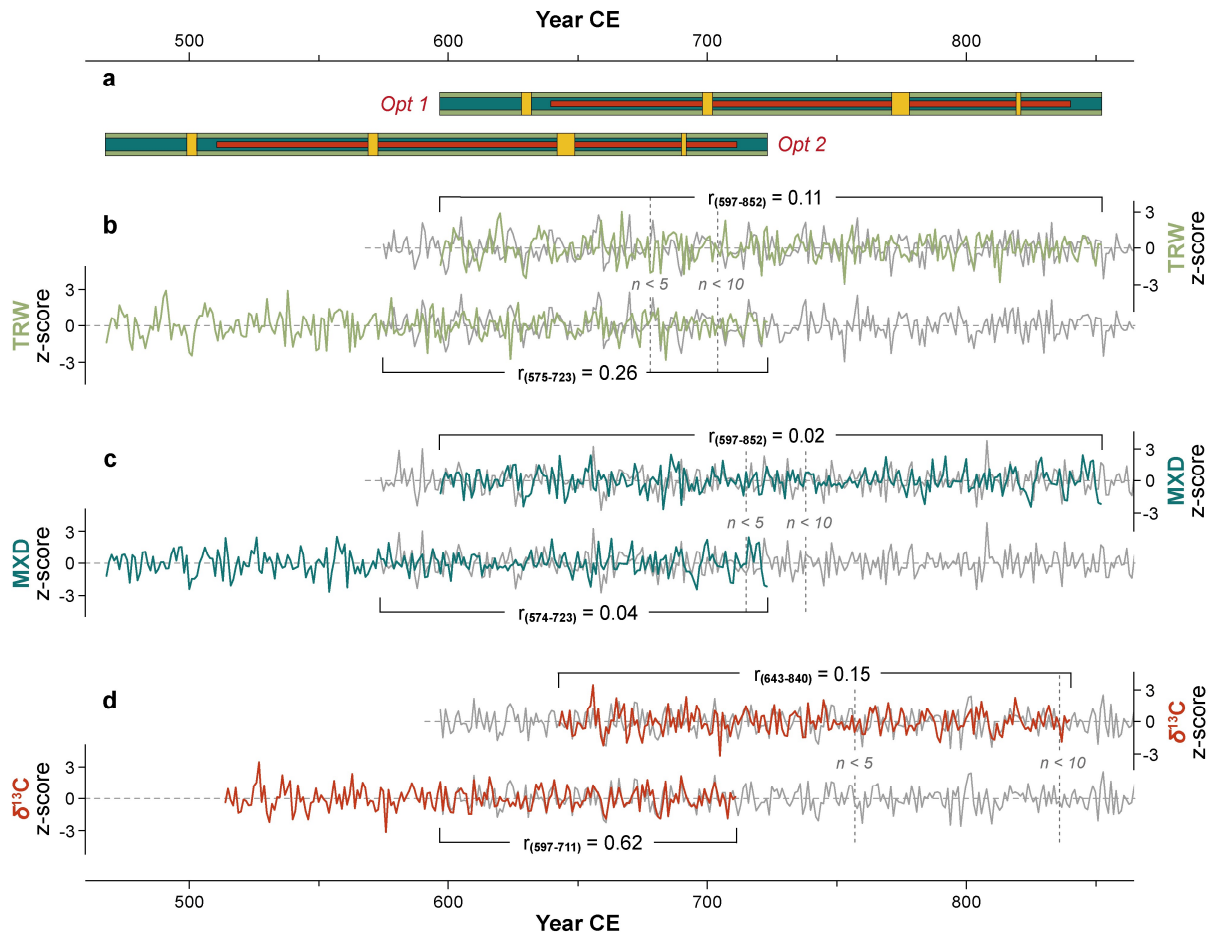


Fig. 5.2 Crossdating of *Pine16a*. (a) Bars indicating the two potential dating positions: *Opt1* (597-852 CE) and *Opt2* (468-723 CE) with color code as in Fig. 5.1. High-pass filtered (b) TRW, (c) MXD, and (d) $\delta^{13}\text{C}$ time series of *Pine16a* (color) and the master chronologies (grey). All series are z-transformed for better comparison. Brackets highlight the maximum overlap and corresponding Pearson correlations.

5.3.3 Radiocarbon verification

The ^{14}C measurements on *Pine16a* and *Pine44b*, calibrated against the *IntCal20* record, provide unambiguous results. Wiggle-matching and calibrated ^{14}C ages of *Pine44b* are in line with the dendrochronological derived position. The innermost ring, dated to 699 CE by both TRW and $\delta^{13}\text{C}$, returns a ^{14}C age of 1307 ± 19 BP that is calibrated to 688-711 CE at 99.7% (3σ), 689-706 CE at 95.4% (2σ), and 691-700 CE at 68.3% probability (1σ). The dating accuracy of the twelve remaining rings along *Pine44b* is similarly accurate (Table S5.1). Furthermore, the sharp decline in uncalibrated ^{14}C ages of rings dated to 773-776 CE, ranging from 1318 ± 19 BP to 1159 ± 19 BP, coincides with the 774/775 CE cosmic event (Fig. 5.3) and thus confirms the annual dating precision of the Mt. Smolikas tree-ring chronology. In contrast, no similar ^{14}C anomaly is found in the corresponding rings of *Pine16a*. Wiggle-matching of *Pine16a* results in a calibrated ^{14}C age of $487-678 \pm 28$ CE (3σ), supporting *Opt2* as the correct dating position by the distinct agreement between $\delta^{13}\text{C}$ and ^{14}C (Table 5.2, Fig. S5.3).

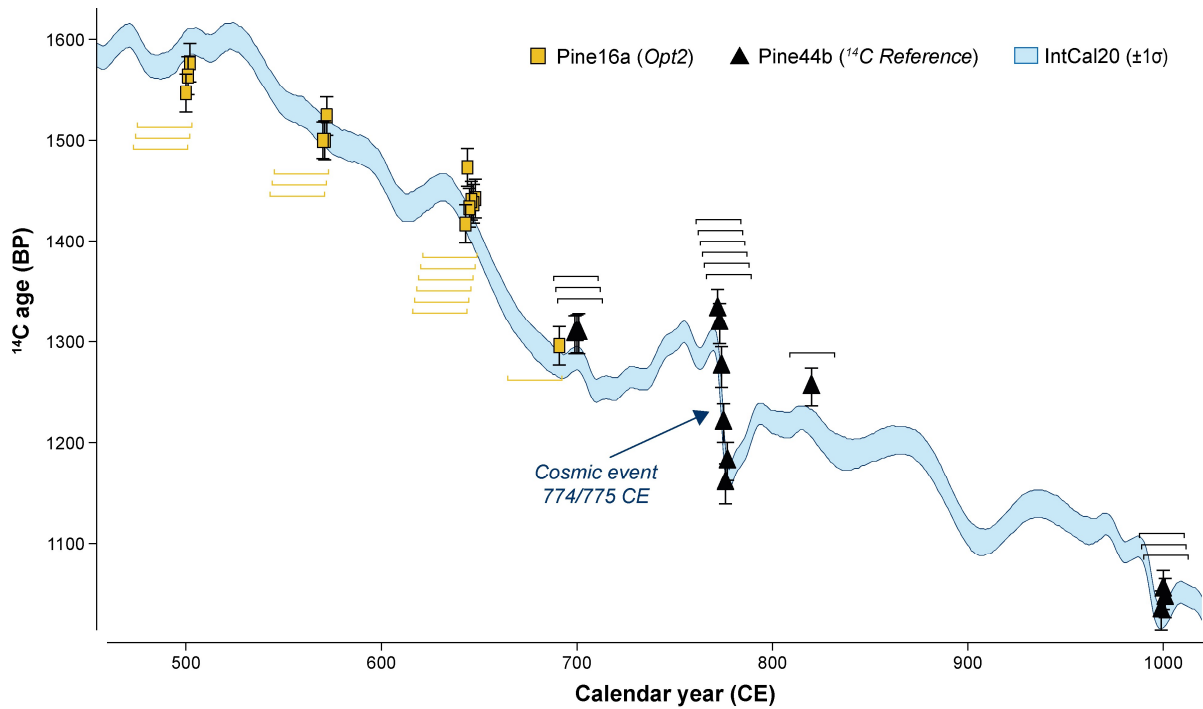


Fig. 5.3 Radiocarbon dating. Symbols represent ^{14}C ages BP $\pm 1\sigma$ (whiskers) of single rings and brackets the calibrated age ranges (CE) at 99.7% probability (Fig. S5.4 for details). The uncalibrated ^{14}C ages (BP) are aligned to their $\delta^{13}\text{C}$ dates (CE). The blue line is the *IntCal20* calibration curve.

Table 5.2 ^{14}C and $\delta^{13}\text{C}$ dating results of sample *Pine16a*.

Ring	$F^{14}\text{C} \pm 1\sigma$	^{14}C age $\pm 1\sigma$	Unmodelled		Modelled		$\delta^{13}\text{C}$	$\delta^{13}\text{C}$ date
			from	to	from	to		
629	0.8248 ± 0.0019	1547 ± 19	430	596	473	501	-	-
630	0.8231 ± 0.0019	1564 ± 19	421	579	474	502	-	-
631	0.8218 ± 0.0019	1577 ± 19	419	565	475	503	-	-
699	0.8296 ± 0.0019	1500 ± 18	540	641	543	571	-21.06	570
700	0.8296 ± 0.0019	1500 ± 19	538	643	544	572	-21.14	571
701	0.8272 ± 0.0020	1524 ± 19	435	634	545	573	-21.60	572
772	0.8383 ± 0.0020	1417 ± 19	591	663	616	644	-21.50	643
773	0.8325 ± 0.0020	1473 ± 19	551	648	617	645	-21.24	644
774	0.8366 ± 0.0020	1433 ± 19	578	658	618	646	-21.14	645
775	0.8359 ± 0.0019	1440 ± 19	572	655	619	647	-20.50	646
776	0.8362 ± 0.0020	1437 ± 19	575	656	620	648	-20.78	647
777	0.8357 ± 0.0020	1442 ± 19	570	655	621	649	-21.64	648
820	0.8510 ± 0.0020	1296 ± 19	659	778	664	692	-20.54	691

Ring: original TRW-based dates CE (*Opt1*). **$F^{14}\text{C}$:** normalized ^{14}C activity ratios ($\pm 1\sigma$). **^{14}C age:** uncalibrated ^{14}C ages BP ($\pm 1\sigma$). **Unmodelled:** individually calibrated ^{14}C age ranges CE (3σ ; 99.7% probability). **Modelled:** wiggle-matched ^{14}C age ranges CE (3σ ; 99.7% probability). **$\delta^{13}\text{C}$:** stable carbon isotope ratios [‰]. **^{13}C date:** $\delta^{13}\text{C}$ -derived dates CE (*Opt2*). Note the discrepancies between the TRW and $\delta^{13}\text{C}$ dates CE (129-year offset).

5.3.4 Chronology improvements

The revised age of *Pine16* extends the existing tree-ring records from Mt. Smolikas by more than a century back in time. The TRW and MXD chronologies now start in 468 CE. Due to the exclusion of juvenile wood portions, the new $\delta^{13}\text{C}$ chronology begins 47 years later (514 CE).

The corrected records show greater year-to-year variability, a higher common signal strength, and reduced error ranges in the 6th and 7th centuries CE (**Fig. 5.4**). These findings are in line with error simulations by Black et al. (2016), which demonstrate the loss of distinct high-frequency variability by adding incorrectly dated tree-ring sequences.

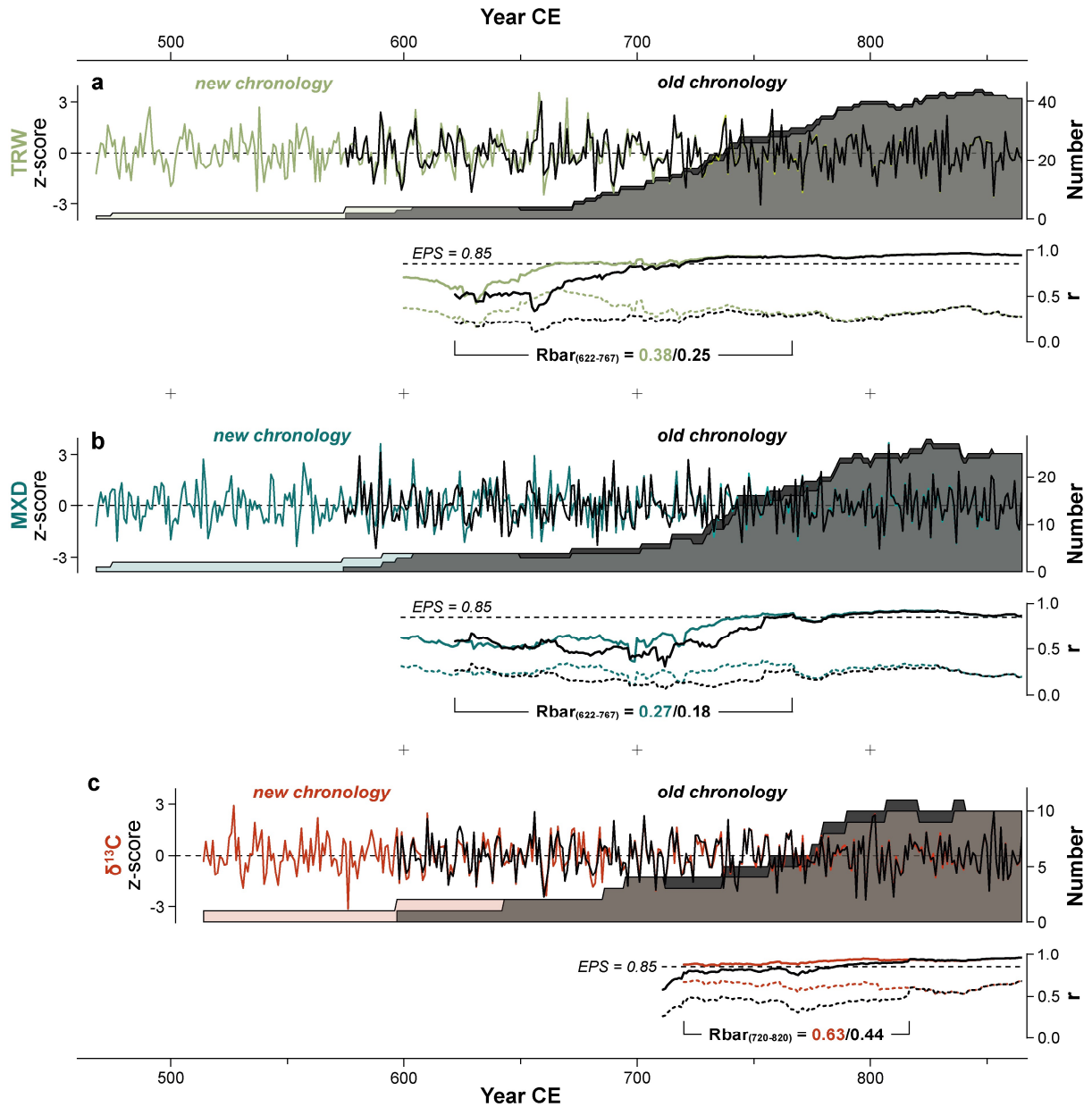


Fig. 5.4 Changes in the (a) TRW, (b) MXD, and (c) $\delta^{13}\text{C}$ chronologies. Upper panels show the re-dated, new chronologies (color) compared to their old versions (black). Filled areas in the background indicate the underlying sample replication. Lower panels show the expressed population signal (EPS; solid lines) and mean inter-series correlation (Rbar; dashed lines) of the new (color) and old (black) chronologies calculated over 50-year windows with a lag of 49 years and truncated at $n < 2$ correlations. Horizontal, black-dashed lines mark the EPS threshold of 0.85. All chronologies are high-pass filtered and z-transformed.

Due to higher inter-series correlations, the EPS values of the corrected proxy records exceed the 0.85 threshold up to 65 years longer into the past, indicating stronger temporal robustness in the first millennium. However, using the EPS as an indicator of sufficient sample replication – to explain $\geq 85\%$ of the variance of a theoretical population (Wigley et al. 1984) – outlines notable differences between the proxies. While more than ten series are necessary to obtain a representative stand-level signal in TRW and MXD, only three $\delta^{13}\text{C}$ series are required to produce a robust isotope chronology. This result is consistent with previous TRSI studies that outline a sample replication of four to six trees sufficient for developing robust site-representative chronologies (Belmecheri et al. 2022; Leavitt 2010). The application of high-pass filters and the calculation of coherence statistics that neglect inter-tree differences in absolute isotope ratios (up to $\sim 3.5\text{‰}$), however, limit the assessment of the entire $\delta^{13}\text{C}$ variance spectrum and restrict the explanatory power of this study to the high-frequency domain.

5.4 Applications, limitations, and conclusions

Interannual $\delta^{13}\text{C}$ variability of *Pinus heldreichii* α -cellulose holds great potential to overcome tentative crossdating of relict wood and improve robust chronology development. Several studies have previously shown that TRSIs can support conventional ring-width dating of living trees (Leavitt et al. 1985; Roden 2008) and historical construction wood (Loader et al. 2019, 2021) when isotopic reference chronologies are sufficiently replicated. In this study, we now demonstrate that combining TRW and non-pooled $\delta^{13}\text{C}$ measurements enable robust dating in the earliest chronology period, overcoming typical crossdating issues such as low sample replication and poor inter-series correlations. Although the $\delta^{13}\text{C}$ record is only based on a single tree prior to 683 CE, the highly consistent year-to-year variations among the individual pines ensure a precise age determination that is independently confirmed by high-resolution ^{14}C dating.

Due to the exclusion of juvenile tree rings, it remains unclear whether these strong inter-series correlations in $\delta^{13}\text{C}$ are stable within the innermost stem sections. Even though juvenile effects are primarily described as low-frequency phenomena in the scientific literature (Bert et al. 1997; Duquesnay et al. 1998; Esper et al. 2010; Gagen et al. 2008; Raffalli-Delerce et al. 2004), $\delta^{13}\text{C}$ depletions in early growth rings may challenge an isotope-based dating of relict tree samples with highly decayed sapwood (Reinig et al. 2018). We, therefore, recommend further in-depth investigations on interannual $\delta^{13}\text{C}$ variability incorporating initial tree rings to assess whether juvenile effects exist in *Pinus heldreichii* and how they may affect the common variability among trees.

Despite many technological and methodological advances in recent decades (e.g., Andreu-Hayles et al. 2019; Schollaen et al. 2017), it is unlikely that TRSIs will replace TRW for routine crossdating due to resource-intensive sample preparation and measurement. Traditional

dendrochronological dating techniques, such as pointer year analysis, skeleton plotting, and consideration of wood anatomical features, remain key for the development of long tree-ring chronologies (Schweingruber et al. 1990). However, the observed robust $\delta^{13}\text{C}$ covariance among individual trees provides a unique opportunity to date problematic samples with reasonable effort. Annually resolved and non-pooled $\delta^{13}\text{C}$ measurements thus offer a high-quality alternative to ^{14}C dating if suitable reference records exist. The strong high-frequency coherence is likely related to climatic drivers that require further in-depth investigations. It is important to note that crossdating success was only possible through annually performed $\delta^{13}\text{C}$ measurements across various trees containing common high-frequency variability. Although the pooling of material from different trees significantly reduces costs and analysis time, and is often the only way to develop multicentennial TRSI records with sufficient sample depth, our results highlight the superior advantage of annual and tree-individual isotope measurements for quasi-independent age validation through multi-proxy crossdating. Moreover, non-pooled TRSIs provide the opportunity to enhance our knowledge of isotopic age trends, low-frequency variability, and underlying physiological processes, topics that are lively debated in the dendro-isotopic community (e.g., Büntgen et al. 2020b; Esper et al. 2010; Helama et al. 2015; Torben-son et al. 2022). Thus, our results stress the need for more high-resolution TRSI measurements on an individual tree level.

The new Mt. Smolikas $\delta^{13}\text{C}$ chronology spanning from 514-1235 CE is the oldest, high-resolution TRSI record in the Mediterranean Basin. Our results call for renewed efforts to reassess the still significant amount of undated Mt. Smolikas relict wood and extend the existing tree-ring records further back in time. Moreover, the new $\delta^{13}\text{C}$ record can serve as a benchmark for the development of robust stable isotope records in neighboring Mediterranean regions. The unique synchronicity between the individual $\delta^{13}\text{C}$ measurements, hinting at a common climatic driver, underscores the need for further investigation of the paleoclimatic value of $\delta^{13}\text{C}$, preferably by extending the isotope record into the 21st century. Several multicentennial tree-ring records from the Mediterranean region exist (Luterbacher et al. 2012) and our results highlight the potential for supra-regional reconstruction based on $\delta^{13}\text{C}$ measurements.

5.5 Acknowledgments

Not available online.

5.6 References

- Andreu-Hayles L, Lévesque M, Martin-Benito D, Huang W, Harris R, Oelkers R, Leland C, Martin-Fernández J, Anchukaitis KJ, Helle G (2019) A high yield cellulose extraction system for small whole wood samples and dual measurement of carbon and oxygen stable isotopes. *Chem Geol* 504: 53-65.
- Belmecheri S, Wright WE, Szejner P (2022) Sample collection and preparation for annual and intra-annual tree-ring isotope chronologies. In: Siegwolf RTW, Brooks JR, Roden J, Saurer M (eds) *Stable isotopes in tree rings – inferring physiological, climatic and environmental responses*. Springer, Cham, Switzerland: pp 103-134.
- Bert D, Leavitt SW, Dupouey JL (1997) Variations of wood $\delta^{13}\text{C}$ and water-use efficiency of *Abies alba* during the last century. *Ecology* 78: 1588-1596.
- Björklund J, von Arx G, Nievergelt D, Wilson R, van den Bulcke J, Günther B, Loader NJ, Rydval M, Fonti P, Scharnweber T, et al. (2019) Scientific merits and analytical challenges of tree-ring densitometry. *Rev Geophys* 57: 1224-1264.
- Black BA, Griffin D, Sleen P, Wanamaker AD, Speer JH, Frank DC, Stahle DW, Pederson N, Copenheaver C, Trouet V, et al. (2016) The value of crossdating to retain high-frequency variability, climate signals, and extreme events in environmental proxies. *Glob Change Biol* 22: 2582-2595.
- Boettger T, Haupt M, Knöllner K, Weise SM, Waterhouse JS, Rinne KT, Loader NJ, Sonninen E, Jungner H, Masson-Delmotte V, et al. (2007) Wood cellulose preparation methods and mass spectrometric analyses of $\delta^{13}\text{C}$, $\delta^{18}\text{O}$, and nonexchangeable $\delta^2\text{H}$ values in cellulose, sugar, and starch: an interlaboratory comparison. *Anal Chem* 79: 4603-4612.
- Brock F, Higham T, Ditchfield P, Ramsey CB (2010) Current pretreatment methods for AMS radiocarbon dating at the Oxford Radiocarbon Accelerator Unit (ORAU). *Radiocarbon* 52: 103-112.
- Bronk Ramsey C (2009) Bayesian analysis of radiocarbon dates. *Radiocarbon* 51: 337-360.
- Bronk Ramsey C, van der Plicht J, Weninger B (2001) 'Wiggle matching' radiocarbon dates. *Radiocarbon* 43: 381-389.
- Büntgen U, Arseneault D, Boucher E, Churakova OJ, Gennaretti F, Crivellaro A, Hughes MK, Kirilyanov AV, Klippel L, Krusic PJ, et al. (2020a) Prominent role of volcanism in Common Era climate variability and human history. *Dendrochronologia* 64: 125757.
- Büntgen U, Kolář T, Rybníček M, Koňasová E, Trnka M, Ač A, Krusic PJ, Esper J, Treydte K, Reinig F, et al. (2020b) No age trends in stable isotopes. *Paleoceanogr Paleoclimatol* 35: e2019PA003831.
- Büntgen U, Urban O, Krusic PJ, Rybníček M, Kolář T, Kyncl T, Ač A, Koňasová E, Čáslavský J, Esper J, et al. (2021) Recent European drought extremes beyond Common Era background variability. *Nat Geosci* 14: 190-196.

- Büntgen U, Wacker L, Galván JD, Arnold S, Arseneault D, Baillie M, Beer J, Bernabei M, Bleicher N, Boswijk G, et al. (2018) Tree rings reveal globally coherent signature of cosmogenic radiocarbon events in 774 and 993 CE. *Nat Commun* 9: 3605.
- Cook ER (1985) *A time series analysis approach to tree-ring standardization*. Dissertation, University of Arizona, Tucson, AZ, USA.
- Cook ER, Krusic PJ (2016) *Program ARSTAN: a tree-ring standardization program based on detrending and autoregressive time series modeling, with interactive graphs*. Lamont-Doherty Observatory, Columbia University, Palisades, NY, USA.
- Cook ER, Peters K (1981) The smoothing spline: a new approach to standardizing forest interior tree-ring width series for dendroclimatic studies. *Tree-Ring Bull* 41: 45-43.
- Dorado-Liñán I, Gutiérrez E, Helle G, Heinrich I, Andreu-Hayles L, Planells O, Leuenberger M, Bürger C, Schleser G (2011) Pooled versus separate measurements of tree-ring stable isotopes. *Sci Total Environ* 409: 2244-2251.
- Duquesnay A, Bréda N, Stievenard M, Dupouey JL (1998) Changes of tree-ring $\delta^{13}\text{C}$ and water-use efficiency of beech (*Fagus sylvatica* L.) in north-eastern France during the past century. *Plant Cell Environ* 21: 565-572.
- Esper J, Büntgen U, Frank DC, Nievergelt D, Liebhold A (2007) 1200 years of regular outbreaks in alpine insects. *Proc Royal Soc B* 274: 671-679.
- Esper J, Frank DC, Battipaglia G, Büntgen U, Holert C, Treydte K, Siegwolf R, Saurer M (2010) Low-frequency noise in $\delta^{13}\text{C}$ and $\delta^{18}\text{O}$ tree ring data: a case study of *Pinus uncinata* in the Spanish Pyrenees. *Glob Biogeochem Cycles* 24: GB4018.
- Esper J, Klippel L, Krusic PJ, Konter O, Raible CC, Xoplaki E, Luterbacher J, Büntgen U (2020a) Eastern Mediterranean summer temperatures since 730 CE from Mt. Smolikas tree-ring densities. *Clim Dyn* 54: 1367-1382.
- Esper J, Konter O, Klippel L, Krusic PJ, Büntgen U (2021) Pre-instrumental summer precipitation variability in northwestern Greece from a high-elevation *Pinus heldreichii* network. *Int J Climatol* 41: 2828-2839.
- Esper J, Krusic PJ, Ljungqvist FC, Luterbacher J, Carrer M, Cook ER, Davi NK, Hartl-Meier C, Kirilyanov AV, Konter O, et al. (2016) Ranking of tree-ring based temperature reconstructions of the past millennium. *Quat Sci Rev* 145: 134-151.
- Esper J, Riechelmann DFC, Holzkämper S (2020b) Circumferential and longitudinal $\delta^{13}\text{C}$ variability in a *Larix decidua* trunk from the Swiss Alps. *Forests* 11: 117.
- Esper J, Schneider L, Smerdon JE, Schöne BR, Büntgen U (2015) Signals and memory in tree-ring width and density data. *Dendrochronologia* 35: 62-170.
- Frank DC, Esper J, Cook ER (2007) Adjustment for proxy number and coherence in a large-scale temperature reconstruction. *Geophys Res Lett* 34: L16709.

- Franke J, Frank DC, Raible CC, Esper J, Brönnimann S (2013) Spectral biases in tree-ring climate proxies. *Nat Clim Change* 3: 360-364.
- Fritts HC (1976) *Tree rings and climate*. Blackburn Press, Caldwell, NJ, USA.
- Gagen M, McCarroll D, Loader NJ, Robertson I, Jalkanen R, Anchukaitis KJ (2007) Exorcising the 'segment length curse': summer temperature reconstruction since AD 1640 using non-detrended stable carbon isotope ratios from pine trees in northern Finland. *Holocene* 17: 435-446.
- Gagen M, McCarroll D, Robertson I, Loader NJ, Jalkanen R (2008) Do tree ring $\delta^{13}\text{C}$ series from *Pinus sylvestris* in northern Fennoscandia contain long-term non-climatic trends? *Chem Geol* 252: 42-51.
- Hartl-Meier C, Zang C, Büntgen U, Esper J, Rothe A, Göttelein A, Dirnböck T, Treydte K (2015) Uniform climate sensitivity in tree-ring stable isotopes across species and sites in a mid-latitude temperate forest. *Tree Physiol* 35: 4-15.
- Helama S, Arppe L, Timonen M, Mielikainen K, Oinonen M (2015) Age-related trends in sub-fossil tree-ring $\delta^{13}\text{C}$ data. *Chem Geol* 416: 28-35.
- Holmes RL (1983) Computer-assisted quality control in tree-ring dating and measurement. *Tree-Ring Bull* 43: 69-78.
- Klippel L, Büntgen U, Konter O, Kyncl T, Esper J (2020) Climate sensitivity of high- and low-elevation *Larix decidua* MXD chronologies from the Tatra Mountains. *Dendrochronologia* 60: 125674.
- Klippel L, Krusic PJ, Brandes R, Hartl-Meier C, Trouet V, Meko M, Esper J (2017) High-elevation inter-site differences in Mount Smolikas tree-ring width data. *Dendrochronologia* 44: 164-173.
- Klippel L, Krusic PJ, Konter O, St George S, Trouet V, Esper J (2019) A 1200+ year reconstruction of temperature extremes for the northeastern Mediterranean region. *Int J Climatol* 39: 2336-2350.
- Konter O, Holzkämper S, Helle G, Büntgen U, Saurer M, Esper J (2014) Climate sensitivity and parameter coherency in annually resolved $\delta^{13}\text{C}$ and $\delta^{18}\text{O}$ from *Pinus uncinata* tree-ring data in the Spanish Pyrenees. *Chem Geol* 337: 12-19.
- Kromer B, Lindauer S, Synal HA, Wacker L (2013) MAMS – a new AMS facility at the Curt-Engelhorn-Centre for Archaeometry, Mannheim, Germany. *Nucl Instrum Methods Phys Res B* 294: 11-13.
- Labuhn I, Daux V, Girardclos O, Stievenard M, Pierre M, Masson-Delmotte V (2016) French summer droughts since 1326 CE: a reconstruction based on tree ring cellulose $\delta^{18}\text{O}$. *Clim Past* 12: 1101-1117.
- Leavitt SW (2010) Tree-ring C-H-O isotope variability and sampling. *Sci Total Environ* 408: 5244-5253.

- Leavitt SW, Long A, Dean JS (1985) Tree-ring dating through pattern-matching of stable-carbon isotope time series. *Tree-Ring Bull* 45: 1-10.
- Ljungqvist FC, Piermattei A, Seim A, Krusic PJ, Büntgen U, He M, Kirilyanov AV, Luterbacher J, Schneider L, Seftigen K, et al. (2020) Ranking of tree-ring based hydroclimate reconstructions of the past millennium. *Quat Sci Rev* 230: 106074.
- Loader NJ, McCarroll D, Miles D, Young GHF, Davies D, Ramsey CB (2019) Tree ring dating using oxygen isotopes: a master chronology for central England. *J Quat Sci* 34: 475-490.
- Loader NJ, McCarroll D, Miles D, Young GHF, Davies D, Ramsey CB, Williams M, Fudge M (2021) Dating of non-oak species in the United Kingdom historical buildings archive using stable oxygen isotopes. *Dendrochronologia* 69: 125862.
- Lukač L, Mikac S, Urban O, Kolář T, Rybníček M, Ač A, Trnka M, Marek MV (2021) Stable isotopes in tree rings of *Pinus heldreichii* can indicate climate variability over the eastern Mediterranean region. *Forests* 12: 350.
- Luterbacher J, García-Herrera R, Akcer-On S, Allan R, Alvarez-Castro MC, Benito G, Booth J, Büntgen U, Cagatay N, Colombaroli D, et al. (2012) A review of 2000 years of paleoclimatic evidence in the Mediterranean. In: Lionello P (ed) *The climate of the Mediterranean region: from the past to the future*. Elsevier, Amsterdam, The Netherlands: pp 87-185.
- McCarroll D, Loader NJ (2004) Stable isotopes in tree rings. *Quat Sci Rev* 23: 771-801.
- Miyake F, Nagaya K, Masuda K, Nakamura T (2012) A signature of cosmic-ray increase in AD 774-775 from tree rings in Japan. *Nature* 486: 240-242.
- Němec M, Wacker L, Gäggeler H (2010) Optimization of the graphitization process at AGE-1. *Radiocarbon* 52: 1380-1393.
- Raffalli-Delercé G, Masson-Delmotte V, Dupouey JL, Stievenard M, Bréda N, Moisselin JM (2004) Reconstruction of summer droughts using tree-ring cellulose isotopes: a calibration study with living oaks from Brittany (western France). *Tellus B Chem Phys Meteorol* 56: 160-174.
- Reimer PJ, Austin WEN, Bard E, Bayliss A, Blackwell PG, Bronk Ramsey C, Butzin M, Cheng H, Lawrence Edwards R, Friedrich M, et al. (2020) The IntCal20 Northern Hemisphere radiocarbon age calibration curve (0-55 cal kBP). *Radiocarbon* 62: 725-757.
- Reinig F, Gärtner H, Crivellaro A, Nievergelt D, Pauly M, Schweingruber F, Sookdeo A, Wacker L, Büntgen U (2018) Introducing anatomical techniques to subfossil wood. *Dendrochronologia* 52: 146-151.
- Rinn F (2012) *TSAP-Win: time series analysis and presentation for dendrochronology and related applications – version 4.6x for Microsoft Windows*. Rinntech GmbH, Heidelberg, Germany.
- Roden J (2008) Cross-dating of tree ring $\delta^{18}\text{O}$ and $\delta^{13}\text{C}$ time series. *Chem Geol* 252: 72-79.

- Rydval M, Druckenbrod DL, Svoboda M, Trotsiuk V, Janda P, Mikoláš M, Čada V, Bače R, Teodosiu M, Wilson R (2018) Influence of sampling and disturbance history on climatic sensitivity of temperature-limited conifers. *Holocene* 28: 1574-1587.
- Saurer M, Cherubini P, Reynolds-Henne CE, Treydte K, Anderson WT, Siegwolf RTW (2008) An investigation of the common signal in tree ring stable isotope chronologies at temperate sites. *J Geophys Res* 113: G04035.
- Schollaen K, Baschek H, Heinrich I, Slotta F, Pauly M, Helle G (2017) A guideline for sample preparation in modern tree-ring stable isotope research. *Dendrochronologia* 44: 133-145.
- Schweingruber F, Borner A, Schulze E (2008) *Atlas of woody plant stems. Evolution, structure, and environmental modifications*. Springer Science & Business Media, Jena, Germany.
- Schweingruber F, Eckstein D, Serre-Bachet F, Bräker OU (1990) Identification, presentation and interpretation of event years and pointer years in dendrochronology. *Dendrochronologia* 8: 9-38.
- Sigl M, Winstrup M, McConnell JR, Welten KC, Plunkett G, Ludlow F, Büntgen U, Caffee M, Chellman N, Dahl-Jensen D, et al. (2015) Timing and climate forcing of volcanic eruptions for the past 2,500 years. *Nature* 523: 543-549.
- Sookdeo A, Wacker L, Fahrni S, McIntyre CP, Friedrich M, Reinig F, Nievergelt D, Tegel W, Kromer B, Büntgen U (2016) Speed dating: a rapid way to determine the radiocarbon age of wood by EA-AMS. *Radiocarbon* 59: 933-939.
- Stokes MA, Smiley TL (1996) *An introduction to tree-ring dating*. The University of Arizona Press, Tucson, AZ, USA.
- Synal HA, Stocker M, Suter M (2007) MICADAS: a new compact radiocarbon AMS system. *Nucl Instrum Methods Phys Res B* 259: 7-13.
- Szymczak S, Joachimski MM, Bräuning A, Hetzer T, Kuhlemann J (2012) Are pooled tree ring $\delta^{13}\text{C}$ and $\delta^{18}\text{O}$ series reliable climate archives? – a case study of *Pinus nigra* spp. *laricio* (Corsica/France). *Chem Geol* 308-309: 40-49.
- Torbenson M, Klippel L, Hartl C, Reinig F, Treydte K, Büntgen U, Trnka M, Schöne BR, Schneider L, Esper J (2022) Investigation of age trends in tree-ring stable carbon and oxygen isotopes from northern Fennoscandia over the past millennium. *Quat Int* 631: 105-114.
- Treydte K, Frank DC, Esper J, Andreu L, Bednarz Z, Berninger F, Boettger T, D'Alessandro CM, Etien N, Filot M, et al. (2007) Signal strength and climate calibration of a European tree-ring isotope network. *Geophys Res Lett* 34: L24302.
- Wacker L, Bonani G, Friedrich M, Hajdas I, Kromer B, Němec M, Ruff M, Suter M, Synal HA, Vockenhuber C (2010b) MICADAS: routine and high-precision radiocarbon dating. *Radiocarbon* 52: 252-262.

- Wacker L, Güttler D, Goll J, Hurni J, Synal H, Walti N (2014) Radiocarbon dating to a single year by means of rapid atmospheric ^{14}C changes. *Radiocarbon* 56: 573-579.
- Wacker L, Němec M, Bourquin J (2010a) A revolutionary graphitization system: fully automated, compact and simple. *Nucl Instrum Methods Phys Res B* 268: 931-934.
- Wigley TML, Briffa KR, Jones PD (1984) On the average of correlated time series, with applications in dendroclimatology and hydrometeorology. *J Appl Meteorol Climatol* 23: 201-213.
- Wigley TML, Jones PD, Briffa KR (1987) Cross-dating methods in dendrochronology. *J Archaeol Sci* 14: 51-64.
- Young GHF, Demmler JC, Gunnarson BE, Kirchhefer AJ, Loader NJ, McCarroll D (2011) Age trends in tree ring growth and isotopic archives: a case study of *Pinus sylvestris* L. from northwestern Norway. *Glob Biogeochem Cycles* 25: GB2020.

5.7 Supplementary materials

Table S5.1 ^{14}C and $\delta^{13}\text{C}$ dating results of sample *Pine44b*.

Ring	$F^{14}\text{C} \pm 1\sigma$	$\text{C}^{14} \text{ age} \pm 1\sigma$	Unmodelled		Modelled		$\delta^{13}\text{C}$	$\delta^{13}\text{C} \text{ date}$
			from	to	from	to		
699	0.8499 ± 0.0020	1307 ± 19	656	777	688	711	-20.71	699
700	0.8497 ± 0.0020	1308 ± 19	656	777	689	712	-21.02	700
701	0.8498 ± 0.0021	1308 ± 19	656	777	690	713	-21.45	701
772	0.8472 ± 0.0021	1332 ± 18	646	778	761	784	-20.79	772
773	0.8487 ± 0.0021	1318 ± 19	651	778	762	785	-20.42	773
774	0.8533 ± 0.0021	1275 ± 19	661	829	763	786	-20.95	774
775	0.8592 ± 0.0021	1219 ± 19	685	890	764	787	-20.74	775
776	0.8656 ± 0.0022	1159 ± 19	771	986	765	788	-20.76	776
777	0.8633 ± 0.0021	1181 ± 19	770	973	766	789	-20.56	777
820	0.8554 ± 0.0021	1255 ± 19	669	879	809	832	-20.17	820
999	0.8793 ± 0.0021	1034 ± 19	899	1040	988	1011	-	-
1000	0.8771 ± 0.0021	1054 ± 19	895	1034	989	1012	-	-
1001	0.8779 ± 0.0021	1046 ± 19	896	1035	990	1013	-	-

Ring: TRW-based dates CE, **$F^{14}\text{C}$:** normalized ^{14}C activity ratios ($\pm 1\sigma$). **^{14}C age:** uncalibrated ^{14}C ages BP ($\pm 1\sigma$). **Unmodelled:** individually calibrated ^{14}C age ranges CE (3 σ ; 99.7% probability). **Modelled:** wiggle-matched ^{14}C age ranges CE (3 σ ; 99.7% probability). **$\delta^{13}\text{C}$:** stable carbon isotope ratios [‰]. **^{13}C date:** $\delta^{13}\text{C}$ -derived dates CE.

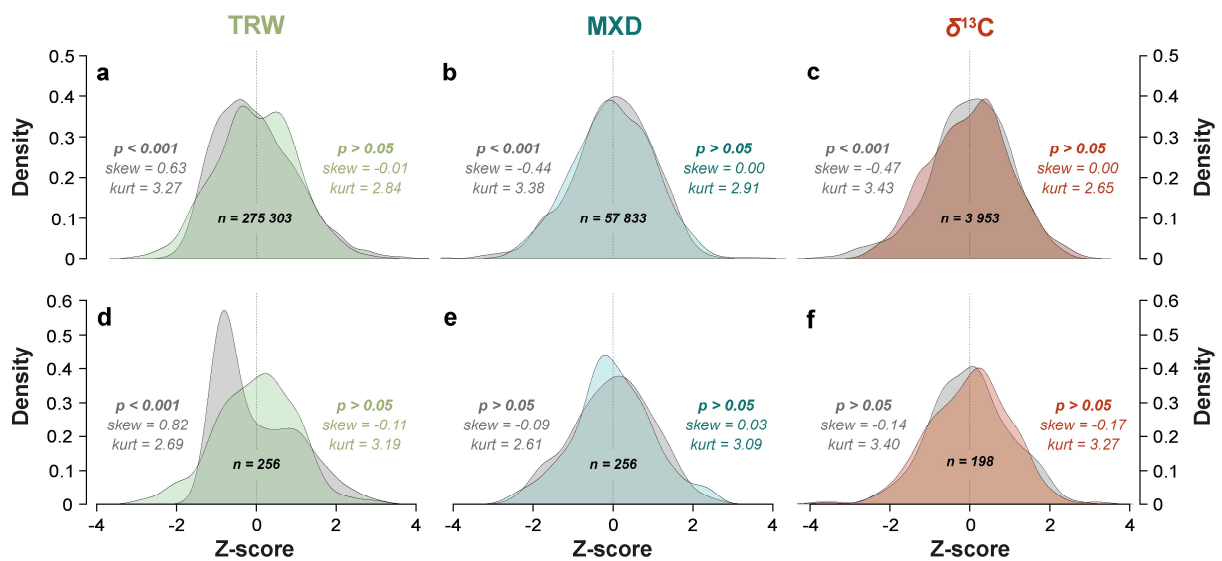


Fig. S5.1 Effects of high-pass filtering. Distribution of z-scored proxy data for (a-c) the entire dataset and for (d-f) *Pine16a*. Probability density of the raw (grey) and detrended (color) data with Shapiro-Wilk test results (p-values), skewness (skew), kurtosis (kurt), and sample size (n; total number of rings). Note that high-pass filtering pushes the data closer to normal distribution and reduces skewness and kurtosis, especially in the large datasets (a-c).

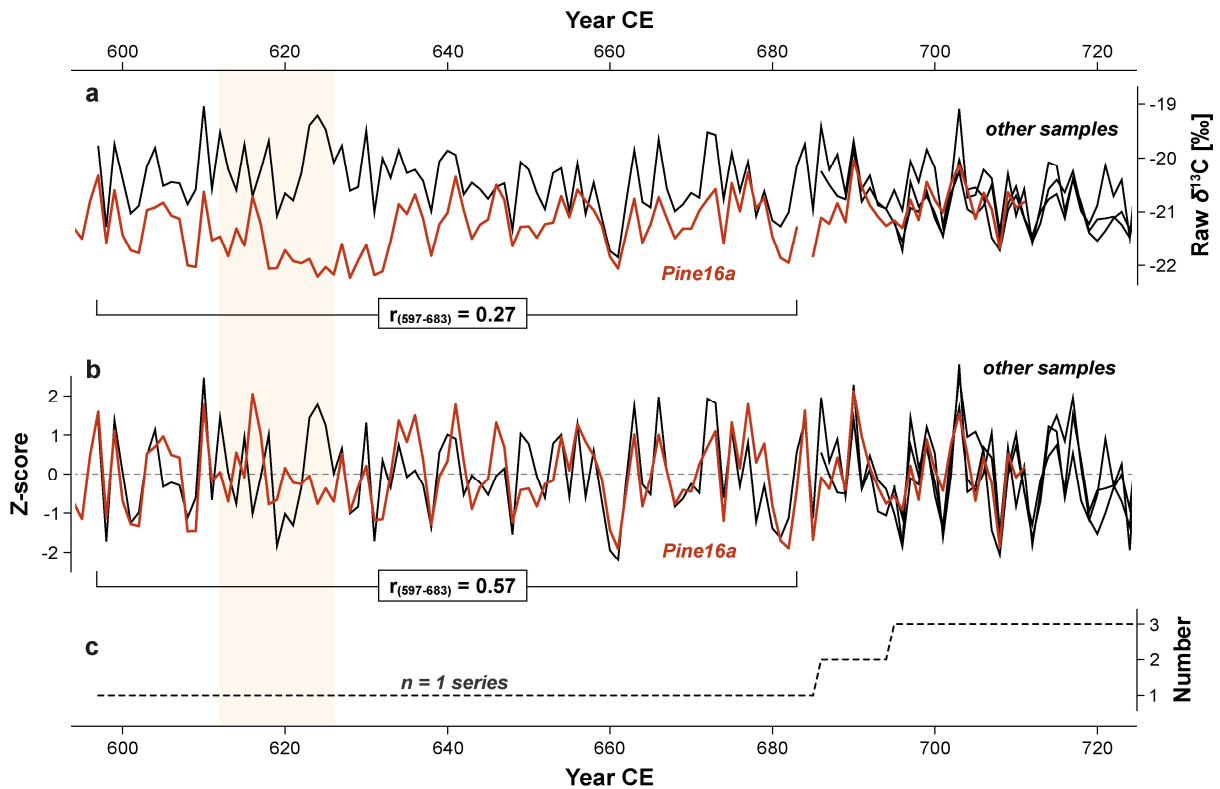


Fig. S5.2 *Pine 16a* at *Opt2* (468-723 CE). (a) Raw and (b) high-pass filtered $\delta^{13}\text{C}$ series with corresponding Pearson correlations between *Pine 16a* and the master chronology when $n = 1$ series (597-683 CE). Note the strong covariance between the two time series. The yellow area in the background highlights a short period (613-625 CE) of high-frequency mismatch. (c) Sample replication of the $\delta^{13}\text{C}$ chronology.

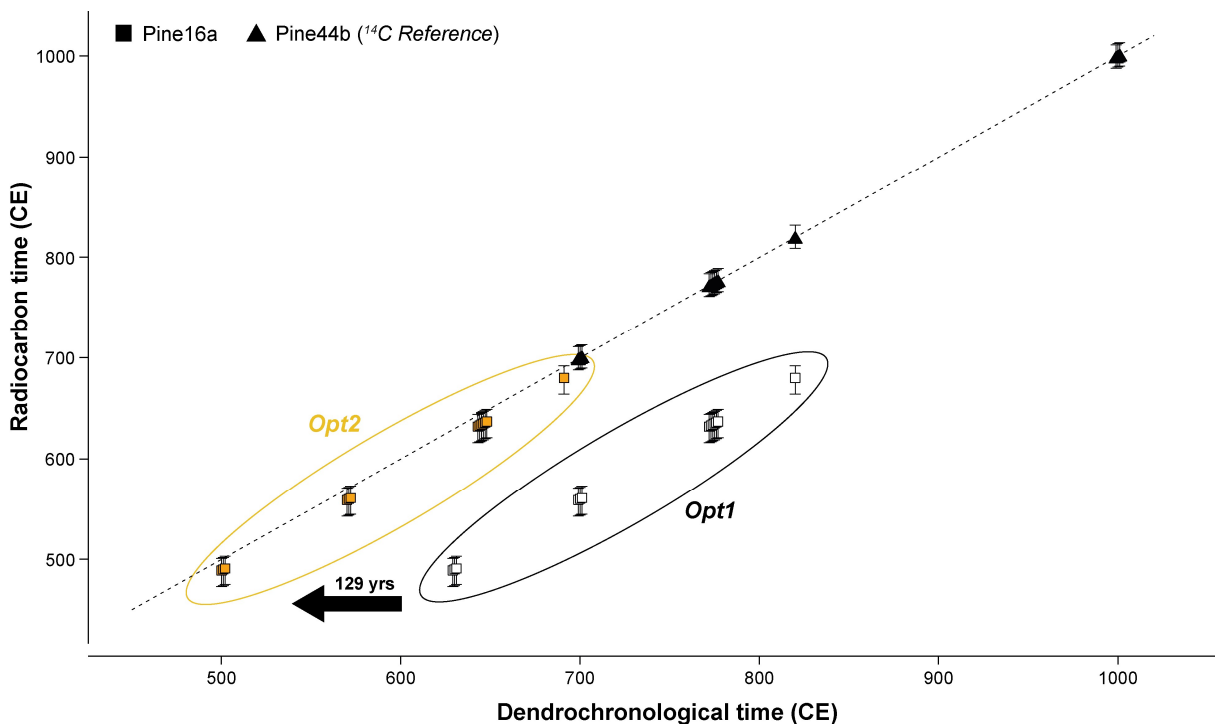


Fig. S5.3 Independent age validation. Symbols represent the mean calendric ages CE of the ^{14}C wiggle-match and whiskers the age ranges at 99.7% probability. The dashed line denotes similar years between calibrated ^{14}C ages and dendrochronological dates. Note that *Pine 44b* and *Opt2* whiskers consistently overlap with the dashed line and are therefore considered correct.

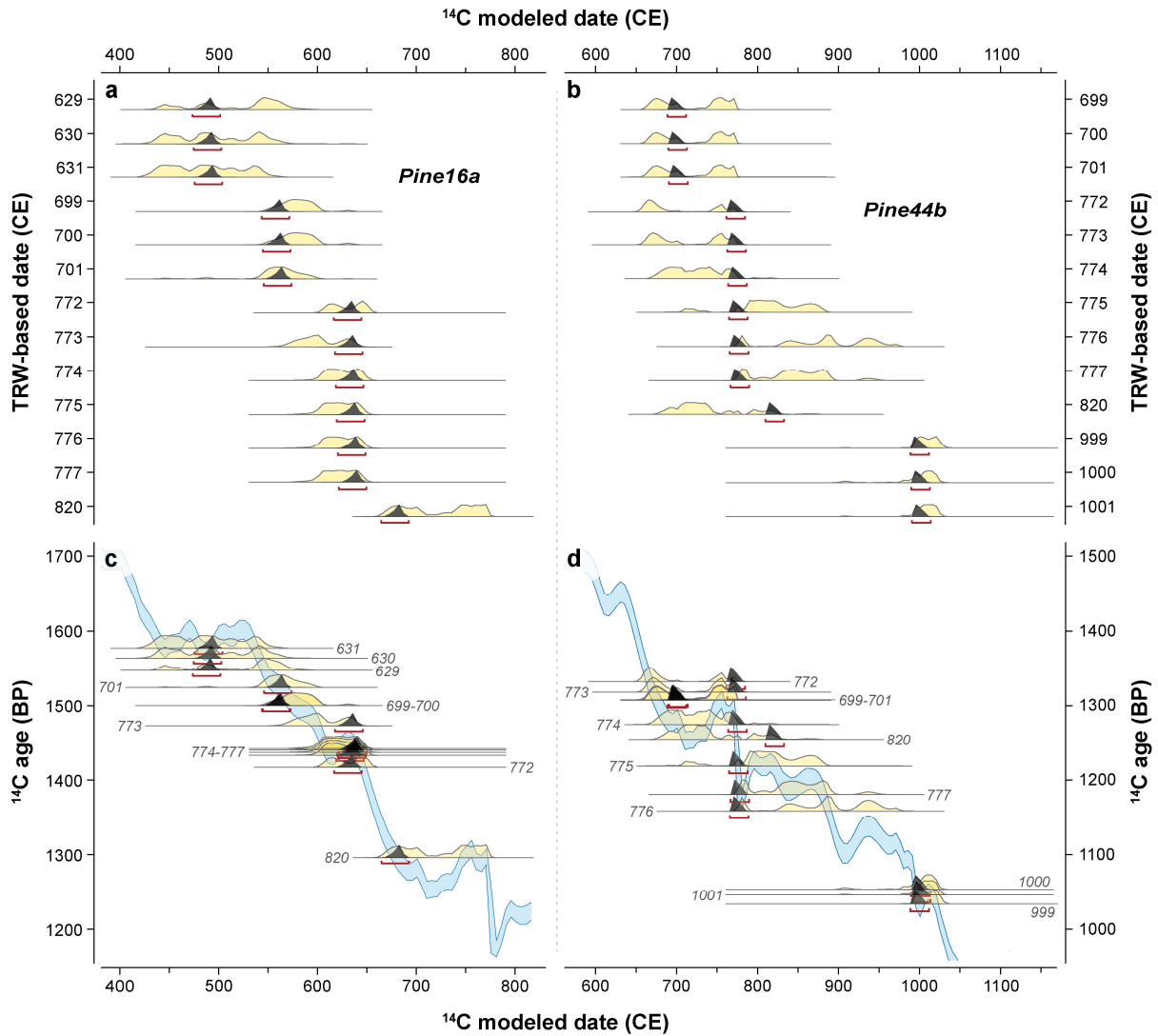


Fig. S5.4 OxCal results of (a) *Pine16a* and (b) *Pine44b*. The individual rings are coded by their TRW-based dates. Smoothed histograms represent the probability distributions of the individual (yellow) and wiggle-match (grey) age ranges (CE) at 99.7% probability. The wiggle-match results are highlighted by red brackets. Uncalibrated ^{14}C ages (BP) of (c) *Pine16a* and (d) *Pine44b* plotted against *IntCal20*.

6 Tree-ring stable isotopes in cellulose and lignin methoxy groups reveal different age-related behaviour

Authors: Anna Wieland*, Philipp Römer*, Max Torbenson, Markus Greule, Otmar Urban, Josef Čáslavský, Natálie Pernicová, Miroslav Trnka, Ulf Büntgen, Jan Esper, Frank Keppler

Status: Published in *Quaternary International* 693 (2024): 38-48.

<https://doi.org/10.1016/j.quaint.2024.02.004>

Abstract

Tree-ring stable isotopes (TRSI) have the unique ability to capture interannual to multimillennial climate trends and extremes if the appropriate data and methods are combined. However, there is still an ongoing debate about age-related biases in TRSI measurements that potentially affect the fidelity of their chronologies and subsequent climate reconstructions. Here, we investigate stable carbon and oxygen isotope ratios in cellulose ($\delta^{13}\text{C}_c$ and $\delta^{18}\text{O}_c$), and carbon and hydrogen ratios in lignin methoxy groups ($\delta^{13}\text{C}_m$ and $\delta^2\text{H}_m$) of more than 60 living and relict pines (*Pinus heldreichii*) from northern Greece that span the period 512-2020 CE continuously. We identify significant ($p < 0.01$) level offsets between living and relict $\delta^{18}\text{O}_c$ values (1.49 mUr) that prevent the combination of living and relict wood series for reliable age-trend assessment, and we observe differences between cellulose and methoxy TRSI chronologies, including contrasting recent trends in carbon, oxygen, and hydrogen isotope ratios, suggesting that varying environmental signals are retained in the proxies. Assessments are supported by comparisons with ontogenetic trends in tree-ring width and latewood maximum density to identify significant ($p < 0.01$) trends in relict $\delta^{18}\text{O}_c$ between 50-190 years of cambial age, and in relict $\delta^{13}\text{C}_m$ and $\delta^2\text{H}_m$ in tree rings older than 100 years. Relict $\delta^{13}\text{C}_c$ values, on the other hand, show increasing values between 50-80 years of cambial age ($p < 0.01$) but no evidence for long-term age trends beyond these early stages. The assessment of TRSIs from cellulose and methoxy groups contributes to a better understanding of underlying physiological processes and extends the range of extractable climate information from the utilized proxies. Our findings demonstrate that raw $\delta^{13}\text{C}_c$ data from Mt. Smolikas can be used for climate reconstruction purposes without the need for standardization (except for rings ≤ 80 years of cambial age), potentially providing new insights into long-term climate variability in the eastern Mediterranean region. $\delta^{18}\text{O}_c$, $\delta^{13}\text{C}_m$, and $\delta^2\text{H}_m$, however, require detrending due to long-term age-related trends.

Keywords: age trends, cellulose, lignin methoxy groups, Greece, *Pinus heldreichii*, tree-ring stable isotopes.

6.1 Introduction

Tree-ring stable isotope (TRSI) measurements of cellulose and lignin methoxy groups are important proxies for high-resolution paleoclimate reconstruction. While TRSI measurements of methoxy groups are relatively new compared to measurements of cellulose, both compounds are used to assess past climate information (e.g., Anhäuser et al. 2017; Büntgen et al. 2021; Esper et al. 2015; Hafner et al. 2011; Lu et al. 2022; Riechelmann et al. 2017; Treydte et al. 2001; Wieland et al. 2022). Combining proxies with different controlling factors, such as growing-season temperatures or precipitation totals, increases the potential to reconstruct different seasonal climate variations at varying spatiotemporal scales from the same material (McCarroll et al. 2003). Moreover, comparing various plant components provides additional information on differences in isotopic fractionation within variable biochemical pathways. To date, however, only two studies have compared the stable isotope ratios of cellulose and methoxy groups from the same material: Gori et al. (2013) and Mischel et al. (2015). Both studies compared stable carbon ($\delta^{13}\text{C}$), oxygen ($\delta^{18}\text{O}$), and hydrogen ($\delta^2\text{H}$) ratios of whole wood, cellulose, and methoxy groups and found that TRSI values of methoxy groups are influenced by different environmental and biochemical factors than those of cellulose and whole wood.

Classic tree-ring proxies such as tree-ring width (TRW) and maximum latewood density (MXD) need to be standardized prior to climate interpretation as both parameters include age-related trends (Bräker 1981). However, removing age-related trends from a chronology induces a loss of low-frequency climate information (Cook et al. 1995). Several methods have been developed to preserve low-frequency variability (Briffa et al. 1992; Esper et al. 2003; Melvin & Briffa 2008, 2014), but these techniques require large datasets that are typically composed of living and dead trees (Esper et al. 2004). Age trends can generally be divided into juvenile trends, including the first few decades of tree growth, and long-term trends throughout the trees' (varying) lifespans. Juvenile effects have been documented in many TRSI chronologies (Duquesnay et al. 1998; Gagen et al. 2006, 2008; McCarroll & Loader 2004; Raffalli-Delercé et al. 2004; Torbenson et al. 2022). To avoid biases from these trends, the first decades of tree rings can simply be omitted (Gagen et al. 2008). However, this is not applicable in the presence of long-term age-related trends (Helama et al. 2015). Esper et al. (2010) found age trends in cellulose TRSI chronologies, at a rate of $-0.089 \text{ mUr decade}^{-1}$ in $\delta^{18}\text{O}$ and $+0.064 \text{ mUr decade}^{-1}$ in $\delta^{13}\text{C}$ over the first 100 years of tree growth in *Pinus uncinata* trees from Spain. Similar values were found in other studies, with $+0.035 \text{ mUr decade}^{-1}$ in $\delta^{13}\text{C}$ of pines from northern Scandinavia (Torbenson et al. 2022) and $+0.04 \text{ mUr decade}^{-1}$ in *Pinus sylvestris* from northern Finnish Lapland (Helama et al. 2015). However, there are also studies reporting no age trends in $\delta^{18}\text{O}$ and $\delta^{13}\text{C}$ values of oaks from the Czech Republic (Büntgen et al. 2020) and in $\delta^{18}\text{O}$ values of pines from northern Scandinavia (Torbenson et al. 2022), suggesting that detrending is not needed

for paleoclimate reconstruction. Given the current state of knowledge, any isotopic data should therefore be tested for ontogenetic trends before using TRSI data for reconstruction purposes (Helama et al. 2015).

Discrepancies among studies could be related to species- and site-effects as well as methodological approaches including sample preparation, data pooling, and truncation (Borella et al. 1999; Büntgen et al. 2020; Daux et al. 2018; Duffy et al. 2019; Leavitt 2010; Loader et al. 2013; McCarroll & Loader 2004). For reliable age-trend analyses, tree-ring data must contain a large number of samples, with at least ten individual series from different trees distributed over a range of centuries and thus growing under different climatic conditions. For $\delta^{13}\text{C}$ analysis, it is advantageous to use trees that grew prior to the strong atmospheric CO_2 changes during recent decades, as $\delta^{13}\text{C}$ values after 1850 CE must be corrected for the so-called Suess effect (decrease in atmospheric $\delta^{13}\text{C}_{\text{CO}_2}$ values; Keeling 1979; McCarroll & Loader 2004) and physiological responses due to increasing CO_2 concentrations (Keeling et al. 2017). These correction methods are still subject to large uncertainties, and the trends added by statistical corrections could cover potential age-related trends.

In this study, we present 62 individual $\delta^{18}\text{O}$ and $\delta^{13}\text{C}$ series of cellulose and 65 $\delta^{13}\text{C}$ and $\delta^2\text{H}$ series of methoxy groups from living and relict wood samples of *Pinus heldreichii* from Mt. Smolikas in Greece. The data are of annual and decadal resolution and developed from pines with different germination and end dates over the last 1500 years, making them well suited for assessing biological (non-climatic) age trends. However, significant ($p < 0.01$) offsets between living and relict $\delta^{18}\text{O}$ and $\delta^2\text{H}$ values preclude the combination of living and relict wood series for reliable age-trend assessment. Therefore, to evaluate potential biological trends in TRSIs, we used only the relict wood series, converted the TRSI series to a uniform decadal resolution as the methoxy-based relict wood samples were measured decadally, and compared the new TRSI data to the well-established TRW and MXD data from Mt. Smolikas (Esper et al. 2020a, 2021). Here, we (I) describe the key characteristics of the new TRSI measurements, (II) quantify the differences between living and relict TRSI series, (III) assess the temporal persistence, stability, and magnitude of age-related trends, and (IV) infer important insights into chronology development for future paleoclimatic work.

6.2 Material and methods

6.2.1 Study site and tree-ring data

Between 2011 and 2020, 751 core and disc samples of *Pinus heldreichii* were collected at 2000-2100 m asl on Mt. Smolikas (40.1°N/21.0°E), Pindus Mountains in northern Greece (**Fig. 6.1a**). Wood samples were processed according to standard dendrochronological techniques (Stokes & Smiley 1996). TRW was measured using the high-precision LINTAB 6 (Rinntech,

Heidelberg, Germany) and Velmex (Velmex, Bloomfield, NY, USA) devices, and MXD data was produced using the Walesch high-precision DENDRO2003 X-ray densitometer (Walesch Electronic, Effretikon, Switzerland). Pith offsets were estimated by visually matching the curvature of the innermost rings with a set of concentric circles on a template (details in Klippel et al. 2017). TRSI measurements were performed on a representative subset of the wood collection, including well-preserved samples from living and relict trees. Stable carbon isotope measurements were produced on methoxy groups and cellulose ($\delta^{13}\text{C}_m$ and $\delta^{13}\text{C}_c$), whereas stable oxygen isotopes were only measured from cellulose ($\delta^{18}\text{O}_c$) and stable hydrogen isotopes only from lignin methoxy groups ($\delta^2\text{H}_m$).

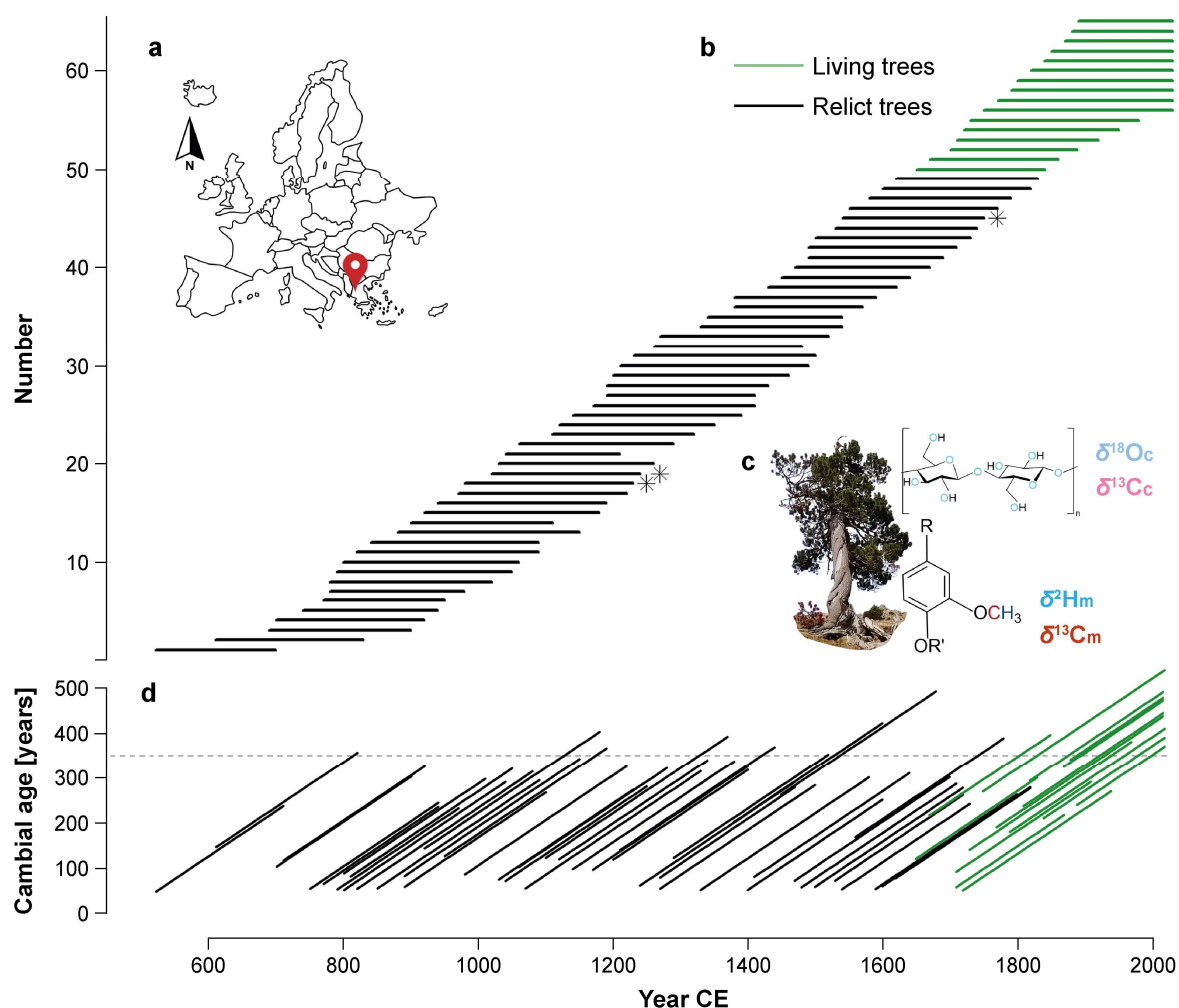


Fig. 6.1 Study site and proxy data. **(a)** Location of Mt. Smolikas in Europe. **(b)** Temporal distribution of the tree-ring stable isotope (TRSI) series. Asterisks denote series with only methoxy data. **(c)** *Pinus heldreichii* tree and schematic illustration of plant components used for TRSI measurement. **(d)** Cambial age of the individual tree-ring series.

The TRSI data of methoxy (cellulose) include 65 (62) samples from the same 49 (46) relict and 16 living trees (**Fig. 6.1b-c**, **Table 6.1**). The individual TRSI series range from 512 to 2020 CE, with a constant sample replication ≥ 10 series from 841 to 2020 CE. Please note the stepwise distribution of uniformly aged TRSI samples with different start and end dates throughout the

1st and 2nd millennium CE. Since isotopic measurements of methoxy groups prior to 1861 CE are decadal resolved, all other datasets, including annually resolved TRW, MXD, $\delta^{13}\text{C}_c$, and $\delta^{18}\text{O}_c$, were converted to the same resolution by averaging the annual values of each decade. Comparison of the annual (only available for cellulose TRSIs over the entire chronology period) and decadal $\delta^{13}\text{C}_c$ and $\delta^{18}\text{O}_c$ mean chronologies support the accuracy of this averaging procedure for the assessment of long-term trends (Fig. S6.1). The TRSI data were compared with previously established TRW and MXD records from Mt. Smolikas (Esper et al. 2020a, 2021), which were truncated to meet the temporal length of the isotope series.

Table 6.1 Proxy characteristics.

	TRW	MXD	$\delta^{13}\text{C}_c$	$\delta^{13}\text{C}_m$	$\delta^{18}\text{O}_c$	$\delta^2\text{H}_m$
No. series	751	192	62	65	62	65
No. living relict series	398 353	56 136	16 46	16 49	16 46	16 49
MSL (SD)	320 (150)	294 (160)	224 (30)	220 (31)	224 (30)	220 (31)
Mean living (SD)	0.76 (0.47)	0.70 (0.05)	-21.75 (0.68)	-25.65 (1.14)	33.00 (0.71)	-259.12 (9.80)
Mean relict (SD)	0.68 (0.45)	0.68 (0.06)	-21.43 (0.73)	-25.77 (1.19)	31.50 (1.51)	-252.60 (9.90)

No. series: total number of integrated series (divided into living and relict series in the 2nd row). **MSL:** mean segment length in years (± 1 standard deviation). **Mean:** arithmetic means of the living and relict TRW [mm], MXD [g/cm³], $\delta^{13}\text{C}_c$, $\delta^{18}\text{O}_c$, $\delta^{13}\text{C}_m$, $\delta^2\text{H}_m$ [mUr] series (\pm SD). The $\delta^{13}\text{C}$ data are corrected for the Suess effect.

6.2.2 Stable isotope measurements

The modified Zeisel method (Greule et al. 2008, 2009; Keppler et al. 2004, 2007) was used for the determination of $\delta^{13}\text{C}_m$ and $\delta^2\text{H}_m$ values. For 5 mg ($\delta^{13}\text{C}$) or 7 mg ($\delta^2\text{H}$) grounded or sliced wood material, 250 μl hydroiodic acid was added, and based on the reaction between methyl ethers and esters and hydroiodic acid, iodomethane was formed (Zeisel 1885). The samples were sealed with crimp caps in 1.5 ml crimp glass vials and heated for 30 minutes at 130°C, followed by sample equilibration at room temperature. Afterwards, for $\delta^{13}\text{C}_m$ ($\delta^2\text{H}_m$) measurements, an aliquot of headspace between 10 and 90 μl was injected into a gas chromatograph - combustion (thermo conversion) - isotope ratio mass spectrometer (GC-C(TC)-IRMS) via an autosampler (A200S, CTC Analytics, Zwingen, Switzerland). For $\delta^2\text{H}_m$ measurements, an HP 6890N (Agilent, Santa Clara, USA) and, for $\delta^{13}\text{C}_m$ measurements, a TraceGC (ThermoQuest Finnigan) were used. Both gas chromatographs were fitted with a DB-5ms, Agilent J&W capillary column (length 30 m, internal diameter 0.25 mm, film thickness 0.5 μm).

For $\delta^2\text{H}_m$ measurements, we used a 4:1 split injection and helium as carrier gas at a constant flow rate of 0.6 ml min⁻¹. A pyrolysis reactor (ceramic tube (Al₂O₃), length 320 mm, 0.5 mm i.d., reactor temperature 1450°C) converted CH₃I to molecular hydrogen (H₂). For $\delta^{13}\text{C}_m$

measurements, a 20:1 split injection and helium as carrier gas at a constant flow rate of 1.8 ml min⁻¹ was used. An oxidation reactor (ceramic tube (Al₂O₃), length 320 mm, internal diameter 0.5 mm) with Cu, Ni, and Pt wires inside (activated by oxygen), and a reaction temperature of 960°C, oxidized CH₃I to CO₂. Stable isotopes in the resulting CO₂ and H₂ gases were transferred through a GC-Combustion III interface (ThermoQuest Finnigan) into the IRMS (Delta-plusXL, ThermoQuest Finnigan). The samples were normalized against two HUBG reference materials, respectively. For $\delta^2\text{H}_m$ measurements, HUBG 1 and 3, and for $\delta^{13}\text{C}_m$ measurements, HUBG 2 and 4 were used (Greule et al. 2019, 2020).

For the determination of $\delta^{18}\text{O}_c$ and $\delta^{13}\text{C}_c$, the modified Jayme-Wise isolation method was used (Boettger et al. 2007). About 0.5 mm wide shredded wood samples were packed into Teflon filter bags and washed twice for 2 hours at 60°C with 5% NaOH solution, followed by an additional wash with 7% NaClO₂ solution for 30 hours at 60°C. To keep the pH between 4 and 5, acetic acid (99.8%) was added to the solution. Afterwards, the samples were dried at 50°C for 24 hours and locked in Eppendorf microtubes. For the isotope measurements, 0.5-1.0 mg of α -cellulose were placed into tin ($\delta^{13}\text{C}_c$) and silver ($\delta^{18}\text{O}_c$) capsules (Elementar Analysensysteme, Langenselbold, Germany). For $\delta^{18}\text{O}_c$ determination, the samples were pyrolyzed to CO₂ at 960°C in oxygen, and for $\delta^{13}\text{C}_c$ analyses, they were combusted to CO at 1450°C in an inert atmosphere (helium) using an elemental analyzer varioPYRO cube (Elementar Analysensysteme, Germany). The resulting CO₂ and CO gases were transferred by a continuous flow into the IRMS system (ISOPRIME 100, Manchester, UK). The isotope results were normalized using certified reference materials from the International Atomic Energy Agency (IAEA) and the United States Geological Survey (USGS). $\delta^{13}\text{C}_c$ values were referenced to caffeine (IAEA-600) and graphite (USGS24), and $\delta^{18}\text{O}_c$ values to benzoic acids (IAEA-601 and IAEA-602).

Prior to the measurements, the IRMS systems were centered, tuned, and tested for precision (ten pulses of monitoring gas) and linearity ($1\sigma < 0.4$ mUr and < 1 mUr/V for $\delta^2\text{H}_m$, < 0.02 mUr and < 0.04 mUr/nA for $\delta^{18}\text{O}_c$, 0.018 mUr and < 0.06 mUr/V for $\delta^{13}\text{C}_m$, < 0.03 mUr and 0.04 mUr/nA for $\delta^{13}\text{C}_c$). For $\delta^2\text{H}_m$ measurements, the H₃⁺ factor was quantified prior to each set of isotopic measurements (< 3.5 ppm/nA). Measurement accuracy was determined by analyzing six (cellulose) or five (methoxy groups) consecutive samples. Average standard deviation was 0.042 mUr for $\delta^{13}\text{C}_c$ (Römer et al. 2023), 0.089 mUr for $\delta^{18}\text{O}_c$, between 0.01 and 0.25 mUr for $\delta^{13}\text{C}_m$ (Greule et al. 2009), and 0.5 to 2 mUr for $\delta^2\text{H}_m$ (Greule et al. 2008).

6.2.3 Data treatment

The delta (δ) notation is used for all TRSI values. It is important to note that the commonly used 'unit' per mil (‰) is not considered acceptable in the International System of Units (SI), as the SI discourages the use of one-dimensional units (Newell & Tiesinga 2019), and ‰ is a

'quantity of dimension one', denoted by the symbol unit 1 in the SI (Brand & Coplen 2012; Dybkaer 2004). To address this issue and adhere to the principles of the SI, we use the term "Urey" (Ur; Urey 1948) as the unit for expressing δ values. One mUr is equivalent to ‰. $\delta^{18}\text{O}$, $\delta^2\text{H}$, and $\delta^{13}\text{C}$ values were calculated as deviations from the Vienna Standard Mean Ocean Water (VSMOW; $\delta^{18}\text{O}_c$ and $\delta^2\text{H}_m$) and the Vienna Pee Dee Belemnite (VPDB; $\delta^{13}\text{C}$).

$\delta^{13}\text{C}$ values after 1860 CE were corrected for the $\delta^{13}\text{C}_{\text{CO}_2}$ decline in the atmosphere, the so-called Suess effect (Keeling 1979). Since this negative trend is a non-climatic, CO_2 -driven effect, $\delta^{13}\text{C}$ values were corrected by adding the differences between $\delta^{13}\text{C}_{\text{CO}_2}$ and the pre-industrial value (-6.41 mUr) to the measured $\delta^{13}\text{C}$ values for each year (McCarroll & Loader 2004). Here, we used the $\delta^{13}\text{C}_{\text{CO}_2}$ series from McCarroll & Loader (2004) and the Mauna Loa Observatory (Keeling et al. 2005). Coherences between the individual isotope series were assessed by calculating mean inter-series correlations (R_{bar}) over the 512-2020 CE chronology period using the R package *dplR* (Bunn 2008).

6.2.4 Age-trend analysis

An essential criterion for age-trend assessments is the even distribution of tree rings across a wide range of calendar years, including rings grown under different climate conditions. In our study, we present decadal resolved TRSI data from 512 to 2020 CE characterized by a gradual distribution of samples over this extensive time span. The datasets consist of 46 (cellulose) and 49 (methoxy) relict and 16 living wood samples. TRSI series of relict wood start between 512 and 1611 CE, while for living wood start dates range from 1641-1881 CE. Hence, the relict wood TRSI series span over 1000 years, while the living-tree TRSI series cover the recent 350 years, including the significant climate and air composition changes since the mid-19th century. The average pith offset (PO) of the relict samples is 84 years, compared to 201 years for the living trees. This difference in mean PO estimates indicates that the TRSI values of living trees represent distinct older trees. When generating age-aligned TRSI series, tree ages above 350 years are therefore predominantly represented by living wood samples (**Fig. 6.1d**), which are strongly influenced by recent trend changes. To avoid the impact of the Suess effect and physiological response correction in the age-aligned $\delta^{13}\text{C}_m$ and $\delta^{13}\text{C}_c$ series, age-trend analyses for these proxies have been conducted using the relict wood only. The age-trend analysis in this study focuses primarily on long-term age-related trends over the tree's lifespan, rather than on juvenile effects that typically occur in the first few decades of growth. Hence, the first 50 years of cambial age were omitted, and with a sample replication of ≥ 10 series, the age range from 50 to 355 years is covered. Age-trend analyses of the cellulose TRSI series start at a cambial age of 54 years to meet this minimum sample replication criterion.

To classify age-related trends, the TRSI chronologies were compared with 353 TRW and 136 MXD relict wood series. Age trends in TRW, MXD, $\delta^{13}\text{C}_m$, $\delta^2\text{H}_m$, $\delta^{18}\text{O}_c$, and $\delta^{13}\text{C}_c$ were analyzed using the raw tree-ring data. For an accurate comparison among the proxies, all series were z-transformed before calculating mean chronologies. Individual series were aligned by cambial age considering the pith offset of each sample. Age trends were estimated using linear regressions fitted to the age-aligned series (**Fig. S6.2**) and the arithmetic mean of the z-transformed series. This procedure was performed considering different time intervals. We started the regression windows with variable lengths, always beginning at tree age 50. The endpoint, on the other hand, initially began at a tree age of 70 or 170 years and was subsequently shifted in 10-year intervals. Due to the calculation of z-scores, trends within individual series are preserved, but level offsets among the series are removed, leading to a potential underestimation of long-term trends across the series. To test whether the trend calculations are biased by the z-transformation, we additionally estimated age trends using TRSI anomalies derived from subtracting the mean of the common period (202-238 years) from each series. The significance of trends was calculated using the modified Mann-Kendall test (Hamed & Rao 1998), adapted for auto-correlated datasets.

6.3 Results

6.3.1 Data characteristics

Mean Rbar values of annual $\delta^{13}\text{C}_c$ and $\delta^{18}\text{O}_c$ are significant ($p < 0.001$) over the chronology period (512-2020 CE) with $r = 0.74$ and $r = 0.56$, respectively, pointing to a strong environmental forcing of the two cellulose isotopes. By transforming the data to decadal resolution, however, mean Rbar values decrease to 0.43 ($\delta^{13}\text{C}_c$) and 0.44 ($\delta^{18}\text{O}_c$) ($p < 0.05$). Rbar values of $\delta^{13}\text{C}_c$ and $\delta^{18}\text{O}_c$ calculated from 512 to 2020 CE are higher than those of the decadal resolved $\delta^{13}\text{C}_m$ and $\delta^2\text{H}_m$, with $r = 0.25$ and $r = 0.34$, respectively (**Table 6.2**).

The $\delta^{13}\text{C}_c$ and $\delta^{13}\text{C}_m$ values show a constantly decreasing trend from 512 to 1860 CE, followed by an increasing trend in $\delta^{13}\text{C}_m$ values and a decreasing trend in $\delta^{13}\text{C}_c$ values thereafter (**Fig. 6.2**). $\delta^{18}\text{O}_c$ and $\delta^2\text{H}_m$ display more variability over time, as both proxies show an early decreasing trend until ~750 CE, followed by relatively stagnant values until ~1000 CE. After 1500 CE, $\delta^{18}\text{O}_c$ values increase strongly at $0.004 \text{ mUr decade}^{-1}$, while $\delta^2\text{H}_m$ values decrease steadily at $-0.02 \text{ mUr decade}^{-1}$.

Table 6.2 Proxy covariance and age-trend estimates.

	Raw data					
	TRW	MXD	$\delta^{13}C_c$	$\delta^{13}C_m$	$\delta^{18}O_m$	δ^2H_m
Rbar annual (<i>p</i> -value)	0.55 (<i>< 0.001</i>)	0.55 (<i>< 0.001</i>)	0.74 (<i>< 0.001</i>)	–	0.56 (<i>< 0.001</i>)	–
Rbar decadal (<i>p</i> -value)	0.43 (0.03)	0.27 (0.13)	0.43 (0.04)	0.25 (0.20)	0.44 (0.04)	0.34 (0.11)
Trend decade ⁻¹ for 1820-2020	+0.0012	+3.68 × 10 ⁻⁵	-0.00086	+0.0097	+0.003	-0.055
	Age-aligned normalized data					
Age trend for 50-350 CA	-0.0042	-0.0021	-0.0009	-0.0022	-0.0005	+0.0031
Age trend (subset period)	-0.02 (50-70)	+0.012 (50-70)	+0.027 (50-80)	-0.003 (100-350)	-0.0074 (50-120)	+0.004 (100-350)

Rbar: mean inter-series correlations at annual and decadal resolution. **Trend decade⁻¹**: decadal trends in the TRW [mm], MXD [g/cm³], $\delta^{13}C_c$, $\delta^{18}O_c$, $\delta^{13}C_m$, δ^2H_m [mUr] chronologies calculated for 1820-2020 CE. **Age trend for 50-350 CA**: trends in the age-aligned data calculated from 50-350 years of cambial age. **Age trend (subset period)**: strongest trends in the age-aligned proxy data. Numbers in brackets indicate the subset period.

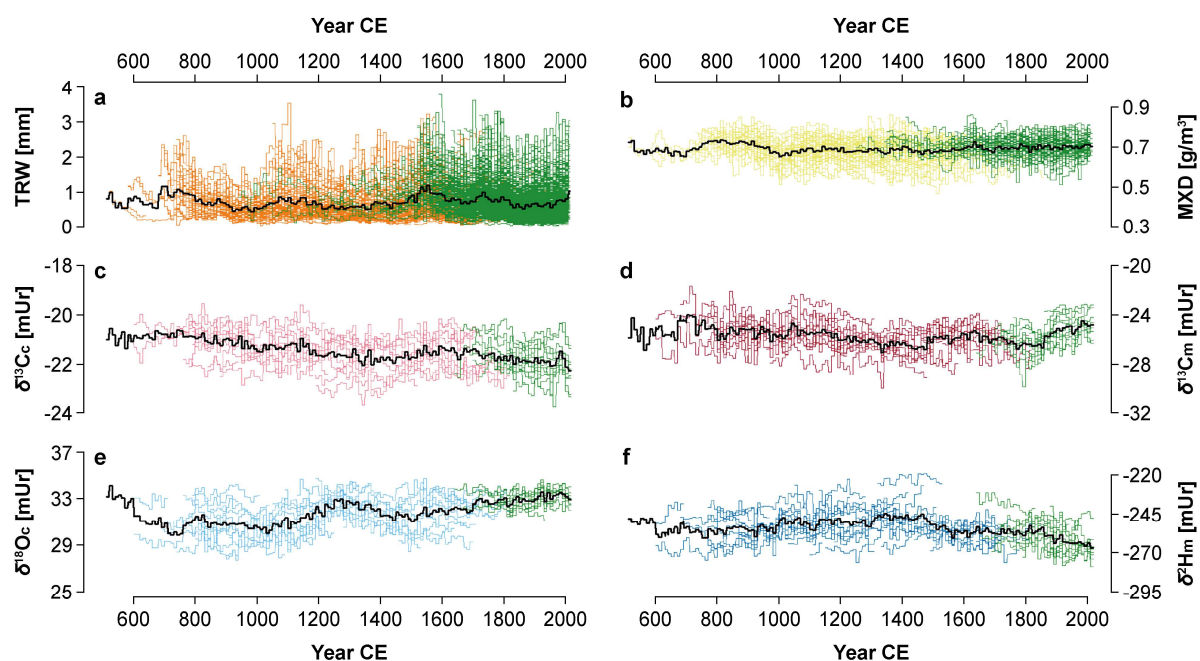


Fig. 6.2 Decadally resolved (a) TRW, (b) MXD, (c) $\delta^{13}C_c$, (d) $\delta^{13}C_m$, (e) $\delta^{18}O_c$, and (f) δ^2H_m series from 512 to 2020 CE. Green curves are measurements from living trees and colored series from relict wood. Black curves are the mean chronologies.

To assess the variability of the TRSI data and discern the influence of environmental changes or other factors, we calculated and compared the ranges of living and relict wood values for all proxies (**Fig. 6.3**). While there are almost no differences between the living and relict wood of TRW, MXD, $\delta^{13}C_c$, and $\delta^{13}C_m$ ($\Delta_{liv/rel}$: mean difference between values of living and relict wood calculated across all series and calendar years), the $\delta^{18}O_c$ values of living trees are +1.49 mUr higher than those of the relict wood. In contrast, the living-tree δ^2H_m values are -6.57 mUr lower

than their relict wood counterparts. Variance of living and relict wood is similar in TRW, MXD, $\delta^{13}\text{C}_c$, $\delta^{13}\text{C}_m$, and $\delta^2\text{H}_m$, except for $\delta^{18}\text{O}_c$ showing increased interquartile ranges in relict wood (2.4) compared to the living wood (1.1). Comparable level offsets in $\delta^{18}\text{O}_c$ between living and relict wood are also seen when considering the common period from 1641-1820 CE, whereas offsets in $\delta^2\text{H}_m$ values are no longer visible (**Fig. S6.3**).

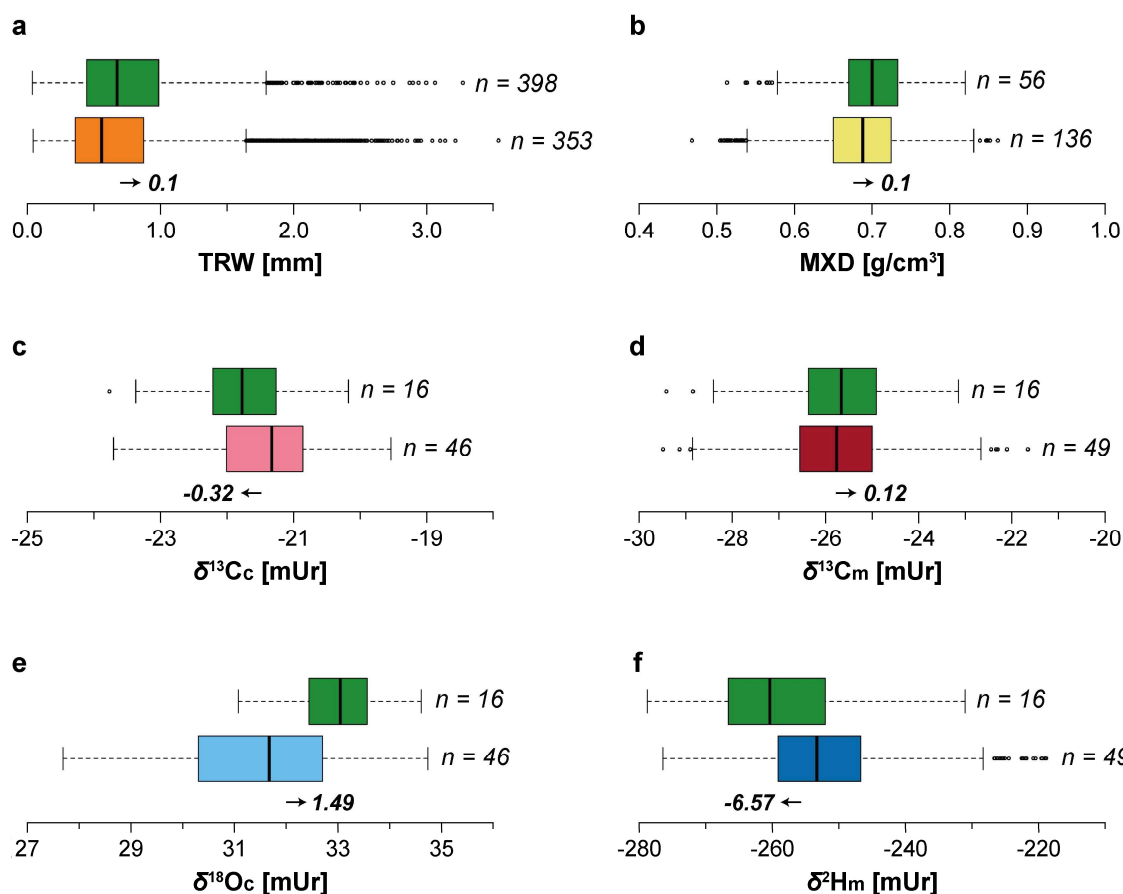


Fig. 6.3 Distribution and range of (a) TRW, (b) MXD, (c) $\delta^{13}\text{C}_c$, (d) $\delta^{13}\text{C}_m$, (e) $\delta^{18}\text{O}_c$, and (f) $\delta^2\text{H}_m$ values. Green boxes correspond to living trees, while other colors represent the proxy-specific relict wood (same color code as in Fig. 6.2). Vertical black lines are the median (50th percentile), boxes the 25th and 75th percentiles, whiskers the 95% confidence interval, and points denote outliers. Numbers next to the arrows indicate the offsets between living and relict means ($\Delta_{\text{liv/rel}}$). Numbers next to the boxplots indicate the sample replication.

Fig. 6.4 shows the mean intra-series standard deviation (SD of the individual series), the mean inter-series SD (SD among the series in each decade), and the $\Delta_{\text{liv/rel}}$. Intra-series SD is smaller than inter-series SD for all six proxies. Intra- and inter-series SD of methoxy TRSIs are higher compared to those of the cellulose TRSIs. Comparison between intra- and inter-series SD and $\Delta_{\text{liv/rel}}$ shows that $\Delta_{\text{liv/rel}}$ values in TRW, MXD, and $\delta^{13}\text{C}_m$ are negligible compared to the intra- and inter-series SD. $\Delta_{\text{liv/rel}}$ in $\delta^{13}\text{C}_c$ reaches similar amounts as the intra-series variation, indicating that the signal in the $\delta^{13}\text{C}_c$ series is as high as the mean offset between living and relict wood values. $\Delta_{\text{liv/rel}}$ in $\delta^{18}\text{O}_c$ and $\delta^2\text{H}_m$ values are even more pronounced, as the $\Delta_{\text{liv/rel}}$ of $\delta^{18}\text{O}_c$

exceeds the intra- and inter-series SD, and the $\Delta_{\text{liv/rel}}$ of $\delta^2\text{H}_m$ is considerably higher than the intra-series SD.

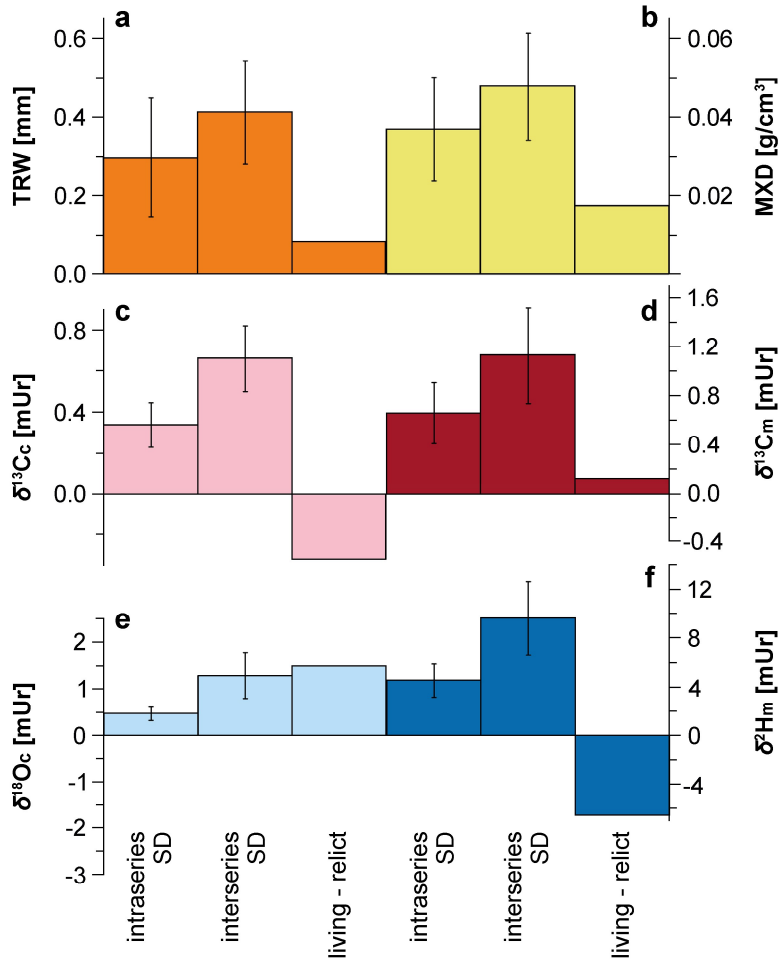


Fig. 6.4 Intra-series standard deviation (mean SD within individual series), inter-series standard deviation (mean SD between all series in a certain decade), and mean offset between living and relict wood ($\Delta_{\text{liv/rel}}$) calculated for (a) TRW, (b) MXD, (c) $\delta^{13}\text{C}_c$, (d) $\delta^{13}\text{C}_m$, (e) $\delta^{18}\text{O}_c$, and (f) $\delta^2\text{H}_m$.

6.3.2 Age-trend observations

The age-aligned raw and z-transformed TRW and MXD series show clear ontogenetic trends (**Fig. 6.5**). Similar to an exponential curve, the decline in TRW is more pronounced in early years compared to later stages. As a result, mean TRW in year 350 is less than half of that in year 50. In contrast, the MXD series show a slight increase between 50 and 70 years of cambial age, followed by a persistent negative trend thereafter. The $\delta^{13}\text{C}_c$ series show an initial increasing trend between 50 and 80 years, whereas the $\delta^{18}\text{O}_c$ series show a decreasing trend until a tree age of 190 years. Thereafter, neither the $\delta^{13}\text{C}_c$ nor the $\delta^{18}\text{O}_c$ series show any trend. In contrast, the $\delta^2\text{H}_m$ series show decreasing values between 50 and 70 years of cambial age, and the $\delta^{13}\text{C}_m$ series show short-term increasing trends between 90 and 100 years. Both $\delta^{13}\text{C}_m$ and $\delta^2\text{H}_m$ series exhibit further trends, especially after 200 years of tree age.

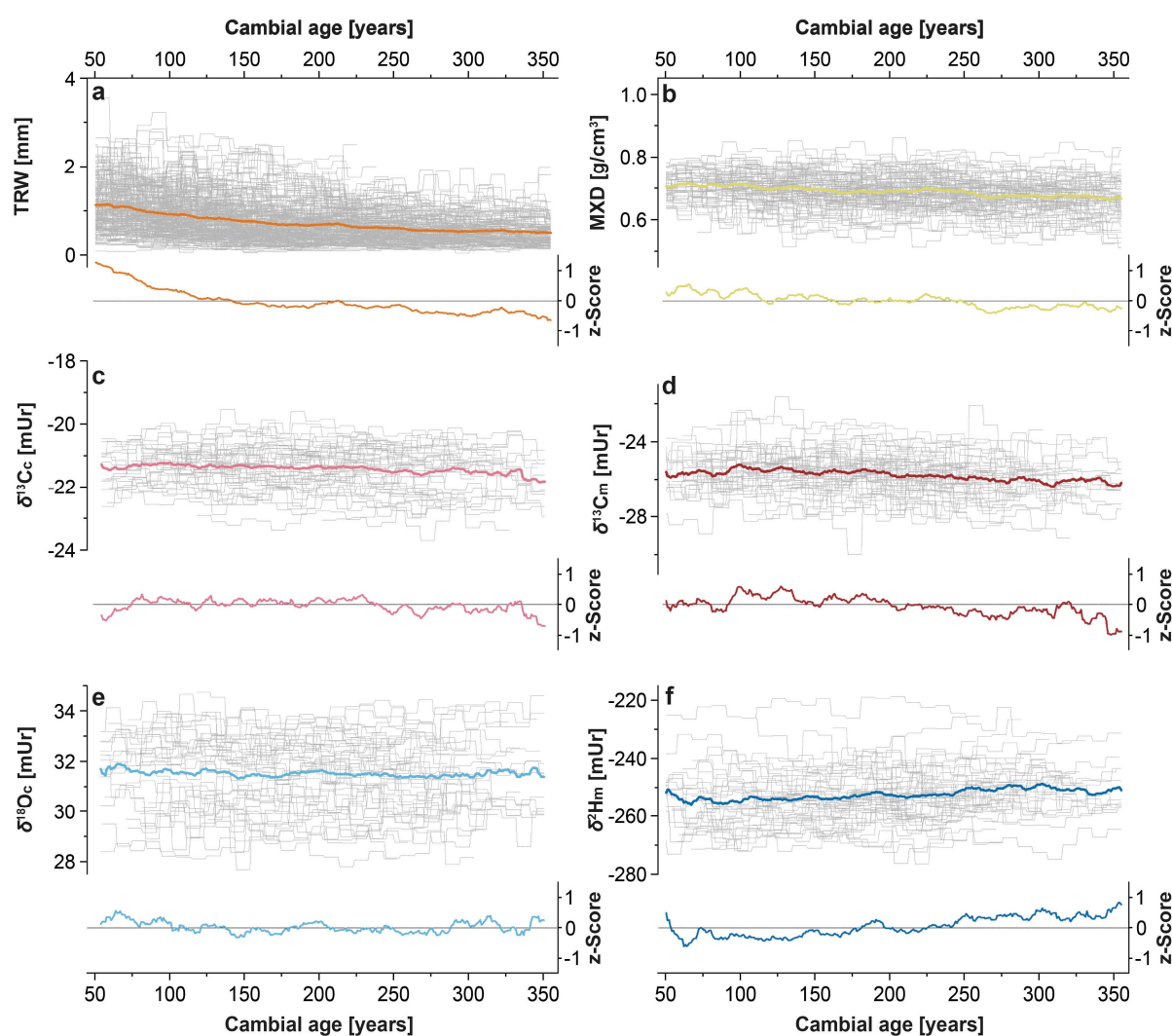


Fig. 6.5 Age-aligned (a) TRW, (b) MXD, (c) $\delta^{13}C_c$, (d) $\delta^{13}C_m$, (e) $\delta^{18}O_c$, and (f) δ^2H_m relict wood series. Top panels show the raw series (grey curves) and their arithmetic means (colored curves). Lower panels show the means of the normalized data.

A detailed slope examination of the z-transformed data (**Fig. 6.6**) verifies the trend observations in the raw data. TRW shows a consistent and significant ($p < 0.01$) decreasing trend over 50-350 years of cambial age at a rate of $-0.004 \text{ mm decade}^{-1}$. On the other hand, MXD shows an initial increasing trend between 50 and 70 years, but this trend reverses and becomes significantly ($p < 0.01$) negative after 50-120 years. The initial positive trend in $\delta^{13}C_c$ ($p < 0.01$ up to 50-100 years) is related to comparatively low $\delta^{13}C_c$ values at young tree ages (50-80 years), as no significant trend is found after an age of 100 years (**Fig. S6.4, S6.5**). The initial decrease in $\delta^{18}O_c$ values is significant between 50 and 190 years ($p < 0.01$, maximum slope from 50 to 120 years at $-0.007 \text{ mUr decade}^{-1}$). For $\delta^{13}C_m$, an increasing trend is found from 50-120 to 50-140 years ($p < 0.01$). However, significant negative $\delta^{13}C_m$ trends of $-0.002 \text{ mUr decade}^{-1}$ are observed from 50 to 290 years. For δ^2H_m , initially decreasing values at $-0.04 \text{ mUr decade}^{-1}$ are recorded at young ages (between 50 and 70 years), followed by significantly increasing values from 50 to 210 years ($p < 0.01$).

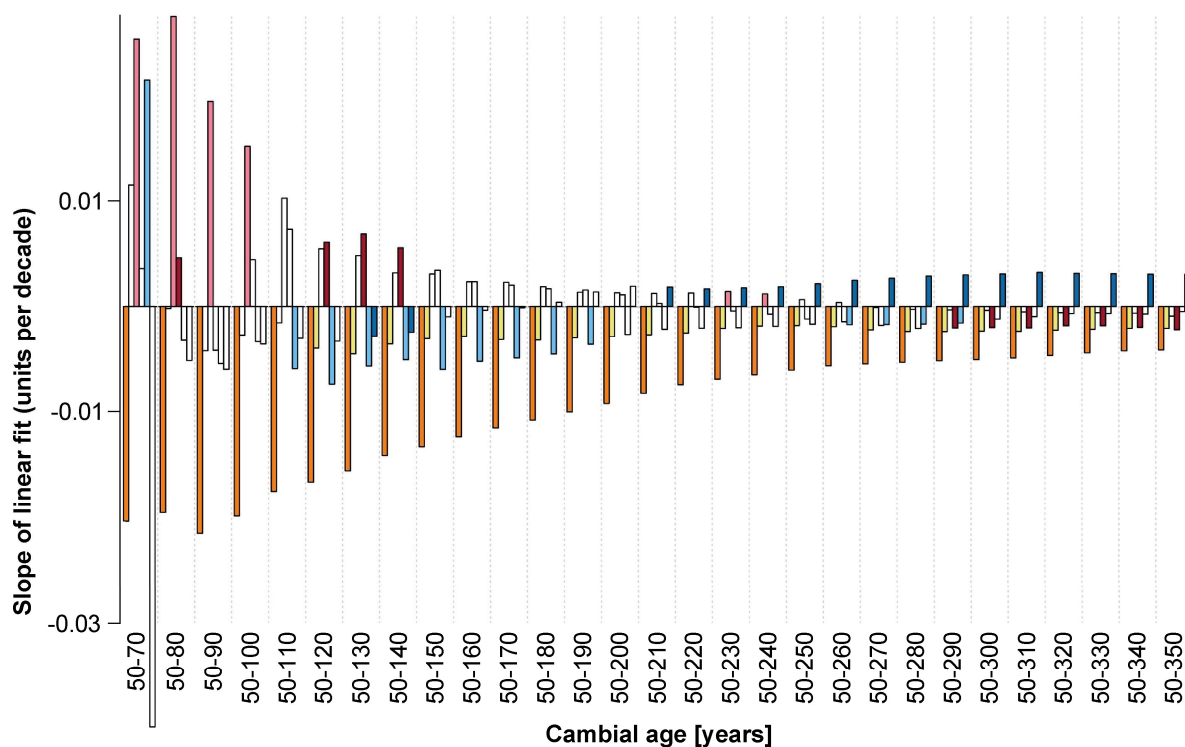


Fig. 6.6 Linear slopes of the mean z-transformed TRW (orange), MXD (yellow), $\delta^{13}C_c$ (light red), $\delta^{13}C_m$ (dark red), $\delta^{18}O_c$ (light blue), and δ^2H_m (dark blue) series. White bars represent non-significant ($p > 0.01$) and colored bars significant slopes at $p < 0.01$.

Trend analyses of the mean relative chronologies (**Fig. S6.6**) support these findings and reveal significant ($p > 0.01$) positive trends in $\delta^{13}C_c$ between 50-100 years, as well as significant negative trends in $\delta^{13}C_m$ and significant positive trends in δ^2H_m over the last third and the second half of the age-aligned data, respectively. However, trend analyses reveal significant slopes in $\delta^{13}C_m$ and δ^2H_m to start earlier, from 50 to 270 years and from 50 to 200 years, respectively, compared to the z-transformed series. These differences, as well as the varying initial trends in $\delta^{18}O_c$ and δ^2H_m series, are considered in the following discussion.

6.4 Discussion

6.4.1 Inter- and intra-proxy differences

The notable variations in stable carbon isotope values of cellulose, ranging from -22.2 to -20.9 mUr, and methoxy groups, ranging from -26.6 to -24.9 mUr, originate from different physiological processes that lead to considerable fractionation differences during the formation of the two plant components. While lignin methoxy groups are depleted of ^{13}C by ~ 4 mUr compared to cellulose, the $\delta^{13}C$ values of cellulose and lignin methoxy groups vary within the same range, with 1.3 mUr for $\delta^{13}C_c$ and 1.7 mUr for $\delta^{13}C_m$. Therefore, by combining different plant components from the same trees, it is possible to gain a deeper insight into the varying biochemical formation processes. In addition, the combination of different climate proxies, deliberately chosen for their dissimilarity, offers the potential to increase climate signal strength and the range

of extractable climate information. The high R_{bar} values between 512-2020 CE, especially in $\delta^{13}C_c$ ($r = 0.74$) and $\delta^{18}O_c$ ($r = 0.56$), are in line with previous observations from the Mediterranean (Konter et al. 2014; Lukač et al. 2021; Römer et al. 2023) and support the importance of climate drivers on interannual to decadal TRSI variability.

In this study we found discrepancies between the TRSI chronologies of cellulose and methoxy groups, particularly during the most recent 200 years CE, where contrasting long-term trends in the carbon, oxygen, and hydrogen values of the two plant components are observed. Differences among TRSI data may be attributed to several factors. One plausible explanation is that the isotopic signature of the plant components is affected by varying environmental determinants, likely climatic factors such as temperature, drought, or precipitation. An alternative explanation is that the proxies may capture the same climate signal, but the seasonality of this signal varies due to temporal differences in the biosynthetic formation of these compounds. It is also possible that a mixture of factors collectively contributes to the observed variations. A previous study, comparing the isotopic composition of cellulose and lignin methoxy groups in *Pinus sylvestris* from central Germany, found that $\delta^{13}C_c$ values are more sensitive to climatic variables of the entire growing season (March to October), while $\delta^{13}C_m$ values are more sensitive to climatic conditions at the beginning of the growing season (Mischel et al. 2015). Similar observations have been made for $\delta^{18}O_c$ and δ^2H_m . While $\delta^{18}O_c$ was described to be primarily related to maximum air temperatures from March-October, δ^2H_m revealed significant ($p < 0.01$) correlations with maximum air temperatures from March-May (Mischel et al. 2015).

The observed level offsets between living and relict δ^2H_m values over the full chronology period (512-2020 CE), and the absence of similar offsets over the common period of living and relict wood (1641-1820 CE), show that $\Delta_{liv/rel}$ is mainly influenced by the strong negative trend inherent in the last 200 years of the chronology, which may reflect a significant change in environmental conditions. In contrast, the $\Delta_{liv/rel}$ of the $\delta^{18}O_c$ series seems to be influenced by a factor other than recent environmental change, as we find an offset between living and relict $\delta^{18}O_c$ values over the entire chronology period as well as over the common period of living and relict wood. In addition to the isotopically lighter relict wood, strong level differences are observed in the relict wood series, with relict $\delta^{18}O_c$ values covering a distinctly wider range than the living $\delta^{18}O_c$ values. The $\Delta_{liv/rel}$ of the $\delta^{18}O_c$ data is of practical importance, as it exceeds the intra- and inter-series SD and is thus higher than the common isotope signal preserved in the chronology. The wider distribution of relict $\delta^{18}O_c$ values could be related to cellulose decomposition associated with exchange processes with the surrounding water. Water exchange in $\delta^{18}O_c$ but stable δ^2H_m values could be explained by the fact that the lignin content in trees is more resistant to degradation than cellulose. Anhäuser et al. (2015) detailed losses of cellulose and lignin in foliar litter over a 27-month period for four different tree species. While three of the four species

showed minor lignin losses up to 0.4%, all species revealed large cellulose decreases ranging from 50.7% to 86.1%. Although, the process of litter decomposition on a forest floor cannot be directly equated with the conditions observed at Mt. Smolikas, where climatic factors contribute to a slow rate of wood decomposition, the study by Anhäuser et al. (2015) shows that cellulose decomposition is accelerated compared to lignin decomposition.

A second and more likely explanation for the high level differences in relict $\delta^{18}\text{O}_c$ values is the influence of the sampled tree height. While living tree cores were always taken at breast height ~ 1.3 m above the ground, the disc samples of relict wood are from unknown tree heights due to centuries of decomposition (**Fig. S6.7**). Gaglioti et al. (2017) documented isotopically lighter $\delta^{18}\text{O}_c$ values with increasing trunk height, and if the relict stems in this study are affected by a similar trend, the samples seem to represent mainly material from higher tree heights. In addition to the negative $\Delta_{\text{liv/rel}}$ value, this would also explain the wider data distribution of the relict wood, as the series represent samples from diverse heights. Esper et al. (2020b) documented systematic changes in $\delta^{13}\text{C}_c$ with stem height and sharply increasing values toward the crown. The $\delta^{13}\text{C}$ values in this study, however, appear to be unaffected by this tree-height bias, as none of the two $\delta^{13}\text{C}$ chronologies shows substantially higher $\Delta_{\text{liv/rel}}$ values or strong differences in the data distribution of relict logs and living trees. Possible explanations for stem-longitudinal $\delta^{13}\text{C}$ shifts include microclimatic changes and/or CO_2 stratification with tree height (Ehleringer et al. 1986; Esper et al. 2020b; Francey et al. 1985; Vogel 1978). However, the trees used in this study grow in a rather open forest, and microclimatic differences and CO_2 stratification with tree height appear unlikely. Future studies should incorporate multiple stem-height measurements to assess this source of uncertainty.

6.4.2 Age trends in TRSI series

The gradual distribution of relict wood series and the multi-proxy approach of this study provide important insights into age-dependent trends in *Pinus heldreichii* tree-ring proxies. The trees used grew over several centuries, from 512 to 1820 CE, including both warm and cold periods (Esper et al. 2020a), and climatic signals in the age-aligned series should therefore be leveled out (Esper et al. 2003). Our results demonstrate distinct age trends in the traditional growth parameters, including a decrease of -0.004 mm decade⁻¹ in TRW and -0.002 g cm⁻³ decade⁻¹ in MXD between 50 and 350 years of cambial age (Bräker 1981).

Age-related trends are also apparent in all TRSI chronologies. We found initial short-term age-related trends in $\delta^{13}\text{C}_c$ and $\delta^2\text{H}_m$, decreasing trends in $\delta^{18}\text{O}_c$ until a tree age of 190 years, and significant negative and positive trends in $\delta^{13}\text{C}_m$ and $\delta^2\text{H}_m$ from 50 to 290 and 50 to 210 years, respectively. Most of the age trends in TRSI were of lesser magnitude than TRW and of shorter duration than MXD. While $\delta^{13}\text{C}_c$ values clearly increase between 50-80 years of cambial age,

no significant age-related trends are recorded thereafter. Compared to the age trends in TRW, the juvenile $\delta^{13}\text{C}_c$ trends are of comparable magnitude. Several $\delta^{13}\text{C}$ studies have documented this juvenile $\delta^{13}\text{C}$ trend during the first decades of cambial age (Esper et al. 2010, 2018; Konter et al. 2015; McCarroll & Pawellek 2001; Torbenson et al. 2022; Treydte et al. 2001). The initially increasing $\delta^{13}\text{C}_c$ values could therefore be classified as a juvenile effect, which appears to be extended (up to 80 years) in relation to the high tree ages of *Pinus heldreichii* at Mt. Smolikas (Konter et al. 2017). Common explanations for such juvenile effect in the early years of growth include shading of smaller trees and depleted CO_2 respiration from the forest floor (Francey & Farquhar 1982; van der Merwe & Medina 1991). These explanations, however, are unlikely to account for the juvenile trends in our $\delta^{13}\text{C}_c$ series, as these trees grow at high altitudes with an open canopy and almost permanent air mixing due to ever present wind. An alternative explanation refers to changes in hydraulic conductivity affecting stomatal conductance, which in turn affects carbon isotope values (McCarroll & Loader 2004). With increasing tree height, soil-to-leaf hydraulic conductivity decreases, coupled with a reduction in stomatal conductance, which would lead to increasing $\delta^{13}\text{C}$ values until tree growth ceases (Esper et al. 2010; McDowell et al. 2002). Tree growth may not be completed after 80 years, but the observed increasing $\delta^{13}\text{C}_c$ values may coincide with periods of greatest height growth.

In contrast, $\delta^2\text{H}_m$ values show an initially decreasing trend until an age of 70 years, from -251 to -255 mUr or $-0.16 \text{ mUr decade}^{-1}$ ($p < 0.01$), followed by a smaller increasing trend starting at 100 years from -254 mUr to -251 mUr. Our study is the first to analyze long-term age trends in TRSIs of wood lignin methoxy groups, and there are no comparable methoxy-based results yet. Arosio et al. (2020) documented age-related trends in *Larix decidua* $\delta^2\text{H}_c$ with a decreasing trend of $\sim 7 \text{ mUr}$ in the first 50 years, followed by an increasing trend of $\sim 2.5 \text{ mUr}$ over the remaining tree ages up to 480 years. These findings are consistent with our observations. A possible explanation for juvenile $\delta^2\text{H}_m$ trends could be that the shallow root systems of younger trees access different water sources than the deeply rooted older trees. In particular, soil water has often been characterized by an enrichment in ^2H from the deep to the shallow soil layers due to evaporation processes and the loss of isotopically lighter water molecules (Allison et al. 1983; Lin & Sternberg 1993). The $\delta^{13}\text{C}_m$ chronology shows a steep increase at a cambial age of ~ 100 years, followed by a constant decline, resulting in long-term trends of $-0.002 \text{ mUr decade}^{-1}$ (50-350 years) and $-0.003 \text{ mUr decade}^{-1}$ (100-350 years). These trends are comparable in magnitude to the age-related trends in MXD.

The $\delta^{18}\text{O}_c$ values show a negative trend at the beginning, which is significant between 50 and 190 years of cambial age. This negative trend is not solely attributed to the relatively high $\delta^{18}\text{O}_c$ values in younger tree ages (between 50-80 years), as significant ($p < 0.01$) negative trends are also observed when analyzing cambial ages ranging from 100 to 170 and 100 to 180 years.

Changes in hydraulic conductivity with plant age could explain the juvenile trends in $\delta^{13}\text{C}_c$, but not the decreasing trends in $\delta^{18}\text{O}_c$, as reduced stomatal conductance would lead to higher $\delta^{18}\text{O}$ values (Barbour et al. 2004). However, similar to the initial negative trend in $\delta^2\text{H}_m$, a change in the root system from shallower to deeper soils could also affect $\delta^{18}\text{O}_c$. Positive trends in $\delta^2\text{H}$ and negative trends in $\delta^{18}\text{O}$ of cellulose were also observed by Nakatsuka et al. (2020), while negative trends in $\delta^{18}\text{O}_c$ were documented by Esper et al. (2010) and Treydte et al. (2006).

With the exception of juvenile trends in $\delta^{13}\text{C}_c$ and $\delta^2\text{H}_m$, none of the observed long-term trends in TRSIs are comparable to the age trends in TRW. However, long-term trends in $\delta^{13}\text{C}_m$ and $\delta^2\text{H}_m$ are similar or even higher than the observed age trends in MXD. Juvenile effects in $\delta^{13}\text{C}_c$ and $\delta^2\text{H}_m$ should be considered when using the Mt. Smolikas TRSI data for climate reconstruction. $\delta^{18}\text{O}_c$, $\delta^{13}\text{C}_m$, and $\delta^2\text{H}_m$ series must be detrended for proper climate signal determination, whereas no standardization is required for $\delta^{13}\text{C}_c$. The current literature does not show a common pattern of long-term age-related trends in TRSI measurements. While some studies found age-related trends during the juvenile period in $\delta^{13}\text{C}_c$ of pines from the Swiss Alps (*Pinus cembra*; Arosio et al. 2020) and northern Finland (*Pinus sylvestris*; Gagen et al. 2008), others found age-related trends throughout the trees' lifespans in pines from the Spanish Pyrenees (*Pinus uncinata*; Esper et al. 2010), northern Scandinavia (*Pinus sylvestris*; Torbenson et al. 2022), and Lapland (*Pinus sylvestris*; Helama et al. 2015). However, there are also studies that found no evidence for age-related trends in oaks from the Czech Republic (Büntgen et al. 2020) and larches from the UK (Kilroy et al. 2016). A similar inhomogeneous pattern can be observed for $\delta^{18}\text{O}_c$, with significant age trends reported in pines (*Pinus uncinata*) from the Spanish Pyrenees (Esper et al. 2010), and the absence of such trends in pines from northern Scandinavia (*Pinus sylvestris*; Torbenson et al. 2022) and oaks from the Czech Republic (Büntgen et al. 2020), as well as after 100 years of tree age in pines from the Swiss Alps (*Pinus cembra*; Arosio et al. 2020). These contrasting observations could be related to the use of different tree species from different environments, but could also be due to different methodological approaches, such as measurements on different ring components (whole-ring vs. latewood), pooling procedures, or data pruning. Therefore, age dependencies must be tested in each isotopic dataset before TRSI measurements can be used for climate reconstructions.

6.5 Conclusion

In this study, we analyze isotope data from two different plant components, cellulose and lignin methoxy groups, to investigate biochemical fractionation differences and age trends. We compare stable carbon, oxygen, and hydrogen isotope ratios and observe significant temporal variations between cellulose and lignin methoxy groups, particularly over the past two centuries.

Our findings suggest that different environmental factors control decadal variability and long-term trends of the two plant components.

While age dependencies in TRW and MXD are well-known and widely accepted in dendrochronological literature, the existence of age-related trends in TRSIs is still strongly debated. Notably, no previous research has examined age dependencies in stable isotopes of methoxy groups. Our analysis of cellulose and methoxy TRSI data reveals initially increasing age trends in $\delta^{13}\text{C}_c$ and decreasing trends in $\delta^2\text{H}_m$, indicating the presence of extended juvenile effects in both proxies. $\delta^{18}\text{O}_c$ series show significantly decreasing trends over the first 190 years of cambial age, whereas $\delta^{13}\text{C}_m$ and $\delta^2\text{H}_m$ series indicate decreasing and increasing trends starting at tree ages of ~100 years, respectively. Hence, $\delta^{18}\text{O}_c$, $\delta^{13}\text{C}_m$, and $\delta^2\text{H}_m$ series require detrending prior to climate reconstruction, whereas $\delta^{13}\text{C}_c$ data may be used in paleoclimate analyses without detrending and therefore offer the unique potential to preserve low-frequency climate variability throughout the last two millennia CE. So far, the mechanisms behind age-related trends in TRSIs are not fully understood and the findings of this study highlight the complexity of age trends in TRSI data. It is therefore still important to test each site and tree species before using TRSI data for climate reconstructions.

6.6 Acknowledgements

Not available online.

6.7 References

- Allison GB, Barnes CJ, Hughes MW (1983) The distribution of deuterium and ^{18}O in dry soils. *J Hydrol* 64: 377-397.
- Anhäuser T, Greule M, Polag D, Bowen GJ, Keppler F (2017) Mean annual temperatures of mid-latitude regions derived from $\delta^2\text{H}$ values of wood lignin methoxyl groups and its implications for paleoclimate studies. *Sci Total Environ* 574: 1276-1282.
- Anhäuser T, Greule M, Zech M, Kalbitz K, McRoberts C, Keppler F (2015) Stable hydrogen and carbon isotope ratios of methoxyl groups during plant litter degradation. *Isot Environ Health Stud* 51: 143-154.

- Arosio T, Ziehmer MM, Nicolussi K, Schlüchter C, Leuenberger M (2020) Alpine Holocene tree-ring dataset: age-related trends in the stable isotopes of cellulose show species-specific patterns. *Biogeosciences* 17: 4871-4882.
- Barbour MM, Roden JS, Farquhar GD, Ehleringer JR (2004) Expressing leaf water and cellulose oxygen isotope ratios as enrichment above source water reveals evidence of a Péclet effect. *Oecologia* 138: 426-435.
- Boettger T, Haupt M, Knöllner K, Weise SM, Waterhouse JS, Rinne KT, Loader NJ, Sonninen E, Jungner H, Masson-Delmotte V, et al. (2007) Wood cellulose preparation methods and mass spectrometric analyses of $\delta^{13}\text{C}$, $\delta^{18}\text{O}$, and nonexchangeable $\delta^2\text{H}$ values in cellulose, sugar, and starch: an interlaboratory comparison. *Anal Chem* 79: 4603-4612.
- Borella S, Leuenberger M, Saurer M (1999) Analysis of $\delta^{18}\text{O}$ in tree rings: wood-cellulose comparison and method dependent sensitivity. *J Geophys Res Atmos* 104: 19267-19273.
- Bräker OU (1981) Der Alterstrend bei Jahrringdichten und Jahrringbreiten von Nadelhölzern und sein Ausgleich. *Mitteilungen der forstlichen Bundes-Versuchsanstalt Wien* 142: 75-102.
- Brand WA, Coplen TB (2012) Stable isotope deltas: tiny, yet robust signatures in nature. *Isot Environ Health Stud* 48: 393-409.
- Briffa KR, Jones PD, Bartholin TS, Eckstein D, Schweingruber FH, Karlén W, Zetterberg P, Eronen M (1992) Fennoscandian summers from AD 500: temperature changes on short and long timescales. *Clim Dyn* 7: 111-119.
- Bunn AG (2008) A dendrochronology program library in R (dplR). *Dendrochronologia* 26: 115-124.
- Büntgen U, Kolář T, Rybníček M, Koňasová E, Trnka M, Ač A, Krusic PJ, Esper J, Treydte K, Reinig F, et al. (2020) No age trends in stable isotopes. *Paleoceanogr Paleoclimatol* 35: e2019PA003831.
- Büntgen U, Urban O, Krusic PJ, Rybníček M, Kolář T, Kyncl T, Ač A, Koňasová E, Čáslavský J, Esper J, et al. (2021) Recent European drought extremes beyond Common Era background variability. *Nat Geosci* 14: 190-196.
- Cook ER, Briffa KR, Meko DM, Graybill DA, Funkhouser G (1995) The 'segment length curse' in long tree-ring chronology development for palaeoclimatic studies. *Holocene* 5: 229-237.
- Daux V, Michelot-Antalik A, Lavergne A, Pierre M, Stievenard M, Bréda N, Damesin C (2018) Comparisons of the performance of $\delta^{13}\text{C}$ and $\delta^{18}\text{O}$ of *Fagus sylvatica*, *Pinus sylvestris*, and *Quercus petraea* in the record of past climate variations. *J Geophys Res Biogeosciences* 123: 1145-1160.

- Duffy JE, McCarroll D, Loader NJ, Young GHF, Davies D, Miles D, Bronk Ramsey C (2019) Absence of age-related trends in stable oxygen isotope ratios from oak tree rings. *Glob Biogeochem Cycles* 33: 841-848.
- Duquesnay A, Bréda N, Stievenard M, Dupouey JL (1998) Changes of tree-ring $\delta^{13}\text{C}$ and water-use efficiency of beech (*Fagus sylvatica* L.) in north-eastern France during the past century. *Plant Cell Environ* 21: 565-572.
- Dybkaer R (2004) Units for quantities of dimension one. *Metrologia* 41: 69-73.
- Ehleringer JR, Field CB, Lin Z, Kuo C (1986) Leaf carbon isotope and mineral composition in subtropical plants along an irradiance cline. *Oecologia* 70: 520-526.
- Esper J, Cook ER, Krusic PJ, Peters K, Schweingruber F (2003) Tests of the RCS method for preserving low-frequency variability in long tree-ring chronologies. *Tree-Ring Res* 70: 81-98.
- Esper J, Frank DC, Battipaglia G, Büntgen U, Holert C, Treydte K, Siegwolf R, Saurer M (2010) Low-frequency noise in $\delta^{13}\text{C}$ and $\delta^{18}\text{O}$ tree ring data: a case study of *Pinus uncinata* in the Spanish Pyrenees. *Glob Biogeochem Cycles* 24: 1-11.
- Esper J, Frank DC, Wilson R (2004) Climate reconstructions: low-frequency ambition and high-frequency ratification. *Eos* 85: 113-120.
- Esper J, Holzkämper S, Büntgen U, Schöne BR, Keppler F, Hartl C, St George S, Riechelmann DFC, Treydte K (2018) Site-specific climatic signals in stable isotope records from Swedish pine forests. *Trees* 32: 855-869.
- Esper J, Klippel L, Krusic PJ, Konter O, Raible CC, Xoplaki E, Luterbacher J, Büntgen U (2020a) Eastern Mediterranean summer temperatures since 730 CE from Mt. Smolikas tree-ring densities. *Clim Dyn* 54: 1367-1382.
- Esper J, Konter O, Klippel L, Krusic PJ, Büntgen U (2021) Pre-instrumental summer precipitation variability in northwestern Greece from a high-elevation *Pinus heldreichii* network. *Int J Climatol* 41: 2828-2839.
- Esper J, Konter O, Krusic PJ, Saurer M, Holzkämper S, Büntgen U (2015) Long-term summer temperature variations in the Pyrenees from detrended stable carbon isotopes. *Geochronometria* 42: 53-59.
- Esper J, Riechelmann DFC, Holzkämper S (2020b) Circumferential and longitudinal $\delta^{13}\text{C}$ variability in a *Larix decidua* trunk from the Swiss Alps. *Forests* 11: 1-13.
- Francey RJ, Farquhar GD (1982) An explanation of $^{13}\text{C}/^{12}\text{C}$ variations in tree rings. *Nature* 297: 28-31.
- Francey RJ, Gifford RM, Sharkey TD, Weir B (1985) Physiological influences on carbon isotope discrimination in huon pine (*Lagarostrobos franklinii*). *R J Aust J Plant Physiol* 66: 211-218.

- Gagen M, McCarroll D, Loader NJ, Robertson I, Jalkanen R, Anchukaitis KJ (2007) Exorcising the 'segment length curse': summer temperature reconstruction since AD 1640 using non-detrended stable carbon isotope ratios from pine trees in northern Finland. *Holocene* 17: 435-446.
- Gagen M, McCarroll D, Robertson I, Loader NJ, Jalkanen R (2008) Do tree ring $\delta^{13}\text{C}$ series from *Pinus sylvestris* in northern Fennoscandia contain long-term non-climatic trends? *Chem Geol* 252: 42-51.
- Gaglioti BV, Mann DH, Wooller MJ, Jones BM, Wiles GC, Groves P, Kunz ML, Baughman CA, Reanier RE (2017) Younger-Dryas cooling and sea-ice feedbacks were prominent features of the Pleistocene-Holocene transition in Arctic Alaska. *Quat Sci Rev* 169: 330-343.
- Gori Y, Wehrens R, Greule M, Keppler F, Ziller L, La Porta N, Camin F (2013) Carbon, hydrogen and oxygen stable isotope ratios of whole wood, cellulose and lignin methoxyl groups of *Picea abies* as climate proxies. *Rapid Commun Mass Spectrom* 27: 265-275.
- Greule M, Moossen H, Geilmann H, Brand WA, Keppler F (2019) Methyl sulfates as methoxy isotopic reference materials for $\delta^{13}\text{C}$ and $\delta^2\text{H}$ measurements. *Rapid Commun Mass Spectrom* 33: 343-350.
- Greule M, Moossen H, Lloyd MK, Geilmann H, Brand WA, Eiler JM, Qi H, Keppler F (2020) Three wood isotopic reference materials for $\delta^2\text{H}$ and $\delta^{13}\text{C}$ measurements of plant methoxy groups. *Chem Geol* 533: 119428.
- Greule M, Mosandl A, Hamilton JTG, Keppler F (2008) A rapid and precise method for determination of D/H ratios of plant methoxyl groups. *Rapid Commun Mass Spectrom* 22: 3983-3988.
- Greule M, Mosandl A, Hamilton JTG, Keppler F (2009) A simple rapid method to precisely determine $^{13}\text{C}/^{12}\text{C}$ ratios of plant methoxyl groups. *Rapid Commun Mass Spectrom* 23: 1710-1714.
- Hafner P, Robertson I, McCarroll D, Loader NJ, Gagen M, Bale RJ, Jungner H, Sonninen E, Hiltunen E, Levanič T (2011) Climate signals in the ring widths and stable carbon, hydrogen and oxygen isotopic composition of *Larix decidua* growing at the forest limit in the southeastern European Alps. *Trees* 25: 1141-1154.
- Hamed KH, Rao AR (1998) A modified Mann-Kendall trend test for autocorrelated data. *J Hydrol* 204: 182-196.
- Helama S, Arppe L, Timonen M, Mielikäinen K, Oinonen M (2015) Age-related trends in sub-fossil tree-ring $\delta^{13}\text{C}$ data. *Chem Geol* 416: 28-35.
- Keeling CD (1979) The Suess effect: ^{13}C - ^{14}C interrelations. *Environ Int* 2: 229-300.
- Keeling CD, Piper SC, Bacastow RB, Wahlen M, Whorf TP, Heimann M, Meijer HA (2005) Atmospheric CO_2 and $^{13}\text{CO}_2$ exchange with the terrestrial biosphere and oceans from

- 1978 to 2000: observations and carbon cycle implications. In: Baldwin I, Caldwell MM, Heldmaier G, Jackson RB, Lange OL, Mooney HA, Schulze ED, Sommer U, Ehleringer JR, Dearing MD, et al. (eds) *A history of atmospheric CO² and its effects on plants, animals, and ecosystems*. Springer, New York, NY, USA: pp 83-113.
- Keeling RF, Graven HD, Welp LR, Resplandy L, Bi J, Piper SC, Sun Y, Bollenbacher A, Meijer HAJ (2017) Atmospheric evidence for a global secular increase in carbon isotopic discrimination of land photosynthesis. *PNAS* 114: 10361-10366.
- Keppler F, Harper DB, Kalin RM, Meier-Augenstein W, Farmer N, Davis S, Schmidt HL, Brown DM, Hamilton JTG (2007) Stable hydrogen isotope ratios of lignin methoxyl groups as a paleoclimate proxy and constraint of the geographical origin of wood. *New Phytol* 176: 600-609.
- Keppler F, Kalin RM, Harper DB, McRoberts WC, Hamilton JTG (2004) Carbon isotope anomaly in the major plant C₁ pool and its global biogeochemical implications. *Biogeosciences* 1: 123-131.
- Kilroy E, McCarroll D, Young GHF, Loader NJ, Bale RJ (2016) Absence of juvenile effects confirmed in stable carbon and oxygen isotopes of European larch trees. *Acta Silvae Ligni* 111: 27-33.
- Klippel L, Krusic PJ, Brandes R, Hartl-Meier C, Trouet V, Meko M, Esper J (2017) High-elevation inter-site differences in Mount Smolikas tree-ring width data. *Dendrochronologia* 44: 164-173.
- Konter O, Esper J, Liebhold A, Kyncl T, Schneider L, Dũthorn E, Bũntgen U (2015) Tree-ring evidence for the historical absence of cyclic larch budmoth outbreaks in the Tatra Mountains. *Trees* 29: 809-814.
- Konter O, Holzkãmpfer S, Helle G, Bũntgen U, Saurer M, Esper J (2014) Climate sensitivity and parameter coherency in annually resolved $\delta^{13}\text{C}$ and $\delta^{18}\text{O}$ from *Pinus uncinata* tree-ring data in the Spanish Pyrenees. *Chem Geol* 337: 12-19.
- Konter O, Krusic PJ, Trouet V, Esper J (2017) Meet Adonis, Europe's oldest dendrochronologically dated tree. *Dendrochronologia* 42: 12.
- Leavitt SW (2010) Tree-ring C-H-O isotope variability and sampling. *Sci Total Environ* 408: 5244-5253.
- Lin G, Sternberg L (1993) Hydrogen isotopic fractionation by plant roots during water uptake in coastal wetland plants. In: Saugier B, Ehleringer JR, Hall AE, Farquhar GD (eds) *Stable isotopes and plant carbon-water relations*. Elsevier, Amsterdam, The Netherlands: pp 497-510.
- Loader NJ, Young GHF, Grudd H, McCarroll D (2013) Stable carbon isotopes from Tornetrãsk, northern Sweden provide a millennial length reconstruction of summer sunshine and its relationship to Arctic circulation. *Quat Sci Rev* 62: 97-113.

- Lu Q, Liu X, Tan L, Keppler F, Treydte K, Wieland A, Zhang L, Shi X, Zhang Y, Wang Y, et al. (2022) Tree-ring $\delta^2\text{H}$ records of lignin methoxy indicate spring temperature changes since 20th century in the Qinling Mountains, China. *Dendrochronologia* 76: 126020.
- Lukač L, Mikac S, Urban O, Kolář T, Rybníček M, Ač A, Trnka M, Marek MV (2021) Stable isotopes in tree rings of *Pinus heldreichii* can indicate climate variability over the eastern Mediterranean region. *Forests* 12: 350.
- McCarroll D, Loader NJ (2004) Stable isotopes in tree rings. *Quat Sci Rev* 23: 771-801.
- McCarroll D, Pawellek F (2001) Stable carbon isotope ratios of *Pinus sylvestris* from northern Finland and the potential for extracting a climate signal from long Fennoscandian chronologies. *Holocene* 11: 517-526.
- McCarroll D, Jalkanen R, Hicks S, Tuovinen M, Gagen M, Pawellek F, Eckstein D, Schmitt U, Autio J, Heikkinen O (2003) Multiproxy dendroclimatology: a pilot study in northern Finland. *Holocene* 13: 829-838.
- McDowell NG, Phillips N, Lurch C, Bond BJ, Ryan MG (2002) An investigation of hydraulic limitation and compensation in large, old Douglas-fir trees. *Tree Physiol* 22: 763-774.
- Melvin TM, Briffa KR (2008) A “signal-free” approach to dendroclimatic standardisation. *Dendrochronologia* 26: 71-86.
- Melvin TM, Briffa KR (2014) CRUST: software for the implementation of Regional Chronology Standardisation: part 1. Signal-free RCS. *Dendrochronologia* 32: 7-20.
- Mischel M, Esper J, Keppler F, Greule M, Werner W (2015) $\delta^2\text{H}$, $\delta^{13}\text{C}$ and $\delta^{18}\text{O}$ from whole wood, α -cellulose and lignin methoxyl groups in *Pinus sylvestris*: a multi-parameter approach. *Isot Environ Health Stud* 51: 553-568.
- Nakatsuka T, Sano M, Li Z, Xu C, Tsushima A, Shigeoka Y, Sho K, Ohnishi K, Sakamoto M, Ozaki H, et al. (2020) A 2600-year summer climate reconstruction in central Japan by integrating tree-ring stable oxygen and hydrogen isotopes. *Clim Past* 16: 2153-2172.
- Newell DB, Tiesinga E (2019) *The International System of Units (SI), 2019 Edition*. National Institute of Standards and Technology, Special Publication 330, Gaithersburg, MD, USA.
- Raffalli-Delercé G, Masson-Delmotte V, Dupouey JL, Stievenard M, Bréda N, Moisselin JM (2004) Reconstruction of summer droughts using tree-ring cellulose isotopes: a calibration study with living oaks from Brittany (western France). *Tellus B Chem Phys Meteorol* 56: 160-174.
- Riechelmann DFC, Greule M, Siegwolf RTW, Anhäuser T, Esper J, Keppler F (2017) Warm season precipitation signal in $\delta^2\text{H}$ values of wood lignin methoxyl groups from high elevation larch trees in Switzerland. *Rapid Commun Mass Spectrom* 31: 1589-1598.
- Römer P, Reinig F, Konter O, Friedrich R, Urban O, Čáslavský J, Pernicová N, Trnka M, Büntgen U, Esper J (2023) Multi-proxy crossdating extends the longest high-elevation tree-ring chronology from the Mediterranean. *Dendrochronologia* 79: 126085.

- Stokes MA, Smiley TL (1996) *An introduction to tree-ring dating*. The University of Arizona Press, Tucson, AZ, USA.
- Torbenson M, Klippel L, Hartl C, Reinig F, Treydte K, Büntgen U, Trnka M, Schöne BR, Schneider L, Esper J (2022) Investigation of age trends in tree-ring stable carbon and oxygen isotopes from northern Fennoscandia over the past millennium. *Quat Int* 631: 105-114.
- Treydte K, Schleser G, Helle G, Frank DC, Winiger M, Haug GH, Esper J (2006) The twentieth century was the wettest period in northern Pakistan over the past millennium. *Nature* 440: 1179-1182.
- Treydte K, Schleser G, Schweingruber F, Winiger M (2001) The climatic significance of $\delta^{13}\text{C}$ in subalpine spruces (Lötschental, Swiss Alps): a case study with respect to altitude, exposure and soil moisture. *Tellus B Chem Phys Meteorol* 53: 593-611.
- Urey HC (1948) Oxygen isotopes in nature and in the laboratory. *Science* 108: 489-496.
- Van der Merwe NJ, Medina E (1991) The canopy effect, carbon isotope ratios and foodwebs in Amazonia. *J Archaeol Sci* 18: 249-259.
- Vogel J (1978) Recycling of carbon in a forest environment. *Oecol Plant* 13: 89-94.
- Wieland A, Greule M, Römer P, Esper J, Keppler F (2022) Climate signals in stable carbon and hydrogen isotopes of lignin methoxy groups from southern German beech trees. *Clim Past* 18: 1849-1866.
- Zeisel S (1885) Über ein Verfahren zum quantitativen Nachweise von Methoxyl. *Monatsh Chem*: 989-997.

6.8 Supplementary materials

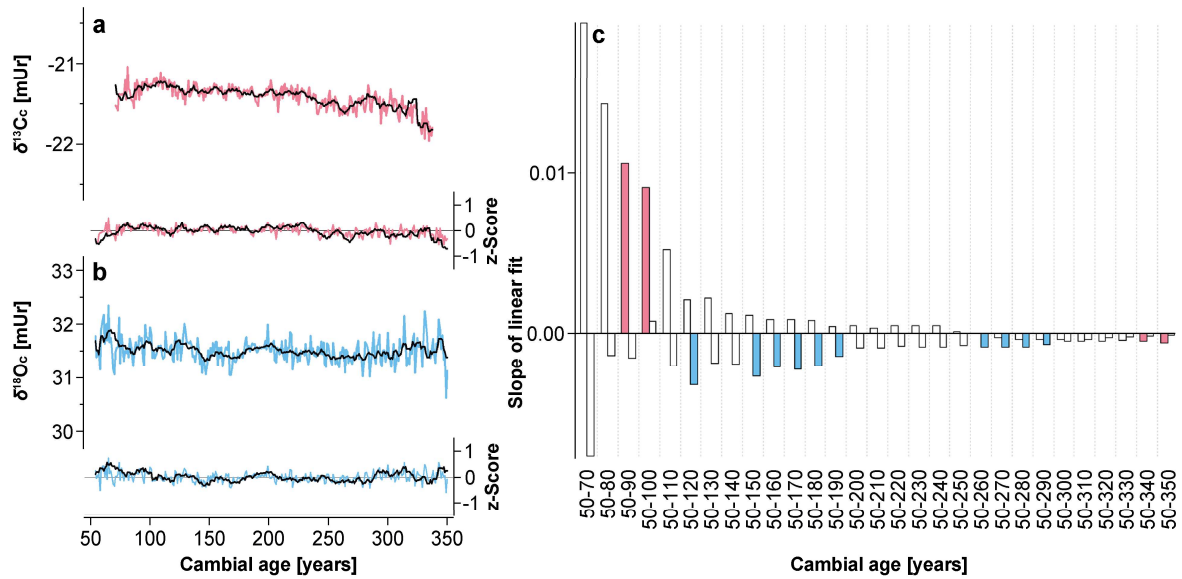


Fig. S6.1 Mean age-aligned (a) $\delta^{13}\text{C}_c$ and (b) $\delta^{18}\text{O}_c$ chronologies of the decadal (black lines) and annual (colored lines) relict wood series. (c) Linear slopes of the mean z-transformed $\delta^{13}\text{C}_c$ and $\delta^{18}\text{O}_c$ series at annual resolution. White bars represent non-significant ($p > 0.01$) and colored bars significant slopes at $p < 0.01$.

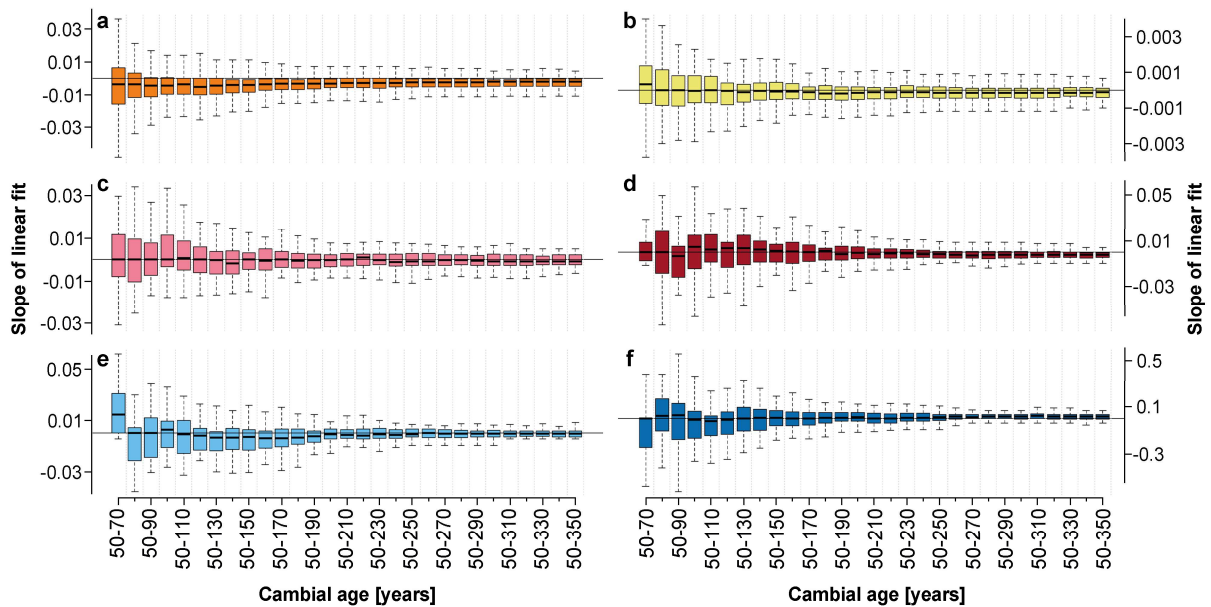


Fig. S6.2 Linear slopes (unit per decade) of the raw, age-aligned (a) TRW, (b) MXD, (c) $\delta^{13}\text{C}_c$, (d) $\delta^{13}\text{C}_m$, (e) $\delta^{18}\text{O}_c$, and (f) $\delta^2\text{H}_m$ series. Horizontal black lines are the median (50th percentile), boxes the 25th and 75th percentiles, and whiskers the 95% confidence interval.

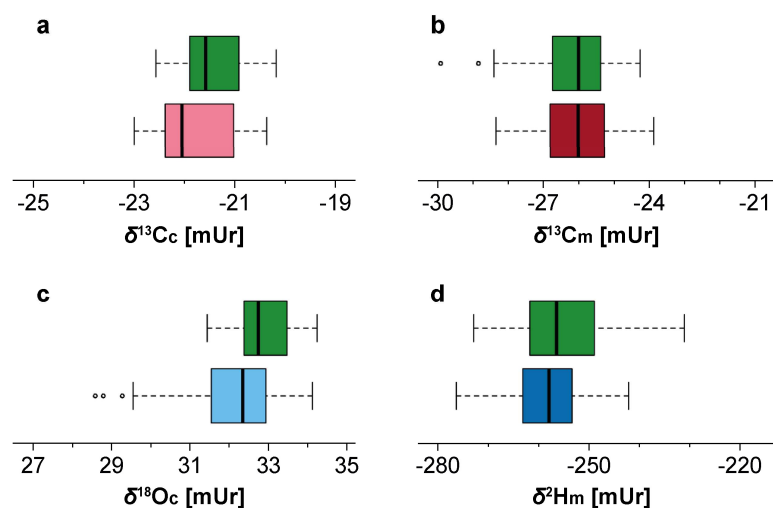


Fig. S6.3 Distribution and range of (a) $\delta^{13}\text{C}_c$, (b) $\delta^{13}\text{C}_m$, (c) $\delta^{18}\text{O}_c$, and (d) $\delta^2\text{H}_m$ values over the common period of living and relict wood (1641-1820 CE). Green boxes correspond to the living trees, while other colors represent the relict wood. Vertical black lines are the median (50th percentile), boxes the 25th and 75th percentiles, whiskers the 95% confidence interval, and points denote outliers.

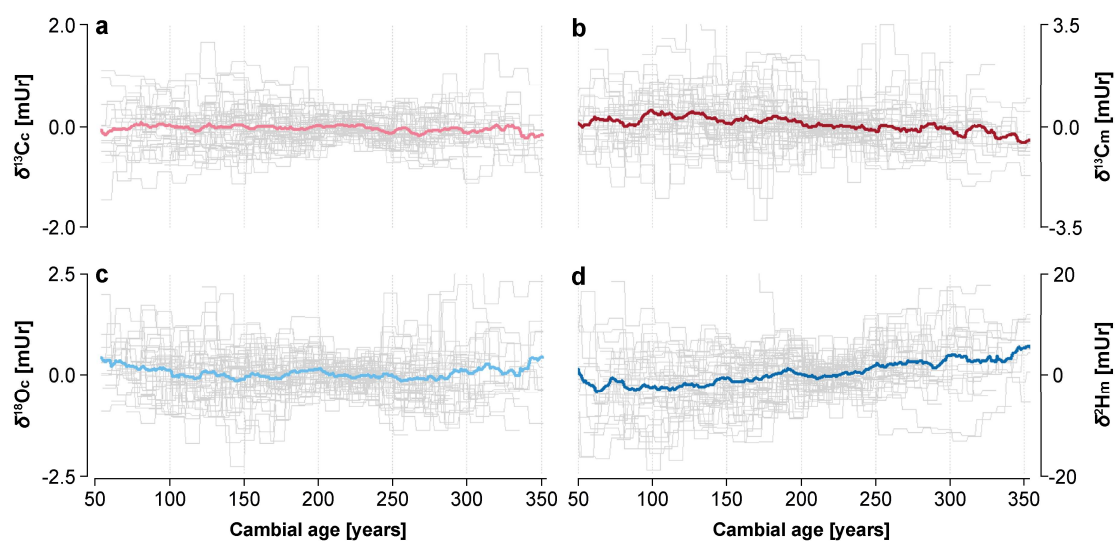


Fig. S6.4 Relative age-aligned (a) $\delta^{13}\text{C}_c$, (b) $\delta^{13}\text{C}_m$, (c) $\delta^{18}\text{O}_c$, and (d) $\delta^2\text{H}_m$ relict wood series. Relative TRSI values were calculated by subtracting the arithmetic mean of the common period (202-238 years). Colored lines represent the means of the individual series.

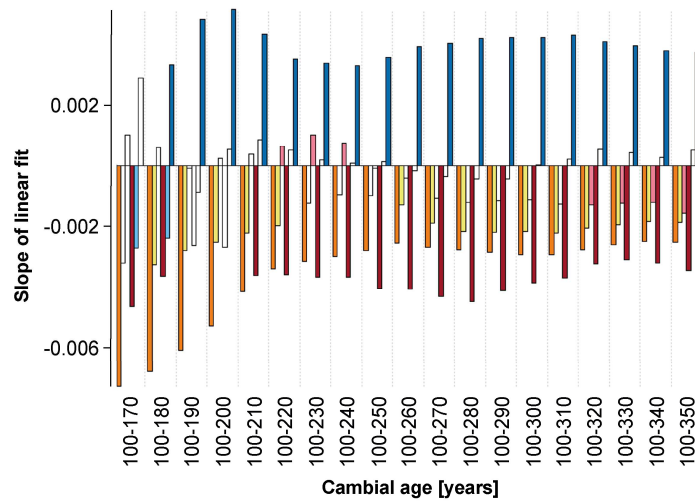


Fig. S6.5 Linear slopes of the mean z-transformed TRW (orange), MXD (yellow), $\delta^{13}\text{C}_c$ (light red), $\delta^{13}\text{C}_m$ (dark red), $\delta^{18}\text{O}_c$ (light blue), and $\delta^2\text{H}_m$ (dark blue) series. White bars represent non-significant ($p > 0.01$) and colored bars significant slopes at $p < 0.01$.

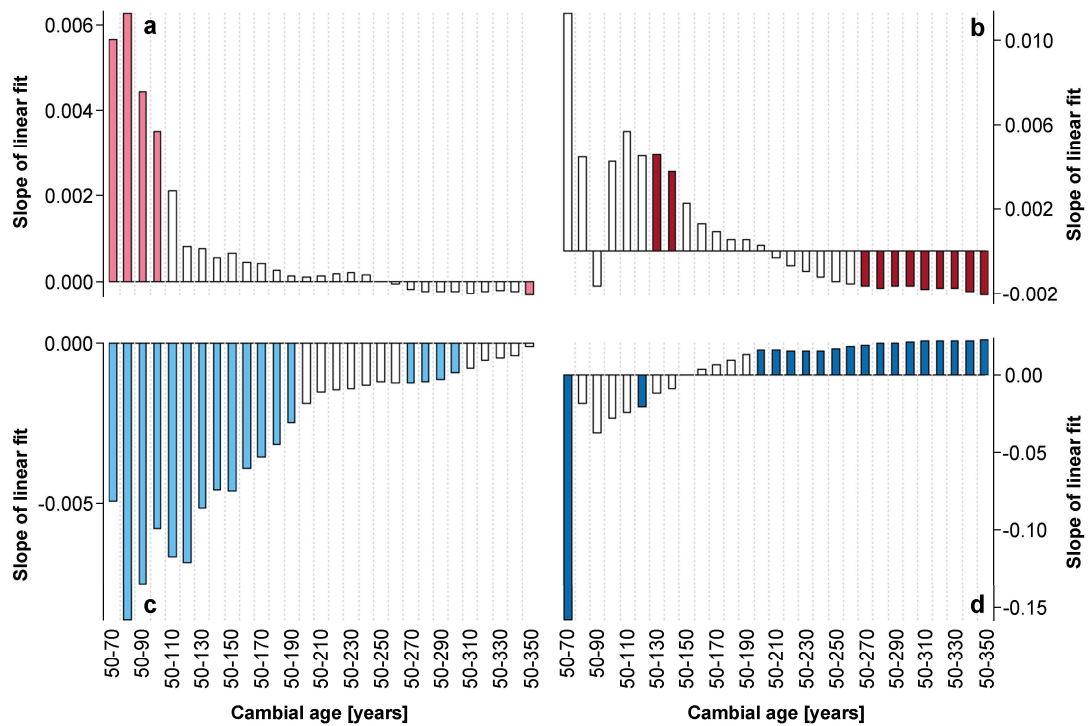


Fig. S6.6 Linear slopes (unit per decade) of the relative (a) $\delta^{13}\text{C}_c$, (b) $\delta^{13}\text{C}_m$, (c) $\delta^{18}\text{O}_c$, and (d) $\delta^2\text{H}_m$ series. White bars represent non-significant ($p > 0.01$) and colored bars significant slopes at $p < 0.01$.



Fig. S6.7 Example of a relict wood fragment where a disc sample was taken from unknown tree height.

7 Covariance and climate signals among state-of-the-art tree-ring proxies

Authors: Philipp Römer*, Anna Wieland*, Max Torbenson, Frederick Reinig, Emanuele Ziaco, Davide Frigo, Markus Greule, Otmar Urban, Josef Čáslavský, Natálie Pernicová, Miroslav Trnka, Marco Carrer, Ulf Büntgen, Frank Keppler, and Jan Esper

Status: Under review in *Quaternary Science Reviews*

Abstract

Tree-ring stable isotopes and wood anatomical traits emerged as powerful proxies for paleoclimate reconstructions, providing information beyond traditional ring width and wood density chronologies. However, comprehensive comparisons of these state-of-the-art tree-ring proxies derived from the same trees have yet to be performed to identify and differentiate their full paleoclimatic skill. Here, we assess covariance and climate signals in tree-ring width (TRW), maximum latewood density (MXD), cellulose stable carbon ($\delta^{13}\text{C}_c$) and oxygen ($\delta^{18}\text{O}_c$) isotopes, lignin methoxy carbon ($\delta^{13}\text{C}_m$) and hydrogen ($\delta^2\text{H}_m$) isotopes, radial cell lumen diameter (D_{rad}), and radial and tangential cell wall thickness ($\text{CWT}_{\text{rad}}/\text{CWT}_{\text{tan}}$) of ten Bosnian pines (*Pinus heldreichii*) from a treeline site on Mt. Smolikas, Greece. Proxy cross-comparison over the period 1861-2020 CE reveals strong covariance between detrended $\delta^{13}\text{C}_c$ and $\delta^{13}\text{C}_m$ ($r \geq 0.81$). $\delta^{13}\text{C}_c$ and $\delta^{18}\text{O}_c$ exhibit the highest inter-series correlations ($r \geq 0.61$) among all proxies. $\delta^{13}\text{C}_c$, $\delta^{13}\text{C}_m$, $\delta^{18}\text{O}_c$, together with D_{rad} , show considerable skill for reconstructing summer precipitation, whereas MXD and $\delta^2\text{H}_m$ may be used for summer temperature reconstructions. Enhanced inter-series and hydroclimate correlations, along with a prolonged seasonality are significant advances of the isotopic and wood anatomical measurements compared to TRW. Our findings highlight the importance of integrating new isotopic, particularly $\delta^{13}\text{C}_c$, and xylem anatomical data into existing TRW networks to enhance our understanding of past hydroclimate variability and contextualize the recent aridification of the Mediterranean region.

Keywords: Mediterranean, paleoclimatology, *Pinus heldreichii*, wood anatomy, tree-ring stable isotopes.

7.1 Introduction

The Mediterranean region is facing significant environmental and socio-economic challenges due to the increasing intensity, frequency, and duration of heatwaves and droughts in the late 20th and 21st centuries (Cramer et al. 2018). The limited number of annually resolved climate reconstructions dating back to the 1st millennium CE, however, constrains our ability to place recent hydrothermal dynamics into a long-term context of natural climate variability. New millennium-length climate reconstructions are therefore urgently needed to disentangle the roles of natural and anthropogenic forcing in the recent aridification of the Mediterranean (Hoerling et al. 2012; Lionello & Scarascia 2018; Spinoni et al. 2019).

The *Pinus heldreichii* treeline ecotone at Mt. Smolikas (**Fig. 7.1a**) in northern Greece is so far the only Mediterranean location where tree-ring width (TRW) and maximum latewood density (MXD) measurements enabled high-resolution climate estimates beyond the Medieval Warm Period (Esper et al. 2020a, 2021; Klippel et al. 2018, 2019). The Smolikas record, which extends back to the 5th century CE, represents the best-replicated tree-ring chronology from a high-elevation southern European site during the 1st millennium CE (Luterbacher et al. 2012; Römer et al. 2021). However, the TRW-based hydroclimate reconstructions lack distinct low-frequency information due to the detrending required to remove ontogenetic trends in growth and mitigate the heteroscedastic nature of these data (Bräker 1981; Osborn et al. 1997). The existing reconstructions may therefore not capture the entire spectrum of hydroclimate variability, underscoring the need for alternative proxies to complete our understanding of high-to-low frequency climate fluctuations in the Eastern Mediterranean region (Büntgen 2022).

Tree-ring stable isotopes (TRSI) derived from wood cellulose, including stable carbon ($\delta^{13}\text{C}_c$), oxygen ($\delta^{18}\text{O}_c$), and hydrogen ($\delta^2\text{H}_c$) isotopes, have proven valuable for reconstructing past climate variability at interannual to multimillennial timescales (Büntgen et al. 2021; Nakatsuka et al. 2020; Yang et al. 2021). TRSI measurements often lack ontogenetic trends and thus do not require standardization (Büntgen et al. 2020; Gagen et al. 2007; Young et al. 2011), exhibit strong inter-series correlations (Hartl-Meier et al. 2015; Treydte et al. 2007), and require small sample sizes to create reliable site chronologies (Belmecheri et al. 2022; Römer et al. 2023). In the Mediterranean, $\delta^{13}\text{C}_c$ and $\delta^{18}\text{O}_c$ revealed great potential for reconstructing past summer precipitation (Dorado Liñán et al. 2012; Levanič et al. 2020; Lukač et al. 2021), temperature (Esper et al. 2015a; Szymczak et al. 2012), and drought variability (Freund et al. 2023).

In recent decades, isotopic measurements of carbon and hydrogen on lignin methoxy groups (**Fig. 7.1b**) have emerged as credible climate proxies, providing a fast and cheap alternative to cellulose isotopic measurements (Greule et al. 2008, 2009; Keppler et al. 2007). $\delta^2\text{H}$ values of lignin methoxy groups ($\delta^2\text{H}_m$) are unaffected by the evaporative ^2H enrichment of leaf water and thus closely reflect the $\delta^2\text{H}$ values of precipitation, which are predominantly controlled by

air temperature (Dansgaard 1964), making $\delta^2\text{H}_m$ a promising temperature proxy in mid-to-high latitudes (Anhäuser et al. 2017, 2020; Feakins et al. 2013; Greule et al. 2021; Keppler et al. 2007; Lu et al. 2020). Lignin methoxy $\delta^{13}\text{C}$ ($\delta^{13}\text{C}_m$) has shown a similar temperature sensitivity at select sites in Europe (Gori et al. 2013; Riechelmann et al. 2016; Wieland et al. 2022) and Asia (Lu et al. 2020; Wang et al. 2020).

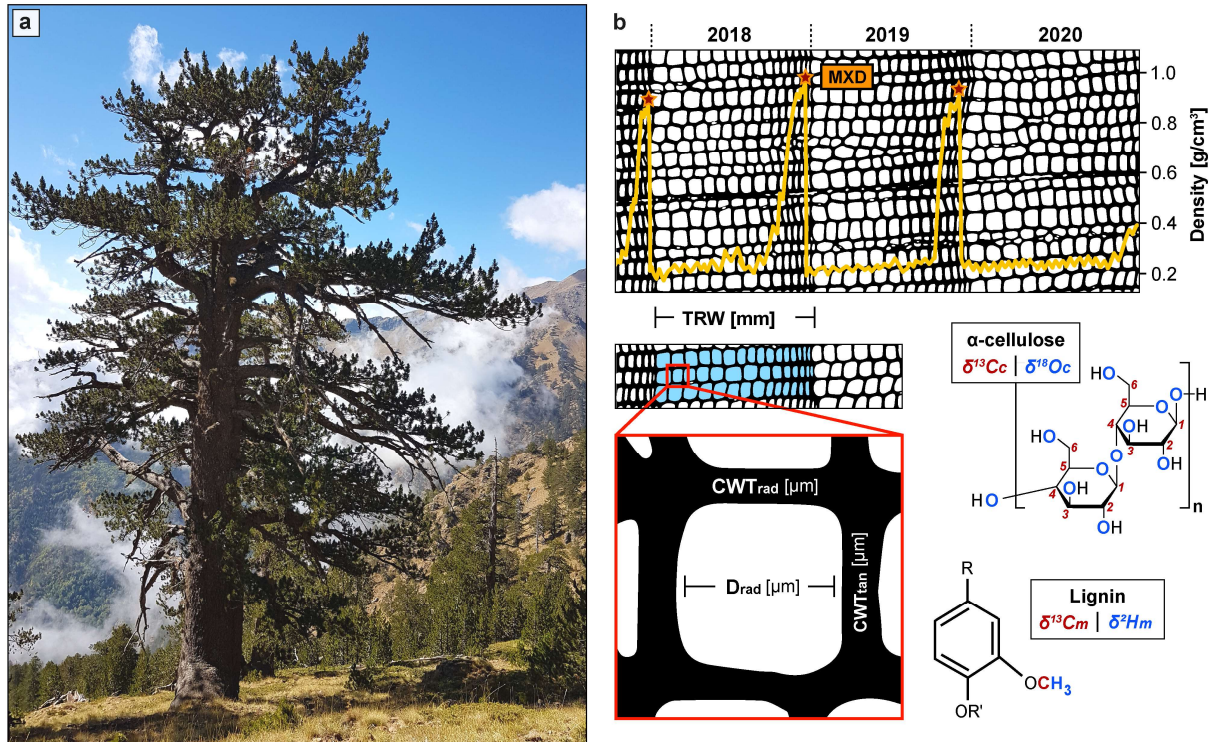


Fig. 7.1 Study material and tree-ring data. **(a)** Living Bosnian pine at Mt. Smolikas, Greece. **(b)** Illustration of tree-ring width (TRW), maximum latewood density (MXD), radial tracheid lumen diameter (D_{rad}), radial and tangential cell wall thickness ($\text{CWT}_{\text{rad}}/\text{CWT}_{\text{tan}}$), cellulose carbon ($\delta^{13}\text{C}_c$) and oxygen isotopes ($\delta^{18}\text{O}_c$), as well as lignin methoxy carbon ($\delta^{13}\text{C}_m$) and hydrogen ($\delta^2\text{H}_m$) isotopes.

In addition, methodological advances in quantitative wood anatomy (QWA) have opened new research perspectives for paleoclimatology (Prendin et al. 2017; von Arx & Carrer 2014). The quantification of wood anatomical features improves the spatiotemporal resolution of traditional proxies and allows for disentangling the effects of environmental conditions on xylem structural properties at a cellular level (Fonti et al. 2010; Pandey 2021). Among numerous anatomical traits, tracheid lumen area, radial lumen diameter (D_{rad}), cell wall thickness (CWT), and inferred wood anatomical densities have proven to be reliable climate predictors (Balanzategui et al. 2021; Björklund et al. 2020, 2023; Carrer et al. 2018; González-Cásares et al. 2019; Lopez-Saez et al. 2023; Ziaco et al. 2016).

Despite their undisputed paleoclimatic potential, an accurate comparison of the various proxies using the same wood has not been conducted yet. Using samples from living Bosnian pines from Mt. Smolikas (Greece), we here combine TRW, MXD, $\delta^{13}\text{C}_c$, $\delta^{18}\text{O}_c$, $\delta^{13}\text{C}_m$, $\delta^2\text{H}_m$, D_{rad} , and CTW measurements to (I) assess covariance both within and among these state-of-the-art

tree-ring proxies and their climate sensitivities. We (II) evaluate whether specific proxies may be combined and (III) provide recommendations on the suitability of individual proxies for future paleoclimate research in the Mediterranean.

7.2 Material and methods

7.2.1 TRW and MXD measurements

Between 2015 and 2019, a total of 878 core and disc samples were collected from living and relict Bosnian pines (*Pinus heldreichii* H. Christ) on Mt. Smolikas in Greece (40.1°N/21.0°E, ≥ 2000 m asl) to establish well-replicated TRW ($n = 878$ series) and MXD ($n = 192$ series) chronologies (Esper et al. 2020a, 2021). In 2021, ten of the living pines were resampled to develop new stable isotopic and wood anatomical records extending to 2020 CE. Two 1-cm increment cores were extracted from each tree at breast height (~ 1.3 m) from the same stem direction (~ 5 cm above each other) perpendicular to the slope. TRW was measured on each core with an accuracy of 0.01 mm using the high-precision LINTAB 6 device (Rinntech, Heidelberg, Germany) and TSAP-Win software (Rinn 2012). Dating precision was verified by comparing the new TRW data with the old measurements (**Fig. S7.1a-b**). One core each was used for isotopic and wood anatomical analyses. No MXD measurements were performed on the new samples. However, to ensure a robust comparison between MXD and the other proxies, a subset of ten living-tree series was selected from the data used in Esper et al. (2020a) to create a representative MXD record (**Fig. S7.1c-d**) with a sample replication equal to the other proxies. A detailed description of the MXD methodology is provided in Klippel et al. (2019).

7.2.2 Stable isotope measurements

The isotopic measurements of $\delta^{13}\text{C}_c$, $\delta^{13}\text{C}_m$, $\delta^{18}\text{O}_c$, and $\delta^2\text{H}_m$ were performed at annual resolution on the same increment cores. The tree rings of each sample were carefully separated with a scalpel, cut into smaller pieces, and divided equally into two Eppendorf microtubes for cellulose and methoxy isotope measurements. When cutting and partitioning, care was taken to ensure that the microtubes contained the original earlywood-latewood proportions.

For cellulose isotopic measurements, α -cellulose was extracted via the modified Jayme-Wise isolation method (Boettger et al. 2007) at the Global Change Research Institute, Czech Republic (details in Wieland et al. 2024). After extraction, 0.5-1.0 mg of α -cellulose was placed in tin ($\delta^{13}\text{C}_c$) and silver ($\delta^{18}\text{O}_c$) capsules. The tin capsules were combusted to CO_2 at 960°C, while the silver capsules were pyrolyzed to CO at 1450°C using the high-temperature cell of the varioPYRO cube elemental analyzer (Elementar Analysensysteme, Langensfeld, Germany). The ratios of heavy to light carbon ($^{13}\text{C}/^{12}\text{C}$ from CO_2) and oxygen ($^{18}\text{O}/^{16}\text{O}$ from CO) isotopes were measured using the ISOPRIME100 continuous-flow isotope ratio mass

spectrometer (IRMS) (Isoprime, Manchester, UK). Isotopic measurements were calibrated using certified reference materials from the International Atomic Energy Agency (IAEA) and the United States Geological Survey (USGS). $^{13}\text{C}/^{12}\text{C}$ ratios were referenced to caffeine (IAEA-600) and graphite (USGS24), and $^{18}\text{O}/^{16}\text{O}$ ratios to benzoic acid (IAEA-601 and IAEA-602).

Isotopic measurements on lignin methoxy groups were performed at the Institute of Earth Sciences, Heidelberg University (Germany), using the modified Zeisel method (Greule et al. 2008, 2009; Keppler et al. 2004, 2007), in which gaseous iodomethane (CH_3I) is formed from the reaction between methyl ethers and esters and hydroiodic acid (Zeisel 1885). For this, 5 mg ($\delta^{13}\text{C}_m$) and 7 mg ($\delta^2\text{H}_m$) of wooden material and 250 μl of hydroiodic acid were heated in crimp glass vials for 30 minutes at 130°C , followed by a sample equilibration at room temperature. Ten to 90 μl aliquot of headspace were injected via an autosampler (A200S, CTC Analytics, Zwingen, Switzerland) into a gas chromatograph (HP 6890N, Agilent, Santa Clara, USA) equipped with a combustion reactor [ceramic tube (Al_2O_3), length 320 mm, 0.5 mm i.d., Cu/Ni/Pt wires inside (activated by oxygen)] for $\delta^{13}\text{C}_m$ measurements or a thermo conversion reactor [ceramic tube (Al_2O_3), length 320 mm, 0.5 mm i.d.] for $\delta^2\text{H}_m$ measurements. CH_3I was oxidized to CO_2 at 960°C and pyrolyzed to H_2 at 1450°C . The resulting gases were transferred through a Finnigan GC-Combustion III interface into a Thermo Finnigan DeltaplusXL IRMS (Thermo Fisher Scientific, Waltham, USA) to measure the ratios of heavy to light carbon ($^{13}\text{C}/^{12}\text{C}$ from CO_2) and hydrogen ($^2\text{H}/^1\text{H}$ from H_2) isotopes. The isotope measurements were normalized using HUBG reference materials (Greule et al. 2019, 2020). HUBG2 and HUBG4 were used for the $\delta^{13}\text{C}_m$ measurements, and HUBG1 and HUBG3 for the $\delta^2\text{H}_m$ measurements.

Isotope ratios are expressed in the conventional δ notation in Urey (Ur) relative to the Vienna Pee Dee Belemnite standard ($\delta^{13}\text{C}$) and the Vienna Standard Mean Ocean Water ($\delta^{18}\text{O}_c$ and $\delta^2\text{H}_m$). One mUr is equivalent to 1 per mille (Brand & Coplen 2012). The ion sources of the IRMS systems were centered, tuned, and tested for stability ($1\sigma < 0.03$ mUr for $\delta^{13}\text{C}_c$, < 0.02 mUr for $\delta^{13}\text{C}_m$, < 0.02 mUr for $\delta^{18}\text{O}_c$, < 0.04 mUr for $\delta^2\text{H}_m$, on ten pulses of monitoring gas) and linearity (< 0.04 mUr/nA for $\delta^{13}\text{C}_c$, < 0.06 mUr/V for $\delta^{13}\text{C}_m$, < 0.04 mUr/nA for $\delta^{18}\text{O}_c$, < 1 mUr/V for $\delta^2\text{H}_m$) before each sequence of isotopic measurements. The H_3^+ factor was quantified before each set of $\delta^2\text{H}_m$ measurements (< 3.5 ppm/nA). Six (cellulose) and five (lignin methoxy) consecutive measurements on the same samples were performed to assess the precision of the isotopic measurements. Average standard deviations were 0.04 mUr for $\delta^{13}\text{C}_c$, 0.09 mUr for $\delta^{18}\text{O}_c$, between 0.01-0.25 mUr for $\delta^{13}\text{C}_m$, and between 0.5-2 mUr for $\delta^2\text{H}_m$.

7.2.3 Quantitative wood anatomy

To produce high-quality wood anatomical images, increment cores were cut into 4-5 cm long pieces and boiled in distilled water. Ten micrometer [μm] thick transverse microsections were

cut from each piece using a rotary microtome (Leica, Wetzlar, Germany). The microsections were bleached in 10% NaOCl for 10 minutes, stained with a 1:1 safranin and astra blue solution, dehydrated successively in 50% and 100% ethanol baths, and permanently mounted on microscope slides with Euparal (Carl Roth, Karlsruhe, Germany). The permanent slides were scanned at a resolution of 2.2 pixels/ μm using a Hamamatsu NanoZoomer slide scanner (Hamamatsu Photonics, Shizuoka, Japan).

The obtained images were processed using ROXAS v4.0 (Prendin et al. 2017; von Arx & Carrer 2014) to quantify xylem anatomical traits, including radial cell lumen diameter (D_{rad}) as well as radial and tangential cell wall thickness ($\text{CWT}_{\text{rad}}/\text{CWT}_{\text{tan}}$). After the automated detection of individual cells by ROXAS, a manual editing was performed to remove incorrectly recognized features, such as resin ducts and parenchyma cells. Tree-ring sequences were crossdated by comparing the TRW output of ROXAS with the LINTAB measurements. To quantify intra-annual variability in the wood anatomical structures, we computed standardized tracheidograms (Vaganov 1990; Ziaco 2020) by aligning cell radial files for each ring using the R package *RAPTOR* (Peters et al. 2018), normalizing cell numbers to 30 using the *tgram* function, and dividing each ring into ten tangential sectors. Tree-ring sectoring allows for the refinement of climatic signals encoded in xylem cellular traits (Ziaco & Liang 2019), with ten sectors generally considered an appropriate compromise between higher temporal resolution and maintaining a reliable cell count in each sector (Belokopytova et al. 2019; Carrer et al. 2018). A principal component analysis (PCA) was applied to assess similarities and differences between the sectorial QWA chronologies and the annual TRW, MXD, and TRSI chronologies. The principal components (PCs) were tested for significance using randomization tests and the Rnd-Lambda stopping rule (Peres-Neto et al. 2005).

7.2.4 Data treatment and chronology development

To account for the depletion of atmospheric ^{13}C due to anthropogenic CO_2 emissions, the $\delta^{13}\text{C}_c$ and $\delta^{13}\text{C}_m$ series were corrected for the Suess effect (Keeling 1979) by adding residuals to pre-industrial levels of -6.41 mUr to the tree-ring values after 1860 CE (**Fig. S7.2**). The atmospheric ^{13}C data were obtained from McCarroll & Loader (2004) and the Mauna Loa Observatory (<https://scrippsco2.ucsd.edu>; Keeling et al. 2005). Both $\delta^{13}\text{C}$ records were further corrected for the increasing leaf-internal ^{13}C discrimination under elevated CO_2 concentrations using a loess regression model proposed by McCarroll et al. (2009). However, since the latter so-called pin-correction was developed using cellulose-derived isotope data and its application might lead to increasing uncertainty in the isotopic measurements on lignin methoxy groups, we used the Suess-effect-corrected $\delta^{13}\text{C}$ data for inter-proxy comparisons and climate calibration. Results on the pin-corrected $\delta^{13}\text{C}$ data can be found in the supplementary material.

The individual time series of each proxy were detrended using the ARSTAN software (Cook & Krusic 2017) by calculating residuals from horizontal means (HOM) and cubic smoothing splines with 50% frequency cutoffs at 100 years (100SP) and 30 years (30SP) to emphasize high-to-low frequency variance. The tree-ring records were power-transformed and variance-stabilized (Cook & Peters 1997; Frank et al. 2007), and mean chronologies were developed by computing bi-weight robust means of the individual series. Series covariance was assessed by calculating average inter-series correlations (R_{bar}) over the 1861-2020 CE common period (Wigley et al. 1984), except for MXD which was confined to 1861-2017 CE.

7.2.5 Meteorological data and climate signal detection

The proxy chronologies were correlated against monthly temperature, precipitation, and cloud cover data (CRU TS4.07; Harris et al. 2020), as well as against the Palmer Drought Severity Index (PDSI; Wells et al. 2004). The meteorological data were retrieved for the closest 0.5° grid ($40.0\text{-}40.5^\circ\text{N}/20.5\text{-}21.0^\circ\text{E}$) using the KNMI climate explorer (<https://climexp.knmi.nl>). To reduce uncertainty arising from the limited number of meteorological stations reaching back to the early 20th century (Fig. 7.2), climate correlations were calculated from 1931-2020 CE. The year 1931 CE was selected as the starting year as two nearby precipitation stations (Kerkyra and Thessaloniki) are included in the grid thereafter.

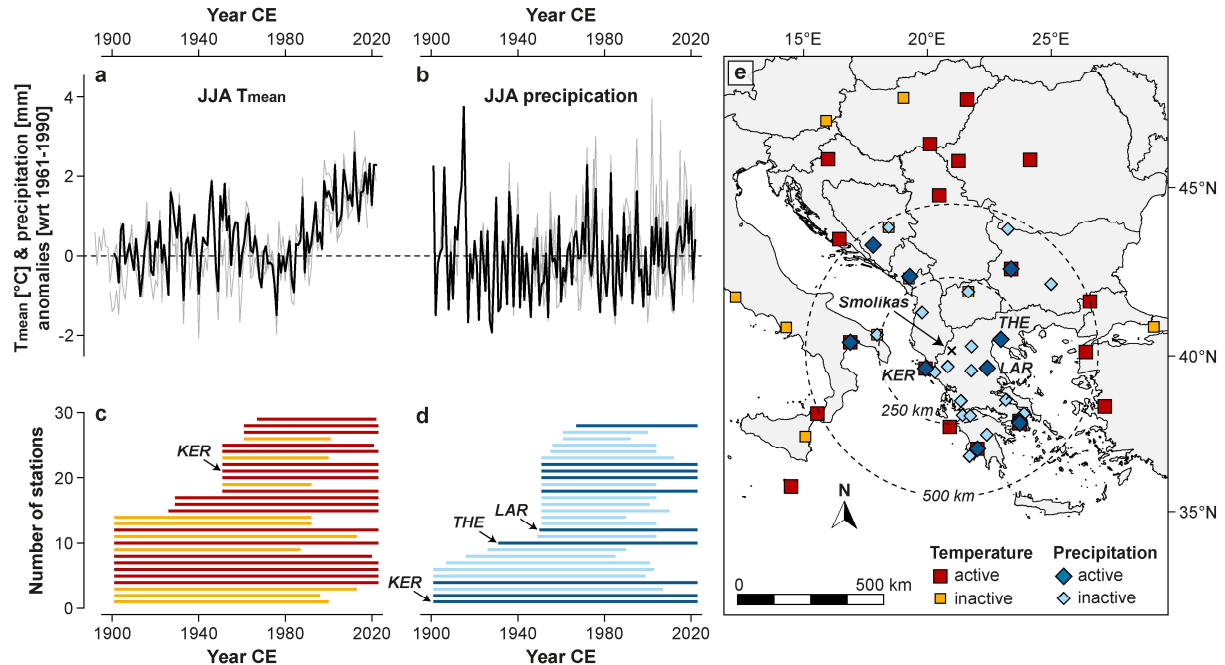


Fig. 7.2 Climate data. June-August (JJA) (a) mean air temperature (T_{mean}) and (b) precipitation anomalies (wrt. 1961-1990 CE) from the CRU TS4.07 grid (black lines) closest to Mt. Smolikas and the meteorological stations (grey lines) in Kerkyra (KER), Larissa (LAR), and Thessaloniki (THE). (c-d) Temporal coverage of the temperature and precipitation stations used to interpolate the gridded data. Each horizontal bar represents one station. The dark red and dark blue bars highlight (“active”) stations providing measurements until 2020 CE. (e) Spatial coverage of the “active” and “inactive” stations integrated into the gridded data. The dashed circles indicate linear distances (250 and 500 km) from the study site.

The meteorological data were tested for normal distribution and climate-proxy relationships were assessed by using Pearson (temperature and cloud cover) and Spearman rank (precipitation and PDSI) correlations. Prior to the correlation calculations, the climate data were standardized the same way as the tree-ring data. Thirty-one-year running and field correlations were computed to test the temporal robustness and spatial extent of climate signals.

7.3 Results

7.3.1 Proxy characteristics and covariance

Mean cambial age of the TRW, TRSI, and QWA series ranges from 298 years in 1861 to 457 years in 2020 CE. In contrast, the MXD series are, on average, ~40 years younger (**Fig. S7.3**) and terminate in 2017 CE. Mean segment lengths (MSL) vary slightly among the proxies due to different measurement periods, ranging from 157 years for $\delta^{13}\text{C}_m$ and $\delta^2\text{H}_m$ to 218 years for D_{rad} and CWT. However, all proxy chronologies are well replicated ($n \geq 8$ series) over the 1861-2020 CE period (**Table 7.1**).

Table 7.1 Proxy characteristics.

Proxy	n	Period (≥ 5 series)	MSL $\pm 1\sigma$	AC1				Rbar		
				RAW	HOM	100SP	30SP	HOM	100SP	30SP
TRW	10	1810-2020	205 \pm 47	0.72	0.73	0.56	0.25	0.38	0.34	0.37
MXD	10	1810-2017	201 \pm 47	0.53	0.53	0.36	0.16	0.18	0.23	0.28
$\delta^{13}\text{C}_c$	10	1810-2020	205 \pm 47	0.30	0.30	0.16	0.00	0.56	0.62	0.67
$\delta^{13}\text{C}_m$	10	1861-2020	157 \pm 07	0.41	0.43	0.18	-0.01	0.40	0.30	0.33
$\delta^{18}\text{O}_c$	10	1810-2020	205 \pm 47	0.25	0.25	0.16	0.06	0.39	0.61	0.62
$\delta^2\text{H}_m$	10	1861-2020	157 \pm 07	0.41	0.41	0.24	0.09	0.34	0.36	0.40
D_{rad}	10	1807-2020	218 \pm 47	0.45	0.45	0.16	0.00	0.27	0.36	0.43
CWT_{rad}	10	1807-2020	218 \pm 47	0.65	0.65	0.48	0.18	0.08	0.15	0.21
CWT_{tan}	10	1807-2020	218 \pm 47	0.65	0.65	0.46	0.21	0.12	0.17	0.22

n: total number of series. **MSL**: mean segment length ± 1 standard deviation (1σ). **AC1**: first-order autocorrelation of the raw and detrended chronologies. **Rbar**: average inter-series correlation between the detrended series. The latter two statistics are calculated for 1861-2020 CE (MXD for 1861-2017 CE).

The raw TRW and CWT (CWT_{rad} and CWT_{tan}) chronologies show the highest first-order autocorrelations ($\text{AC1} \geq 0.65$) for 1861-2020 CE. AC1 is higher in methoxy ($\text{AC1}_{\text{raw}} = 0.41$) than in cellulose isotopes ($\text{AC1}_{\text{raw}} \leq 0.30$), reflecting the stronger trends in $\delta^{13}\text{C}_m$ ($+0.004 \text{ mUr a}^{-1}$) and $\delta^2\text{H}_m$ (-0.03 mUr a^{-1}) from 1861 to 2020 CE (**Fig. 7.3**). $\delta^{13}\text{C}_c$ decreases, on average, by $-0.002 \text{ mUr a}^{-1}$ and $\delta^{18}\text{O}_c$ increases by $+0.001 \text{ mUr a}^{-1}$ over the same period. TRW and D_{rad} increase by $+0.002 \text{ mm a}^{-1}$ and $+0.008 \text{ } \mu\text{m a}^{-1}$, while trends in CWT and MXD are $< 0.001 \text{ } \mu\text{m a}^{-1}$ and $\text{g cm}^{-3} \text{ a}^{-1}$, respectively. Similar AC1 values between the raw and HOM-detrended data indicate retention of low-frequency variability after detrending. Lower AC1 values after spline detrending demonstrate the removal of this low-frequency information, but coincide with an increase

in covariance among series. The spline-detrended $\delta^{13}\text{C}_c$ and $\delta^{18}\text{O}_c$ series exhibit the highest $R_{\text{bar}} \geq 0.61$. R_{bar} values of the methoxy isotopes are noticeably lower and similar to those of TRW and D_{rad} . MXD, CWT_{rad} , and CWT_{tan} indicate the lowest $R_{\text{bar}} \leq 0.28$ (**Fig. S7.4**).

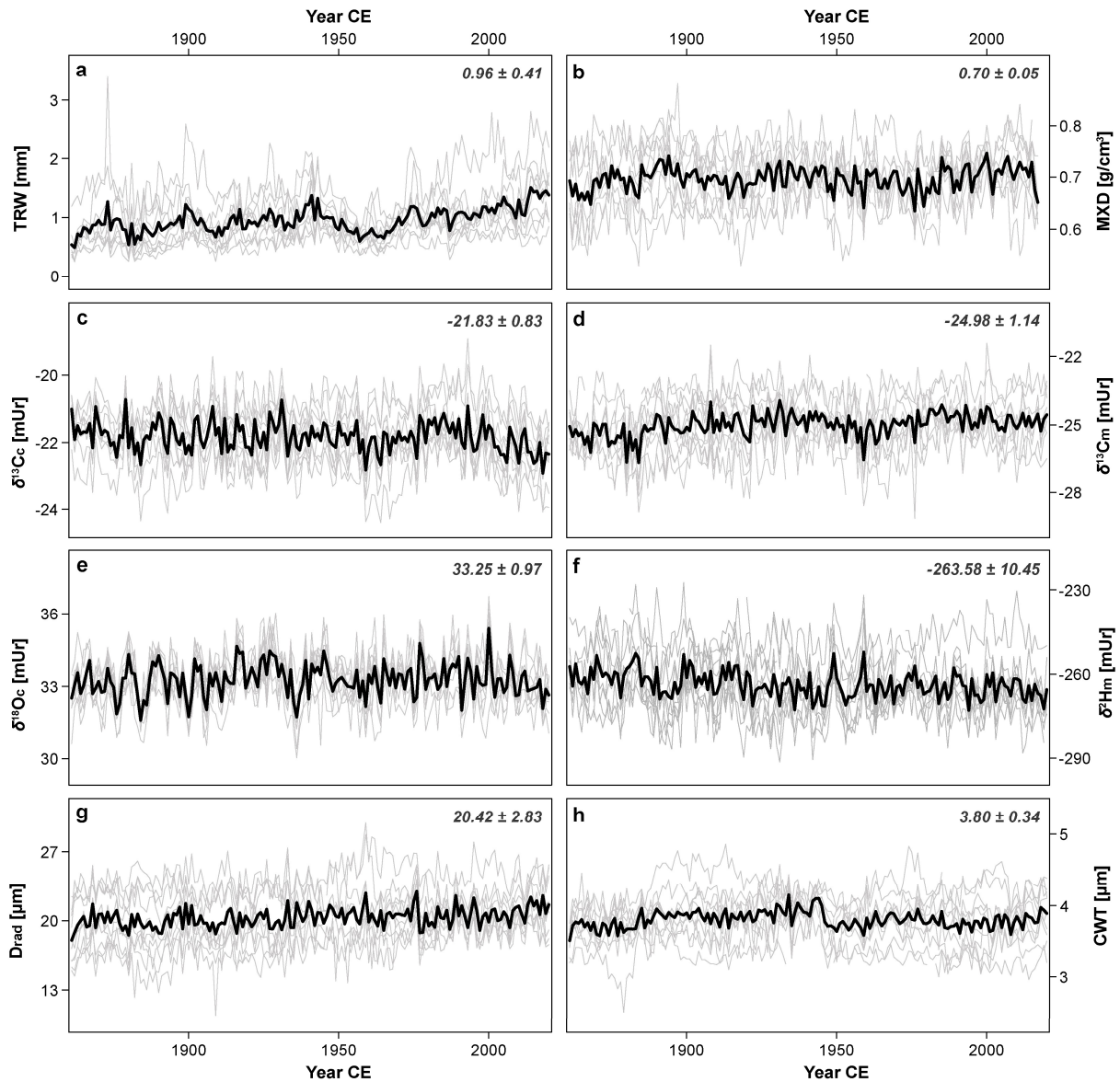


Fig. 7.3 Individual series (grey curves) and mean chronologies (black curves) of raw (a) TRW, (b) MXD, (c) $\delta^{13}\text{C}_c$, (d) $\delta^{13}\text{C}_m$, (e) $\delta^{18}\text{O}_c$, (f) $\delta^2\text{H}_m$, (g) D_{rad} , (h) and CWT. The latter represents the mean of CWT_{rad} and CWT_{tan} (details in Fig. S7.4). The $\delta^{13}\text{C}$ series are corrected for the Suess effect. Values at the right top are the arithmetic mean ± 1 standard deviation calculated over all tree rings between 1861-2020 CE (1861-2017 CE for MXD).

The Suess-effect-corrected $\delta^{13}\text{C}_c$ values fluctuate around -21.83 ± 0.83 mUr and are on average 3.15 mUr higher than the $\delta^{13}\text{C}_m$ values (-24.98 ± 1.14 mUr). However, high correlations ($r = 0.81$, $p < 0.001$) between the spline-detrended $\delta^{13}\text{C}$ chronologies indicate a close association between $\delta^{13}\text{C}_c$ and $\delta^{13}\text{C}_m$. Inter-proxy correlations are overall higher after the 30SP detrending than after 100SP detrending (**Table 7.2**). The 30SP-detrended $\delta^{13}\text{C}$ records are positively correlated with MXD ($r \geq 0.51$) and $\delta^{18}\text{O}_c$ ($r \geq 0.44$), and negatively correlated with D_{rad} ($r \leq -0.32$),

with overall higher correlations for $\delta^{13}\text{C}_c$ than for $\delta^{13}\text{C}_m$. $\delta^{18}\text{O}_c$ is most strongly correlated with $\delta^{13}\text{C}_c$ ($r = 0.59$) and D_{rad} ($r = -0.51$). $\delta^2\text{H}_m$ displays negative correlations with MXD and CWT_{rad} ($r \leq -0.28$) and a positive correlation with D_{rad} ($r = 0.30$). TRW is positively correlated with D_{rad} and CWT_{tan} ($r = 0.41$), while MXD shows significant ($p < 0.001$) correlations with all proxies except TRW. A correlation of $r = 0.71$ between CWT_{tan} and CWT_{rad} indicates a strong association between the two CWT orientations, but only CWT_{rad} shows significant ($p < 0.001$) correlations with $\delta^{18}\text{O}_c$, $\delta^2\text{H}_m$, and D_{rad} .

Table 7.2 Correlations between the spline-detrended proxy chronologies for 1861-2020 CE.

	TRW	MXD	$\delta^{13}\text{C}_c$	$\delta^{13}\text{C}_m$	$\delta^{18}\text{O}_c$	$\delta^2\text{H}_m$	D_{rad}	CWT_{rad}	CWT_{tan}
TRW		0.12	-0.04	0.19	-0.08	0.12	0.41	-0.03	0.35
MXD	0.15		0.52	0.51	0.44	-0.33	-0.46	0.47	0.28
$\delta^{13}\text{C}_c$	0.03	0.45		0.81	0.59	-0.20	-0.59	0.11	-0.15
$\delta^{13}\text{C}_m$	0.27	0.44	0.81		0.44	-0.14	-0.32	0.02	-0.09
$\delta^{18}\text{O}_c$	-0.04	0.37	0.57	0.42		-0.05	-0.51	0.33	0.10
$\delta^2\text{H}_m$	0.05	-0.40	-0.20	-0.17	-0.06		0.30	-0.28	-0.14
D_{rad}	0.38	-0.38	-0.55	-0.27	-0.49	0.25		-0.45	0.09
CWT_{rad}	0.11	0.38	0.12	0.12	0.28	-0.29	-0.41		0.71
CWT_{tan}	0.48	0.30	-0.12	0.03	0.09	-0.18	0.13	0.70	

Note: Values in the left bottom are correlations between the 100SP chronologies, values in the right top are correlations between the 30SP chronologies. Bold numbers indicate significance ($p < 0.001$). Significant positive correlations are red; significant negative correlations are blue. Correlations with MXD are computed for 1861-2017 CE.

7.3.2 Climate signals

Climate signals are most distinct in summer and after 30SP detrending, but maximum seasonal responses vary slightly among the proxies (**Fig. 7.4**). TRW correlations with mean temperature (T_{mean}), precipitation, and the PDSI are all insignificant ($p > 0.01$) for 1931-2020 CE. Significant ($p < 0.01$) TRW correlations are restricted to June-July (JJ) cloud cover ($r = 0.28$) and diurnal temperature range ($r = -0.38$; **Fig. S7.5**). MXD shows the highest correlations with July-September T_{mean} ($r = 0.55$), precipitation ($r = -0.41$) and cloud cover data ($r = -0.62$). TRW and MXD correlations with the PDSI are insignificant for all months, except for MXD in September. TRW and MXD correlations with previous-year climate are weak and only significant between 30SP-detrended MXD and July T_{mean} ($r = -0.29$), as well as between TRW and August precipitation ($r = 0.32$) and cloud cover ($r = 0.33$; **Fig. S7.6**).

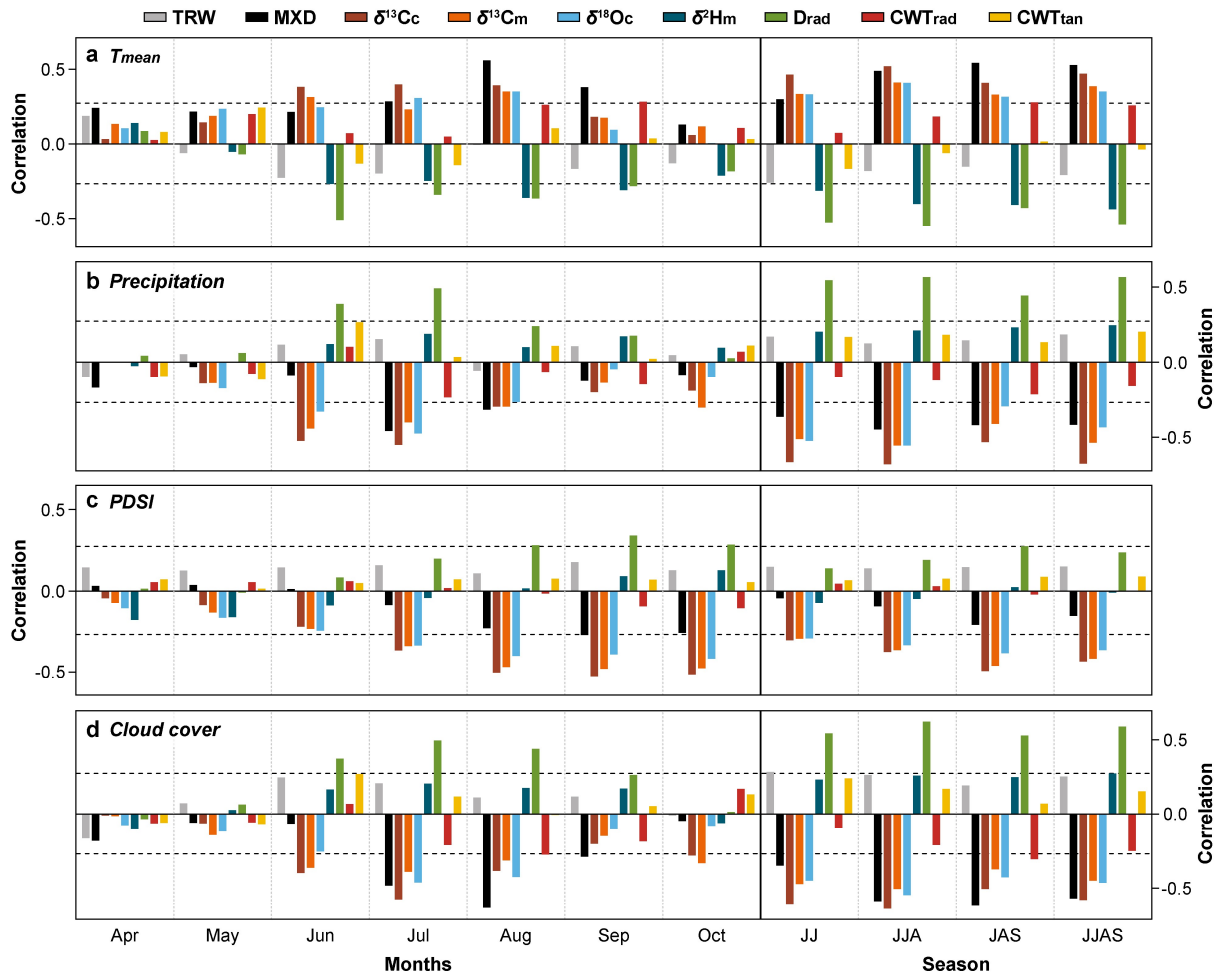


Fig. 7.4 Climate signals. Correlations between the 30SP-detrended chronologies and monthly/seasonal (a) mean air temperature (T_{mean}), (b) precipitation, (c) the PDSI, and (d) cloud cover data calculated for 1931-2020 CE. Horizontal dashed lines indicate the significance level of $p < 0.01$. Please note that the significance level for MXD is marginally higher (~ 0.004) due to the shorter calibration period (1931-2017 CE), but is not displayed for the sake of clarity.

The 30SP-detrended $\delta^{13}\text{C}_c$, $\delta^{13}\text{C}_m$, and $\delta^{18}\text{O}_c$ records show the highest correlations with June-August (JJA) T_{mean} ($r = 0.52/0.40/0.40$), precipitation ($r = -0.69/-0.55/-0.55$), and cloud cover data ($r = -0.64/-0.50/-0.55$, $p < 0.001$). Correlations with the PDSI are lower overall and range from $r = -0.38$ in $\delta^{18}\text{O}_c$ to $r = -0.49$ in $\delta^{13}\text{C}_c$. While the correlations with JJA precipitation are temporally stable for all detrendings, T_{mean} correlations decrease toward the lower frequency domain (Fig. 7.5). Spectral coherence analyses between the isotope and climate data support these findings and point to precipitation as the dominant climatic factor for $\delta^{13}\text{C}_c$, $\delta^{13}\text{C}_m$, and $\delta^{18}\text{O}_c$ variability (Fig. S7.7). Similar results are found for the pin-corrected $\delta^{13}\text{C}$ data (Fig. S7.8). For $\delta^2\text{H}_m$, the highest correlation is found with June-September (JJAS) T_{mean} ($r = -0.44$, $p < 0.001$), while no significant correlations are obtained with precipitation. Running correlations between $\delta^2\text{H}_m$ and JJAS T_{mean} are stable over time and for all detrendings, but $\delta^2\text{H}_m$ lacks significant coherence with temperature data at mid-to-low frequencies (~ 2 -4 and > 10 years; Fig. S7.9). Correlations between TRSI and previous-year climate data are weak and significant

($p < 0.01$) only for $\delta^{13}\text{C}$ and August T_{mean} ($r = -0.29$ for $\delta^{13}\text{C}_c$ and -0.33 for $\delta^{13}\text{C}_m$), and for $\delta^2\text{H}_m$ and June T_{mean} ($r = -0.31$).

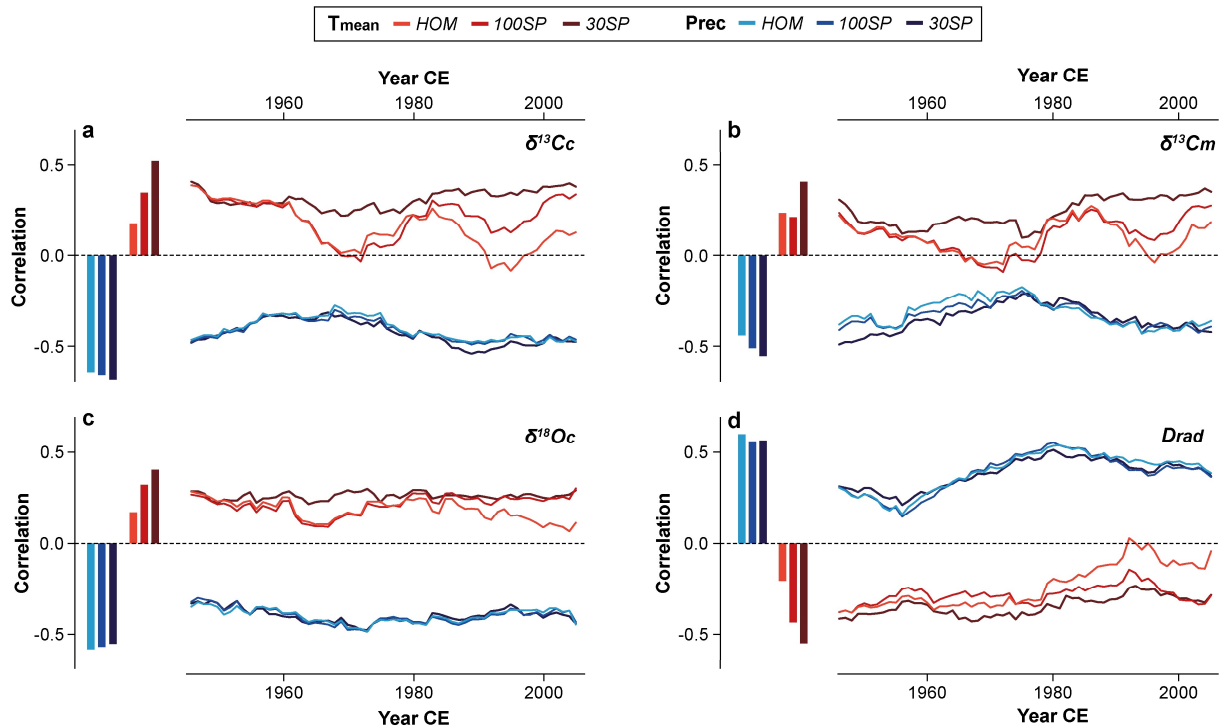


Fig. 7.5 Temporal stability of the temperature (T_{mean}) and precipitation (Prec) signals in (a) $\delta^{13}\text{C}_c$, (b) $\delta^{13}\text{C}_m$, (c) $\delta^{18}\text{O}_c$, and (d) D_{rad} . Vertical bars (left) show correlations between the HOM, 30SP, and 100SP proxy records and June-August T_{mean} (red) and precipitation (blue) calculated for 1931-2020 CE. Curves in the right panels show 31-year running correlations for the different detrendings.

The climate sensitivity of D_{rad} is inverse to that of $\delta^{13}\text{C}_c$, $\delta^{13}\text{C}_m$, and $\delta^{18}\text{O}_c$, yet similar in terms of seasonality and strength. The annual D_{rad} record, which represents the average radial lumen diameter of earlywood and latewood cells, shows the highest 30SP correlations with JJA precipitation ($r = 0.56$), T_{mean} ($r = -0.55$), and cloud cover ($r = 0.62$, all $p < 0.001$). Although 30SP correlations between D_{rad} and cloud cover are slightly higher than those with precipitation, considerably lower correlations obtained for the HOM-detrended data ($r = 0.43$) indicate a stronger low-frequency coherence with precipitation ($r = 0.60$; **Fig. S7.10**). The 30SP correlations with the PDSI are significant from August to October ($r = 0.28$ - 0.34 , $p < 0.01$) and about as strong as with previous-year June T_{mean} ($r = 0.38$). CWT_{rad} and CWT_{tan} indicate almost no significant climate correlations at annual resolution. Only CWT_{rad} correlates significantly with September T_{mean} ($r = 0.28$) and cloud cover in current and previous August ($r = -0.28$ and 0.28 , $p < 0.01$).

7.3.3 QWA sector chronologies

The total QWA data comprise ~ 2.5 million individual cell measurements. The ten anatomical sectors, ranging from the early- (I) to the latewood (X), represent the intra-annual variability of D_{rad} , CWT_{rad} , and CWT_{tan} from 1861-2020 CE (**Fig. 7.6a**). D_{rad} decreases from $30.3 \pm 4.2 \mu\text{m}$

($\pm 1\sigma$, sector I) to $6.7 \pm 1.5 \mu\text{m}$ (sector X) throughout the ring. CWT_{tan} increases from $3.2 \pm 0.3 \mu\text{m}$ in sector I to $3.8 \pm 0.5 \mu\text{m}$ in sector VIII and decreases to $3.3 \pm 0.4 \mu\text{m}$ in sector X, whereas CWT_{rad} increases from $3.7 \pm 0.4 \mu\text{m}$ (I) to $5.0 \pm 0.5 \mu\text{m}$ (X). Consequently, CWT_{rad} is, on average, $0.8 \mu\text{m}$ larger than CWT_{tan} . D_{rad} displays higher Rbar values than CWT in all sectors. The Rbar values of D_{rad} and CWT_{rad} generally increase toward the latewood, while those of CWT_{tan} remain relatively stable throughout the ring (**Table S7.1**). AC1 values of CWT (0.43-0.67) are overall higher than those of D_{rad} (0.23-0.44).

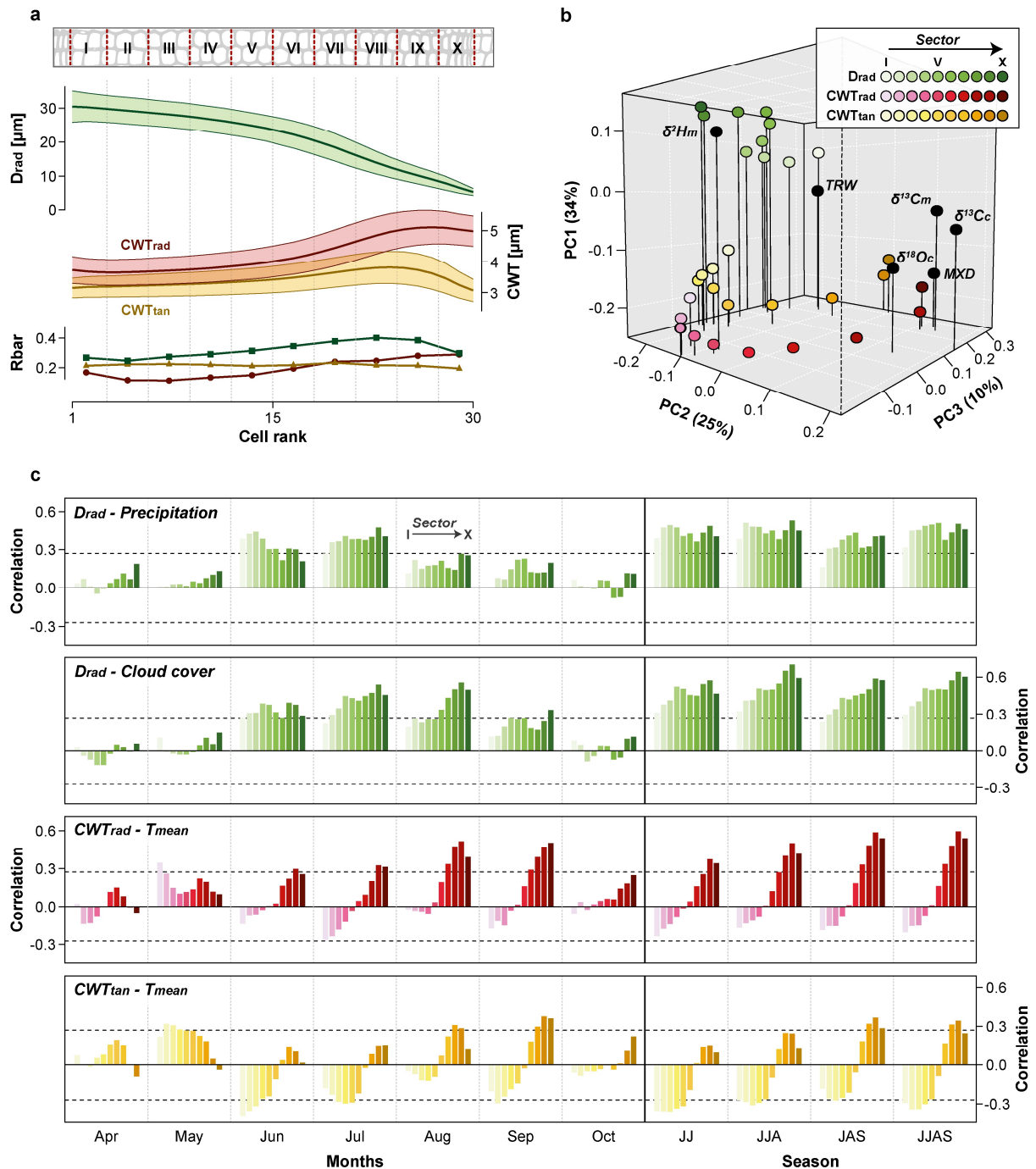


Fig. 7.6 Intra-ring sectors of wood anatomical traits. **(a)** Tracheidograms of D_{rad} (upper panel), CWT_{rad} , and CWT_{tan} (middle panel), shown together with the mean Rbar of each 30SP sector chronology calculated for 1861-2020 CE (bottom panel). Shaded areas indicate $\pm 1\sigma$. The sectors are labeled with Roman

numerals (I-X). **(b)** Three-dimensional PCA plot showing the first three principal components computed on the 30SP-detrended TRW, MXD, $\delta^{13}\text{C}_c$, $\delta^{13}\text{C}_m$, $\delta^{18}\text{O}_c$, $\delta^2\text{H}_m$ (black circles) records, and the 30 D_{rad} , CWT_{rad} , and CWT_{tan} sector chronologies (colored circles). **(c)** Correlations between the anatomical sector chronologies (I = left, X = right) and their main climate targets for 1861-2020 CE. Horizontal dashed lines indicate the significance level of $p < 0.01$.

PCA on the 30 sector chronologies and the six annually resolved TRW, MXD, and TRSI records reveals close similarities in interannual variability between the final three CWT sectors (VIII-X) and MXD, $\delta^{18}\text{O}_c$, $\delta^{13}\text{C}_c$, and $\delta^{13}\text{C}_m$, as well as between the initial D_{rad} sectors (I-II) and TRW, and the subsequent D_{rad} sectors (III-X) and $\delta^2\text{H}_m$ (**Fig. 7.6b**). The first three components (PC1-3) explain 69% of the variance and are significant according to the Rnd-Lambda stopping rule (**Table S7.2**). PC1 separates D_{rad} from CWT. The CWT sectors show a smooth transition along PC2 and PC3, while PC3 primarily separates the D_{rad} sectors.

Correlations between the D_{rad} sectors and climate data support the results obtained from the annually resolved D_{rad} record, indicating precipitation as the dominant climatic factor for radial cell expansion (**Fig. 7.6c**). D_{rad} displays significant ($p < 0.01$) correlations with JJA precipitation across all sectors, with r ranging from 0.38 (I) to 0.54 (IX) for the 30SP data (1931-2020 CE). Although D_{rad} lacks significant correlation with August precipitation ($p > 0.01$), the scores for June-August are consistently higher than for June-July in all sectors and for all detrendings. In addition, all D_{rad} sectors indicate significant positive correlations with JJA cloud cover ($r = 0.32$ - 0.71), particularly prominent in the final three sectors ($r_{\text{VIII-X}} \geq 0.60$). The strong D_{rad} response to JJA cloud cover in sectors VIII-X coincides with the pronounced sensitivity of these data to August T_{mean} ($r \geq 0.42$; **Fig. S7.11**) and the strong negative relationship between August T_{mean} and cloud cover ($r = -0.67$). For comparison, in June and July, both climate variables are notably less correlated ($r = -0.45$ and -0.38).

The sectorial CWT chronologies show the strongest response to T_{mean} , particularly in sectors VIII-X. The highest correlations are found between CWT_{rad} sectors VIII-X and JJAS T_{mean} ($r = 0.46$ - 0.57 , $p < 0.01$ for the 30SP data). The equivalent CWT_{tan} sectors correlate substantially weaker with JJAS T_{mean} ($r = 0.24$ - 0.34), suggesting a stronger temperature response in CWT_{rad} compared to CWT_{tan} . Combining the final three CWT_{rad} sectors (VIII-X) into one mean chronology representing the latewood ($\text{CWT}_{\text{rad,LW}}$) results in a 30SP correlation of $r = 0.55$ with JJAS T_{mean} ($p < 0.001$). The $\text{CWT}_{\text{rad,LW}}$ record covaries with T_{mean} at interannual to decadal scales (2-10 years) but exhibits inconsistencies at lower frequencies (**Fig. S7.8c**).

7.4 Discussion

7.4.1 Proxy characteristics and covariance

Among the Mt. Smolikas proxies, cellulose stable carbon and oxygen isotope ratios show the highest inter-series correlations. The strong $\delta^{13}\text{C}_c$ and $\delta^{18}\text{O}_c$ coherence is particularly reflected in the high-frequency domain ($R_{\text{bar}} \geq 0.62$ for the 30SP data) but is also evident in closely aligned low-frequency trends among the individual series (**Fig. 7.3**). These findings are in line with previous studies on Mt. Smolikas relict wood (Römer et al. 2023) and living Bosnian pines from the Dinaric Alps (Lukač et al. 2021). Methoxy isotopes show less agreement among the series, with R_{bar} values ranging from 0.30 to 0.40, which are similar those reported for *Larix decidua* from the Western Alps (Riechelmann et al. 2016, 2017) and *Fagus sylvatica* from southern Germany (Anhäuser et al. 2020; Wieland et al. 2022).

Despite lignin methoxy groups exhibiting an average ^{13}C depletion of 3.15 mUr compared to cellulose, which is consistent with estimates between cellulose and lignin $\delta^{13}\text{C}$ (Loader et al. 2003; Robertson et al. 2004; Wilson & Grinsted 1977), the $\delta^{13}\text{C}$ records of both compounds display significant coherence at interannual to decadal timescales (~2-20 years; **Fig. S7.12**), indicating that these proxies capture similar environmental signals. The lack of lower-frequency covariance (> 20 years) partially results from opposing multidecadal trends, which are particularly evident before ~1910 CE and after ~2000 CE, but weaken when the $\delta^{13}\text{C}_c$ data is pin-corrected (McCarroll et al. 2009; **Fig. S7.13**).

The anatomical trait profiles of *Pinus heldreichii* closely resemble those of other pine species in central and southern Europe (Carrer et al. 2018; Cuny et al. 2014; Hetzer et al. 2014). The gradual decline in D_{rad} from early- to latewood agrees well with that of *Pinus nigra* from Corsica (Hetzer et al. 2014), but is noticeably stronger due to the formation of smaller latewood cells ($6.7 \pm 1.5 \mu\text{m}$ in sector X). CWT shows a monotonic increase toward the latewood, marked by a decline in the final sector, which is more pronounced in CWT_{tan} than CWT_{rad} . The CWT increase in the earlywood and the decline in the final latewood portion are characteristic for most conifer species (e.g., Babushkina et al. 2024; Cuny et al. 2014; Zharkov et al. 2022; Ziaco et al. 2014). The CWT_{tan} values of *Pinus heldreichii* are similar to those reported for *Pinus cembra* growing at the upper treeline in the Alps (~2100 m asl), while CWT_{rad} values are, on average, $0.7 \mu\text{m}$ higher at Mt. Smolikas (Carrer et al. 2018).

The R_{bar} values of the D_{rad} sector chronologies, ranging from $r = 0.25$ to 0.40 after the 30SP detrending, are consistently higher than those of CWT_{rad} and CWT_{tan} . The highest R_{bar} value for D_{rad} is found at annual resolution ($r = 0.43$), indicating that intra-ring partitioning does not enhance the covariance among the individual series. A similar pattern is observed for CWT_{tan} . However, CWT_{rad} sectors VIII-X exhibit notably higher R_{bar} values (≥ 0.25 for the 30SP data)

than the annual record, suggesting a stronger climatic signal in latewood CWT. The obtained R_{bar} values of the last CWT_{rad} sectors VIII-X are similar to those of MXD (Esper et al. 2020a, 2020b; Römer et al. 2021) and latewood CWT at other high-elevation southern European pine sites (Carrer et al. 2018; Lopez-Saez et al. 2023; Ştirbu et al. 2022).

The high AC1 values of TRW and CWT (≥ 0.6), particularly evident in the earlywood sectors (**Table S7.1**), likely reflect carry-over effects resulting from remobilized photoassimilates during earlywood formation (Kagawa et al. 2006) and indicate greater biological memory effects in TRW and CWT compared to the other proxies (Esper et al. 2015b). D_{rad} exhibits lower AC1 values than CWT in all sectors, with higher first-order autocorrelations in the early- than in the latewood. Low AC1 values in $\delta^{13}\text{C}_c$, $\delta^{13}\text{C}_m$, $\delta^{18}\text{O}_c$, and $\delta^2\text{H}_m$ (≤ 0.41) point to negligible memory effects in the TRSI measurements and are consistent with the fact that the isotopic composition of the samples is not systematically biased by changing earlywood-latewood proportions (Torbenson et al. 2023).

7.4.2 Climate signals in TRW and MXD

TRW and MXD measurements on Bosnian pines from Mt. Smolikas have proven to be valuable hydroclimate and temperature proxies. However, while the observed temperature sensitivity in MXD agrees well with previous studies in terms of seasonality and correlation (Esper et al. 2020a; Klippel et al. 2019), the lack of significant hydroclimate signals in TRW is striking (Esper et al. 2021; Klippel et al. 2018). Although the updated TRW chronology shares more than 72% of variance with the well-replicated ($n = 872$ series) and precipitation-sensitive TRW record of Esper et al. (2021) from 1861-2016 CE, TRW correlations with climate are weak and significant only with diurnal temperature range and summer cloud cover (**Fig. 7.7a**). The lack of significant precipitation correlations can be attributed to the fading sensitivity in the early to mid-20th century, likely due to the limited number of nearby precipitation stations included in the CRU data (Esper et al. 2021; Klippel et al. 2018).

For MXD, we found significant correlations with late-summer (July-September) temperature, precipitation, and cloud cover. Given the weak correlation between temperature and precipitation in July-September ($r_{\text{JAS}} = -0.19$, $p > 0.05$), the observed MXD responses indicate that *Pinus heldreichii* reacts to both elevated temperatures and low water availability with the formation of denser latewood (Cook et al. 2015; Leonelli et al. 2017). Summer temperature, however, is the dominant climatic driver of MXD formation (**Fig. 7.7b**). The strong cloud-cover correlations reflect the significant dependence of summer precipitation and air temperature on cloud cover ($r_{\text{JAS}} = 0.56$ and -0.52 , $p < 0.001$), which can significantly modulate solar radiation fluxes, evapotranspiration processes, and rainfall patterns at the surface level (Geiger et al. 2009).

7 Covariance and climate signals among state-of-the-art tree-ring proxies

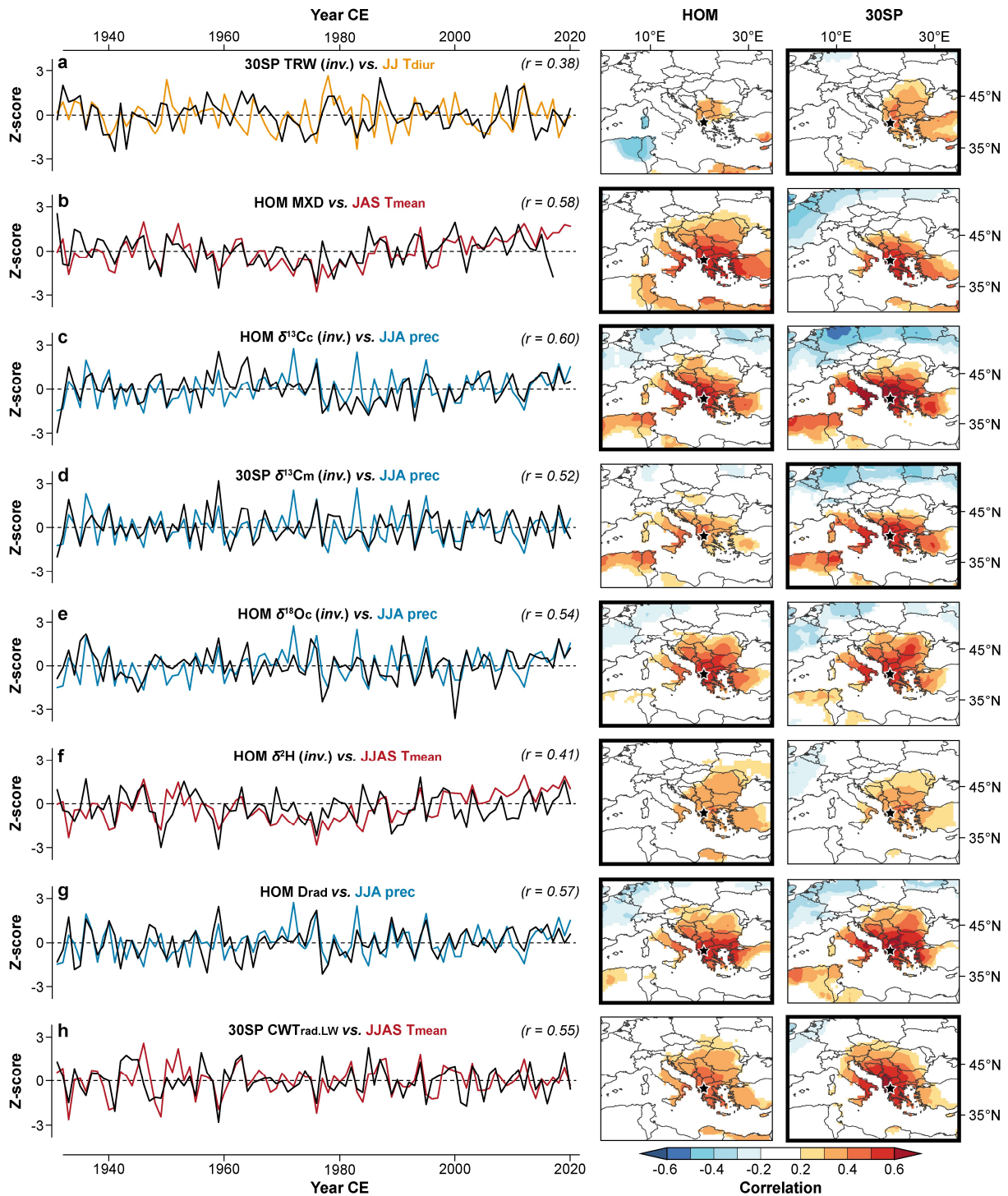


Fig.7.7 Best-fit climate targets. Horizontal-mean (HOM) or 30-year-spline (30SP) detrended proxy chronologies (black curves), shown with the best-correlated climate records (colored curves). All records are z-transformed. TRW, $\delta^{13}C_c$, $\delta^{13}C_m$, $\delta^{18}O_c$, and δ^2H_m are inverted. R values indicate the corresponding correlations between the tree-ring and climate data for 1931-2020 CE (2017 CE for MXD). Right panels display field correlations ($p < 0.05$) between the HOM and 30SP-detrended proxies and their climate targets (CRU TS4.07). Thick frames highlight the best fitting frequency (HOM data is preferred). Black stars mark the study site.

7.4.3 Climate signals in stable isotopes

Stable carbon and oxygen isotopes from cellulose and lignin methoxy groups reflect significant temperature and hydroclimatic signals that support previous findings from the Mediterranean (Andreu et al. 2008; Konter et al. 2014; Levanič et al. 2020; Lukac et al. 2021; Szymczak et al. 2012; Treydte et al. 2007). The positive $\delta^{13}\text{C}$ correlation with summer temperature and negative correlation with summer precipitation appear physiologically meaningful, as high air temperatures and vapor-pressure deficits (VPD) impair CO_2 diffusion into the needles by stomatal closure, thereby reducing internal CO_2 concentrations and carboxylation discrimination against ^{13}C , leading to higher $\delta^{13}\text{C}$ values (Farquhar et al. 1982). Precipitation events otherwise reduce VPD and allow stomata to open. Moreover, high temperatures and low humidity increase transpiration, which leads to a loss of lighter oxygen isotopes (^{16}O) at the leaf level and therefore to higher $\delta^{18}\text{O}$ values than those of the source water (McCarroll & Loader 2004). Hence, both $\delta^{13}\text{C}$ and $\delta^{18}\text{O}$ are closely linked to summer temperature and moisture conditions, as reflected in the strong correlations of $\delta^{13}\text{C}_c$, $\delta^{13}\text{C}_m$, and $\delta^{18}\text{O}_c$ with these climate variables.

Higher and more robust correlations with June-August precipitation than with air temperature suggest that summer precipitation is the dominant climatic forcing of $\delta^{13}\text{C}$ and $\delta^{18}\text{O}$ variability. This conclusion is supported by significant correlations between $\delta^{18}\text{O}_c$ and the $\delta^{18}\text{O}$ of precipitation (**Fig. S7.14**), revealing that $\delta^{18}\text{O}_c$ reflects the $\delta^{18}\text{O}$ signature of the precipitation-derived source water, but is modulated by soil evaporation and transpiration-induced ^{18}O enrichment (Yakir & Sternberg 2000). The lack of significant correlations with previous-year climate data and the low AC1 values of $\delta^{18}\text{O}_c$ indicate that the water used for photosynthetic carbohydrate formation primarily originates from recent precipitation events. Correlations with precipitation are robust over time and for all detrendings, suggesting that both $\delta^{13}\text{C}$ and $\delta^{18}\text{O}$ reliably reflect summer moisture variations at interannual to multidecadal timescales. Only $\delta^{13}\text{C}_m$ reveals a weaker association at lower frequencies. The robust precipitation signals and the fading temperature sensitivities toward the present, particularly evident at lower frequencies (i.e., for the HOM data), support previous results on *Pinus heldreichii* $\delta^{13}\text{C}_c$ and $\delta^{18}\text{O}_c$ from the Dinaric Alps in Montenegro (Levanič et al. 2020; Lukač et al. 2021), the Apennines in Italy, and the Pirin Mountains in Bulgaria (Freund et al. 2023; Treydte et al. 2007).

Unlike carbon and oxygen isotopes, $\delta^2\text{H}_m$ is negatively correlated with June-September temperature ($p < 0.01$). Given the lack of studies assessing the climate sensitivity of $\delta^2\text{H}_m$ in similar environments, our results demonstrate for the first time that $\delta^2\text{H}_m$ may serve as a reliable temperature proxy in the Mediterranean (**Fig. 7.7f**). However, most previous studies reported positive correlations between $\delta^2\text{H}_m$ and air temperatures at mid-latitudes and lower altitudes (Anhäuser et al. 2020; Lu et al. 2020; Mischel et al. 2015; Wang et al. 2020; Wieland et al. 2022).

Only Riechelmann et al. (2017) found a comparable (negative) temperature response in $\delta^2\text{H}_m$ of *Larix decidua* trees from the Western Alps. One plausible explanation for this inverse temperature response could be related to the seasonally fluctuating $\delta^2\text{H}$ signature of precipitation. Since lignin synthesis takes place in the xylem tissue, $\delta^2\text{H}_m$ is unaffected by the evaporative ^2H enrichment of leaf water and thus closely reflects the $\delta^2\text{H}$ signature of the plant's source water, which is positively related to air temperature (Anhäuser et al. 2017). However, similar to Riechelmann et al. (2017), we found a negative correlation between the $\delta^2\text{H}$ values of methoxy groups and summer precipitation ($r_{\text{JJAS}} = -0.27$). In summer, the $\delta^2\text{H}$ values of precipitation are notably higher compared to the other seasons (**Fig. S7.15**), resulting in elevated $\delta^2\text{H}$ values in soil water during years with abundant summer rain and cooler temperatures. Vice versa, in warm and dry summers, the $\delta^2\text{H}$ values of soil water decrease due to the lower contribution of ^2H -enriched summer rain. Hence, $\delta^2\text{H}_m$ seems to reflect the seasonal origin of the source water used for lignin methoxy group formation (Allen et al. 2019). The use of deeper ground water sources may also explain the missing association with precipitation $\delta^2\text{H}$, but seems unlikely due to the shallow soils at Mt. Smolikas.

7.4.4 Climate signals in wood anatomical traits

The wood anatomical features of *Pinus heldreichii* are highly sensitive to hydrothermal conditions in summer. D_{rad} , which primarily determines the conductive xylem area, shows a strong summer precipitation response at annual resolution, surpassing that of the sectorial chronologies (**Fig. 7.7g**). Greater covariance among the series and stronger climatic responses in D_{rad} , compared to tangential diameter and lumen area (not shown), support that climatic imprints are distinctly stronger in the radial than in the tangential lumen diameter (Cuny et al. 2014). The precipitation sensitivity of D_{rad} is likely transmitted through soil moisture deficits controlling turgor pressure and cell enlargement (Carvalho et al. 2015; Ziaco 2020). Abundant rainfall, on the other hand, can promote the formation of larger tracheid lumina (Fonti et al. 2010; Peters et al. 2021). The precipitation response of D_{rad} aligns with studies on western Mediterranean pine species, providing empirical evidence for the importance of summer water availability on conductive xylem features (Hetzer et al. 2014; Pacheco et al. 2016), and confirms similar hydroclimate signals in *Pinus heldreichii* from high-elevation Eastern Mediterranean sites.

The distinction between CWT_{rad} and CWT_{tan} , along with the intra-ring partitioning, reveals that Bosnian pines primarily respond to high summer temperatures through radial wall thickening of the latewood cells. The final three CWT sectors VIII-X show significant positive temperature responses, which are notably stronger in CWT_{rad} than in CWT_{tan} . These results are supported by the regular displacement of the PCA loadings, suggesting a higher agreement with MXD for latewood CWT_{rad} than for CWT_{tan} . The latewood CWT_{rad} record is positively correlated with

MXD ($r_{1861-2017} = 0.68$, $p < 0.001$ for 30SP data) and shows a strong temperature signal from June to September (**Fig. 7.7h**). The temperature sensitivity of latewood CWT and the lack of similar climatic responses in earlywood CWT are in line with studies on *Pinus nigra* (Hetzer et al. 2014), *Picea abies* (Castagneri et al. 2017), and *Larix decidua* (Carrer et al. 2016), but differ from those on *Pinus cembra* growing in the Alps and Carpathians, reporting consistent temperature signals in both earlywood and latewood CWT (Carrer et al. 2018; Lopez-Saez et al. 2023; Ştirbu et al. 2022).

7.4.5 Paleoclimatic skill of the tree-ring proxies

Among all proxies, $\delta^{13}\text{C}_c$ shows the greatest potential to reconstruct the full spectrum of high-to-low-frequency summer precipitation variability (**Fig. 7.8**). The $\delta^{13}\text{C}_c$ data is characterized by an exceptionally strong covariance among the series and stationary correlations with June-August precipitation throughout the 20th and 21st centuries. The lack of long-term ontogenetic trends in $\delta^{13}\text{C}_c$ precludes biologically induced low-frequency noise, supporting the use of raw $\delta^{13}\text{C}_c$ data for climate calibration (Wieland et al. 2024). Given the high inter-series correlation and hydroclimate signal strength, along with the prolonged climate seasonality compared to TRW (June-July) and the absence of age-related trends, we conclude that annually resolved and non-pooled $\delta^{13}\text{C}_c$ measurements are a superior proxy to reconstruct past summer precipitation in the Mediterranean, far exceeding the skill of traditional TRW chronologies.

8. Workload								References (1) Esper et al. 2021 (2) Esper et al. 2020a (3) Wieland et al. 2024	
7. Detrending									
6. Covariance									
5. Stationarity									
4. Correlation									
3. Frequency									
2. Seasonality									
1. Climate signal									
TRW	T_{diur}	JJ	high	-0.38	no	0.32	required ⁽¹⁾	●	
MXD	T_{mean}	JAS	full	0.58	yes	0.26	required ⁽²⁾	●	
$\delta^{13}\text{C}_c$	Precipitation	JJA	full	-0.60	yes	0.56	no ⁽³⁾	●	
$\delta^{13}\text{C}_m$	Precipitation	JJA	high	-0.52	yes	0.30	required ⁽³⁾	●	
$\delta^{18}\text{O}_c$	Precipitation	JJA	full	-0.54	yes	0.55	required ⁽³⁾	●	
$\delta^2\text{H}_m$	T_{mean}	JJAS	full	-0.41	yes	0.24	required ⁽³⁾	●	
Drad	Precipitation	JJA	full	0.57	yes	0.29	likely required	●	
CWT _{rad.LW}	T_{mean}	JJAS	high	0.55	yes	0.36	likely required	●	

Fig. 7.8 Paleoclimatic skill of the tree-ring proxies. Summary of the best-fit climate calibrations computed for 1931-2020 CE (1931-2017 CE for MXD). Please note that correlation and covariance values refer to the optimum frequency (high = 30SP, full = HOM data) and may deviate slightly from the values in Table 7.1 due to the shorter period.

$\delta^{18}\text{O}_c$, $\delta^{13}\text{C}_m$, and D_{rad} also exhibit strong summer precipitation signals. However, these proxies face stronger statistical limitations due to long-term age-related trends in $\delta^{18}\text{O}_c$ and $\delta^{13}\text{C}_m$ and substantial $\delta^{18}\text{O}_c$ offsets between living and relict wood (Wieland et al. 2024). Significant ontogenetic trends are also characteristic for D_{rad} , particularly over the first 100-150 years of tree age (Carrer et al. 2015). Future QWA measurements of relict wood will improve our understanding of such non-climatic noise inherent in anatomical traits. The overlapping precipitation seasonality and strong covariance among $\delta^{13}\text{C}_c$, $\delta^{18}\text{O}_c$, $\delta^{13}\text{C}_m$, and D_{rad} at interannual to multidecadal timescales, despite minor low-frequency discrepancies in $\delta^{13}\text{C}_m$, suggest that proxy combinations could be useful to improve reconstruction skills and assess uncertainties. Moreover, the close association between D_{rad} and summer cloud cover, driven by the dependence of precipitation on cloud cover and particularly evident at high frequencies, underscores the potential to gain new insights into past climatic extremes.

MXD shows the greatest skill to reconstruct the full range of interannual to multidecadal summer temperature variability. Although MXD requires standardization prior to chronology development and climate calibration (Bräker 1981), its stronger temperature sensitivity compared to $\text{CWT}_{\text{rad,LW}}$ and $\delta^2\text{H}_m$, along with its lower workload, highlight MXD's superior paleoclimatic skill in high-elevation Mediterranean environments (Büntgen et al. 2017, 2024; Esper et al. 2020a, 2020b). While latewood CWT_{rad} lacks significant correlation with observational temperatures at decadal to multidecadal scales and can thus only provide valuable information on past temperature extremes, $\delta^2\text{H}_m$ can be considered as an alternative temperature proxy to MXD. However, further research is needed to consolidate the inverse temperature response of $\delta^2\text{H}_m$ in the Mediterranean and to assess signals strengths at lower elevations (Feakins et al. 2013; Greule et al. 2021), where MXD typically fails as a climate proxy.

7.5 Conclusion

Our assessment of covariance and climate signals in TRW, MXD, $\delta^{13}\text{C}_c$, $\delta^{18}\text{O}_c$, $\delta^{13}\text{C}_m$, $\delta^2\text{H}_m$, D_{rad} , and CTW from Mt. Smolikas (Greece) reveals advantages of TRSI and QWA measurements over traditional TRW for reconstructing past hydroclimate variability, thereby opening new avenues for an enhanced understanding of past climate dynamics in the Mediterranean over the Common Era (Anchukaitis et al. 2024; Cook et al. 2015). Among all proxies, $\delta^{13}\text{C}_c$ exhibits the greatest potential for an inter-regional summer precipitation reconstruction, which would be key to contextualize the recent aridification of the Mediterranean. MXD proves to be the most skilful summer temperature proxy, driven by temperature-induced reductions in D_{rad} and increases in CWT, especially in August and September. However, while the temperature signals of the wood anatomical traits alone do not surpass those of MXD, $\delta^2\text{H}_m$ may serve as

an alternative temperature proxy, potentially capable of capturing climate signals in lower-elevation regions where MXD typically fails as a climate predictor.

7.6 Acknowledgments

Not available online.

7.7 References

- Allen ST, Kirchner JW, Braun S, Siegwolf RTW, Goldsmith GR (2019) Seasonal origins of soil water used by trees. *Hydrol Earth Syst Sci* 23: 1199-1210.
- Anchukaitis KJ, Touchan R, Meko DM, Kherchouche D, Slimani S, Sivrikaya F, Ilmen R, Mitsopoulos I, Stephan J, Attieh J, et al. (2024) Enhancing spatiotemporal paleoclimate reconstructions of hydroclimate across the Mediterranean over the last millennium. *Clim Dyn*, <https://doi.org/10.1007/s00382-024-07166-6>.
- Andreu L, Planells O, Gutierrez E, Helle G, Schleser GH (2008) Climatic significance of tree-ring width and $\delta^{13}\text{C}$ in a Spanish pine forest network. *Tellus B Chem Phys Meteorol* 60: 771-781.
- Anhäuser T, Greule M, Polag D, Bowen GJ, Keppler F (2017) Mean annual temperatures of mid-latitude regions derived from $\delta^2\text{H}$ values of wood lignin methoxyl groups and its implications for paleoclimate studies. *Sci Total Environ* 574: 1276-1282.
- Anhäuser T, Sehls B, Thomas W, Hartl C, Greule M, Scholz D, Esper J, Keppler F (2020) Tree-ring $\delta^2\text{H}$ values from lignin methoxyl groups indicate sensitivity to European scale temperature changes. *Palaeogeogr Palaeoclimatol Palaeoecol* 546: 109665.
- Babushkina EA, Dergunov DR, Zharkov MS, Belokopytova LV, Zhirnova DF, Yang B, Liu J, Peng X, Vaganov EA (2024) Wood anatomy chronologies of Scots pine in the foothills of the Western Sayan (Siberia). *J For Res* 35: 45.
- Balanzategui D, Nordhauß H, Heinrich I, Biondi F, Miley N, Hurley AG, Ziaco E (2021) Wood anatomy of Douglas-fir in eastern Arizona and its relationship with Pacific Basin climate. *Front Plant Sci* 12: 702442.

- Belmecheri S, Wright WE, Szejner P (2022) Sample collection and preparation for annual and intra-annual tree-ring isotope chronologies. In: Siegwolf RTW, Brooks JR, Roden J, Saurer M (eds) *Stable isotopes in tree rings – inferring physiological, climatic and environmental responses*. Springer, Cham, Switzerland: pp 103-134.
- Belokopytova LV, Babushkina EA, Zhirnova DF, Panyushkina IP, Vaganov EA (2019) Pine and larch tracheids capture seasonal variations of climatic signal at moisture-limited sites. *Trees* 33: 227-242.
- Björklund J, Seftigen K, Fonti P, Nievergelt D, von Arx G (2020) Dendroclimatic potential of dendroanatomy in temperature-sensitive *Pinus sylvestris*. *Dendrochronologia* 60: 125673.
- Björklund J, Seftigen K, Stoffel M, Fonti MV, Kottlow S, Frank DC, Esper J, Fonti P, Goosse H, Gunnarson BE, et al. (2023) Fennoscandian tree-ring anatomy shows a warmer modern than medieval climate. *Nature* 620: 97-103.
- Boettger T, Haupt M, Knöllner K, Weise SM, Waterhouse JS, Rinne KT, Loader NJ, Sonninen E, Jungner H, Masson-Delmotte V, et al. (2007) Wood cellulose preparation methods and mass spectrometric analyses of $\delta^{13}\text{C}$, $\delta^{18}\text{O}$, and nonexchangeable $\delta^2\text{H}$ values in cellulose, sugar, and starch: an interlaboratory comparison. *Anal Chem* 79: 4603-4612.
- Bräker OU (1981) Der Alterstrend bei Jahrringdichten und Jahrringbreiten von Nadelhölzern und sein Ausgleich. *Mitteilungen der forstlichen Bundes-Versuchsanstalt Wien* 142: 75-102.
- Brand WA, Coplen TB (2012) Stable isotope deltas: tiny, yet robust signatures in nature. *Isot Environ Health Stud* 48: 393-409.
- Büntgen U (2022) Scrutinizing tree-ring parameters for Holocene climate reconstructions. *WIREs Clim Change* 13: e778.
- Büntgen U, Kolář T, Rybníček M, Koňasová E, Trnka M, Ač A, Krusic PJ, Esper J, Treydte K, Reinig F, et al. (2020) No age trends in stable isotopes. *Paleoceanogr Paleoclimatol* 35: e2019PA003831.
- Büntgen U, Krusic PJ, Verstege A, Sangüesa-Barreda G, Wagner S, Camarero JJ, Ljungqvist FC, Zorita E, Oppenheimer C, Konter O, et al. (2017) New tree-ring evidence from the Pyrenees reveals Western Mediterranean climate variability since medieval times. *J Clim* 30: 5295-5318.
- Büntgen U, Reinig F, Verstege A, Piermattei A, Kunz M, Krusic PJ, Slavin P, Štěpánek P, Torbenson M, Martínez del Castillo E, et al. (2024) Recent summer warming over the western Mediterranean region is unprecedented since medieval times. *Glob Planet Change* 232: 104336.

- Büntgen U, Urban O, Krusic PJ, Rybníček M, Kolář T, Kyncl T, Ač A, Koňasová E, Čáslavský J, Esper J, et al. (2021) Recent European drought extremes beyond Common Era background variability. *Nat Geosci* 14: 190-196.
- Carrer M, Brunetti M, Castagneri D (2016) The imprint of extreme climate events in century-long time series of wood anatomical traits in high-elevation conifers. *Front Plant Sci* 7: 683.
- Carrer M, Unterholzner L, Castagneri D (2018) Wood anatomical traits highlight complex temperature influence on *Pinus cembra* at high elevation in the Eastern Alps. *Int J Biometeorol* 62: 1745-1753.
- Carrer M, von Arx G, Castagneri D, Petit G (2015) Distilling allometric and environmental information from time series of conduit size: the standardization issue and its relationship to tree hydraulic architecture. *Tree Physiol* 35: 27-33.
- Carvalho A, Nabais C, Vieira J, Rossi S, Campelo F (2015) Plastic response of tracheids in *Pinus pinaster* in a water-limited environment: adjusting lumen size instead of wall thickness. *PLoS One* 10: e0136305.
- Castagneri D, Fonti P, von Arx G, Carrer M (2017) How does climate influence xylem morphogenesis over the growing season? Insights from long-term intra-ring anatomy in *Picea abies*. *Ann Bot* 119: 1011-1020.
- Cook ER, Peters K (1997) Calculating unbiased tree-ring indices for the study of climatic and environmental change. *Holocene* 7: 361-370.
- Cook ER, Krusic PJ, Peters K, Holmes RL (2017) *Program ARSTAN (ARS41d), autoregressive tree-ring standardization program*. Tree-ring laboratory of the Lamont-Doherty Earth Observatory, Palisades, NY, USA.
- Cook ER, Seager R, Kushnir Y, Briffa KR, Büntgen U, Frank D, Krusic PJ, Tegel W, van der Schrier G, Andreu-Hayles L, et al. (2015) Old World megadroughts and pluvials during the Common Era. *Sci Adv* 1: e1500561.
- Cramer W, Guiot J, Fader M, Garrabou J, Gattuso J-P, Iglesias A, Lange MA, Lionello P, Llasat MC, Paz S, et al. (2018) Climate change and interconnected risks to sustainable development in the Mediterranean. *Nat Clim Change* 8: 972-980.
- Cuny HE, Rathgeber CBK, Frank DC, Fonti P, Fournier M (2014) Kinetics of tracheid development explain conifer tree-ring structure. *New Phytol* 203: 1231-1241.
- Dansgaard W (1964) Stable isotopes in precipitation. *Tellus A Dyn Meteorol Oceanogr* 16: 436-468.
- Dorado Liñán I, Gutiérrez E, Heinrich I, Andreu-Hayles L, Muntán E, Campelo F, Helle G (2012) Age effects and climate response in trees: a multi-proxy tree-ring test in old-growth life stages. *Eur J Forest Res* 131: 933-944.

- Esper J, Hartl C, Tejedor E, de Luis M, Günther B, Büntgen U (2020b) High-resolution temperature variability reconstructed from Black pine tree ring densities in southern Spain. *Atmosphere* 11: 748.
- Esper J, Klippel L, Krusic PJ, Konter O, Raible CC, Xoplaki E, Luterbacher J, Büntgen U (2020a) Eastern Mediterranean summer temperatures since 730 CE from Mt. Smolikas tree-ring densities. *Clim Dyn* 54: 1367-1382.
- Esper J, Konter O, Klippel L, Krusic PJ, Büntgen U (2021) Pre-instrumental summer precipitation variability in northwestern Greece from a high-elevation *Pinus heldreichii* network. *Int J Climatol* 41: 2828-2839.
- Esper J, Konter O, Krusic PJ, Saurer M, Holzkämper S, Büntgen U (2015a) Long-term summer temperature variations in the Pyrenees from detrended stable carbon isotopes. *Geochronometria* 42: 53-59.
- Esper J, Schneider L, Smerdon JE, Schöne BR, Büntgen U (2015b) Signals and memory in tree-ring width and density data. *Dendrochronologia* 35: 62-70.
- Farquhar GD, O'Leary MH, Berry JA (1982) On the relationship between carbon isotope discrimination and the intercellular carbon dioxide concentration in leaves. *Aust J Plant Physiol* 9: 121-137.
- Feakins SJ, Ellsworth PV, Sternberg L (2013) Lignin methoxyl hydrogen isotope ratios in a coastal ecosystem. *Geochim Cosmochim Acta* 121: 54-66.
- Fonti P, von Arx G, García-González I, Eilmann B, Sass-Klaassen U, Gärtner H, Eckstein D (2010) Studying global change through investigation of the plastic responses of xylem anatomy in tree rings. *New Phytol* 185: 42-53.
- Frank DC, Esper J, Cook ER (2007) Adjustment for proxy number and coherence in a large-scale temperature reconstruction. *Geophys Res Lett* 34: L16709.
- Freund MB, Helle G, Balting DF, Ballis N, Schleser GH, Cubasch U (2023) European tree-ring isotopes indicate unusual recent hydroclimate. *Commun Earth Environ* 4: 26.
- Gagen M, McCarroll D, Loader NJ, Robertson I, Jalkanen R, Anchukaitis KJ (2007) Exorcising the 'segment length curse': summer temperature reconstruction since AD 1640 using non-detrended stable carbon isotope ratios from pine trees in northern Finland. *Holocene* 17: 435-446.
- Geiger R, Aron RH, Todhunter P (2009) *The climate near the ground*. Rowman & Littlefield Publishing Group, Lanham, MD, USA.
- González-Cásares M, Camarero JJ, Colangelo M, Rita A, Pompa-García M (2019) High responsiveness of wood anatomy to water availability and drought near the equatorial rear edge of Douglas-fir. *Can J For Res* 49: 1114-1123.

- Gori Y, Wehrens R, Greule M, Keppler F, Ziller L, La Porta N, Camin F (2013) Carbon, hydrogen and oxygen stable isotope ratios of whole wood, cellulose and lignin methoxyl groups of *Picea abies* as climate proxies. *Rapid Commun Mass Spectrom* 27: 265-275.
- Greule M, Moossen H, Geilmann H, Brand WA, Keppler F (2019) Methyl sulfates as methoxy isotopic reference materials for $\delta^{13}\text{C}$ and $\delta^2\text{H}$ measurements. *Rapid Commun Mass Spectrom* 33: 343-350.
- Greule M, Moossen H, Lloyd MK, Geilmann H, Brand WA, Eiler JM, Qi H, Keppler F (2020) Three wood isotopic reference materials for $\delta^2\text{H}$ and $\delta^{13}\text{C}$ measurements of plant methoxy groups. *Chem Geol* 533: 119428.
- Greule M, Mosandl A, Hamilton JTG, Keppler F (2008) A rapid and precise method for determination of D/H ratios of plant methoxyl groups. *Rapid Commun Mass Spectrom* 22: 3983-3988.
- Greule M, Mosandl A, Hamilton JTG, Keppler F (2009) A simple rapid method to precisely determine $^{13}\text{C}/^{12}\text{C}$ ratios of plant methoxyl groups. *Rapid Commun Mass Spectrom* 23: 1710-1714.
- Greule M, Wieland A, Keppler F (2021) Measurements and applications of $\delta^2\text{H}$ values of wood lignin methoxy groups for paleoclimatic studies. *Quat Sci Rev* 268: 107107.
- Harris I, Osborn TJ, Jones P, Lister D (2020) Version 4 of the CRU TS monthly high-resolution gridded multivariate climate dataset. *Sci Data* 7: 109.
- Hartl-Meier C, Zang C, Büntgen U, Esper J, Rothe A, Göttlein A, Dirnböck T, Treydte K (2015) Uniform climate sensitivity in tree-ring stable isotopes across species and sites in a mid-latitude temperate forest. *Tree Physiol* 35: 4-15.
- Hetzer T, Bräuning A, Leuschner HH (2014) High-resolution climatic analysis of wood anatomical features in Corsican pine from Corsica (France) using latewood tracheid profiles. *Trees* 28: 1279-1288.
- Hoerling M, Eischeid J, Perlwitz J, Quan X, Zhang T, Pegion P (2012) On the increased frequency of Mediterranean drought. *J Clim* 25: 2146-2161.
- Kagawa A, Sugimoto A, Maximov TC (2006) $^{13}\text{CO}_2$ pulse-labelling of photoassimilates reveals carbon allocation within and between tree rings. *Plant Cell Environ* 29: 1571-1584.
- Keeling CD (1979) The Suess effect: ^{13}C - ^{14}C interrelations. *Environ Int* 2: 229-300.
- Keeling CD, Piper SC, Bacastow RB, Wahlen M, Whorf TP, Heimann M, Meijer HA (2005) Atmospheric CO_2 and $^{13}\text{CO}_2$ exchange with the terrestrial biosphere and oceans from 1978 to 2000: observations and carbon cycle implications. In: Baldwin IT, Caldwell MM, Heldmaier G, Jackson RB, Lange OL, Mooney HA, Schulze ED, Sommer U, Ehleringer JR, Dearing MD, et al. (eds) *A history of atmospheric CO_2 and its effects on plants, animals, and ecosystems*. Springer, New York, USA: pp 83-113.

- Keppler F, Harper DB, Kalin RM, Meier-Augenstein W, Farmer N, Davis S, Schmidt HL, Brown DM, Hamilton JTG (2007) Stable hydrogen isotope ratios of lignin methoxyl groups as a paleoclimate proxy and constraint of the geographical origin of wood. *New Phytol* 176: 600-609.
- Keppler F, Kalin RM, Harper DB, McRoberts WC, Hamilton JTG (2004) Carbon isotope anomaly in the major plant C₁ pool and its global biogeochemical implications. *Biogeosciences* 1: 123-131.
- Klippel L, Krusic PJ, Brandes R, Hartl C, Belmecheri S, Dienst M, Esper J (2018) A 1286-year hydro-climate reconstruction for the Balkan Peninsula. *Boreas* 47: 1218-1229.
- Klippel L, Krusic PJ, Konter O, St George S, Trouet V, Esper J (2019) A 1200+ year reconstruction of temperature extremes for the northeastern Mediterranean region. *Int J Climatol* 39: 2336-2350.
- Konter O, Holzkämper S, Helle G, Büntgen U, Saurer M, Esper J (2014) Climate sensitivity and parameter coherency in annually resolved $\delta^{13}\text{C}$ and $\delta^{18}\text{O}$ from *Pinus uncinata* tree-ring data in the Spanish Pyrenees. *Chem Geol* 377: 12-19.
- Leonelli G, Coppola A, Salvatore MC, Baroni C, Battipaglia G, Gentilesca T, Ripullone F, Borghetti M, Conte E, Tognetti R, et al. (2017) Climate signals in a multispecies tree-ring network from central and southern Italy and reconstruction of the late summer temperatures since the early 1700s. *Clim Past* 13: 1451-1471.
- Levanič T, Jevšenak J, Hafner P (2020) Stable isotopes reveal climate signal hidden in tree rings of endemic Balkan pines. *Atmosphere* 11: 135.
- Lionello P, Scarascia L (2018) The relation between climate change in the Mediterranean region and global warming. *Reg Environ Change* 18: 1481-1493.
- Loader NJ, Robertson I, McCarroll D (2003) Comparison of stable carbon isotope ratios in the whole wood, cellulose and lignin of oak tree-rings. *Palaeogeogr Palaeoclimatol Palaeoecol* 196: 395-407.
- Lopez-Saez J, Corona C, von Arx G, Fonti P, Slamova L, Stoffel M (2023) Tree-ring anatomy of *Pinus cembra* trees opens new avenues for climate reconstructions in the European Alps. *Sci Total Environ* 855: 158605.
- Lu Q, Liu X, Anhäuser T, Keppler F, Wang Y, Zeng X, Zhang Q, Zhang L, Wang K, Zhang Y (2020) Tree-ring lignin proxies in *Larix gmelinii* forest growing in a permafrost area of northeastern China: temporal variation and potential for climate reconstructions. *Ecol Indic* 118: 106750.
- Lukač L, Mikac S, Urban O, Kolář T, Rybníček M, Ač A, Trnka M, Marek MV (2021) Stable isotopes in tree rings of *Pinus heldreichii* can indicate climate variability over the Eastern Mediterranean region. *Forests* 12:350.

- Luterbacher J, García-Herrera R, Akcer-On S, Allan R, Alvarez-Castro MC, Benito G, Booth J, Büntgen U, Cagatay N, Colombaroli D, et al. (2012) A review of 2000 years of paleoclimatic evidence in the Mediterranean. In: Lionello P (ed) *The climate of the Mediterranean region: from the past to the future*. Elsevier, Amsterdam, The Netherlands: pp 87-185.
- McCarroll D, Loader NJ (2004) Stable isotopes in tree rings. *Quat Sci Rev* 23: 771-801.
- McCarroll D, Gagen M, Loader NJ, Robertson I, Anchukaitis KJ, Los S, Young GHF, Jalkanen R, Kirchhefer A, Waterhouse JS (2009) Correction of tree ring stable carbon isotope chronologies for changes in the carbon dioxide content of the atmosphere. *Geochim Cosmochim Acta* 73: 1539-1547.
- Mischel M, Esper J, Keppler F, Greule M, Werner W (2015) $\delta^2\text{H}$, $\delta^{13}\text{C}$ and $\delta^{18}\text{O}$ from whole wood, α -cellulose and lignin methoxyl groups in *Pinus sylvestris*: a multi-parameter approach. *Isot Environ Health Stud* 51: 553-568.
- Nakatsuka T, Sano M, Li Z, Xu C, Tsushima A, Shigeoka Y, Sho K, Ohnishi K, Sakamoto M, Ozaki H, et al. (2020) A 2600-year summer climate reconstruction in central Japan by integrating tree-ring stable oxygen and hydrogen isotopes. *Clim Past* 16: 2153-2172.
- Osborn TJ, Briffa KR, Jones PD (1997) Adjusting variance for sample-size in tree-ring chronologies and other regional mean timeseries. *Dendrochronologia* 15: 89-99.
- Pacheco A, Camarero JJ, Carrer M (2016) Linking wood anatomy and xylogenesis allows pinpointing of climate and drought influences on growth of coexisting conifers in continental Mediterranean climate. *Tree Physiol* 36: 502-512.
- Pandey S (2021) Climatic influence on tree wood anatomy: a review. *J Wood Sci* 67: 24.
- Peres-Neto PR, Jackson DA, Somers KM (2005) How many principal components? Stopping rules for determining the number of non-trivial axes revisited. *Comput Stat Data Anal* 49: 974-997.
- Peters RL, Balanzategui D, Hurley AG, von Arx G, Prendin AL, Cuny HE, Björklund J, Frank DC, Fonti P (2018) RAPTOR: row and position tracheid organizer in R. *Dendrochronologia* 47: 10-16.
- Peters RL, Steppe K, Cuny HE, De Pauw DJW, Frank DC, Schaub M, Rathgeber CBK, Cabon A, Fonti P (2021) Turgor – a limiting factor for radial growth in mature conifers along an elevational gradient. *New Phytol* 229: 213-229.
- Prendin AL, Petit G, Carrer M, Fonti P, Björklund J, von Arx G (2017) New research perspectives from a novel approach to quantify tracheid wall thickness. *Tree Physiol* 37: 976-983.
- Riechelmann DFC, Greule M, Siegwolf RTW, Anhäuser T, Esper J, Keppler F (2017) Warm season precipitation signal in $\delta^2\text{H}$ values of wood lignin methoxyl groups from high elevation larch trees in Switzerland. *Rapid Commun Mass Spectrom* 31: 1589-1598.

- Riechelmann DFC, Greule M, Treydte K, Esper J, Keppler F (2016) Climate signals in $\delta^{13}\text{C}$ of wood lignin methoxyl groups from high-elevation larch trees. *Palaeogeogr Palaeoclimatol Palaeoecol* 445: 60-71.
- Rinn F (2012) *TSAP-Win: time series analysis and presentation for dendrochronology and related applications – version 4.6x for Microsoft Windows*. Rinntech GmbH, Heidelberg, Germany.
- Robertson I, Loader NJ, McCarroll D, Carter AHC, Cheng L, Leavitt SW (2004) $\delta^{13}\text{C}$ of tree-ring lignin as an indirect measure of climate change. *Water Air Soil Pollut Focus* 4: 531-544.
- Römer P, Hartl C, Schneider L, Bräuning A, Szymczak S, Huneau F, Lebre S, Reinig F, Büntgen U, Esper J (2021) Reduced temperature sensitivity of maximum latewood density formation in high-elevation Corsican pines under recent warming. *Atmosphere* 12: 804.
- Römer P, Reinig F, Konter O, Friedrich R, Urban O, Čáslavský J, Pernicová N, Trnka M, Büntgen U, Esper J (2023) Multi-proxy crossdating extends the longest high-elevation tree-ring chronology from the Mediterranean. *Dendrochronologia* 79: 126085.
- Spinoni J, Barbosa P, De Jager A, McCormick N, Naumann G, Vogt JV (2019) A new global database of meteorological drought events from 1951 to 2016. *J Hydrol* 22: 100593.
- Știrbu MI, Roibu C-C, Carrer M, Mursa A, Unterholzner L, Prendin AL (2022) Contrasting climate sensitivity of *Pinus cembra* tree-ring traits in the Carpathians. *Front Plant Sci* 13: 855003.
- Szymczak S, Joachimski MM, Bräuning A, Hetzer T, Kuhlemann J (2012) A 560 yr summer temperature reconstruction for the Western Mediterranean basin based on stable carbon isotopes from *Pinus nigra* ssp. *laricio* (Corsica/France). *Clim Past* 8: 1737-1749.
- Torbenson M, Büntgen U, Römer P, Urban O, Trnka M, Ač A, Reinig F, Rybníček M, Kolář T, Arosio T, et al. (2023) Assessing earlywood-latewood proportion influence on tree-ring stable isotopes. *Dendrochronologia* 82: 126147.
- Treydte K, Frank DC, Esper J, Andreu L, Bednarz Z, Berninger F, Boettger T, D'Alessandro CM, Etien N, Filot M, et al. (2007) Signal strength and climate calibration of a European tree-ring isotope network. *Geophys Res Lett* 34: L24302.
- Vaganov EA (1990) The tracheidogram method in tree-ring analysis and its application. In: Cook ER, Kairiukstis LA (eds) *Methods of Dendrochronology*. Kluwer Academic Publishers, Dordrecht, Boston, and London, The Netherlands, USA and UK: pp 63-76.
- von Arx G, Carrer M (2014) ROXAS – a new tool to build centuries-long tracheid-lumen chronologies in conifers. *Dendrochronologia* 32: 290-293.

- Wang Y, Liu X, Anhäuser T, Lu Q, Zeng X, Zhang Q, Wang K, Zhang L, Zhang Y, Keppler F (2020) Temperature signal recorded in $\delta^2\text{H}$ and $\delta^{13}\text{C}$ values of wood lignin methoxyl groups from a permafrost forest in northeastern China. *Sci Total Environ* 727: 138558.
- Wells N, Goddard S, Hayes MJ (2004) A self-calibrating Palmer Drought Severity Index. *J Clim* 17: 2335-2351.
- Wieland A, Greule M, Römer P, Esper J, Keppler F (2022) Climate signals in stable carbon and hydrogen isotopes of lignin methoxy groups from southern German beech trees. *Clim Past* 18: 1849-1866.
- Wieland A, Römer P, Torbenson M, Greule M, Urban O, Čáslavský J, Pernicová N, Trnka M, Büntgen U, Esper J, et al. (2024) Tree-ring stable isotopes in cellulose and lignin methoxy groups reveal different age-related behaviour. *Quat Int* 693: 38-48.
- Wigley TML, Briffa KR, Jones PD (1984) On the average of correlated time series, with applications in dendroclimatology and hydrometeorology. *J Appl Meteorol Clim* 23: 201-213.
- Wilson AT, Grinsted MJ (1977) $^{12}\text{C}/^{13}\text{C}$ in cellulose and lignin as palaeothermometers. *Nature* 265: 133-135.
- Yakir D, Sternberg L (2000) The use of stable isotopes to study ecosystem gas exchange. *Oecologia* 123: 297-311.
- Yang B, Qin C, Bräuning A, Osborn TJ, Trouet V, Ljungqvist FC, Esper J, Schneider L, Griesinger J, Büntgen U (2021) Long-term decrease in Asian monsoon rainfall and abrupt climate change events over the past 6,700 years. *PNAS* 118: e2102007118.
- Young GHF, Demmler JC, Gunnarson BE, Kirchhefer AJ, Loader NJ, McCarroll D (2011) Age trends in tree ring growth and isotopic archives: a case study of *Pinus sylvestris* L. from northwestern Norway. *Glob Biogeochem Cycles* 25: GB2020.
- Zeisel S (1885) Über ein Verfahren zum quantitativen Nachweise von Methoxyl. *Monatshefte für Chemie* 6: 989-997.
- Zharkov MS, Huang JG, Yang B, Babushkina EA, Belokopytova LV, Vaganov EA, Zhirnova DF, Ilyin VA, Popkova MI, Shishov VV (2022) Tracheidogram's classification as a new potential proxy in high-resolution dendroclimatic reconstructions. *Forests* 13: 970.
- Ziaco E (2020) A phenology-based approach to the analysis of conifers intra-annual xylem anatomy in water-limited environments. *Dendrochronologia* 59: 125662.
- Ziaco E, Liang E (2019) New perspectives on sub-seasonal xylem anatomical responses to climatic variability. *Trees* 33: 973-975.
- Ziaco E, Biondi F, Heinrich I (2016) Wood cellular dendroclimatology: testing new proxies in Great Basin bristlecone pine. *Front Plant Sci* 7: 1602.
- Ziaco E, Biondi F, Rossi S, Deslauriers A (2014) Climatic influences on wood anatomy and tree-ring features of Great Basin conifers at a new mountain observatory. *Appl Plant Sci* 2: 1400054.

7.8 Supplementary materials

Table S7.1 Summary statistics of the sub-seasonal radial lumen diameter (D_{rad}) and cell wall thickness (CWT_{rad} and CWT_{tan}) chronologies.

Sec	D_{rad}			CWT_{rad}			CWT_{tan}		
	Mean $\pm 1\sigma$	AC1	Rbar	Mean $\pm 1\sigma$	AC1	Rbar	Mean $\pm 1\sigma$	AC1	Rbar
I	30.3 \pm 4.2	0.35	0.27	3.7 \pm 0.4	0.63	0.17	3.2 \pm 0.3	0.62	0.21
II	29.3 \pm 3.9	0.40	0.25	3.7 \pm 0.4	0.67	0.12	3.2 \pm 0.3	0.59	0.22
III	28.1 \pm 3.8	0.44	0.27	3.7 \pm 0.4	0.65	0.11	3.3 \pm 0.4	0.60	0.23
IV	26.7 \pm 3.8	0.43	0.29	3.8 \pm 0.4	0.63	0.13	3.3 \pm 0.4	0.58	0.22
V	24.8 \pm 3.7	0.40	0.31	3.9 \pm 0.5	0.58	0.15	3.4 \pm 0.4	0.53	0.21
VI	22.2 \pm 4.0	0.31	0.35	4.1 \pm 0.5	0.51	0.20	3.5 \pm 0.4	0.48	0.22
VII	18.4 \pm 4.0	0.24	0.38	4.4 \pm 0.6	0.44	0.24	3.7 \pm 0.5	0.45	0.23
VIII	14.0 \pm 3.3	0.23	0.40	4.8 \pm 0.6	0.44	0.25	3.8 \pm 0.5	0.48	0.22
IX	10.2 \pm 2.4	0.31	0.39	5.1 \pm 0.5	0.46	0.28	3.7 \pm 0.5	0.56	0.21
X	6.7 \pm 1.5	0.29	0.30	5.0 \pm 0.5	0.43	0.29	3.3 \pm 0.4	0.58	0.20

Sec: sector. **Mean $\pm 1\sigma$:** arithmetic mean [μm] \pm 1 standard deviation (1σ) calculated over all rings between 1861-2020 CE. **AC1:** first-order autocorrelation of the raw chronologies. **Rbar:** average inter-series correlation between the 30SP-detrended series. All statistics are calculated for the period 1861-2020 CE.

Table S7.2 Results of the principal component analysis (PCA) applied on the annual TRW, MXD, $\delta^{13}\text{C}_c$, $\delta^{13}\text{C}_m$, $\delta^{18}\text{O}_c$, $\delta^2\text{H}_m$, and the 30 D_{rad} , CWT_{rad} , and CWT_{tan} sector chronologies.

Principal component	Eigenvalue	Explained variance [%]	Cumulative percentage of variance [%]	P value of randomization
1	12.27	34.09	34.09	< 0.001
2	8.99	24.97	59.06	< 0.001
3	3.54	9.83	68.89	< 0.001
4	2.04	5.66	74.55	< 0.001
5	1.65	4.59	79.14	> 0.05

Note that according to the Random-Lambda rule, PC4 is the last useful axis.

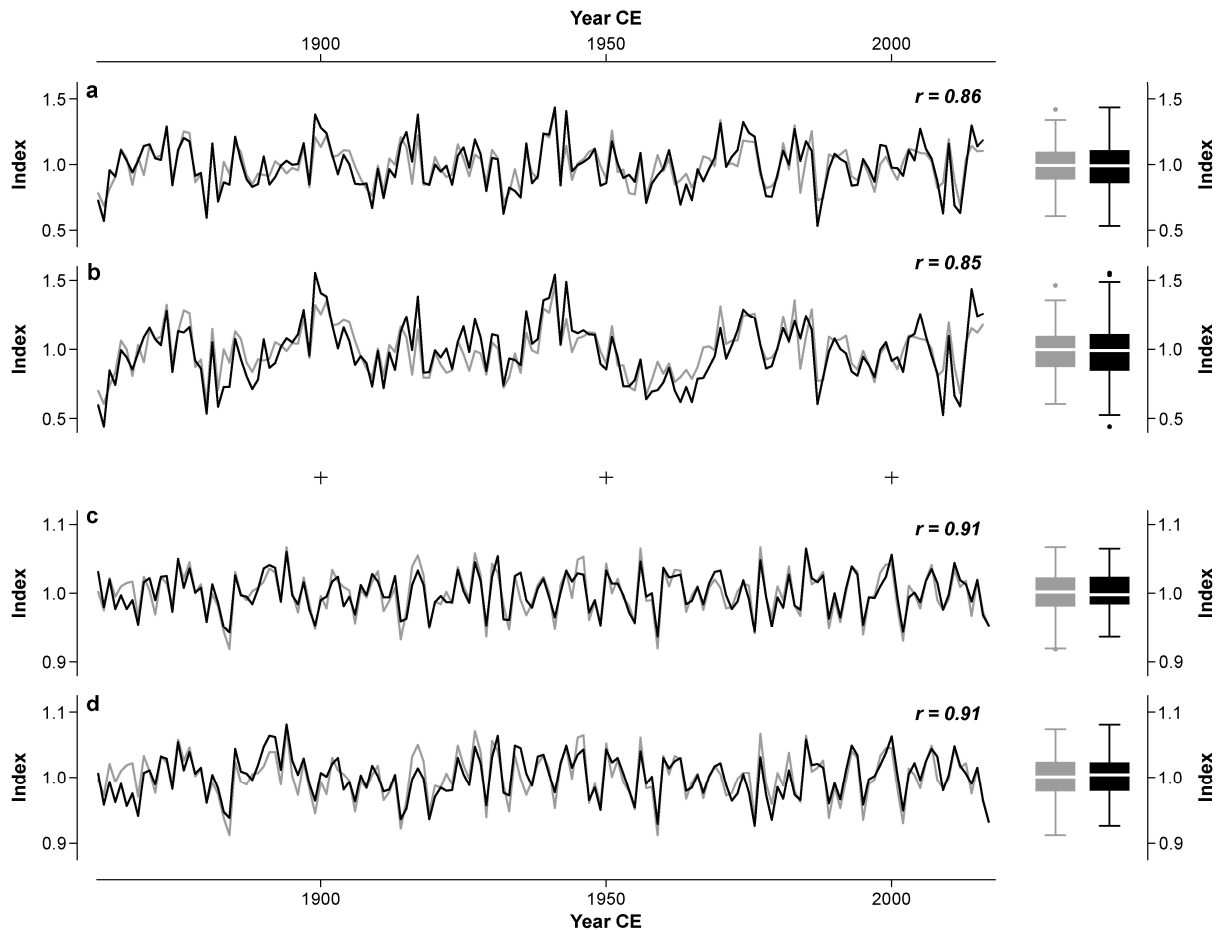


Fig. S7.1 Tree-ring width (TRW) chronology of this study (black curves) compared to the well-replicated ($n = 872$ series) TRW chronology of Esper et al. (2021; grey curves) after detrending with (a) 30-year and (b) 100-year cubic smoothing splines (left panels). Boxplots (right panels) show the distribution of TRW indices over the 1861-2016 CE common period. Maximum latewood density (MXD) chronology of this study (black curves) compared to the well-replicated ($n = 192$ series) MXD chronology of Esper et al. (2020; grey curves) after detrending with (c) 30-year and (d) 100-year cubic smoothing splines. Boxplots show the distribution of MXD indices over the 1861-2017 CE common period. R values indicate correlations between the TRW and MXD chronologies calculated from 1861 to 2016 (TRW) and 2017 CE (MXD), respectively. All correlations are significant at $p < 0.001$.

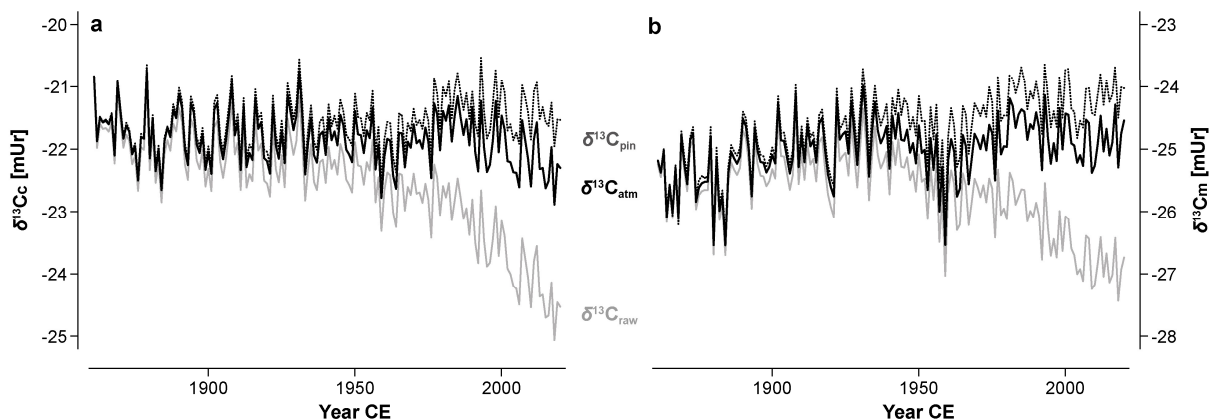


Fig. S7.2 Carbon isotope corrections. Raw mean chronologies of (a) cellulose ($\delta^{13}C_c$) and (b) methoxy ($\delta^{13}C_m$) stable carbon isotopes. Grey curves are the raw chronologies ($\delta^{13}C_{raw}$), black solid curves are the Suess-effect-corrected chronologies ($\delta^{13}C_{atm}$), and black dashed curves are the pin-corrected chronologies ($\delta^{13}C_{pin}$).

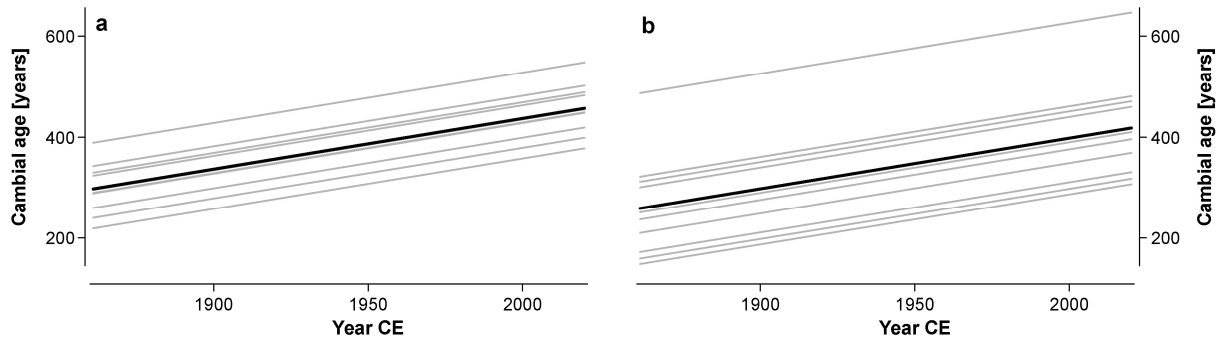


Fig. S7.3 Cambial ages of the individual series (grey lines) and their arithmetic mean (black lines) over the 1861-2020 CE period for (a) the TRW, TRSI and QWA data, and (b) the MXD data.

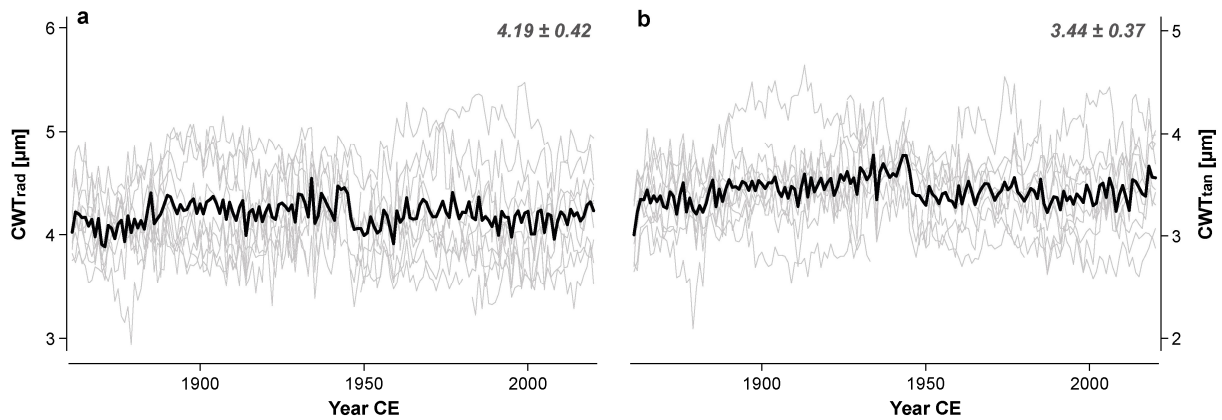


Fig. S7.4 Individual series (grey lines) and mean chronologies (black lines) of raw (a) CWT_{rad} and (b) CWT_{tan}. Values (right top) are the arithmetic mean \pm 1 standard deviation calculated over all tree rings between 1861-2020 CE. The mean chronologies of CWT_{rad} and CWT_{tan} correlate at $r = 0.77$ ($p < 0.001$) over the 1861-2020 CE common period.

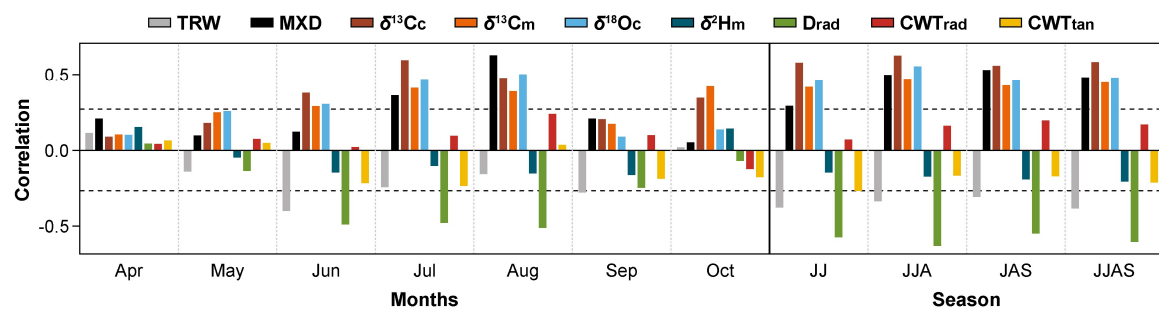


Fig. S7.5 Correlations between the 30SP-detrended proxy chronologies and diurnal temperature range for 1931-2020 CE. The $\delta^{13}C$ data are corrected for the Suess effect. Horizontal dashed lines indicate the significance level of $p < 0.01$. Please note that the significance level for MXD is marginally higher due to the shorter calibration period (1931-2017 CE), but is not displayed for the sake of clarity.

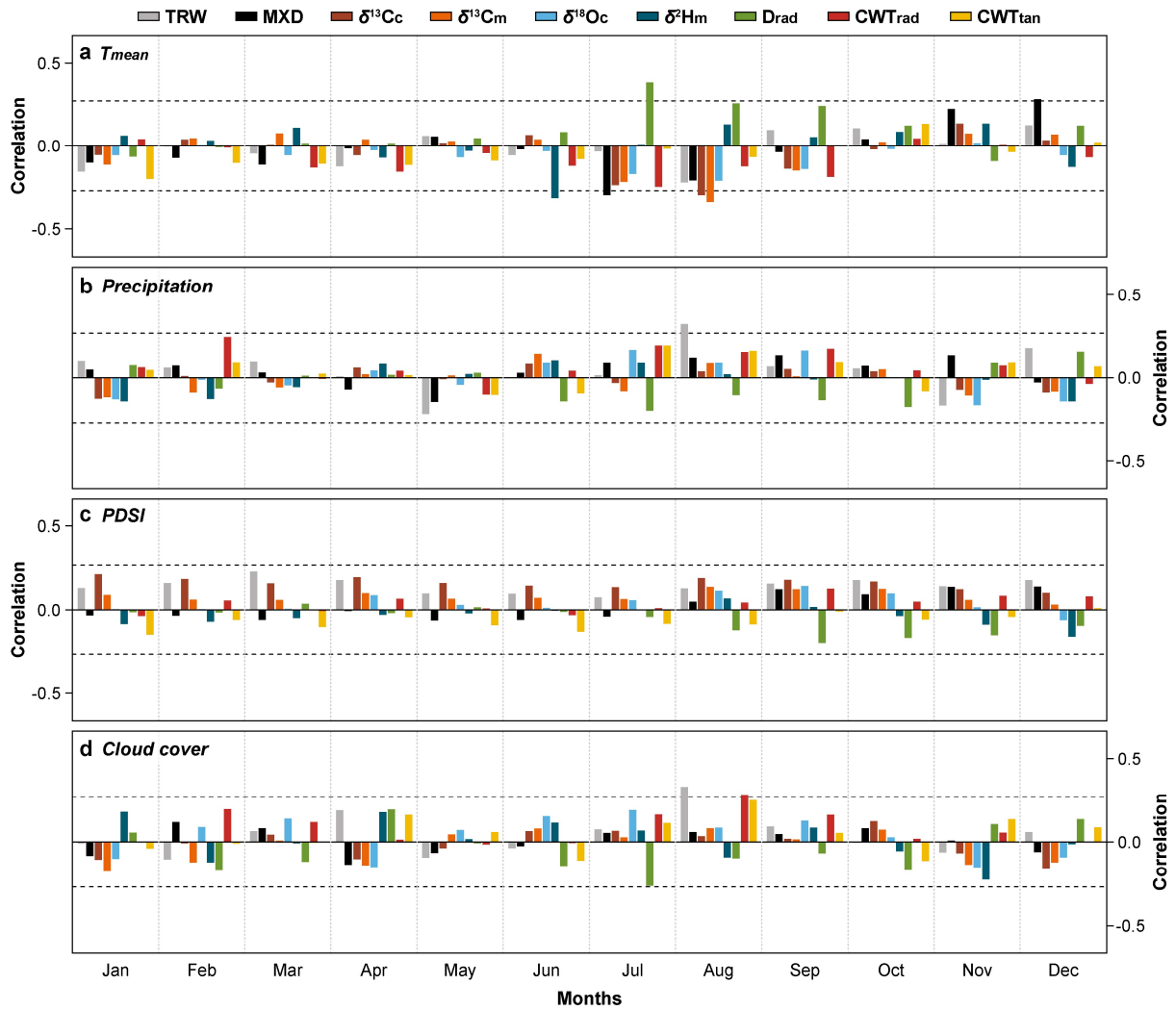


Fig. S7.6 Correlations between the 30SP-detrended proxy chronologies and previous-year (a) mean air temperature (T_{mean}), (b) precipitation, (c) the PDSI, and (d) cloud cover data calculated for 1931-2020 CE. The $\delta^{13}\text{C}$ data are corrected for the Suess effect. Horizontal dashed lines indicate the significance level of $p < 0.01$. Please note that the significance level for MXD is marginally higher due to the shorter calibration period (1931-2017 CE), but is not displayed for the sake of clarity.

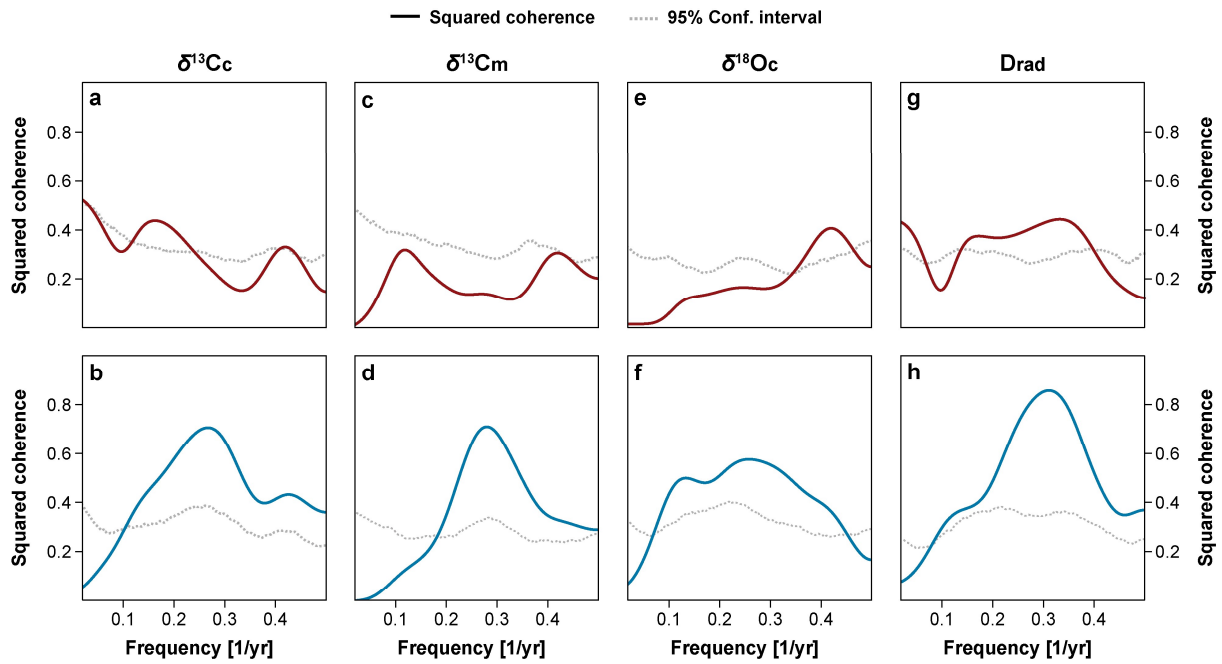


Fig. S7.7 Squared coherence (1931-2020 CE) between (a-b) $\delta^{13}C_c$, (c-d) $\delta^{13}C_m$, (e-f) $\delta^{18}O_c$, (g-h) D_{rad} and June-August temperature (top panels) and precipitation (bottom panels). Grey dashed lines are the 95% confidence intervals.

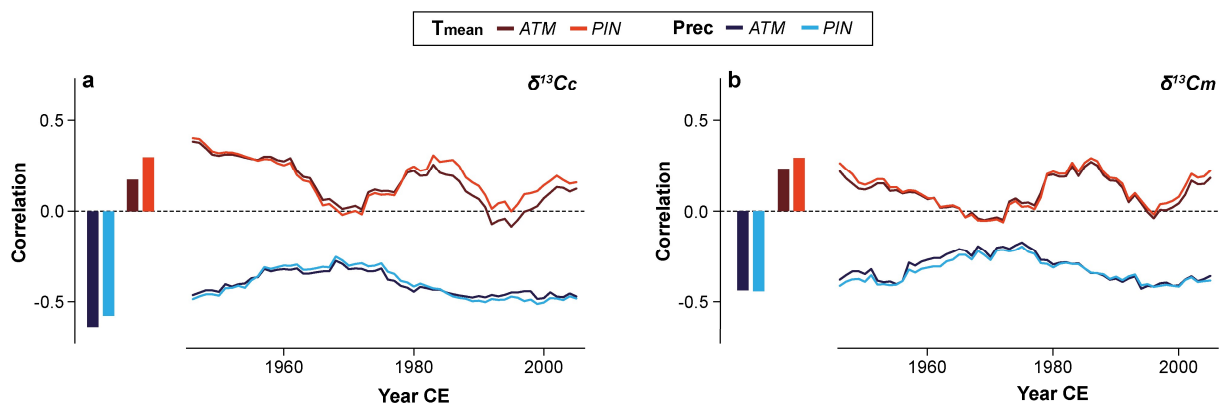


Fig. S7.8 Temperature (T_{mean}) and precipitation (Prec) signals in the Suess-effect-corrected (ATM) and pin-corrected (PIN) (a) $\delta^{13}C_c$ and (b) $\delta^{13}C_m$ data. Vertical bars (left) show correlations between the HOM-detrended $\delta^{13}C$ records and June-August T_{mean} (red) and precipitation (blue) for 1931-2020 CE. Curves in the right panels show 31-year running correlations for the different detrendings.

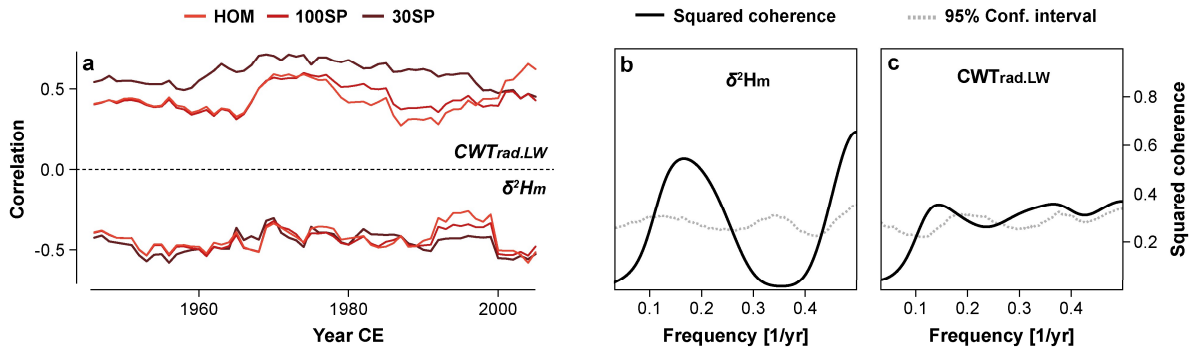


Fig. S7.9 (a) Thirty-one-year running correlations between the detrended δ^2H_m chronologies and June-September mean temperature (JJAS T_{mean}) and between the detrended $CWT_{rad.LW}$ chronologies (mean of sectors VIII-X) and JJAS T_{mean} . Squared coherence between (b) δ^2H_m and JJAS T_{mean} and between (c) $CWT_{rad.LW}$ and JJAS T_{mean} for 1931-2020 CE. Grey dashed lines are the 95% confidence intervals.

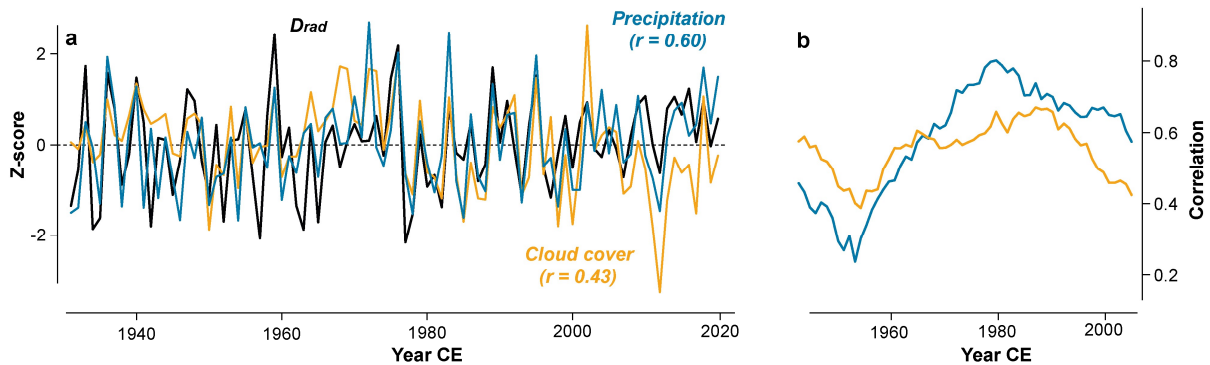


Fig. S7.10 (a) Z-scores of the HOM-detrended (annual) D_{rad} record (black line), raw June-August (JJA) precipitation (blue line), and JJA cloud cover (orange line). R values indicate correlations between D_{rad} and the climate records. (b) Corresponding 31-year running correlations between the HOM-detrended D_{rad} chronology and JJA precipitation and cloud cover, respectively (same colors as in panel a).

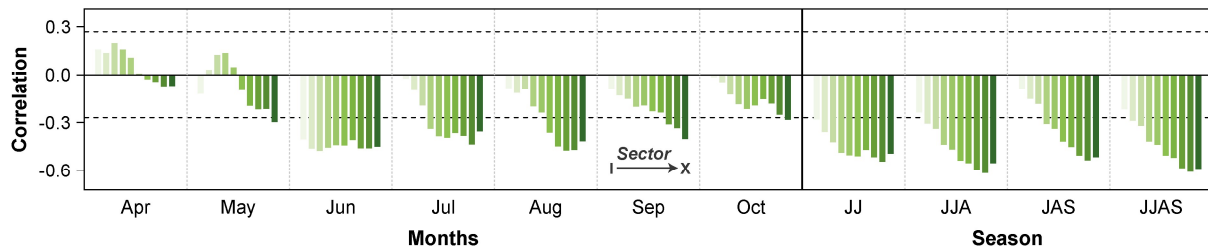


Fig. S7.11 Correlations between the 30SP-detrended D_{rad} sector chronologies (I = left, X = right) and T_{mean} calculated for 1931-2020 CE. Horizontal dashed lines indicate the significance level of $p < 0.01$.

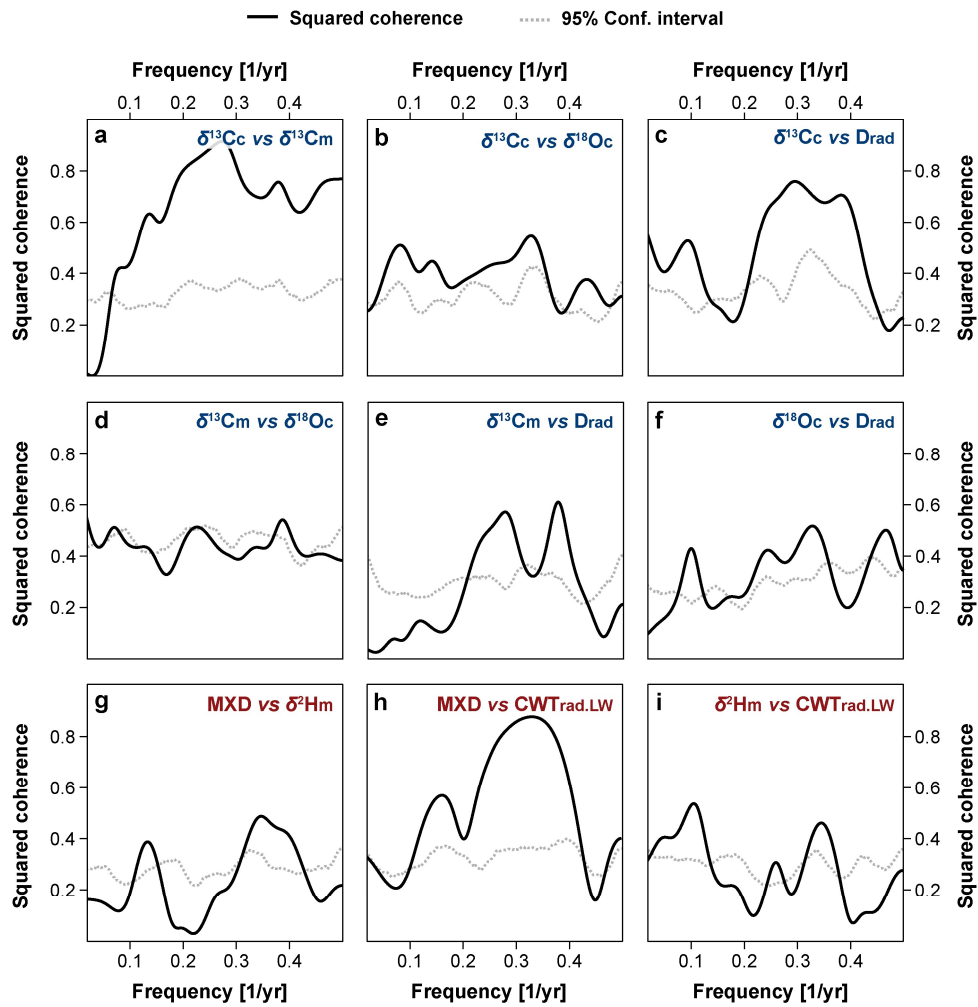


Fig. S7.12 Squared coherence between the (a-f) precipitation-sensitive (blue labels) and (g-i) temperature-sensitive (red labels) proxies calculated for 1861-2020 CE (MXD for 1861-2017 CE). Grey dashed lines represent the 95% confidence intervals.

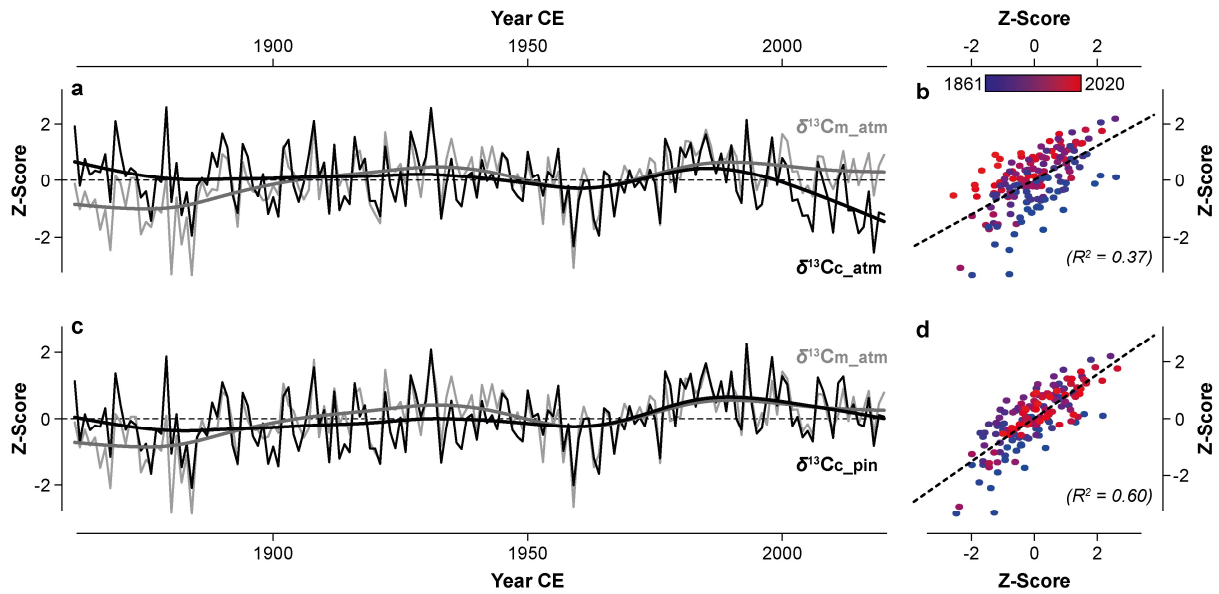


Fig. S7.13 Z-Scores of the (a-b) Suess-effect-corrected $\delta^{13}\text{C}_{c_atm}$ (black lines) and $\delta^{13}\text{C}_{m_atm}$ (grey lines) records, and (c-d) pin-corrected $\delta^{13}\text{C}_{c_pin}$ and Suess-effect-corrected $\delta^{13}\text{C}_{m_atm}$ records. Thick lines are 50-year cubic smoothing splines. Scatterplots on the right show the relationship between the $\delta^{13}\text{C}$ data. The single points are colored according to their year. Dashed lines are the linear trends.

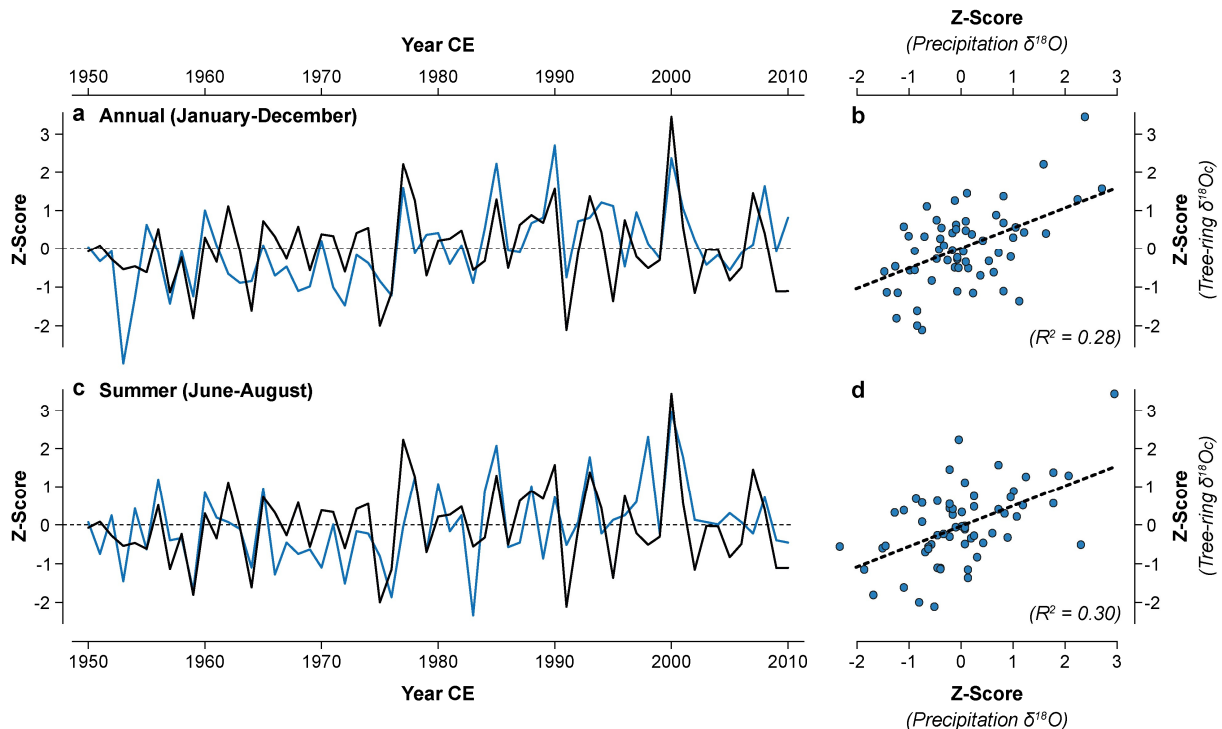


Fig. S7.14 Z-scores of the $\delta^{18}\text{O}_c$ record (black lines) together with (a-b) annual and (c-d) summer precipitation $\delta^{18}\text{O}$ (blue lines). The precipitation $\delta^{18}\text{O}$ data are from Nelson et al. (2021) and were calculated for the Mt. Smolikas site (<https://isotope.bot.unibas.ch/PisoAI>). Scatterplots on the right show the relationships between $\delta^{18}\text{O}_c$ and seasonal precipitation $\delta^{18}\text{O}$ for 1950-2010 CE. Dashed lines are the linear trends.

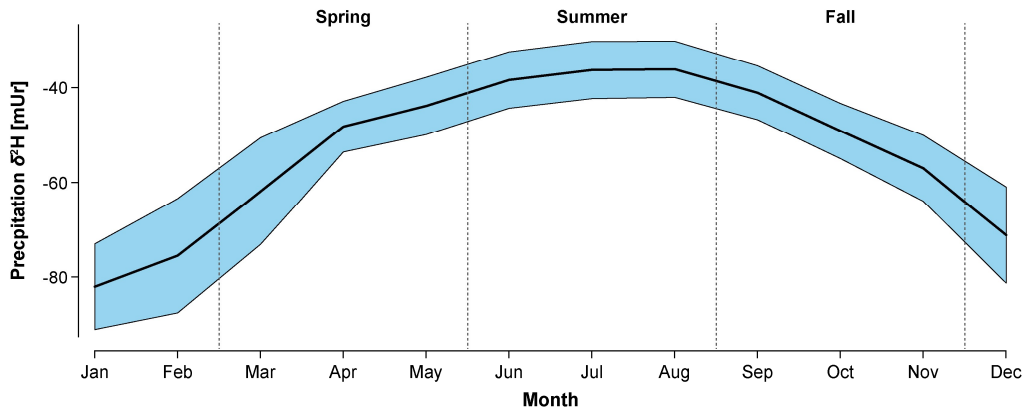


Fig. S7.15 Seasonality of precipitation $\delta^2\text{H}$. The precipitation $\delta^2\text{H}$ data are from Nelson et al. (2021) and were calculated for the Mt. Smolikas site (<https://isotope.bot.unibas.ch/PisoAI>). The thick black line is the arithmetic mean and the shaded area indicates ± 1 standard deviation for 1950-2010 CE.

Supplemental references

- Esper J, Klippel L, Krusic PJ, Konter O, Raible C, Xoplaki E, Luterbacher J, Büntgen U (2020) Eastern Mediterranean summer temperatures since 730 CE from Mt. Smolikas tree-ring densities. *Clim Dyn* 54: 1367-1382.
- Esper J, Konter O, Klippel L, Krusic PJ, Büntgen U (2021) Pre-instrumental summer precipitation variability in northwestern Greece from a high-elevation *Pinus heldreichii* network. *Int J Climatol* 41: 2828-2839.
- Nelson DB, Basler D, Kahmen A (2021) Precipitation isotope time series predictions from machine learning applied in Europe. *PNAS* 118: e2024107118.

8 Conclusion and outlook

This dissertation examines the preservation of climate signals in multi-proxy tree-ring chronologies from Europe, providing new insights into the paleoclimatic value of state-of-the-art tree-ring proxies, including TRW, MXD, $\delta^{13}\text{C}$, $\delta^{18}\text{O}$, $\delta^2\text{H}$, as well as several wood anatomical traits. Key findings include the advantage of TRSI measurements over traditional TRW data for reconstructing past hydroclimate variability at interannual to multimillennial timescales, methodological advances in QWA data development, and the effectiveness of multi-proxy approaches in enhancing dating precision and preserving climate signals in early chronology periods.

First, the paleoclimatic limitations of TRW (**chapter 2**) and MXD (**chapter 3**) are contextualized by analyzing non-stationary climate-growth responses and diverging trends between summer temperatures and MXD chronologies in the 21st century. The analysis of low-elevation spruce and pine growth across southwest Germany (100-800 m asl), including the application of various detrending techniques, calibration against multiple climate variables, and comparison with nearby forest sites, confirms a pronounced drought vulnerability for both conifers and reveals that temperate forest growth has become increasingly sensitive to late-winter/early-spring temperatures in recent decades (Diers et al. 2023, 2024; Harvey et al. 2020; Janecka et al. 2020; Stolz et al. 2021). The non-stationary climate-growth responses of spruce and pine, along with the restriction of significant climate signals to the high-frequency domain, emphasize key challenges in climate signal preservation using TRW from low- and mid-elevation Central European forests (Büntgen et al. 2010; Wilson et al. 2005).

Chapter 3 presents a new 850-year-long MXD chronology for the central Mediterranean region, which fills a spatial gap in the Mediterranean MXD network (Büntgen & Esper 2024). The MXD record aligns well with the world's best replicated MXD chronology from the Spanish Pyrenees (Büntgen et al. 2017, 2024), but diverges from regional temperature trends in the 21st century. The observed divergence between colder reconstructed and warmer instrumental temperatures suggests a warming-induced shift from initially temperature-controlled to drought-prone MXD formation and prevents the reconstruction of past summer temperatures using Corsican pine MXD. Confirmation of these results at other Mediterranean sites would substantially question the reliability of existing MXD-based temperature reconstructions in the Mediterranean. In light of recent warming, there is thus a crucial need to update existing MXD records toward the present to assess whether increasing drought conditions in the 21st century may alter the relationship between MXD and instrumental temperatures. QWA studies on Corsican pines (*Pinus nigra* ssp. *laricio*) may help elucidate the effects of recent climatic change on xylem anatomical properties (Hetzler et al. 2014). Future research should focus on the development of long QWA chronologies to unveil the drivers of the observed MXD divergence and refine existing climate reconstructions by incorporating insights from wood anatomical traits (Björklund et al. 2023).

Despite various methodological advances in QWA, the development of long wood anatomical records remains time-consuming due to elaborate slide preparation (Gärtner & Schweingruber 2013), digital image analyses (von Arx & Carrer 2014), and subsequent post-processing steps (DeSoto et al. 2011; Peters et al. 2018). Further improvements are needed to accelerate and enhance data development. In **chapter 4**, we show that high-quality microslide preparation for QWA analyses can be achieved without paraffin embedding, a step that typically adds over 20 hours to preparation time (Rossi et al. 2006). By comparing CWT, MLA, and D_h chronologies of embedded and non-embedded microsections from various European tree species, including *Fagus sylvatica*, *Larix decidua*, and *Pinus cembra*, we demonstrate that water boiling for 5-10 minutes is sufficient to produce thin sections of comparable quality to those obtained with embedding. Given the high similarity between the anatomical chronologies of embedded and non-embedded samples, we recommend using water boiling instead of paraffin embedding to improve QWA efficiency by reducing preparation time and eliminating the need for costly equipment and harmful chemicals. Additionally, integrating machine-learning approaches into digital image analysis and post-processing holds significant potential for advancing data development (Garcia-Pedrero et al. 2020; Katzenmaier et al. 2023; Keret et al. 2024; Resente et al. 2021). Future research should focus on incorporating these advanced techniques into standard QWA workflows to enhance data processing and analytical precision.

Over recent decades, the integration of stable isotopes into dendrochronological analyses significantly advanced high-resolution paleoclimatology (Büntgen et al. 2021; Freund et al. 2023; Nakatsuka et al. 2020; Torbenson et al. 2023; Yang et al. 2021), forest ecology (Adams et al. 2020; Guerrieri et al. 2019; Lavergne et al. 2022), and archaeology (Loader et al. 2019, 2021; Roden 2008). By comparing new $\delta^{13}\text{C}$ measurements on first millennium CE relict pine samples from Mt. Smolikas (Greece) with previous TRW and MXD records, we show that annually resolved and non-pooled $\delta^{13}\text{C}$ measurements on cellulose can help overcome crossdating issues in early chronology periods where sample sizes are insufficient for accurate TRW and/or MXD crossdating (**chapter 5**). The associated redating of relict pine samples extends the TRW and MXD chronologies by over a century back in time (from 575/574 to 468 CE) and eliminates errors that previously diminished the covariance among series, thereby enhancing the ability of TRW and MXD to preserve environmental signals in early chronology periods. The corrected proxy records show greater variance and reduced error ranges for the 6th and 7th centuries CE. While traditional dendrochronological crossdating methods, such as pointer-year analysis and skeleton plots, remain crucial for developing long tree-ring chronologies (Schweingruber et al. 1990), the strong $\delta^{13}\text{C}_c$ covariance among *Pinus heldreichii* trees provides a unique opportunity to date challenging samples with reasonable effort, calling for renewed efforts to reassess the

still significant amount of undated relict wood from Mt. Smolikas, which could potentially extend the existing tree-ring records even further back in time.

Chapter 6 addresses an ongoing debate in the dendro-isotope community regarding long-term age trends in TRSIs. Isotopic measurements on living and relict pines from Mt. Smolikas, covering various germination and end dates over the past 1500 years, provide an ideal framework for determining ontogenetic trends in α -cellulose and lignin methoxy isotopes, including $\delta^{13}\text{C}_c$, $\delta^{13}\text{C}_m$, $\delta^{18}\text{O}_c$, and $\delta^2\text{H}_m$. Significant level offsets between living and relict $\delta^{18}\text{O}_c$ and $\delta^2\text{H}_m$ values prevent the combined use of living and relict wood for reliable age-trend assessment and stress the need for in-depth investigations on circumferential and longitudinal $\delta^{18}\text{O}_c$ and $\delta^2\text{H}_m$ variability within *Pinus heldreichii* stems. Such investigations are crucial for addressing uncertainties related to incorporating subfossil material of unknown sampling heights into TRSI chronologies (Esper et al. 2020c), and should also be conducted on other paleoclimatically significant tree species. Cambial-age-alignment of the isotopic series reveals significant age trends in $\delta^{13}\text{C}_m$, $\delta^{18}\text{O}_c$, and $\delta^2\text{H}_m$, but no significant trends in $\delta^{13}\text{C}_c$ beyond a tree age of 80 years. This suggests that raw $\delta^{13}\text{C}_c$ data can be used for climate reconstruction purposes without the need for standardization, except for rings younger than 80 years. The absence of age trends in $\delta^{13}\text{C}_c$, beyond juvenile trends in the first 100 years of tree age, aligns with previous studies on various European pine species (Arosio et al. 2020; Esper et al. 2010; Gagen et al. 2007; Torbenson et al. 2022; Young et al. 2011). This large-scale consistency highlights the potential of pine $\delta^{13}\text{C}_c$ to address one of the key challenges in high-resolution paleoclimatology: the preservation of low-frequency climate variability (Esper et al. 2002). However, further assessments of different ring compounds (whole-ring *versus* latewood) are needed to determine if age trends in $\delta^{13}\text{C}_c$ differ when using varying ring materials.

Chapter 7 compares new isotopic ($\delta^{13}\text{C}_c$, $\delta^{13}\text{C}_m$, $\delta^{18}\text{O}_c$, and $\delta^2\text{H}_m$) and wood anatomical measurements (D_{rad} and CWT) from ten Bosnian pines at Mt. Smolikas with existing TRW and MXD data to evaluate their palaeoclimatic skills. The comprehensive assessment of covariance both within and among these proxies, along with their climate sensitivities, highlights significant advances in TRSI and wood anatomical measurements over TRW in reconstructing past summer hydroclimate variability across the Eastern Mediterranean region. In particular, $\delta^{13}\text{C}_c$ emerges as a superior hydroclimate proxy due to high inter-series correlations, strong precipitation dependencies, a prolonged seasonality compared to TRW, and the lack of long-term ontogenetic trends (chapter 6). These results support previous studies on *Pinus heldreichii* $\delta^{13}\text{C}_c$ from the Dinarides (Levanič et al. 2020; Lukač et al. 2021), the southern Apennines in Italy and the Pirin Mountains in Bulgaria (Freund et al. 2023). If it holds true that *Pinus heldreichii* $\delta^{13}\text{C}_c$ does not show any significant age trends at other locations, developing and integrating more centennial-to-millennial $\delta^{13}\text{C}_c$ chronologies from this long-lived tree species (Konter et al. 2017; Piovesan

et al. 2018) could significantly enhance existing large-scale hydroclimate reconstructions, such as the Old World Drought Atlas (Anchukaitis et al. 2024; Cook et al. 2015), by preserving higher levels of low-frequency variability (Büntgen 2022). Future research should thus aim to develop new high-resolution (annual and non-pooled) $\delta^{13}\text{C}_c$ records from high-elevation Mediterranean pines, ideally spanning several centuries and using both living and relict wood, to improve our understanding of late-Holocene natural hydroclimate variability. $\delta^2\text{H}_m$ may serve as an alternative summer temperature proxy to MXD. However, further research at other Mediterranean sites is needed to consolidate the inverse temperature response of $\delta^2\text{H}_m$ (Anhäuser et al. 2020; Lu et al. 2020; Mischel et al. 2015; Wang et al. 2020; Wieland et al. 2022) and assess whether $\delta^2\text{H}_m$ also provides robust temperature signals at lower elevations (Feakins et al. 2013; Greule et al. 2021), where MXD typically fails as a temperature proxy.

This dissertation delivers a comprehensive evaluation of the strengths and limitations of state-of-the-art tree-ring proxies for paleoclimatic, archaeological, and ecological research. In rejecting age-related limitations and demonstrating enhanced climate dependencies, it provides new insights into the significant advances of $\delta^{13}\text{C}_c$ for reconstructing past hydroclimate variability at interannual to multicentennial timescales and improving crossdating precision in early chronology periods. The collection of 14,148 individual $\delta^{13}\text{C}_c$ measurements from living and relict Bosnian pines offers the unique opportunity to develop a new summer precipitation reconstruction for the Eastern Mediterranean region. This reconstruction will advance our knowledge of long-term hydroclimatic trends beyond existing TRW-based reconstructions (Esper et al. 2021) and may help disentangle the contributions of natural and anthropogenic forces in the recent aridification of the Mediterranean (Hoerling et al. 2012; Lionello & Scarascia 2018; Spinoni et al. 2019). $\delta^{18}\text{O}_c$ (annual resolution) and $\delta^{13}\text{C}_m$ (decadal resolution before 1860 CE) data may help assess reconstruction uncertainties, while the annual and sub-seasonal D_{rad} and CWT records could provide new insights into past cloud cover and temperature extremes. For developing a mean $\delta^{18}\text{O}_c$ chronology, however, different correction procedures should be tested to account for the significant offsets between living and relict $\delta^{18}\text{O}_c$ values (Arosio et al. 2024).

The frequent occurrence of “Blue rings” (Piermattei et al. 2015) on the stained microsections of *Pinus heldreichii* from Mt. Smolikas (**Fig. 8.1**), enables the development of a 1500-year-long blue-ring chronology. Blue rings, which represent un lignified latewood portions associated with low late-growing season temperatures at treeline sites (Crivellaro et al. 2022; Piermattei et al. 2020; Siekacz et al. 2024; Tardif et al. 2020), can enhance the dating of past volcanic eruptions and provide deeper insights into sub-seasonal relationships between volcanism, weather, and society that TRW or MXD records might not capture (Büntgen et al. 2020a). A new 1500-year blue-ring chronology from Mt. Smolikas could therefore help identify and elucidate the impact

of weather extremes on human history, potentially offering insights beyond existing documentary and tree-ring evidence (e.g., Brázdil et al. 2005; Piermattei et al. 2020; Telelis 2008).

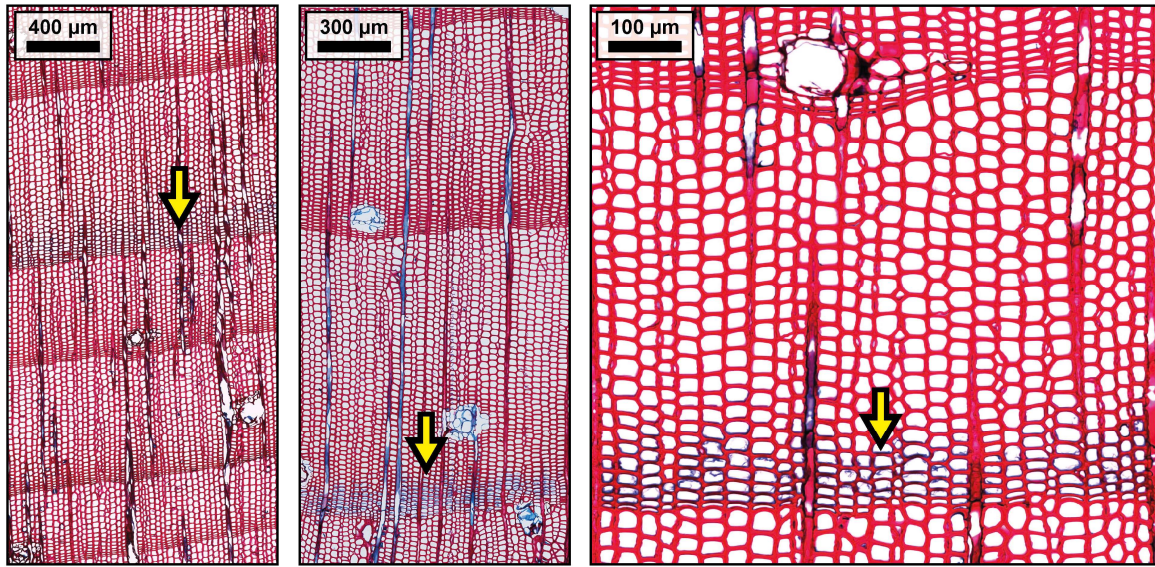


Fig. 8.1 “Blue Rings” on stained microsections of *Pinus heldreichii* from Mt. Smolikas.

Despite various technological and methodological advances over recent decades, increasing TRSI and QWA measurement efficiency by decreasing time and costs remains one of the key challenges in dendrochronological research. Improvements in tree-ring dissecting (Dodd et al. 2008; Schollaen et al. 2014), chemical extraction (Andreu-Hayles et al. 2019; Kagawa et al. 2015; Keppler et al. 2007; Schollaen et al. 2017), IRMS systems (Zech et al. 2013), microslide preparation (Gärtner et al. 2015), and digital image analyses (Katzenmaier et al. 2023; von Arx & Carrer 2014) have significantly advanced both approaches. However, the development of long isotopic and anatomical chronologies still requires substantially more labor than traditional TRW and radiodensitometric measurements, despite their superior paleoclimatic skill (Allen et al. 2022; Björklund et al. 2023; Büntgen et al. 2021; Lopez-Saez et al. 2023; Nakatsuka et al. 2020; Seftigen et al. 2022; Yang et al. 2021). Further methodological advances are therefore urgently needed to enhance the efficiency and accessibility of both TRSI and QWA measurements for the broader scientific community in the near future.

9 References

- Adams MA, Buckley TN, Turnbull TL (2020) Diminishing CO₂-driven gains in water-use efficiency of global forests. *Nat Clim Change* 10: 466-471.
- Allen KJ, Nichols SC, Evans R, Baker P (2022) Characteristics of a multi-species conifer network of wood properties chronologies from southern Australia. *Dendrochronologia* 76: 125997.
- Anchukaitis KJ, Touchan R, Meko DM, Kherchouche D, Slimani S, Sivrikaya F, Ilmen R, Mitsopoulos I, Stephan J, Attieh J, et al. (2024) Enhancing spatiotemporal paleoclimate reconstructions of hydroclimate across the Mediterranean over the last millennium. *Clim Dyn*, <https://doi.org/10.1007/s00382-024-07166-6>.
- Anchukaitis KJ, Wilson R, Briffa KR, Büntgen U, Cook ER, D'Arrigo R, Davi N, Esper J, Frank DC, Gunnarson BE, et al. (2017) Last millennium Northern Hemisphere summer temperatures from tree rings: part II, spatially resolved reconstructions. *Quat Sci Rev* 163: 1-22.
- Andreu-Hayles L, Levesque M, Martin-Benito D, Huang W, Harris R, Oelkers R, Leland C, Martin-Fernández J, Anchukaitis KJ, Helle G (2019) A high yield cellulose extraction system for small whole wood samples and dual measurement of carbon and oxygen stable isotopes. *Chem Geol* 504: 53-65.
- Anhäuser T, Greule M, Polag D, Bowen GJ, Keppler F (2017) Mean annual temperatures of mid-latitude regions derived from $\delta^2\text{H}$ values of wood lignin methoxyl groups and its implications for paleoclimate studies. *Sci Total Environ* 574: 1276-1282.
- Anhäuser T, Sehls B, Thomas W, Hartl C, Greule M, Scholz D, Esper J, Keppler F (2020) Tree-ring $\delta^2\text{H}$ values from lignin methoxyl groups indicate sensitivity to European scale temperature changes. *Palaeogeogr Palaeoclimatol Palaeoecol* 546: 109665.
- Arosio T, Torbenson M, Bebbchuk T, Kirilyanov A, Esper J, Nakatsuka T, Sano M, Urban O, Nicolussi K, Leuenberger M, et al. (2024) Methodological constraints of tree-ring stable isotope chronologies. *Quat Sci Rev* 240: 108861.
- Arosio T, Ziehmer M, Nicolussi K, Schlüchter C, Leuenberger M (2020) Alpine Holocene tree-ring dataset: age-related trends in the stable isotopes of cellulose show species-specific patterns. *Biogeosciences* 17: 4871-4882.
- Babst F, Poulter B, Trouet V, Tan K, Neuwirth B, Wilson R, Carrer M, Grabner M, Tegel W, Levanič T, et al. (2013) Site- and species-specific responses of forest growth to climate across the European continent. *Glob Ecol Biogeogr* 22: 706-717.
- Balanzategui D, Nordhauß H, Heinrich I, Biondi F, Miley N, Hurley AG, Ziaco E (2021) Wood anatomy of Douglas-fir in eastern Arizona and its relationship with Pacific Basin climate. *Front Plant Sci* 12: 702442.

- Belmecheri S, Wright WE, Szejner P (2022) Sample collection and preparation for annual and intra-annual tree-ring isotope chronologies. In: Siegwolf RTW, Brooks JR, Roden J, Saurer M (eds) *Stable isotopes in tree rings – inferring physiological, climatic and environmental responses*. Springer, Cham, Switzerland: pp 103-134.
- Björklund J, Seftigen K, Fonti P, Nievergelt D, von Arx G (2020) Dendroclimatic potential of dendroanatomy in temperature-sensitive *Pinus sylvestris*. *Dendrochronologia* 60: 125673.
- Björklund J, Seftigen K, Stoffel M, Fonti MV, Kottlow S, Frank DC, Esper J, Fonti P, Gooose H, Gunnarson BE, et al. (2023) Fennoscandian tree-ring anatomy shows a warmer modern than medieval climate. *Nature* 620: 97-103.
- Björklund J, von Arx G, Nievergelt D, Wilson R, van den Bulcke J, Günther B, Loader NJ, Rydval M, Fonti P, Scharnweber T, et al. (2019) Scientific merits and analytical challenges of tree-ring densitometry. *Rev Geophys* 57: 1224-1264.
- Bräker OU (1981) Der Alterstrend bei Jahrringdichten und Jahrringbreiten von Nadelhölzern und sein Ausgleich. *Mitteilungen der forstlichen Bundes-Versuchsanstalt Wien* 142: 75-102.
- Brázdil R, Pfister C, Wanner H, Von Storch H, Luterbacher J (2005) Historical climatology in Europe – the state of the art. *Clim Change* 70: 363-430.
- Briffa KR, Jones PD, Schweingruber FH, Osborn TJ (1998a) Influence of volcanic eruptions on Northern Hemisphere summer temperature over the past 600 years. *Nature* 393: 450-455.
- Briffa KR, Osborn TJ, Schweingruber FH (2004) Large-scale temperature inferences from tree rings: a review. *Glob Planet Change* 40: 11-26.
- Briffa KR, Osborn TJ, Schweingruber FH, Harris IC, Jones PD, Shiyatov SG, Vaganov EA (2001) Low-frequency temperature variations from a northern tree ring density network. *J Geophys Res* 106: 2929-2941.
- Briffa KR, Osborn TJ, Schweingruber FH, Jones PD, Shiyatov SG, Vaganov EA (2002) Tree-ring width and density data around the Northern Hemisphere: part 1, local and regional climate signals. *Holocene* 12: 737-757.
- Briffa KR, Schweingruber FH, Jones PD, Osborn TJ, Shiyatov SG, Vaganov EA (1998b) Reduced sensitivity of recent tree-growth to temperature at high northern latitudes. *Nature* 391: 678-682.
- Büntgen U (2022) Scrutinizing tree-ring parameters for Holocene climate reconstructions. *WIREs Clim Change* 13: e778.
- Büntgen U, Esper J (2024) Physiological meaning of bimodal tree growth-climate response patterns. *Int J Biometeorol*, <https://doi.org/10.1007/s00484-024-02706-5>.

- Büntgen U, Arseneault D, Boucher É, Churakova OV, Gennaretti F, Crivellaro A, Hughes MK, Kirilyanov AV, Klippel L, Krusic PJ (2020a) Prominent role of volcanism in Common Era climate variability and human history. *Dendrochronologia* 64: 125757.
- Büntgen U, Frank DC, Liebhold A, Johnson D, Carrer M, Urbinati C, Grabner M, Nicolussi K, Levanič T, Esper J (2009) Three centuries of insect outbreaks across the European Alps. *New Phytol* 182: 929-941.
- Büntgen U, Kolář T, Rybníček M, Koňasová E, Trnka M, Ač A, Krusic PJ, Esper J, Treydte K, Reinig F, et al. (2020b) No age trends in stable isotopes. *Paleoceanogr Paleoclimatol* 35: e2019PA003831.
- Büntgen U, Krusic PJ, Verstege A, Sangüesa-Barreda G, Wagner S, Camarero JJ, Ljungqvist FC, Zorita E, Oppenheimer C, Konter O, et al. (2017) New tree-ring evidence from the Pyrenees reveals western Mediterranean climate variability since medieval times. *J Clim* 30: 5295-5318.
- Büntgen U, Reinig F, Verstege A, Piermattei A, Kunz M, Krusic PJ, Slavin P, Štěpánek P, Torbenson M, Martínez del Castillo E, et al. (2024) Recent summer warming over the western Mediterranean region is unprecedented since medieval times. *Glob Planet Change* 232: 104336.
- Büntgen U, Tegel W, Nicolussi K, McCormick M, Frank DC, Trouet V, Kaplan JO, Herzig F, Heussner KU, Wanner H, et al. (2011) 2500 years of European climate variability and human susceptibility. *Science* 331: 578-582.
- Büntgen U, Trouet V, Frank DC, Leuschner HH, Friedrichs D, Luterbacher J, Esper J (2010) Tree-ring indicators of German summer drought over the last millennium. *Quat Sci Rev* 29: 1005-1016.
- Büntgen U, Urban O, Krusic PJ, Rybníček M, Kolář T, Kyncl T, Ač A, Koňasová E, Čáslavský J, Esper J, et al. (2021) Recent European drought extremes beyond Common Era background variability. *Nat Geosci* 14: 190-196.
- Carrer M, Unterholzner L, Castagneri D (2018) Wood anatomical traits highlight complex temperature influence on *Pinus cembra* at high elevation in the Eastern Alps. *Int J Biometeorol* 62: 1745-1753.
- Christiansen B, Ljungqvist FC (2017) Challenges and perspectives for large-scale temperature reconstructions of the past two millennia. *Rev Geophys* 55: 40-96.
- Cook ER, Briffa KR, Meko DM, Graybill DA, Funkhouser G (1995) The 'segment length curse' in long tree-ring chronology development for palaeoclimatic studies. *Holocene* 5: 229-237.
- Cook ER, Seager R, Kushnir Y, Briffa KR, Büntgen U, Frank DC, Krusic PJ, Tegel W, van der Schrier G, Andreu-Hayles L, et al. (2015) Old World megadroughts and pluvials during the Common Era. *Sci Adv* 1: e1500561.

- Cook ER, Woodhouse CA, Eakin CM, Meko DM, Stahle DW (2004) Long-term aridity changes in the western United States. *Science* 306: 1015-1018.
- Crivellaro A, Piermattei A, Dolezal J, Dupree P, Büntgen U (2022) Biogeographic implication of temperature-induced plant cell wall lignification. *Commun Biol* 5: 767.
- Dansgaard W (1964) Stable isotopes in precipitation. *Tellus A Dyn Meteorol Oceanogr* 16: 436-468.
- D'Arrigo R, Wilson R, Jacoby G (2006) On the long-term context for late twentieth century warming. *J Geophys Res* 111: D03103.
- D'Arrigo R, Wilson R, Liepert B, Cherubini P (2008) On the 'divergence problem' in northern forests: a review of the tree-ring evidence and possible causes. *Glob Planet Change* 60: 289-305.
- DeSoto L, De la Cruz M, Fonti P (2011) Intra-annual patterns of tracheid size in the Mediterranean tree *Juniperus thurifera* as an indicator of seasonal water stress. *Can J For Res* 41: 1280-1294.
- Diers M, Leuschner C, Dulamsuren C, Schulz TC, Weigel R (2024) Increasing winter temperatures stimulate Scots pine growth in the North German Lowlands despite stationary sensitivity to summer drought. *Ecosystems* 27: 428-442.
- Diers M, Weigel R, Leuschner C (2023) Both climate sensitivity and growth trend of European beech decrease in the North German Lowlands, while Scots pine still thrives, despite growing sensitivity. *Trees* 37: 523-543.
- Dodd JP, Patterson WP, Holmden C, Brasseur JM (2008) Robotic micromilling of tree-rings: a new tool for obtaining subseasonal environmental isotope records. *Chem Geol* 252: 21-30.
- Esper J, Büntgen U (2021) The future of paleoclimate. *Clim Res* 83: 57-59.
- Esper J, Büntgen U, Frank DC, Nievergelt D, Liebhold A (2007) 1200 years of regular outbreaks in alpine insects. *Proc R Soc B* 274: 671-679.
- Esper J, Cook ER, Schweingruber FH (2002) Low-frequency signals in long tree-ring chronologies and the reconstruction of past temperature variability. *Science* 295: 2250-2253.
- Esper J, Frank DC, Battipaglia G, Büntgen U, Holert C, Treydte K, Siegwolf R, Saurer M (2010) Low-frequency noise in $\delta^{13}\text{C}$ and $\delta^{18}\text{O}$ tree ring data: a case study of *Pinus uncinata* in the Spanish Pyrenees. *Glob Biogeochem Cycles* 24: GB4018.
- Esper J, Hartl C, Tejedor E, de Luis M, Günther B, Büntgen U (2020a) High-resolution temperature variability reconstructed from Black pine tree ring densities in southern Spain. *Atmosphere* 11: 748.
- Esper J, Klippel L, Krusic PJ, Konter O, Raible CC, Xoplaki E, Luterbacher J, Büntgen U (2020b) Eastern Mediterranean summer temperatures since 730 CE from Mt. Smolikas tree-ring densities. *Clim Dyn* 54: 1367-1382.

- Esper J, Konter O, Klippel L, Krusic PJ, Büntgen U (2021) Pre-instrumental summer precipitation variability in northwestern Greece from a high-elevation *Pinus heldreichii* network. *Int J Climatol* 41: 2828-2839.
- Esper J, Krusic PJ, Ljungqvist FC, Luterbacher J, Carrer M, Cook ER, Davi NK, Hartl-Meier C, Kirdyanov A, Konter O, et al. (2016) Ranking of tree-ring based temperature reconstructions of the past millennium. *Quat Sci Rev* 145: 134-151.
- Esper J, Riechelmann DFC, Holzkämper S (2020c) Circumferential and longitudinal $\delta^{13}\text{C}$ variability in a *Larix decidua* trunk from the Swiss Alps. *Forests* 11: 117.
- Esper J, Schneider L, Smerdon JE, Schöne BR, Büntgen U (2015) Signals and memory in tree-ring width and density data. *Dendrochronologia* 35: 62-170.
- Esper J, St George S, Anchukaitis KJ, D'Arrigo R, Ljungqvist FC, Luterbacher J, Schneider L, Stoffel M, Wilson R, Büntgen U (2018) Large-scale, millennial-length temperature reconstructions from tree-rings. *Dendrochronologia* 50: 81-90.
- Esper J, Torbenson M, Büntgen U (2024) 2023 summer warmth unparalleled over the past 2,000 years. *Nature*, <https://doi.org/10.1038/s41586-024-07512-y>.
- Feakins SJ, Ellsworth PV, Sternberg L (2013) Lignin methoxyl hydrogen isotope ratios in a coastal ecosystem. *Geochim Cosmochim Acta* 121: 54-66.
- Fonti P, Eilmann B, García-González I, von Arx G (2009) Expeditious building of ring-porous earlywood vessel chronologies without losing signal information. *Trees* 23: 665-671.
- Frank DC, Esper J (2005) Characterization and climate response patterns of a high-elevation, multi-species tree-ring network in the European Alps. *Dendrochronologia* 22: 107-121.
- Franke J, Frank DC, Raible CC, Esper J, Brönnimann S (2013) Spectral biases in tree-ring climate proxies. *Nat Clim Change* 3: 360-364.
- Freund MB, Helle G, Balting DF, Ballis N, Schleser GH, Cubasch U (2023) European tree-ring isotopes indicate unusual recent hydroclimate. *Commun Earth Environ* 4: 26.
- Frigo D, Römer P, Unterholzner L, Zimmer-Zachmann H, Esper J, Carrer M, Ziaco E (2024) Review of embedding and non-embedding techniques for quantitative wood anatomy. *Dendrochronologia* 88: 126241.
- Fritts HC (1976) *Tree rings and climate*. Blackburn Press, Caldwell, NJ, USA.
- Gagen M, Battipaglia G, Daux V, Duffy J, Dorado-Liñán I, Andreu-Hayles L, Martínez-Sancho E, McCarroll D, Shestakova TA, Treydte K (2022) Climate signals in stable isotope tree-ring records. In: Siegwolf RTW, Brooks JR, Roden J, Saurer M (eds) *Stable isotopes in tree rings – inferring physiological, climatic and environmental responses*. Springer, Cham, Switzerland: pp 537-579.
- Gagen M, McCarroll D, Loader NJ, Robertson I, Jalkanen R, Anchukaitis KJ (2007) Exorcising the 'segment length curse': summer temperature reconstruction since AD 1640 using

- non-detrended stable carbon isotope ratios from pine trees in northern Finland. *Holocene* 17: 435-446.
- Garcia-Pedrero A, García-Cervigón AI, Olano JM, García-Hidalgo M, Lillo-Saavedra M, Gonzalez-Martín C, Caetano C, Calderón-Ramírez S (2020) Convolutional neural networks for segmenting xylem vessels in stained cross-sectional images. *Neural Comput Appl* 32: 17927-17939.
- Gärtner H, Schweingruber FH (2013) *Microscopic preparation techniques for plant stem analysis*. Kessel, Remagen-Oberwinter, Germany.
- Gärtner H, Cherubini P, Fonti P, von Arx G, Schneider L, Nievergelt D, Verstege A, Bast A, Schweingruber FH, Büntgen U (2015) Technical perspective in modern tree-ring research – how to overcome dendroecological and wood anatomical challenges. *J Vis Exp* 97: e52337.
- Gessler A, Ferrio JP, Hommel R, Treydte K, Werner RA, Monson RK (2014) Stable isotopes in tree rings: towards a mechanistic understanding of isotope fractionation and mixing processes from the leaves to the wood. *Tree Phys* 34: 796-818.
- Gori Y, Wehrens R, Greule M, Keppler F, Ziller L, La Porta N, Camin F (2013) Carbon, hydrogen and oxygen stable isotope ratios of whole wood, cellulose and lignin methoxyl groups of *Picea abies* as climate proxies. *Rapid Commun Mass Spectrom* 27: 265-275.
- Greule M, Mosandl A, Hamilton JTG, Keppler F (2008) A rapid and precise method for determination of D/H ratios of plant methoxyl groups. *Rapid Commun Mass Spectrom* 22: 3983-3988.
- Greule M, Mosandl A, Hamilton JTG, Keppler F (2009) A simple rapid method to precisely determine $^{13}\text{C}/^{12}\text{C}$ ratios of plant methoxyl groups. *Rapid Commun Mass Spectrom* 23: 1710-1714.
- Greule M, Wieland A, Keppler F (2021) Measurements and applications of $\delta^2\text{H}$ values of wood lignin methoxy groups for paleoclimatic studies. *Quat Sci Rev* 268: 107107.
- Guerrieri R, Belmecheri S, Ollinger SV, Asbjornsen H, Jennings K, Xiao J, Stocker BD, Martin M, Hollinger DY, Bracho-Garrillo R, et al. (2019) Disentangling the role of photosynthesis and stomatal conductance on rising forest water-use efficiency. *PNAS* 116: 16909-16914.
- Hartl C, Schneider L, Riechelmann DFC, Kuhl E, Kochbeck M, Klippel L, Büntgen U, Esper J (2022) The temperature sensitivity along elevational gradients is more stable in maximum latewood density than tree-ring width. *Dendrochronologia* 73: 125958.
- Hartl-Meier C, Zang C, Büntgen U, Esper J, Rothe A, Göttlein A, Dirnböck T, Treydte K (2015) Uniform climate sensitivity in tree-ring stable isotopes across species and sites in a mid-latitude temperate forest. *Tree Physiol* 35: 4-15.

- Harvey JE, Smiljanić M, Scharnweber T, Buras A, Cedro A, Cruz-García R, Drobyshev I, Janecka K, Jansons Ā, Kaczka R, et al. (2020) Tree growth influenced by warming winter climate and summer moisture availability in northern temperate forests. *Glob Change Biol* 26: 2505-2518.
- Hetzer T, Bräuning A, Leuschner HH (2014) High-resolution climatic analysis of wood anatomical features in Corsican pine from Corsica (France) using latewood tracheid profiles. *Trees* 28: 1279-1288.
- Hoerling M, Eischeid J, Perlwitz J, Quan X, Zhang T, Pegion P (2012) On the increased frequency of Mediterranean drought. *J Clim* 25: 2146-2161.
- Intergovernmental Panel on Climate Change (IPCC) (2021) Summary for policymakers. In: Masson-Delmotte V, Zhai P, Pirani A, Connors SL, Péan C, Berger S, Caud N, Chen Y, Goldfarb L, Gomis MI, et al. (eds) *Climate Change 2021: The Physical Science Basis. Contribution of Working Group I to the Sixth Assessment Report of the Intergovernmental Panel on Climate Change*. Cambridge University Press, Cambridge, United Kingdom and New York, NY, USA: pp 3-32.
- Jacoby GC, D'Arrigo R (1995) Tree-ring width and density evidence of climatic and potential forest change in Alaska. *Glob Biogeochem Cycles* 9: 227-234.
- Janecka K, Harvey JE, Trouillier M, Kaczka RJ, Metslaid S, Metslaid M, Buras A, Wilmking M (2020) Higher winter-spring temperature and winter-spring/summer moisture availability increase Scots Pine growth on coastal dune microsites around the south Baltic Sea. *Front For Glob Change* 3: 578912.
- Kagawa A, Sano M, Nakatsuka T, Ikeda T, Kubo S (2015) An optimized method for stable isotope analysis of tree rings by extracting cellulose directly from cross-sectional laths. *Chem Geol* 393-394: 16-25.
- Katzenmaier M, Garnot VSF, Björklund J, Schneider L, Wegner JD, von Arx G (2023) Towards ROXAS AI: deep learning for faster and more accurate conifer cell analysis. *Dendrochronologia* 81: 126126.
- Keeling CD (1979) The Suess effect: ¹³Carbon-¹⁴Carbon interrelations. *Environ Int* 2: 229-300.
- Keppler F, Harper DB, Kalin RM, Meier-Augenstein W, Farmer N, Davis S, Schmidt HL, Brown DM, Hamilton JTG (2007) Stable hydrogen isotope ratios of lignin methoxyl groups as a paleoclimate proxy and constraint of the geographical origin of wood. *New Phytol* 176: 600-609.
- Keret R, Schliephack PM, Stangler DF, Seifert T, Kahle H-P, Drew DM, Hills PN (2024) An open-source machine-learning approach for obtaining high-quality quantitative wood anatomy data from *E. grandis* and *P. radiata* xylem. *Plant Sci* 340: 111970.
- Konter O, Krusic PJ, Trouet V, Esper J (2017) Meet Adonis, Europe's oldest dendrochronologically dated tree. *Dendrochronologia* 42: 12.

- Labuhn I, Daux V, Girardclos O, Stievenard M, Pierre M, Masson-Delmotte V (2016) French summer droughts since 1326 CE: a reconstruction based on tree ring cellulose $\delta^{18}\text{O}$. *Clim Past* 12: 1101-1117.
- Lavergne A, Hemming D, Prentice IC, Guerrieri R, Oliver RJ, Graven H (2022) Global decadal variability of plant carbon isotope discrimination and its link to gross primary production. *Glob Change Biol* 28: 524-541.
- Leavitt SW (2010) Tree-ring C-H-O isotope variability and sampling. *Sci Total Environ* 408: 5244-5253.
- Leonelli G, Coppola A, Salvatore MC, Baroni C, Battipaglia G, Gentilesca T, Ripullone F, Borghetti M, Conte E, Tognetti R, et al. (2017) Climate signals in a multispecies tree-ring network from central and southern Italy and reconstruction of the late summer temperatures since the early 1700s. *Clim Past* 13: 1451-1471.
- Levanič T, Jevšenak J, Hafner P (2020) Stable isotopes reveal climate signal hidden in tree rings of endemic Balkan pines. *Atmosphere* 11: 135.
- Lionello P, Scarascia L (2018) The relation between climate change in the Mediterranean region and global warming. *Reg Environ Change* 18: 1481-1493.
- Ljungqvist FC, Piermattei A, Seim A, Krusic PJ, Büntgen U, He M, Kirilyanov AV, Luterbacher J, Schneider L, Seftigen K, et al. (2020) Ranking of tree-ring based hydroclimate reconstructions of the past millennium. *Quat Sci Rev* 15: 124016.
- Loader NJ, McCarroll D, Miles D, Young GHF, Davies D, Ramsey CB (2019) Tree ring dating using oxygen isotopes: a master chronology for central England. *J Quat Sci* 34: 475-490.
- Loader NJ, McCarroll D, Miles D, Young GHF, Davies D, Ramsey CB, Williams M, Fudge M (2021) Dating of non-oak species in the United Kingdom historical buildings archive using stable oxygen isotopes. *Dendrochronologia* 69: 125862.
- Lopez-Saez J, Corona C, von Arx G, Fonti P, Slamova L, Stoffel M (2023) Tree-ring anatomy of *Pinus cembra* trees opens new avenues for climate reconstructions in the European Alps. *Sci Total Environ* 855: 158605.
- Lu Q, Liu X, Anhäuser T, Keppler F, Wang Y, Zeng X, Zhang Q, Zhang L, Wang K, Zhang Y (2020) Tree-ring lignin proxies in *Larix gmelinii* forest growing in a permafrost area of northeastern China: temporal variation and potential for climate reconstructions. *Ecol Indic* 118: 106750.
- Lukač L, Mikac S, Urban O, Kolář T, Rybniček M, Ač A, Trnka M, Marek MV (2021) Stable isotopes in tree rings of *Pinus heldreichii* can indicate climate variability over the eastern Mediterranean region. *Forests* 12: 350.
- McCarroll D, Gagen M, Loader NJ, Robertson I, Anchukaitis KJ, Los S, Young GHF, Jalkanen R, Kirchhefer A, Waterhouse JS (2009) Correction of tree ring stable carbon isotope

- chronologies for changes in the carbon dioxide content of the atmosphere. *Geochim Cosmochim Acta* 73: 1539-1547.
- McCormick M, Büntgen U, Cane MA, Cook ER, Harper K, Huybers P, Litt T, Manning SW, Mayewski PA, More AFM, et al. (2012) Climate change during and after the Roman Empire: reconstructing the past from scientific and historical evidence. *J Interdiscipl Hist* 43: 169-220.
- Mischel M, Esper J, Keppler F, Greule M, Werner W (2015) $\delta^2\text{H}$, $\delta^{13}\text{C}$ and $\delta^{18}\text{O}$ from whole wood, α -cellulose and lignin methoxyl groups in *Pinus sylvestris*: a multi-parameter approach. *Isot Environ Health Stud* 51: 553-568.
- Miyake F, Nagaya K, Masuda K, Nakamura T (2012) A signature of cosmic-ray increase in AD 774-775 from tree rings in Japan. *Nature* 486: 240-242.
- Nakatsuka T, Sano M, Li Z, Xu C, Tsushima A, Shigeoka Y, Sho K, Ohnishi K, Sakamoto M, Ozaki H, et al. (2020) A 2600-year summer climate reconstruction in central Japan by integrating tree-ring stable oxygen and hydrogen isotopes. *Clim Past* 16: 2153-2172.
- Neuwirth B, Schweingruber FH, Winiger M (2007) Spatial patterns of central European pointer years from 1901 to 1971. *Dendrochronologia* 24: 79-89.
- Peters RL, Balanzategui D, Hurley AG, von Arx G, Prendin AL, Cuny HE, Björklund J, Frank DC, Fonti P (2018) RAPTOR: row and position tracheid organizer in R. *Dendrochronologia* 47: 10-16.
- Piermattei A, Crivellaro A, Carrer M, Urbinati C (2015) The “blue ring”: anatomy and formation hypothesis of a new tree-ring anomaly in conifers. *Trees* 29: 613-620.
- Piermattei A, Crivellaro A, Krusic PJ, Esper J, Vitek P, Oppenheimer C, Felhofer M, Gierlinger N, Reinig F, Urban O, et al. (2020) A millennium-long ‘Blue Ring’ chronology from the Spanish Pyrenees reveals severe ephemeral summer cooling after volcanic eruptions. *Environ Res Lett* 15: 124016.
- Piovesan G, Biondi F, Baliva M, Presutti Saba E, Calcagnile L, Quarta G, D’Elia M, De Vivo G, Schettino A, Di Filippo A (2018) The oldest dated tree of Europe lives in the wild Pollino massif: Italus, a strip-bark Heldreich's pine. *Ecology* 99: 1682-1684.
- Plomion C, Leprévost G, Stokes A (2001) Wood formation in trees. *Plant Physiol* 127: 1513-1523.
- Prendin AL, Petit G, Carrer M, Fonti P, Björklund J, von Arx G (2017) New research perspectives from a novel approach to quantify tracheid wall thickness. *Tree Physiol* 37: 976-983.
- Rathgeber CBK, Cuny HE, Fonti P (2016) Biological basis of tree-ring formation: a crash course. *Front Plant Sci* 7: 734.

- Resente G, Gillert A, Trouillier M, Anadon-Rosell A, Peters RL, von Arx G, von Lukas U, Wilking M (2021) Mask, train, repeat! Artificial intelligence for quantitative wood anatomy. *Front Plant Sci* 12: 767400.
- Riechelmann DFC, Greule M, Treydte K, Esper J, Keppler F (2016) Climate signals in $\delta^{13}\text{C}$ of wood lignin methoxyl groups from high-elevation larch trees. *Palaeogeogr Palaeoclimatol Palaeoecol* 445: 60-71.
- Roden J (2008) Cross-dating of tree ring $\delta^{18}\text{O}$ and $\delta^{13}\text{C}$ time series. *Chem Geol* 252: 72-79.
- Römer P, Hartl C, Schneider L, Bräuning A, Szymczak S, Huneau F, Lebre S, Reinig F, Büntgen U, Esper J (2021) Reduced temperature sensitivity of maximum latewood density formation in high-elevation Corsican pines under recent warming. *Atmosphere* 12: 804.
- Römer P, Reinig F, Konter O, Friedrich R, Urban O, Čáslavský J, Pernicová N, Trnka M, Büntgen U, Esper J (2023) Multi-proxy crossdating extends the longest high-elevation tree-ring chronology from the Mediterranean. *Dendrochronologia* 79: 126085.
- Rossi S, Anfodillo T, Menardi R (2006) Trephor: a new tool for sampling microcores from tree stems. *IAWA J* 27: 89-97.
- Rydval M, Druckenbrod DL, Svoboda M, Trotsiuk V, Janda P, Mikoláš M, Čada V, Bače R, Teodosiu M, Wilson R (2018) Influence of sampling and disturbance history on climatic sensitivity of temperature-limited conifers. *Holocene* 28: 1574-1587.
- Saurer M, Cherubini P, Reynolds-Henne CE, Treydte K, Anderson WT, Siegwolf RTW (2008) An investigation of the common signal in tree ring stable isotope chronologies at temperate sites. *J Geophys Res* 113: G04035.
- Schneider L, Smerdon JE, Pretis F, Hartl-Meier C, Esper J (2017) A new archive of large volcanic events over the past millennium derived from reconstructed summer temperatures. *Environ Res Lett* 12: 094005.
- Schollaen K, Baschek H, Heinrich I, Slotta F, Pauly M, Helle G (2017) A guideline for sample preparation in modern tree-ring stable isotope research. *Dendrochronologia* 44: 133-145.
- Schollaen K, Heinrich I, Helle G (2014) UV-laser-based microscopic dissection of tree rings – a novel sampling tool for $\delta^{13}\text{C}$ and $\delta^{18}\text{O}$ studies. *New Phytol* 210: 1045-1055.
- Schweingruber F, Eckstein D, Serre-Bachet F, Bräker OU (1990) Identification, presentation and interpretation of event years and pointer years in dendrochronology. *Dendrochronologia* 8: 9-38.
- Seftigen K, Fonti MV, Luckman B, Rydval M, Stridbeck P, von Arx G, Wilson R, Björklund J (2022) Prospects for dendroanatomy in paleoclimatology – a case study on *Picea engelmannii* from the Canadian Rockies. *Clim Past* 18: 1151-1168.

- Siekacz L, Pearson C, Salzer M, Soja-Kukieła N, Koprowski M (2024) Blue rings in Bristlecone pine as a high resolution indicator of past cooling events. *Clim Change* 177: 123.
- Spinoni J, Barbosa P, De Jager A, McCormick N, Naumann G, Vogt JV (2019) A new global database of meteorological drought events from 1951 to 2016. *J Hydrol* 22: 100593.
- St George S (2014) An overview of tree-ring width records across the Northern Hemisphere. *Quat Sci Rev* 95: 132-150.
- Stolz J, van der Maaten E, Kalanke H, Martin J, Wilmking M, van der Maaten-Theunissen M (2021) Increasing climate sensitivity of beech and pine is not mediated by adaptation and soil characteristics along a precipitation gradient in northeastern Germany. *Dendrochronologia* 67: 125834.
- Tardif JC, Salzer MW, Conciatori F, Bunn AG, Hughes MK (2020) Formation, structure and climatic significance of blue rings and frost rings in high elevation bristlecone pine (*Pinus longaeva* D K Bailey). *Quat Sci Rev* 244: 106516.
- Telelis I (2008) Climatic fluctuations in the Eastern Mediterranean and the Middle East AD 300-1500 from Byzantine documentary and proxy physical paleoclimatic evidence – a comparison. *Jahrbuch der Österreichischen Byzantinistik* 58: 167-207.
- Torbenson M, Büntgen U, Esper J, Urban O, Balek J, Reinig F, Krusic PJ, Martínez del Castillo E, Brázdil R, Semerádová D, et al. (2023) Central European agroclimate over the past 2000 years. *J Clim* 36: 4429-4441.
- Torbenson M, Klippel L, Hartl C, Reinig F, Treydte K, Büntgen U, Trnka M, Schöne BR, Schneider L, Esper J (2022) Investigation of age trends in tree-ring stable carbon and oxygen isotopes from northern Fennoscandia over the past millennium. *Quat Int* 631: 105-114.
- Treydte K, Frank DC, Esper J, Andreu L, Bednarz Z, Berninger F, Boettger T, D'Alessandro CM, Etien N, Filot M, et al. (2007) Signal strength and climate calibration of a European tree-ring isotope network. *Geophys Res Lett* 34: L24302.
- Vitali V, Martínez-Sancho E, Treydte K, Andreu-Hayles L, Dorado-Liñán I, Gutierrez E, Helle G, Leuenberger M, Loader NJ, Rinne-Garmston KT, et al. (2022) The unknown third – Hydrogen isotopes in tree-ring cellulose across Europe. *Sci Total Environ* 813: 152281.
- von Arx G, Carrer M (2014) ROXAS – a new tool to build centuries-long tracheid-lumen chronologies in conifers. *Dendrochronologia* 32: 290-293.
- von Arx G, Crivellaro A, Prendin AL, Čufar K, Carrer M (2016) Quantitative wood anatomy – practical guidelines. *Front Plant Sci* 7: 781.
- Wang Y, Liu X, Anhäuser T, Lu Q, Zeng X, Zhang Q, Wang K, Zhang L, Zhang Y, Keppler F (2020) Temperature signal recorded in $\delta^2\text{H}$ and $\delta^{13}\text{C}$ values of wood lignin methoxyl groups from a permafrost forest in northeastern China. *Sci Total Environ* 727: 138558.

- Waterhouse JS, Switsur VR, Barker AC, Carter AHC, Hemming DL, Loader NJ, Robertson I (2004) Northern European trees show a progressively diminishing response to increasing atmospheric carbon dioxide concentrations. *Quat Sci Rev* 23: 803-810.
- Wieland A, Greule M, Römer P, Esper J, Keppler F (2022) Climate signals in stable carbon and hydrogen isotopes of lignin methoxy groups from southern German beech trees. *Clim Past* 18: 1849-1866.
- Wieland A, Römer P, Torbenson M, Greule M, Urban O, Čáslavský J, Pernicová N, Trnka M, Büntgen U, Esper J, et al. (2024) Tree-ring stable isotopes in cellulose and lignin methoxy groups reveal different age-related behaviour. *Quat Int* 693: 38-48.
- Wilson R, Luckman BH, Esper J (2005) A 500 year dendroclimatic reconstruction of spring-summer precipitation from the lower Bavarian forest region, Germany. *Int J Climatol* 25: 611-630.
- Yang B, Qin C, Bräuning A, Osborn TJ, Trouet V, Ljungqvist FC, Esper J, Schneider L, Griesinger J, Büntgen U (2021) Long-term decrease in Asian monsoon rainfall and abrupt climate change events over the past 6,700 years. *PNAS* 118: e2102007118.
- Young GHF, Demmler JC, Gunnarson BE, Kirchhefer AJ, Loader NJ, McCarroll D (2011) Age trends in tree ring growth and isotopic archives: a case study of *Pinus sylvestris* L. from northwestern Norway. *Glob Biogeochem Cycles* 25: GB2020.
- Zech M, Saurer M, Tuthorn M, Rinne K, Werner RA, Siegwolf R, Glaser B, Juchelka D (2013) A novel methodological approach for $\delta^{18}\text{O}$ analysis of sugars using gas chromatography-pyrolysis-isotope ratio mass spectrometry. *Isot Environ Health Stud* 49: 492-502.
- Ziaco E, Biondi F, Heinrich I (2016) Wood cellular dendroclimatology: testing new proxies in Great Basin bristlecone pine. *Front Plant Sci* 7: 1602.

List of figures

Chapter 1

- Fig. 1.1** | Magnified cross-section of a gymnosperm xylem (*Pinus heldreichii* from Mt. Smolikas, Greece). The image shows two consecutive tree rings with large earlywood and smaller latewood cells. Tree-ring boundaries are marked by orange dashed lines **2**
- Fig. 1.2** | Location of the study sites and images of the investigated tree species: *Fagus sylvatica* (FASY), *Larix decidua* (LADE), *Picea abies* (PIAB), *Pinus cembra* (PICE), *Pinus heldreichii* (PIHE), *Pinus nigra* (PINI), and *Pinus sylvestris* (PISY) **5**

Chapter 2

- Fig. 2.1** | Tree-ring and environmental data. (a) Topographic map showing spruce (circles) and pine (triangles) sites colored according to their mean segment lengths (MSL). (b) Periods covered by tree-ring chronologies and environmental records. Grey bars show the full tree-ring records, black bars indicate lengths after truncation at $n \geq 10$ series. The common period of all series (1952-2009 CE) is highlighted in light yellow **12**
- Fig. 2.2** | Climate and soil moisture conditions in southwest Germany. Maps of annual (a) maximum air temperatures (T_{max}), (b) precipitation (Prec), and (c) soil moisture indices (SMI). Time series of annual (d) T_{max} , (e) Prec, and (f) SMI derived from nearby gridded data. Each dot represents one grid. Dashed lines show linear trends from 1952-2009 CE, R^2 values are the coefficients of determination. Monthly (g) T_{max} , (h) Prec, and (i) SMI changes between the subperiods S2 (1981-2009 CE) and S1 (1952-1980 CE). Boxplots show the distribution among grid cells. White bars are the medians, boxes the 25%- and 75%-quartiles, whiskers the min and max values within 1.5x the interquartile range, and dots are outliers. Positive residuals indicate higher values in the recent subperiod S2 compared to subperiod S1 **13**
- Fig. 2.3** | Spruce and pine growth characteristics. Regional curves of the (a) spruce (green) and (b) pine (yellow) sites truncated at < 10 series. Black lines are the arithmetic means at $n \geq 5$ sites. Bottom panels show the number of integrated site chronologies. Relationship between segment length and mean tree-ring width (TRW) of all (c) spruce and (d) pine series. Each dot represents one individual series. Basal area increment (BAI) chronologies of (e) spruce and (f) pine truncated at < 10 series. Black lines are the arithmetic means at $n \geq 5$ sites. Numbers between the vertical dashed lines indicate the mean BAI $\pm 1\sigma$ calculated for 1952-2009 CE. Bottom panels show the number of integrated site chronologies **16**
- Fig. 2.4** | Growth response to soil moisture variability. (a) Basal area increment (BAI) of spruce (green) and pine (yellow) from 1952-2009 CE. Thick curves are the average BAI of all spruce and pine sites, respectively. Colored shadings indicate $\pm 1\sigma$. Red numbers and grey shadings label the ten driest growing seasons (1 = lowest SMI). (b) Band-pass filtered (10-20 years) z-scores of the growing-season SMI (black) shown together with spruce (green) and pine (yellow) BAI. (c-d) Average BAI (1952-2009 CE) of spruce (top panels) and pine (bottom panels) as a function of mean segment length (MSL), (e-f) elevation, (g-h) maximum air temperature (T_{max}), (i-j) precipitation totals, and (k-l) soil moisture indices (SMI). The latter three variables are calculated for the growing season (April-October). Each dot

- represents one site. Dashed lines show linear trends. Colored areas are the 95% confidence intervals of the regression slopes. Asterisks behind R^2 indicate significance at $p < 0.05$ 17
- Fig. 2.5** | Detrended tree-ring width (TRW) chronologies. (a) Spruce (green) and pine (yellow) site chronologies after detrending using 10-year cubic smoothing splines (10SP, top panel) and negative exponential curves (EXP, middle panel), shown together with their 30-year running inter-series correlations (R_{bar} , bottom panel). Thick curves (top and middle panel) are the regional mean chronologies. (b-c) Correlations between the 10SP spruce and pine chronologies as a function of distance. Dashed lines indicate linear trends of all possible spruce ($n = 231$) and pine ($n = 276$) pairings 18
- Fig. 2.6** | Climate-growth relationships. (a) Distribution of bootstrap correlations of the 10SP chronologies (spruce = green, pine = yellow) with seasonal maximum air temperatures (T_{max}) and precipitation (Prec) from 1951-2009 CE. Boxplots show the median (white bar), 25%- and 75%-quartiles (box), min and max values within 1.5x the interquartile range (whiskers), and outliers (points). Horizontal dashed lines mark $p < 0.05$. (b) Corresponding 21-year running correlations between the TRW site chronologies and seasonal T_{max} . Black curves are the mean. (c) Field correlations ($p < 0.05$) between the 10SP regional pine chronology and February-March T_{max} (EOBS). (d) Z-Scores of the 10SP regional pine chronology (brown dashed line) and high-pass filtered February-March T_{max} (black solid line). Yellow shadings represent $\pm 1\sigma$ of all pine chronologies. R values refer to 1952-1980 and 1981-2009 CE 19
- Fig. 2.7** | Soil moisture sensitivity. (a) Distribution of bootstrap correlations of 10SP chronologies (spruce = green, pine = yellow) with monthly and seasonal soil moisture indices from 1951-2009 CE. Boxplots show the median (white bar), 25%- and 75%-quartiles (box), min and max values within 1.5x the interquartile range (whiskers), and outliers (points). Horizontal dashed lines mark $p < 0.05$. (b) Mean 21-year running correlations of the species with current-year July-August (JA) and previous-year August-December (pA-D) SMI. Soil moisture sensitivity of (c) spruce and (d) pine as a function of elevation. Each dot represents one site. Light colors indicate correlations (1952-2009 CE) with the pA-D SMI, dark colors correlations with the JA SMI. Dashed lines show linear trends. Colored areas are the 95% confidence intervals of the regression slopes. Asterisks behind R^2 indicate significance at $p < 0.01$ 21
- Fig. S2.1** | Tree-ring width (TRW) and basal area increment (BAI) data. (a) Stem cross-section of a 60-year-old tree showing the two growth parameters. (b) The AGR of each site is calculated over the first 60 years of cambial age (highlighted by vertical dashed lines) as mean (\bar{X} ; horizontal dashed line) of the regional curve. (c) Effects of standardization and BAI calculation. Top panel shows a raw TRW chronology together with a fitted 10-year cubic smoothing spline (red) and negative exponential curve (green). Middle panel shows the index chronologies after spline (10SP, dotted curve) and negative exponential detrending (EXP, solid curve). Bottom panel shows the BAI record derived from the TRW measurements using the equation shown in panel a 36
- Fig. S2.2** | (a) Principal component gradient analyses (Buras et al. 2016) using 10-year (10SP), 30-year (30SP), 50-year (50SP), 100-year (100SP) spline, negative exponential (EXP), and basal area increment (BAI) chronologies (1952-2009 CE). Each arrow represents a spruce (green) or pine (yellow) site. R values indicate average intra-species correlations. (b)

- Hierarchical cluster analysis of the 10SP site chronologies. Note the distinct separation between spruce and pine in the 10SP data 37
- Fig. S2.3** | Age-aligned basal area increment (BAI) chronologies of the (a) 22 spruce and (b) 24 pine sites truncated at < 10 series. Black lines represent species-specific means calculated for $n \geq 5$ sites. Bottom panels show site chronology replications 37
- Fig. S2.4** | Average growth rate (AGR) of spruce (top panels) and pine (bottom panels) as a function of (a-b) mean segment length (MSL), (c-d) elevation, (e-f) maximum air temperature (T_{\max}), (g-h) precipitation totals, and (i-j) soil moisture indices (SMI). The latter three variables are calculated for the growing season. Each dot represents one site. Dashed lines show linear trends. Colored areas are 95% confidence intervals of the regression slopes for spruce (green) and pine (yellow). Asterisks behind R^2 indicate $p < 0.05$ 38
- Fig. S2.5** | Monthly climate-growth correlations for 1952-2009 CE. Distribution of bootstrap correlations of the 10SP TRW chronologies (spruce = green, pine = yellow) with (a) maximum air temperatures and (b) precipitation from previous-year (lower case letters) May to current-year (upper case letters) October. Boxplots show the median (white bar), 25%- and 75%-quartiles (box), min and max values within 1.5x the interquartile range (whiskers), and outliers (points). Dashed lines mark $p < 0.05$ 38
- Fig. S2.6** | Mean 21-year running correlations of spruce sites below 550 m asl (dashed curves) and above 550 m asl (solid curves) with (a) previous-year August-December (pA-D) and (b) current-year July-August (JA) soil moisture indices (10SP data) 39
- Fig. S2.7** | Linear regressions between (a) annual maximum air temperatures (T_{\max}) and annual precipitation (Prec), (b) elevation and T_{\max} , and (c) elevation and Prec. Green circles represent the spruce sites, yellow triangles the pine sites 39
- Fig. S2.8** | Linear regressions between average growth rates (AGR) calculated over the first 60 years of cambial age and mean segment lengths (MSL) of the (a) 1831 spruce and (b) 1942 pine series. Each circle represents one series 39
- Fig. S2.9** | (a) Percentage of February-March days exceeding daily mean temperatures (daily T_{mean}) of 4°C (yellow), 6°C (orange), 8°C (red), and 10°C (dark red) at the meteorological station in Geisenheim from 1952-2009 CE. (b) Value distributions of the various temperature thresholds from panel a. Boxplots show the median (black bar), 25%- and 75%-quartiles (box), and min and max values within 1.5x the interquartile range (whiskers). The climate station data was downloaded from the German Weather Service (<https://cdc.dwd.de/portal/>) 40
- Fig. S2.10** | (a) February-March maximum air temperatures (T_{\max}) from 1952-2009 CE. Red shading represents ± 1 standard deviation of the 24 grid cells covering the pine sites. Horizontal dashed lines show mean T_{\max} from 1951-1989 and 1990-2009 CE. (b) Correlation matrix of the raw and high-pass filtered monthly T_{\max} series (Jan-Jun). 1σ indicates one standard deviation of the T_{\max} series 40

Chapter 3

- Fig. 3.1** | Study site and climate. (a) Geographical location of Corsica in the Mediterranean. (b) Topographic map of Corsica indicating the sampling sites and meteorological stations.

- (c) Climate diagram showing monthly temperatures (red curve) and precipitation (blue bars) of the combined station data from Ajaccio and Bastia (1961-1990 CE) **43**
- Fig. 3.2** | Corsican pines and wood density. (a) Living trees and (b) relict trunks of *P. nigra* at the upper treeline. (c) Thin section of three consecutive tree rings and their density profile (red curve) across the earlywood (EW) and latewood (LW). Yellow dots indicate the maximum latewood density (MXD) **44**
- Fig. 3.3** | (a) Hugershoff-detrended MXD composite (COR_{HGS}) and site chronologies (*Asc*, *Tar*, and *Sor*) (thin curves), and their 31-year smoothing splines (bold curves). (b) 51-year running correlations between the site chronologies (grey) shown together with their mean (black). The inserted table indicates inter-site correlations calculated over the sufficiently replicated ($n \geq 5$ series) common period 1636-1980 CE (1636 CE is marked by a vertical dashed line). (c) Sample replication of each chronology **47**
- Fig. 3.4** | Effects of age-band decomposition. (a) Detrended composite chronologies (thin curves) and their 31-year smoothing splines (bold curves) considering all MXD data (COR), data from 30-400 years ($ABC400$), 30-300 years ($ABC300$), and 30-200 years ($ABC200$). COR was detrended using HGS (COR_{HGS}) and RCS (COR_{RCS}), while all age-band chronologies were detrended using RCS. (b) Mean tree age of the chronologies. (c-f) Samples (bar plots) and replication (black lines) of the chronologies. Each horizontal bar depicts one individual series. Percentages in brackets indicate the remaining data compared to COR (= 100%). Grey-shaded areas mark the periods when replication in at least one record is $n < 5$ series **49**
- Fig. 3.5** | Comparison of long MXD chronologies from southern Europe. (a) Location of the MXD sites: Cazorla (*CAZ*), Gerber (*GER*), Corsica (*COR*), Serra di Crispo (*CRI*), and Mt. Smolikas (*SMO*). The matrix shows correlations between the HGS-detrended chronologies over their 1360-2004 CE common period – except for *CRI*, which covers 1604-1980 CE. (b) 31-year smoothing splines of the normalized HGS-detrended MXD chronologies from 1375-1989 CE ($n \geq 5$ series). (c) COR_{HGS} shown together with the August-September temperature reconstruction from Corsican pine stable carbon isotopes ($COR_{\delta^{13}C}$) and a May-September temperature reconstruction from the Pyrenees based on MXD (PYR_{MXD}). All records were normalized (COR_{HGS} and PYR_{MXD} from 1360-2005 CE and $COR_{\delta^{13}C}$ from 1448-2005 CE) and smoothed using 31-year splines **51**
- Fig. 3.6** | Site-specific temperature signals. Correlations between the Hugershoff-detrended chronologies and monthly and seasonal temperatures of the combined station records from (a) 1951-1980 and (b) 1951-2016 CE. Note that *Sor* only extends to 1980 CE and indicates same correlations in (a) and (b). (c) Thirty-one-year running correlations between the chronologies and seasonal AMJJ and SO temperatures of the station records (thick solid curves) and CRU data (thin dashed curves) **52**
- Fig. 3.7** | Climate signals of the Corsican MXD composite chronologies. (a) Spatial correlations between $ABC200$ and 0.5° gridded monthly temperatures (CRU) over the Mediterranean Basin (1901-1980 CE). Significant correlations at $p < 0.1$ are colored. (b) Correlations between the composite chronologies and seasonal temperatures from 1901-1980 (left) and 1901-2016 CE (right). Note that $ABC200$ and $ABC300$ only extend until 1980 and 1988 CE, respectively. (c) MXD chronologies scaled from 1901-2016 CE against AMJJ and SO temperature anomalies (CRU). Horizontal lines display mean temperatures from 2000 to 2016

- CE. 31-year running correlations between the MXD chronologies and (d) CRU AMJJ and SO temperatures, and (e) GPCC JJ precipitation **53**
- Fig. S3.1** | Effects of merging site measurements. (a) Hugershoff-detrended MXD composite (COR_{HGS}) and site chronologies (Asc , Tar , Sor) (thin curves) shown together with their 31-year smoothing splines (bold curves), (b) their expressed population signal (EPS) computed for 30-year segments with 15-year overlaps, and (c) their mean tree age curves **68**
- Fig. S3.2** | Effects of mean adjustment. Regional curves (thin curves) shown together with their 300-year splines (bold curves) and boxplots displaying growth rates of the site-specific MXD data (a-b) before mean-adjustment and (c-d) after mean-adjustment. (e) COR chronologies (thin curves) and their 300-year splines (bold curves) after applying RCS to the mean-adjusted data (black), to the unadjusted data (orange), and to the site-specific data before merging (red). Start and end dates were set to $n \geq 5$ series. Note the considerably lower indices of the unadjusted chronology version before ~1600 CE (caused by the dominance of higher elevated trees from Asc) **69**
- Fig. S3.3** | Sample replication and regional curves of the composite MXD data. (a) Replication curves of age-aligned tree rings highlighting the data sections: $ABC200$ contains rings from 30-200 years, $ABC300$ from 30-300 years, and $ABC400$ from 30-400 years. Rings younger than 30 years and older than 400 years are only included in COR . (b) Regional curves of the chronologies (light) shown together with their 100-year low pass filters (bold). Pith-offset estimates are considered. Note the Hugershoff-shaped age trend in COR **69**
- Fig. S3.4** | Temperature signal estimation using the CRU TS4.04 data. Correlations between the HGS-detrended chronologies and monthly and seasonal temperatures from (a) 1901-1980 and (b) 1901-2016 CE. Note that Sor ends in 1980 CE **70**
- Fig. S3.5** | Precipitation signal estimation using the GPCC v2020 data. Correlations between the composite chronologies and monthly and seasonal precipitation totals from (a) 1891-1980 and (b) 1891-2016 CE. Note that $ABC200$ and $ABC300$ end in 1980 and 1988 CE, respectively. (c) 31-year running correlations between the chronologies and June-July (JJ) and August-September (AS) precipitation totals **70**

Chapter 4

- Fig. 4.1** | Visual comparison of microscopic sections (100x magnification) produced from the same samples of *Fagus sylvatica* (FASY), *Larix decidua* (LADE), and *Pinus cembra* (PICE) processed with both paraffin embedding (PAR) and without paraffin embedding ($NoPAR$) (scale bar = 1 mm) **75**
- Fig. 4.2** | Mean (blue curves) and standard deviation (green curves) chronologies of (a) vessel area, (b-c) tracheid lumen area, (d) hydraulic diameter, and (e-f) cell wall thickness measured on the paraffin-embedded (PAR) and non-paraffin-embedded ($NoPAR$) samples of *Fagus sylvatica* (FASY), *Larix decidua* (LADE), and *Pinus cembra* (PICE) **76**
- Fig. 4.3** | Scatterplots showing the relationship between the average values of (a) vessel/tracheid lumen area, (c) hydraulic diameter, (e) cell wall thickness, and (b, d, f) respective standard deviations measured on paraffin-embedded sections (PAR) with the absolute

difference between the mean values measured on *PAR* and *NoPAR* samples. Colored lines are linear regressions (dashed lines indicate $p > 0.05$; solid lines $p < 0.05$) **78**

Fig. 4.4 | Standardized tracheidograms (solid bold lines) of lumen area and cell wall thickness from paraffin-embedded (*PAR*, dark blue lines) and non-paraffin-embedded (*NoPAR*, green lines) samples of (a-b) LADE and (c-d) PICE. Thin curves represent ± 1 standard deviation. Dotted curves show mean differences between the tracheidograms **79**

Fig. S4.1 | *PAR* (blue curves) and *NoPAR* (green curves) distribution of (a) vessel area, (b-c) tracheid lumen area, (d) hydraulic diameter, and (e-f) cell wall thickness measured over 15 rings on *Fagus sylvatica* (FASY), *Larix decidua* (LADE), and *Pinus cembra* (PICE) **84**

Chapter 5

Fig. 5.1 | Mt. Smolikas tree-ring data (as published in Esper et al. 2020a, 2021). (a) Photograph of relict *Pinus heldreichii* trunks and map showing the geographical location of Mt. Smolikas in Europe. (b) Segment length plot indicating the sample replication of the tree-ring width (TRW), maximum latewood density (MXD), stable carbon ($\delta^{13}\text{C}$) and radiocarbon isotope (^{14}C) data in the first millennium. Each horizontal bar represents one measurement series. Vertical dashed lines mark the years when sample replication falls below 10 series/year. (c) Expressed population signal (EPS) and (d) mean inter-series correlation (R_{bar}) for each proxy calculated over 50-year windows, lagged by 49 years. Dotted curves highlight periods when R_{bar} /EPS-calculations are based on two series only. Note the sharp decrease in R_{bar} /EPS of $\delta^{13}\text{C}$ at the early chronology end caused by the misdating of *Pine16a* **88**

Fig. 5.2 | Crossdating of *Pine16a*. (a) Bars indicating the two potential dating positions: *Opt1* (597-852 CE) and *Opt2* (468-723 CE) with color code as in Fig. 5.1. High-pass filtered (b) TRW, (c) MXD, and (d) $\delta^{13}\text{C}$ time series of *Pine16a* (color) and the master chronologies (grey). All series are z-transformed for better comparison. Brackets highlight the maximum overlap and corresponding Pearson correlations **93**

Fig. 5.3 | Radiocarbon dating. Symbols represent ^{14}C ages BP $\pm 1\sigma$ (whiskers) of single rings and brackets the calibrated age ranges (CE) at 99.7% probability (Fig. S5.4 for details). The uncalibrated ^{14}C ages (BP) are aligned to their $\delta^{13}\text{C}$ dates (CE). The blue line is the *IntCal20* calibration curve **94**

Fig. 5.4 | Changes in the (a) TRW, (b) MXD, and (c) $\delta^{13}\text{C}$ chronologies. Upper panels show the re-dated, new chronologies (color) compared to their old versions (black). Filled areas in the background indicate the underlying sample replication. Lower panels show the expressed population signal (EPS; solid lines) and mean inter-series correlation (R_{bar} ; dashed lines) of the new (color) and old (black) chronologies calculated over 50-year windows with a lag of 49 years and truncated at $n < 2$ correlations. Horizontal, black-dashed lines mark the EPS threshold of 0.85. All chronologies are high-pass filtered and z-transformed **95**

Fig. S5.1 | Effects of high-pass filtering. Distribution of z-scored proxy data for (a-c) the entire dataset and for (d-f) *Pine16a*. Probability density of the raw (grey) and detrended (color) data with Shapiro-Wilk test results (p-values), skewness (skew), kurtosis (kurt), and sample size (n; total number of rings). Note that high-pass filtering pushes the data closer to normal distribution and reduces skewness and kurtosis, especially in the large datasets (a-c) ... **104**

- Fig. S5.2** | *Pine16a* at *Opt2* (468-723 CE). (a) Raw and (b) high-pass filtered $\delta^{13}\text{C}$ series with corresponding Pearson correlations between *Pine16a* and the master chronology when $n = 1$ series (597-683 CE). Note the strong covariance between the two time series. The yellow area in the background highlights a short period (613-625 CE) of high-frequency mismatch. (c) Sample replication of the $\delta^{13}\text{C}$ chronology **105**
- Fig. S5.3** | Independent age validation. Symbols represent the mean calendric ages CE of the ^{14}C wiggle-match and whiskers the age ranges at 99.7% probability. The dashed line denotes similar years between calibrated ^{14}C ages and dendrochronological dates. Note that *Pine44b* and *Opt2* whiskers consistently overlap with the dashed line and are therefore considered correct **105**
- Fig. S5.4** | OxCal results of (a) *Pine16a* and (b) *Pine44b*. The individual rings are coded by their TRW-based dates. Smoothed histograms represent the probability distributions of the individual (yellow) and wiggle-match (grey) age ranges (CE) at 99.7% probability. The wiggle-match results are highlighted by red brackets. Uncalibrated ^{14}C ages (BP) of (c) *Pine16a* and (d) *Pine44b* plotted against *IntCal20* **106**
- ## Chapter 6
- Fig. 6.1** | Study site and proxy data. (a) Location of Mt. Smolikas in Europe. (b) Temporal distribution of the tree-ring stable isotope (TRSI) series. Asterisks denote series with only methoxy data. (c) *Pinus heldreichii* tree and schematic illustration of plant components used for TRSI measurement. (d) Cambial age of the individual tree-ring series **110**
- Fig. 6.2** | Decadally resolved (a) TRW, (b) MXD, (c) $\delta^{13}\text{C}_c$, (d) $\delta^{13}\text{C}_m$, (e) $\delta^{18}\text{O}_c$, and (f) $\delta^2\text{H}_m$ series from 512 to 2020 CE. Green curves are measurements from living trees and colored series from relict wood. Black curves are the mean chronologies **115**
- Fig. 6.3** | Distribution and range of (a) TRW, (b) MXD, (c) $\delta^{13}\text{C}_c$, (d) $\delta^{13}\text{C}_m$, (e) $\delta^{18}\text{O}_c$, and (f) $\delta^2\text{H}_m$ values. Green boxes correspond to living trees, while other colors represent the proxy-specific relict wood (same color code as in Fig. 6.2). Vertical black lines are the median (50th percentile), boxes the 25th and 75th percentiles, whiskers the 95% confidence interval, and points denote outliers. Numbers next to the arrows indicate the offsets between living and relict means ($\Delta_{\text{liv/rel}}$). Numbers next to the boxplots indicate the sample replication **116**
- Fig. 6.4** | Intra-series standard deviation (mean SD within individual series), inter-series standard deviation (mean SD between all series in a certain decade), and mean offset between living and relict wood ($\Delta_{\text{liv/rel}}$) calculated for (a) TRW, (b) MXD, (c) $\delta^{13}\text{C}_c$, (d) $\delta^{13}\text{C}_m$, (e) $\delta^{18}\text{O}_c$, and (f) $\delta^2\text{H}_m$ **117**
- Fig. 6.5** | Age-aligned (a) TRW, (b) MXD, (c) $\delta^{13}\text{C}_c$, (d) $\delta^{13}\text{C}_m$, (e) $\delta^{18}\text{O}_c$, and (f) $\delta^2\text{H}_m$ relict wood series. Top panels show the raw series (grey curves) and their arithmetic means (colored curves). Lower panels show the means of the normalized data **118**
- Fig. 6.6** | Linear slopes of the mean z-transformed TRW (orange), MXD (yellow), $\delta^{13}\text{C}_c$ (light red), $\delta^{13}\text{C}_m$ (dark red), $\delta^{18}\text{O}_c$ (light blue), and $\delta^2\text{H}_m$ (dark blue) series. White bars represent non-significant ($p > 0.01$) and colored bars significant slopes at $p < 0.01$ **119**
- Fig. S6.1** | Mean age-aligned (a) $\delta^{13}\text{C}_c$ and (b) $\delta^{18}\text{O}_c$ chronologies of the decadal (black lines) and annual (colored lines) relict wood series. (c) Linear slopes of the mean z-transformed

- $\delta^{13}\text{C}_c$ and $\delta^{18}\text{O}_c$ series at annual resolution. White bars represent non-significant ($p > 0.01$) and colored bars significant slopes at $p < 0.01$ 131
- Fig. S6.2** | Linear slopes (unit per decade) of the raw, age-aligned (a) TRW, (b) MXD, (c) $\delta^{13}\text{C}_c$, (d) $\delta^{13}\text{C}_m$, (e) $\delta^{18}\text{O}_c$, and (f) $\delta^2\text{H}_m$ series. Horizontal black lines are the median (50th percentile), boxes the 25th and 75th percentiles, and whiskers the 95% confidence interval 131
- Fig. S6.3** | Distribution and range of (a) $\delta^{13}\text{C}_c$, (b) $\delta^{13}\text{C}_m$, (c) $\delta^{18}\text{O}_c$, and (d) $\delta^2\text{H}_m$ values over the common period of living and relict wood (1641-1820 CE). Green boxes correspond to the living trees, while other colors represent the relict wood. Vertical black lines are the median (50th percentile), boxes the 25th and 75th percentiles, whiskers the 95% confidence interval, and points denote outliers 132
- Fig. S6.4** | Relative age-aligned (a) $\delta^{13}\text{C}_c$, (b) $\delta^{13}\text{C}_m$, (c) $\delta^{18}\text{O}_c$, and (d) $\delta^2\text{H}_m$ relict wood series. Relative TRSI values were calculated by subtracting the arithmetic mean of the common period (202-238 years). Colored lines represent the means of the individual series 132
- Fig. S6.5** | Linear slopes of the mean z-transformed TRW (orange), MXD (yellow), $\delta^{13}\text{C}_c$ (light red), $\delta^{13}\text{C}_m$ (dark red), $\delta^{18}\text{O}_c$ (light blue), and $\delta^2\text{H}_m$ (dark blue) series. White bars represent non-significant ($p > 0.01$) and colored bars significant slopes at $p < 0.01$ 133
- Fig. S6.6** | Linear slopes (unit per decade) of the relative (a) $\delta^{13}\text{C}_c$, (b) $\delta^{13}\text{C}_m$, (c) $\delta^{18}\text{O}_c$, and (d) $\delta^2\text{H}_m$ series. White bars represent non-significant ($p > 0.01$) and colored bars significant slopes at $p < 0.01$ 133
- Fig. S6.7** | Example of a relict wood fragment where a disc sample was taken from unknown tree height 134

Chapter 7

- Fig. 7.1** | Study material and tree-ring data. (a) Living Bosnian pine at Mt. Smolikas, Greece. (b) Illustration of tree-ring width (TRW), maximum latewood density (MXD), radial tracheid lumen diameter (D_{rad}), radial and tangential cell wall thickness ($\text{CWT}_{\text{rad}}/\text{CWT}_{\text{tan}}$), cellulose carbon ($\delta^{13}\text{C}_c$) and oxygen isotopes ($\delta^{18}\text{O}_c$), as well as lignin methoxy carbon ($\delta^{13}\text{C}_m$) and hydrogen ($\delta^2\text{H}_m$) isotopes 137
- Fig. 7.2** | Climate data. June-August (JJA) (a) mean air temperature (T_{mean}) and (b) precipitation anomalies (wrt. 1961-1990 CE) from the CRU TS4.07 grid (black lines) closest to Mt. Smolikas and the meteorological stations (grey lines) in Kerkyra (*KER*), Larissa (*LAR*), and Thessaloniki (*THE*). (c-d) Temporal coverage of the temperature and precipitation stations used to interpolate the gridded data. Each horizontal bar represents one station. The dark red and dark blue bars highlight (“active”) stations providing measurements until 2020 CE. (e) Spatial coverage of the “active” and “inactive” stations integrated into the gridded data. The dashed circles indicate linear distances (250 and 500 km) from the study site 141
- Fig. 7.3** | Individual series (grey curves) and mean chronologies (black curves) of raw (a) TRW, (b) MXD, (c) $\delta^{13}\text{C}_c$, (d) $\delta^{13}\text{C}_m$, (e) $\delta^{18}\text{O}_c$, (f) $\delta^2\text{H}_m$, (g) D_{rad} , (h) and CWT. The latter represents the mean of CWT_{rad} and CWT_{tan} (details in Fig. S7.4). The $\delta^{13}\text{C}$ series are corrected for the Suess effect. Values at the right top are the arithmetic mean ± 1 standard deviation calculated over all tree rings between 1861-2020 CE (1861-2017 CE for MXD) 143

- Fig. 7.4** | Climate signals. Correlations between the 30SP-detrended chronologies and monthly/seasonal (a) mean air temperature (T_{mean}), (b) precipitation, (c) the PDSI, and (d) cloud cover data calculated for 1931-2020 CE. Horizontal dashed lines indicate the significance level of $p < 0.01$. Please note that the significance level for MXD is marginally higher (~ 0.004) due to the shorter calibration period (1931-2017 CE), but is not displayed for the sake of clarity **145**
- Fig. 7.5** | Temporal stability of the temperature (T_{mean}) and precipitation (Prec) signals in (a) $\delta^{13}\text{C}_c$, (b) $\delta^{13}\text{C}_m$, (c) $\delta^{18}\text{O}_c$, and (d) D_{rad} . Vertical bars (left) show correlations between the HOM, 30SP, and 100SP proxy records and June-August T_{mean} (red) and precipitation (blue) calculated for 1931-2020 CE. Curves in the right panels show 31-year running correlations for the different detrendings **146**
- Fig. 7.6** | Intra-ring sectors of wood anatomical traits. (a) Tracheidograms of D_{rad} (upper panel), CWT_{rad} , and CWT_{tan} (middle panel), shown together with the mean Rbar of each 30SP sector chronology calculated for 1861-2020 CE (bottom panel). Shaded areas indicate $\pm 1\sigma$. The sectors are labeled with Roman numerals (I-X). (b) Three-dimensional PCA plot showing the first three principal components computed on the 30SP-detrended TRW, MXD, $\delta^{13}\text{C}_c$, $\delta^{13}\text{C}_m$, $\delta^{18}\text{O}_c$, $\delta^2\text{H}_m$ (black circles) records, and the 30 D_{rad} , CWT_{rad} , and CWT_{tan} sector chronologies (colored circles). (c) Correlations between the anatomical sector chronologies (I = left, X = right) and their main climate targets for 1861-2020 CE. Horizontal dashed lines indicate the significance level of $p < 0.01$ **147**
- Fig. 7.7** | Best-fit climate targets. Horizontal-mean (HOM) or 30-year-spline (30SP) detrended proxy chronologies (black curves), shown with the best-correlated climate records (colored curves). All records are z-transformed. TRW, $\delta^{13}\text{C}_c$, $\delta^{13}\text{C}_m$, $\delta^{18}\text{O}_c$, and $\delta^2\text{H}_m$ are inverted. R values indicate the corresponding correlations between the tree-ring and climate data for 1931-2020 CE (2017 CE for MXD). Right panels display field correlations ($p < 0.05$) between the HOM and 30SP-detrended proxies and their climate targets (CRU TS4.07). Thick frames highlight the best fitting frequency (HOM data is preferred). Black stars mark the study site **151**
- Fig. 7.8** | Paleoclimatic skill of the tree-ring proxies. Summary of the best-fit climate calibrations computed for 1931-2020 CE (1931-2017 CE for MXD). Please note that correlation and covariance values refer to the optimum frequency (high = 30SP, full = HOM data) and may deviate slightly from the values in Table 7.1 due to the shorter period **154**
- Fig. S7.1** | Tree-ring width (TRW) chronology of this study (black curves) compared to the well-replicated ($n = 872$ series) TRW chronology of Esper et al. (2021; grey curves) after detrending with (a) 30-year and (b) 100-year cubic smoothing splines (left panels). Boxplots (right panels) show the distribution of TRW indices over the 1861-2016 CE common period. Maximum latewood density (MXD) chronology of this study (black curves) compared to the well-replicated ($n = 192$ series) MXD chronology of Esper et al. (2020; grey curves) after detrending with (c) 30-year and (d) 100-year cubic smoothing splines. Boxplots show the distribution of MXD indices over the 1861-2017 CE common period. R values indicate correlations between the TRW and MXD chronologies calculated from 1861 to 2016 (TRW) and 2017 CE (MXD), respectively. All correlations are significant at $p < 0.001$ **166**
- Fig. S7.2** | Carbon isotope corrections. Raw mean chronologies of (a) cellulose ($\delta^{13}\text{C}_c$) and (b) methoxy ($\delta^{13}\text{C}_m$) stable carbon isotopes. Grey curves are the raw chronologies ($\delta^{13}\text{C}_{\text{raw}}$),

- black solid curves are the Suess-effect-corrected chronologies ($\delta^{13}\text{C}_{\text{atm}}$), and black dashed curves are the pin-corrected chronologies ($\delta^{13}\text{C}_{\text{pin}}$) 166
- Fig. S7.3** | Cambial ages of the individual series (grey lines) and their arithmetic mean (black lines) over the 1861-2020 CE period for (a) the TRW, TRSI and QWA data, and (b) the MXD data 167
- Fig. S7.4** | Individual series (grey lines) and mean chronologies (black lines) of raw (a) CWT_{rad} and (b) CWT_{tan} . Values (right top) are the arithmetic mean ± 1 standard deviation calculated over all tree rings between 1861-2020 CE. The mean chronologies of CWT_{rad} and CWT_{tan} correlate at $r = 0.77$ ($p < 0.001$) over the 1861-2020 CE common period 167
- Fig. S7.5** | Correlations between the 30SP-detrended proxy chronologies and diurnal temperature range for 1931-2020 CE. The $\delta^{13}\text{C}$ data are corrected for the Suess effect. Horizontal dashed lines indicate the significance level of $p < 0.01$. Please note that the significance level for MXD is marginally higher due to the shorter calibration period (1931-2017 CE), but is not displayed for the sake of clarity 167
- Fig. S7.6** | Correlations between the 30SP-detrended proxy chronologies and previous-year (a) mean air temperature (T_{mean}), (b) precipitation, (c) the PDSI, and (d) cloud cover data calculated for 1931-2020 CE. The $\delta^{13}\text{C}$ data are corrected for the Suess effect. Horizontal dashed lines indicate the significance level of $p < 0.01$. Please note that the significance level for MXD is marginally higher due to the shorter calibration period (1931-2017 CE), but is not displayed for the sake of clarity 168
- Fig. S7.7** | Squared coherence (1931-2020 CE) between (a-b) $\delta^{13}\text{C}_c$, (c-d) $\delta^{13}\text{C}_m$, (e-f) $\delta^{18}\text{O}_c$, (g-h) D_{rad} and June-August temperature (top panels) and precipitation (bottom panels). Grey dashed lines are the 95% confidence intervals 169
- Fig. S7.8** | Temperature (T_{mean}) and precipitation (Prec) signals in the Suess-effect-corrected (ATM) and pin-corrected (PIN) (a) $\delta^{13}\text{C}_c$ and (b) $\delta^{13}\text{C}_m$ data. Vertical bars (left) show correlations between the HOM-detrended $\delta^{13}\text{C}$ records and June-August T_{mean} (red) and precipitation (blue) for 1931-2020 CE. Curves in the right panels show 31-year running correlations for the different detrendings 169
- Fig. S7.9** | (a) Thirty-one-year running correlations between the detrended $\delta^2\text{H}_m$ chronologies and June-September mean temperature (JJAS T_{mean}) and between the detrended $\text{CWT}_{\text{rad.LW}}$ chronologies (mean of sectors VIII-X) and JJAS T_{mean} . Squared coherence between (b) $\delta^2\text{H}_m$ and JJAS T_{mean} and between (c) $\text{CWT}_{\text{rad.LW}}$ and JJAS T_{mean} for 1931-2020 CE. Grey dashed lines are the 95% confidence intervals 170
- Fig. S7.10** | (a) Z-scores of the HOM-detrended (annual) D_{rad} record (black line), raw June-August (JJA) precipitation (blue line), and JJA cloud cover (orange line). R values indicate correlations between D_{rad} and the climate records. (b) Corresponding 31-year running correlations between the HOM-detrended D_{rad} chronology and JJA precipitation and cloud cover, respectively (same colors as in panel a) 170
- Fig. S7.11** | Correlations between the 30SP-detrended D_{rad} sector chronologies (I = left, X = right) and T_{mean} calculated for 1931-2020 CE. Horizontal dashed lines indicate the significance level of $p < 0.01$ 170

- Fig. S7.12** | Squared coherence between the (a-f) precipitation-sensitive (blue labels) and (g-i) temperature-sensitive (red labels) proxies calculated for 1861-2020 CE (MXD for 1861-2017 CE). Grey dashed lines represent the 95% confidence intervals **171**
- Fig. S7.13** | Z-Scores of the (a-b) Suess-effect-corrected $\delta^{13}\text{C}_{\text{c_atm}}$ (black lines) and $\delta^{13}\text{C}_{\text{m_atm}}$ (grey lines) records, and (c-d) pin-corrected $\delta^{13}\text{C}_{\text{c_pin}}$ and Suess-effect-corrected $\delta^{13}\text{C}_{\text{m_atm}}$ records. Thick lines are 50-year cubic smoothing splines. Scatterplots on the right show the relationship between the $\delta^{13}\text{C}$ data. The single points are colored according to their year. Dashed lines are the linear trends **172**
- Fig. S7.14** | Z-scores of the $\delta^{18}\text{O}_{\text{c}}$ record (black lines) together with (a-b) annual and (c-d) summer precipitation $\delta^{18}\text{O}$ (blue lines). The precipitation $\delta^{18}\text{O}$ data are from Nelson et al. (2021) and were calculated for the Mt. Smolikas site (<https://isotope.bot.unibas.ch/PisoAI>). Scatterplots on the right show the relationships between $\delta^{18}\text{O}_{\text{c}}$ and seasonal precipitation $\delta^{18}\text{O}$ for 1950-2010 CE. Dashed lines are the linear trends **172**
- Fig. S7.15** | Seasonality of precipitation $\delta^2\text{H}$. The precipitation $\delta^2\text{H}$ data are from Nelson et al. (2021) and were calculated for the Mt. Smolikas site (<https://isotope.bot.unibas.ch/PisoAI>). The thick black line is the arithmetic mean and the shaded area indicates ± 1 standard deviation for 1950-2010 CE **173**

Chapter 8

- Fig. 8.1** | “Blue Rings” on stained microsections of *Pinus heldreichii* from Mt. Smolikas **178**

List of tables

Table 2.1 Characteristics of the southwest German tree-ring network	11
Table S2.1 Characteristics of the 46 TRW chronologies	35
Table 3.1 Characteristics of Mediterranean MXD records	50
Table S3.1 MXD site chronology characteristics	68
Table S3.2 MXD composite chronology characteristics	68
Table 4.1 Summary of the measured wood anatomical traits on the paraffin-embedded (<i>PAR</i>) and non-paraffin-embedded sections (<i>NoPAR</i>)	77
Table 5.1 TRW, MXD, and $\delta^{13}\text{C}$ statistics of the Mt. Smolikas tree-ring chronology	91
Table 5.2 ^{14}C and $\delta^{13}\text{C}$ dating results of sample <i>Pine16a</i>	94
Table S5.1 ^{14}C and $\delta^{13}\text{C}$ dating results of sample <i>Pine44b</i>	104
Table 6.1 Proxy characteristics	111
Table 6.2 Proxy covariance and age-trend estimates	115
Table 7.1 Proxy characteristics	142
Table 7.2 Correlations between the spline-detrended proxy chronologies for 1861-2020 CE	144
Table S7.1 Summary statistics of the sub-seasonal radial lumen diameter (D_{rad}) and cell wall thickness (CWT_{rad} and CWT_{tan}) chronologies	165
Table S7.2 Results of the principal component analysis (PCA) applied on the annual TRW, MXD, $\delta^{13}\text{C}_c$, $\delta^{13}\text{C}_m$, $\delta^{18}\text{O}_c$, $\delta^2\text{H}_m$, and the 30 D_{rad} , CWT_{rad} , and CWT_{tan} sector chronologies	165

List of abbreviations

ABC	age-band chronologies
AC1	first-order autocorrelation
AGR	average growth rate
AMS	accelerator mass spectrometer
AMXD	average maximum latewood density
BAI	basal area increment
BMEL	Bundesministerium für Ernährung und Landwirtschaft
CRU	Climate Research Unit
CWT	cell wall thickness (CWT _{rad} = radial orientation/CWT _{tan} = tangential orientation)
$\delta^{13}\text{C}_c$	stable carbon isotope ratio ($^{13}\text{C}/^{12}\text{C}$) of α -cellulose
$\delta^{13}\text{C}_m$	stable carbon isotope ratio ($^{13}\text{C}/^{12}\text{C}$) of lignin methoxy groups
$\delta^2\text{H}_m$	stable carbon hydrogen ratio ($^2\text{H}/^1\text{H}$) of lignin methoxy groups
$\delta^{18}\text{O}_c$	stable oxygen isotope ratio ($^{18}\text{O}/^{16}\text{O}$) of α -cellulose
D_h/D_{rad}	hydraulic/radial cell lumen diameter
EPS	expressed population signal
GLK	gleichläufigkeit
GPCC	Global Precipitation Climatology Centre
HGS	hugershoff curve standardization
IAEA	International Atomic Energy Agency
IntCal20	International Northern Hemisphere Radiocarbon Age Calibration Curve
IPCC	Intergovernmental Panel on Climate Change
IRMS	isotope-ratio mass spectrometer
KNMI	Royal Netherlands Meteorological Institute
MLA	mean lumen area
MSL	mean segment length
mUr	milli-Urey
MXD	maximum latewood density
NoPAR	non-paraffin-embedded samples
PAR	paraffin-embedded samples
PCA	principal component analysis
PDSI	Palmer Drought Severity Index
QWA	quantitative wood anatomy
RCS	regional curve standardization
RBAR	inter-series correlation
SD	standard deviation
SMI	soil moisture index
$T_{\text{mean}}/T_{\text{max}}$	mean/maximum air temperature
TRW	tree-ring width
TRSI	tree-ring stable isotopes
USGS	United States Geological Survey

Curriculum vitae

Not available online.

Scientific publications

Not available online.

Conference contributions

Not available online.